Time-Variable Electromagnetic Star-Planet Interaction in the TRAPPIST-1 System

Inaugural-Dissertation

zur

Erlangung des Doktorgrades

der Mathematisch-Naturwissenschaftlichen Fakultät

der Universität zu Köln

vorgelegt von

Christian Fischer

aus Kempen

Köln 2020

Berichterstatter: Prof. Dr. Joachim Saur
(Gutachter) Prof. Dr. Bülent Tezkan

Tag der mündlichen Prüfung: 11. September 2020

Abstract

Electromagnetic Star-Planet Interaction is the process, when planets in orbit around a star, couple to the star via the stellar magnetic field. The relative motion of the planet through the stellar wind plasma generates magnetohydrodynamic waves. If the stellar wind velocity at the planet is smaller than the local Alfvén speed, the generated Alfvén waves can travel upstream, against the plasma flow, towards the star. These waves establish a coupling between planet and star and transfer energy towards the star.

In our solar system, we have no star-planet interaction, because all planets are too far away from the sun to generate such a coupling. Instead, all planets generate bow shocks. However, the large moons of the giant planets in our solar system generate the similar effect of moon-magnetosphere interaction.

A problem of star-planet interaction is that it is hard to observe. The bright background of the stellar emissions further complicates a definite identification. Several observational studies found enhanced emissions in certain spectral lines of stars. However, it is unknown, what type of emissions star-planet interaction generates in stellar atmospheres. Therefore, one needs a further indicator that a planet generates the observed emissions. Temporal variability of the star-planet interaction can provide this missing information. Previous studies have looked for signals that appear with the planetary orbital period.

We show that temporal variability has a much larger variety than just the orbital period, which we assume as the simplest mechanism for variability. Three additional mechanisms can account for periodic variabilities with their distinct period. Tilted stellar dipole fields generate signals with half the synodic rotation period of the star as seen from the planet. Magnetic anomalies on the star may be triggered by star-planet interaction to erupt flares periodically with the synodic rotation period. The fourth proposed mechanism assumes an interaction between the star-planet interaction of two planets that would appear with the synodic rotation period between both planets. We call this process wing-wing interaction. For our studies, we choose the TRAPPIST-1 system, because its seven close-in planets make the system a perfect candidate for the search of star-planet interaction.

In the following, we conduct a semi-analytic parameter study to determine which planets could generate star-planet interaction. According to this study, the two innermost planets are the best candidates for the search of star-planet interaction. To understand the interaction better, we conduct time-dependent magnetohydrodynamic simulations of star-planet interaction. Our results show that the wave structure going towards the star is indeed purely Alfvénic and the power resembles the analytically predicted value very well. The waves that go away, however, comprise Alfvén waves, Slow Mode waves, Entropy waves and a Slow Shock. Those waves may affect the interaction of outer planets.

We investigate the scenario of wing-wing interaction with both inner planets of the TRAPPIST-1 system. The waves of the inner planet dissipate the coupling wave structure of the outer planet. Later, the compressional wave modes affect the interaction of the outer planet. Due to this simulation, we had to improve our proposed model for wing-wing interaction.

Our model setup also allows inhomogeneous stellar winds with coronal mass ejections. The mutual interaction between star-planet interaction and coronal mass ejection has not been investigated before. Our simulations show that the coronal mass ejection dislocates the coupling Alfvén wave structure.

In the final step of this thesis, we analyse the flares of TRAPPIST-1 that we have read out from a published light curve observed by the K2 mission. We assign each flare a duration and calculate Fourier transform and autocorrelation of the time series. Additionally, we test the significance of the results with statistical tests. These tests show that the obtained result indeed points at flare triggering by interaction with TRAPPIST-1 c.

Zusammenfassung

Im Rahmen dieser Arbeit befassen wir uns mit zeitlich variabler elektromagnetischer Stern-Planeten Kopplung. Das Objekt unseres Interesses ist das TRAPPIST-1 System. In diesem System wurden von *Gillon et al.* (2016, 2017) sieben erdähnliche Planeten gefunden, die aufgrund ihrer Nähe zum Zentralgestirn hervorragend für die Suche nach Stern-Planeten Kopplung geeignet sind. Wir verwenden verschiedene Methoden, um mögliche Stern-Planeten Kopplung im TRAPPIST-1 System zu beschreiben und zu verstehen.

Stern-Planeten Kopplung beschreibt allgemein die Wechselwirkung zwischen einem Stern und einem, den Stern umkreisenden Planeten. Es gibt ganz generell gravitative and elektromagnetische Wechselwirkungen zwischen Sternen und Planeten. Unter gravitative Wechselwirkung fallen beispielsweise Orbitalbewegungen und Gezeiten. Diese Art der Wechselwirkung ist wohlbekannt und verstanden. Die elektromagnetische Kopplung kann wiederum nur über das stellare Magnetfeld stattfinden und auch nur, wenn der Planet nah genug am Stern liegt. Der Stern emittiert einen radialen Plasmaausfluss, den sogenannten Sternwind. Das Magnetfeld rotiert mit dem Stern und ist an den Sternwind gekoppelt. Dadurch krümmt sich das Feld. Auf seiner Bahn um den Stern bremst der Planet nun das Plasma ab und erzeugt Störungen im Magnetfeld. Diese Interaktion passiert entweder über Stöße zwischen Neutralteilchen der Planetenatmosphäre und den Ionen des Plasmas oder über ein intrinsisches planetares Magnetfeld, das mit dem Plasma wechselwirkt. Dabei entstehen magnetohydrodynamische Plasmawellen. Die wichtigste dieser Wellen ist die Alfvénwelle, die nicht-dispersiv ist und sich rein entlang des Magnetfeldes fortbewegt. Dazu gibt es noch die magnetosonischen Wellen und die Entropie-Welle. Wenn die Bedingungen des Sternwindes nun sub-Alfvénisch sind, also die Plasmageschwindigkeit kleiner als die Gruppengeschwindigkeit der Alfvénwelle ist, dann können sich Alfvénwellen stromaufwärts entlang des Magnetfeldes zum Stern hin bewegen. Die fortlaufende Erzeugung von Alfvénwellen am Planeten führt zu einer durchgehenden Wellenstruktur, die im Bezugssystem des Planeten stationär ist. Besagte Wellenstruktur wird Alfvénflügel genannt und geht zurück auf die Erforschung der Interaktion zwischen Jupiter und seinem Mond Io (*Neubauer*, 1980). Der Alfvénflügel transportiert Energie in Form des Poyntingflusses zum Stern (*Saur et al.*, 2013). Dadurch besteht die Möglichkeit, dass Stern-Planeten Kopplung Strahlungsemissionen auf dem Stern erzeugt.

Die Beobachtbarkeit von Stern-Planeten Kopplung wiederum ist ein Problem. Im Sonnensystem kann man Jupiter räumlich auflösen und daher die Aurora-Fußabdrücke der Monde direkt beobachten und identifizieren (*Clarke et al.*, 2002). Bei Sternen, die viele Lichtjahre entfernt sind und dazu selbst hell leuchten, ist die Identifizierung von Signalen der Stern-Planeten Kopplung schwierig und räumliche Auflösung weitestgehend nicht möglich. Deswegen fokussieren sich Beobachtungen auf gewisse spektrale Bereiche, wie chromosphärische Emissionslinien (*Shkolnik et al.*, 2003; *Walker et al.*, 2008; *Staab et al.*, 2017), ultraviolette Emissio-

nen (*France et al.*, 2016; *France et al.*, 2018) oder koronale Röntgenemissionen (*Scharf*, 2010; *Poppenhaeger et al.*, 2010). Um Exzessemissionen eindeutig auf einen planetaren Ursprung zurückführen zu können, muss ein Bezug zum Planeten, zum Beispiel über eine gewisse Periodizität hergestellt werden. *Shkolnik et al.* (2003) haben in einigen der Beobachtungen einen Bezug zwischen erhöhten Emissionen und der Orbitalperiode des Planeten festgestellt. Wir erweitern das Bild der zeitlichen Variabilität in der Stern-Planeten Kopplung. Dazu präsentieren wir vier verschiedene Mechanismen, die verantwortlich für Variabilitäten sein können und eindeutige Perioden aufweisen. Der Einfachste der beschriebenen Mechanismen befasst sich mit der reinen Sichtbarkeit von Emissionen. Der Planet bewegt sich um den Stern und der Alfvénflügel erzeugt Emissionen auf dem Stern. Dabei gibt es eine der Erde zugewandte Hemisphäre, auf der die Emissionen sichtbar sind und eine abgewandte Seite. Dadurch entsteht eine Variabilität mit der Orbitalperiode des Planeten. Der zweite Mechanismus ist ähnlich, nimmt allerdings ein geneigtes Dipolfeld auf dem Stern an. Da der Poyntingfluss von der Magnetfeldstärke um den Planeten herum abhängt, variiert er in einem geneigten Dipolfeld. Da der Planet den Stern umkreist, der Stern samt Magnetfeld rotiert und das Feld geneigt ist, erhält man die halbe synodische Rotationsperiode als Interaktionsperiode. Der dritte Mechanismus nimmt eine nicht-lineare Interaktion zwischen dem planetaren Alfvénflügel und einer lokal begrenzten magnetischen Anomalie auf dem Stern an. Nach *Lanza* (2018) erzeugt diese Interaktion sogenannte Flares auf dem Stern, also immens helle Eruptionen. Da die angenommene Anomalie mit dem Stern rotiert, ist die Interaktionsperiode die synodische Rotationsperiode des Sterns aus Sicht des Planeten. Ein vierter Mechanismus ist die angenommene Interaktion zwischen den Alfvénflügeln zweier Planeten, die sogenannte Flügel-Flügel Wechselwirkung. Die erwartete Variation tritt mit der synodischen Periode zwischen beiden Planeten auf. Insgesamt lässt sich sagen, dass zeitliche Variabilität in Stern-Planeten Kopplung deutlich umfangreicher ist als die reine Orbitalperiode des Planeten.

Als ersten Schritt in unseren Modellstudien führen wir eine semi-analytische Parameterstudie durch. Basierend auf dem Sternwindmodell von *Parker* (1958) und dem Poyntingfluss für Stern-Planeten Kopplung nach *Saur et al.* (2013), versuchen wir zu bestimmen, welche Planeten Stern-Planeten Kopplung erzeugen. Dazu bestimmen wir die Alfvén Machzahl, welche das Verhältnis aus Sternwindgeschwindigkeit zu Alfvéngeschwindigkeit darstellt. Wenn diese Zahl kleiner als Eins ist, liegen sub-Alfvénische Bedingungen vor und Stern-Planeten Kopplung ist möglich. Für all jene Fälle, die die Kopplung ermöglichen, berechnen wir die erwarteten Poyntingflüsse. Die besten Kandidaten für Stern-Planeten Kopplung sind demnach die beiden innersten Planeten von TRAPPIST-1. Allerdings stellt der unbekannte Massenausfluss des Sterns eine große Quelle der Unsicherheit dar. Je nachdem wie stark dieser ist, können theoretisch alle oder gar keiner der Planeten koppeln.

Im nächsten Schritt untersuchen wir die Details der Stern-Planeten Kopplung mit einem magnetohydrodynamischen (MHD) Modell für TRAPPIST-1 b. Dazu erweitern wir den MHD-Code PLUTO (*Mignone et al.*, 2007) um Quellterme, die Stöße zwischen atmosphärischen Neutralteilchen und Ionen des Plasmas berechnen. Damit kann man ein Modellszenario erschaffen, in dem ein Planet als Neutralgaswolke parametrisiert wird und sich um den zentralen Stern bewegt. Die Rechnungen werden in Kugelkoordinaten durchgeführt. Die wichtigste Wellenmode für die Stern-Planeten Kopplung ist die zum Stern laufende Alfvénwelle. Allerdings treten auch andere Wellen auf. In unserer MHD Simulation untersuchen wir die auftretenden Wellenstrukturen detailliert. Der einwärts in Richtung Stern laufende Alfvénflügel ist rein Alfvénisch und verläuft entlang einer Charakeristik, die nur um 2° vom Magnetfeld abweicht. Der Poyntingfluss nah am Planeten bestätigt den analytisch berechneten Wert nach dem Modell von *Saur et al.* (2013). Der Poyntingfluss fällt weitgehend linear zum Stern hin ab, was auf Dissipationsprozesse hindeutet. Es kann bisher nicht genau festgestellt werden, wie stark der Anteil physikalischer Effekte an der Dissipation ist. Allerdings ist die Auflösung des Simulationsgitters zwischen Stern und Planet recht grob, bezogen auf den Planeten. Daher werden numerische Dissipationseffekte eine große Rolle spielen. Da der Sternwind zwar sub-Alfvénisch, aber super-sonisch ist, bewegen sich die anderen Wellen vom Stern weg. Diese Wellen folgen ihrer jeweiligen Wellencharakteristik und sind anhand dessen sowie anhand ihrer Eigenschaften identifizierbar.

Auf Basis der bisherigen Erkenntnisse untersuchen wir im Folgenden Effekte, die eine zeitliche Variabilität der Stern-Planeten Kopplung hervorrufen. Wir führen zuerst Simulationen zur Flügel-Flügel Wechselwirkung zwischen den beiden Planeten TRAPPIST-1 b und c durch. Durch das zeitabhängige MHD Modell kann theoretisch ein ganzes Planetensystem simuliert werden. Die Simulation hat gezeigt, dass die Variabilität darin besteht, dass die am Stern ankommende Leistung um den Anteil des äußeren Planeten reduziert ist. Die Reduktion tritt über die Zeit auf, in der der äußere Planet den äußeren Alfvénflügel des inneren Planeten durchquert plus die Laufzeit der Alfvénwelle zum Stern, da sich der innere Alfvénflügel erst wieder neu aufbauen muss.

Eine weitere MHD Simulation untersucht den Effekt eines koronalen Massenauswurfes auf die Stern-Planeten Kopplung. Der Auswurf lehnt sich an den "schmalen Auswurf" nach *Chen* (2011) an. Demnach ist der simulierte Auswurf mit einem gestreckten Jet zu vergleichen, der entlang der offenen Feldlinien des Sternwindes verläuft. Der Auswurf ist gegeben durch eine erhöhte Dichte und Geschwindigkeit, wodurch in seinem Inneren super-Alfvénische Bedingungen herrschen. Erwartungsgemäß kann sich der Alfvénflügel innerhalb des Auswurfes nicht zum Stern fortbewegen. Stattdessen bildet sich eine Shock-artige Struktur, bei der die Alfvénwellen auswärts verlaufen, am Rand des koronalen Massenauswurfes umdrehen und sich zum Stern bewegen. Der Alfvénflügel wird daher nicht unterbrochen, sondern räumlich versetzt und bewegt sich vorerst nicht weiter. Erst wenn der Planet aus dem Massenauswurf austritt, kann der Alfvénflügel wieder seinem üblichen Pfad folgen. In dieser Form entspricht diese Simulation nicht den Mechanismen, die periodische Variabilitäten erzeugen, sondern ist als Vorstufe zu einer Simulation des Trigger-Mechanismus für Flares zu sehen.

Im letzten Schritt untersuchen wir die Flares von TRAPPIST-1, die im Rahmen der K2-Mission beobachtet wurden. Dazu lesen wir die Flares aus der Lichtkurve, die von *Luger et al.* (2017) publiziert wurde, aus. Im Anschluss wenden wir ein empirisches Modell von *Davenport et al.* (2014) an, um den Flares eine gewisse Dauer zu geben. Basierend darauf können wir die Fouriertransformation und die Autokorrelation der Flare Zeitreihe berechnen. Wir finden eine herausragende Korrelation bei neun Tagen, was der synodischen Rotationsperiode von TRAPPIST-1 c entspricht. Dies ist ein Indiz dafür, dass Flares durch Stern-Planeten Kopplung dieses Planeten ausgelöst werden könnten. Um die Signifikanz des Ergebnisses besser abschätzen zu können, führen wir statistische Tests durch. Als Nullhypothese nehmen wir an, dass Flares ohne Einfluss von Planeten zufällig auftreten. Dazu berechnen wir aus 1000 zufälligen Zeitreihen die Fouriertransformation und Autokorrelation. Demnach hätte das erhaltene Signal eine Signifikanz von ungefähr $2\,\sigma$. Weiterhin führen wir Tests mit künstlichen periodisch auftretenden Flares durch. Demnach kann nur TRAPPIST-1 c die Beobachtungen erklären, wenn man weiterhin annimmt, dass die Flares nicht strikt periodisch auftreten und es eine Form von Clustering gibt, also mehr Flares auftreten, als von einer einzigen Anomalie zu erwarten wären.

Alles in Allem bildet diese Dissertation einen ersten Schritt zu einem besseren Verständnis der dynamischen und nicht-linearen Prozesse, die zu zeitlich variabler Stern-Planeten Kopplung führen. Darüber hinaus haben wir dadurch ein besseres Verständnis von möglicher Stern-Planeten Kopplung im TRAPPIST-1 System und weitere Hinweise für die Existenz dieses Prozesses über eine gänzlich neue Methode erlangt.

Contents

1 Introduction 1

2 Exoplanets, Stars and their Interaction - The State of Knowledge 3

- 2.1 What are Exoplanets? 3
  - 2.1.1 Types of Exoplanets 3
  - 2.1.2 Habitability 5
  - 2.1.3 Detection Methods 6
- 2.2 A Short Note on Stars 8
  - 2.2.1 Types of Stars and Spectral Classes 9
  - 2.2.2 Stellar Structure: Interior and Atmosphere 10
  - 2.2.3 Stellar Magnetic Fields and related Phenomena 11
- 2.3 TRAPPIST-1 12
  - 2.3.1 The Star 12
  - 2.3.2 The Planetary System 13
- 2.4 State of Research about Electromagnetic Star-Planet Interaction . . 15
  - 2.4.1 The Situation in our Solar System 15
  - 2.4.2 Observations of Star-Planet Interaction 17
  - 2.4.3 Theory and Modelling - an Overview 18

3 Star-Planet Interaction - Theory and Concepts 21

- 3.1 Magnetohydrodynamics and Wave Theory 21
  - 3.1.1 MHD Equations 21
  - 3.1.2 MHD Waves 23
- 3.2 Stellar Wind and Magnetic Field 25
- 3.3 Sub-Alfvénic Interaction 27
  - 3.3.1 Alfvén Wing Model 27
  - 3.3.2 Types of Interaction 28
  - 3.3.3 Poynting Flux 30
- 3.4 Time-variability in Star-Planet Interaction 31
  - 3.4.1 Conceptual Basics for Time-Variability 31
  - 3.4.2 Visibility 33
  - 3.4.3 Tilted Stellar Dipole Field 33
  - 3.4.4 Flare Triggering 34
  - 3.4.5 Wing-Wing Interaction 36

4 Is SPI possible at TRAPPIST-1? - A Parameter Study 39

- 4.1 Parameter Space 39
- 4.2 Where can we expect SPI? 40
  - 4.2.1 Alfvén Mach Number 40
  - 4.2.2 Sensitivity of the Alfvén Mach Number to Uncertainties of the Parameters 42

4.3 Expected Strength of the SPI . . . 43
  4.3.1 Poynting Fluxes . . . 44
  4.3.2 Sensitivity of the Poynting flux to Uncertainties of the Parameters . . . 45
  4.3.3 Changes in Case of Intrinsic Planetary Magnetic Fields . . . 46

5 SPI Wave Structures 49
5.1 MHD Simulation Setup . . . 49
  5.1.1 Model Equations and PLUTO Code . . . 49
  5.1.2 Stellar Wind Setup . . . 51
  5.1.3 SPI Setup . . . 55
  5.1.4 Grid Structures and Physical Parameters . . . 58
5.2 Spatial Structure of the Steady-State Stellar Wind . . . 61
5.3 Methods for the Wave Analysis . . . 63
5.4 The Inward Going Alfvén Wing . . . 64
  5.4.1 Path in the Stellar Wind . . . 64
  5.4.2 Properties of the Wing . . . 65
  5.4.3 Energetics of the Alfvén Wing . . . 67
5.5 The Outward Going Wave Structures . . . 73
  5.5.1 Wave pattern . . . 73
  5.5.2 Alfvén Wing . . . 76
  5.5.3 Slow Mode and Slow Shock . . . 77
  5.5.4 Wake . . . 80

6 Wing-Wing Interaction 81
6.1 MHD Setup with Two Planets . . . 81
6.2 SPI From Two Planets . . . 82
6.3 Temporal Evolution of the Star-Planet Interaction . . . 84
  6.3.1 On Wave-Wave Interactions . . . 84
  6.3.2 Alfvén Wings Over Time . . . 84
  6.3.3 Compressional Waves Over Time . . . 88
6.4 Implications for Time-Variability in SPI . . . 89

7 The Effect of a Coronal Mass Ejection on SPI 91
7.1 Modelling CME and Planet . . . 91
  7.1.1 How to Align Planet and CME . . . 92
7.2 The Stellar Wind with a CME . . . 93
7.3 Time-Variable Wave Pattern . . . 95
  7.3.1 The Alfvén Wing at Ingress . . . 96
  7.3.2 The Alfvén Wing at Egress . . . 98

8 Flare Triggering at TRAPPIST-1 101
8.1 Observability of SPI . . . 101
8.2 Flares at TRAPPIST-1 . . . 102
8.3 Analysis of the Flare Time-Series . . . 102
  8.3.1 Giving Flares a Duration . . . 102
  8.3.2 Fourier Analysis and Autocorrelation . . . 103
  8.3.3 Significance Tests . . . 104

8.4 Triggered Flares at TRAPPIST-1? 106
8.4.1 Fourier Spectra and Autocorrelation 106
8.4.2 Null Hypothesis 107
8.4.3 Artificial Triggering Signals 108
8.5 Visibility of Triggered Flares at TRAPPIST-1 114

9 Conclusions **117**

Bibliography **121**

Research Data Management **141**

Acknowledgements **143**

Eidesstattliche Erklärung **145**

1 Introduction

Electromagnetic Star-Planet Interaction (SPI) describes the coupling between planets and their host stars via the stellar magnetic field. This type of coupling does not exist between the Sun and its planets. Therefore, research has to rely on other stellar systems, where the planets are much closer to their star. Accordingly, the field of star-planet interaction is relatively young, like all fields of exoplanet research. *Cuntz et al.* (2000) and *Rubenstein and Schaefer* (2000) were the first who proposed that electromagnetic coupling between planets and their stars may enhance the stellar activity. *Shkolnik et al.* (2003) claimed the first detection of SPI in a system called HD 179949. Soon afterwards, first MHD modelling studies simulated SPI (*Ip et al.*, 2004; *Preusse et al.*, 2005).

The coupling between planet and star establishes via Alfvén waves that move from the planet to the star and carry energy (*Neubauer*, 1980; *Saur et al.*, 2013). However, the stellar wind accelerates with distance from the star, and the Alfvén speed reduces with distance. Therefore, at some point, the wave speed is lower than the wind velocity and the waves cannot travel upstream towards the star anymore. All solar system planets lie outside this so-called Alfvén radius, which is the reason why there is no SPI in the Solar System.

In our solar system, we have the well studied analogous phenomenon of moon-magnetosphere coupling. The prime example of moon-magnetosphere coupling is the interaction between Jupiter and its moon Io. This interaction generates bright auroral spots in Jupiter's ionosphere (*Clarke et al.*, 1996; *Clarke et al.*, 2002), also called auroral footprints. First hints for an interaction between Jupiter and Io came from radio observations (*Bigg*, 1964), followed by in-situ observations with Voyager (*Acuna et al.*, 1981), observations in the infrared (*Connerney et al.*, 1993) and the UV with the Hubble Space Telescope (*Clarke et al.*, 1996).

All observations of the footprints have in common that one can spatially resolve the footprint. Something like that is not (yet) possible in the case of star-planet interaction, which makes it challenging to distinguish related emissions. Observations become especially difficult because stars themselves are very luminous and variable. Therefore, current observational approaches often concentrate on certain wavelength ranges to better resolve excess emissions. Typical examples are the chromospheric Ca II K and H lines (*Shkolnik et al.*, 2003), enhanced coronal X-ray emissions (*Saar et al.*, 2008) or the radio range (*Zarka*, 2007). However, in addition to difficulties with spatial resolution, we have no evidence about the wavelengths that SPI may excite. That makes spectral observations somewhat prone to misinterpretations. Observations, therefore, require additional indicators that point at a planetary origin of the observed emissions.

One possibility that can show a connection between stellar emissions and planets are temporal variabilities in the strength of the SPI. Evidence of certain periodicities that can only appear from an interaction between planet and star help to identify SPI in stellar signals. Such an approach was applied by *Shkolnik et al.*

(2003). The authors identified a short sequence of signals in observations of HD 179949 that appears with the orbital period of the close-in planet. However, the possible range of periods is much larger than the pure orbital period of the planet. In this work, we will, therefore, present and investigate different mechanisms that cause temporal variability in SPI.

To provide a comprehensive overview of the whole topic of star-planet interaction, we present the current state of research in chapter 2. The chapter comprises general introductions towards exoplanets and stars. On that basis, we will introduce the TRAPPIST-1 system. Due to its seven terrestrial planets in close orbit around the star (*Gillon et al.*, 2016, 2017) it is an exciting target for the research of SPI. At the end of the chapter, we will introduce the state of research about star-planet interaction and moon-magnetosphere interaction.

In chapter 3, we introduce the necessary theory for our studies. That involves MHD wave theory, the applied analytic stellar wind model based on *Parker* (1958) and theory towards sub-Alfvénic interaction based on *Neubauer* (1980) and *Saur et al.* (2013). In section 3.4, we present our contribution to the concepts of SPI, with the characterisation of four different mechanisms for time-variable SPI.

Chapter 4 presents the results of the semi-analytic parameter study. The chapter aims to find out if TRAPPIST-1 is a suitable candidate for the search for SPI. Additionally, we determine the expected strengths of SPI.

In chapter 5, we present our MHD model setup to simulate time-variable SPI. We perform an extensive analysis of the wave structures that belong to star-planet interaction. Additionally, to the effects described in chapter 5, we analyse two additional scenarios that require full time-dependence of the model. The first one involves the planets TRAPPIST-1 b and c, which we simulate to investigate their mutual electromagnetic interaction. chapter 6 presents the respective time-dependent results. The final subject of MHD modelling investigates how a coronal mass ejection affects SPI (chapter 7).

The last part of our results in chapter 8 deals with the analysis of flares observed in the TRAPPIST-1 system. We present the results of the Fourier transform and the autocorrelation that are published in *Fischer and Saur* (2019). Additionally, we perform statistical tests to determine the significance of the obtained results.

Finally, in chapter 9, we wrap everything up and conclude our findings.

2 Exoplanets, Stars and their Interaction - The State of Knowledge

In this chapter, we will introduce the reader to the current state of knowledge about Star-Planet Interaction (SPI) and the main target of our studies, the TRAPPIST-1 system. However, first we will introduce exoplanets and stars with their respective properties.

2.1 What are Exoplanets?

Planets outside our solar system are called 'extrasolar planets' or, more commonly, 'exoplanets'. Currently we know about 4141 confirmed exoplanets (NASA Exoplanet Archive, 26th March 2020). About 1254 planets have radii below two Earth radii and from these about 403 have radii smaller than $1.25\,R_{\mathrm{E}}$.

Our Solar System hosts eight planets, plus a large number of dwarf planets and moons. The Solar System planets have strongly influenced cultures and religions here on Earth and today they wear the names of ancient gods. About as much influence as our planets have on us, the stars we see in the night sky caught our interest and stimulated our imagination. The idea of unknown, inhabited worlds around other stars has even inspired modern popular culture. We still do not know whether we are alone in the universe or not, but for 25 years already, we know about the existence of planets outside our solar system (*Mayor and Queloz*, 1995).

In this section we will introduce exoplanets in general. We start with an overview of the different types of exoplanets. The question if we are alone or not is an important driver for the enormous interest in exoplanets. Therefore we will talk briefly about the topic of habitable zones and planets therein. Finally we address the most important detection methods for exoplanets.

2.1.1 Types of Exoplanets

A unified classification of exoplanets is yet to be established, as exoplanets show a large variation in their properties. Possible characteristics for a classification are for example size and mass, composition or orbital properties. However, the most common classification is the one applied for the Solar System planets, which takes size, mass and composition into account. This system typically divides planets into the three classes of gas giants, ice giants and rocky terrestrial planets. In the context of exoplanets, several subclasses appear due to the large variations of their properties mentioned above. In this section we will introduce the three main classes and their corresponding subclasses.

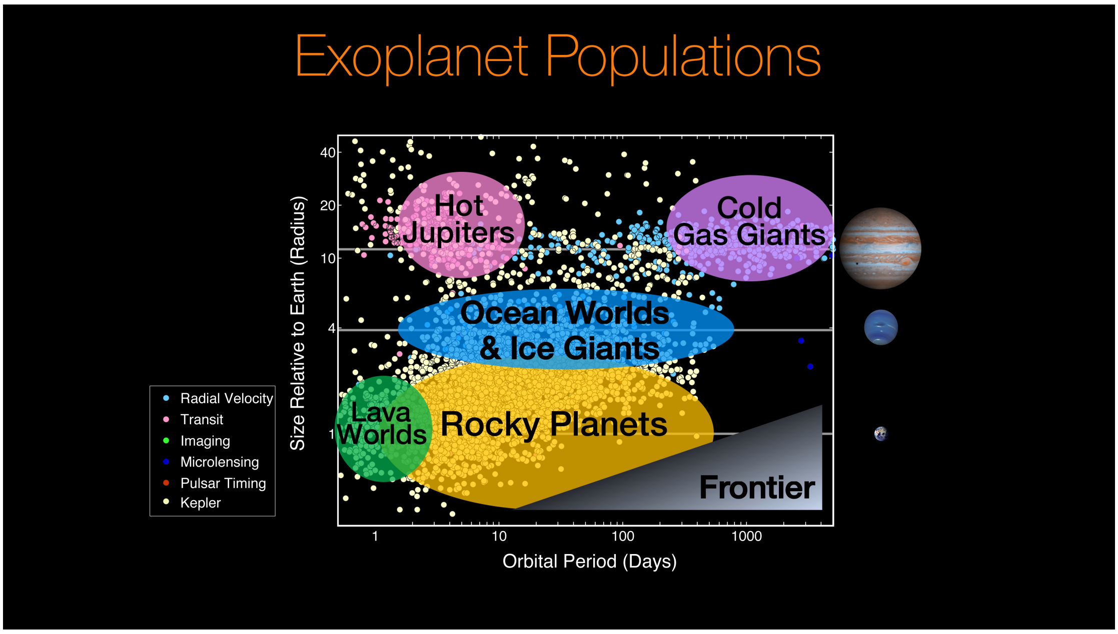

Figure 2.1: Exoplanet population as of August 2017 with sketched approximate classification. (Credit: NASA/Ames Research Center/Natalie Batalha/Wendy Stenzel, `https://www.nasa.gov/image-feature/ames/kepler/exoplanet-populations`).

Some of the typical classes and subclasses of exoplanets are sketched in Figure 2.1. The figure shows a scatter plot of all detected exoplanets until August 2017 plotting the planet radius in units of Earth radii against the orbital period in days. For comparison Jupiter, Neptune and Earth are drawn at their respective position on the y-axis. Different classes of exoplanets are indicated by different shadings.

We will start with the gas giants. In Figure 2.1 those are the planets at the very top, shaded with red and purple. In the Solar System, Jupiter and Saturn belong to this class. Jupiter is often used as a default for gas giant exoplanets, much like Earth for the smaller, rocky planets. Gas giants represent the largest and heaviest planets that consist mostly of hydrogen and helium (*Militzer et al.*, 2016). Masses lie in the range between approximately 1 and 13 Jupiter masses. The lower mass boundary is not clearly defined, whereas the upper boundary represents the minimum mass where deuterium fusion sets in and the object is classified as a brown dwarf (*Burgasser*, 2008). From Jupiter and Saturn are expected to have a solid core (*Militzer et al.*, 2016) and a thick layer of metallic hydrogen (*Militzer et al.*, 2016). At Jupiter this layer is considered to extend from the core up to $0.85\,R_\mathrm{J}$ (*Connerney et al.*, 2018). This layer acts as Jupiter's dynamo region and is responsible for the strong jovian magnetic field (*Militzer et al.*, 2016). A subclass of gas giants are the so-called Hot Jupiters. Those planets are extremely close to their host stars, most of them with orbital periods of a few days (Figure 2.1), where strong stellar irradiation heats up the planets' atmospheres. For comparison, Jupiter's orbital period is 4330 days. The first detected and confirmed Hot Jupiter was the planet 51 Peg b (*Mayor and Queloz*, 1995).

The next smaller class of planets are the ice giants with an approximate radius of four Earth radii. In the Solar System Uranus and Neptune belong to this class. Ice giants like Neptune consist largely of methane, ammonia and water (*Hubbard* *et al.*, 1991) and to lesser extent of hydrogen and helium, unlike the gas giants. Therefore ice giants are expected to harbour thick layers of ice beneath a gaseous surface layer (*Helled et al.*, 2020). To date most known planets of this kind are much closer to their host star than Uranus and Neptune are to the Sun. Among the ice giants, there two notable subclasses: Mini-Neptunes and Warm/Hot Neptunes. The latter class, just like Hot Jupiters, are planets that are very close to their host star and receive high irradiation. The first class differs in size from the ice giants and poses a conflict with the terrestrial planets, which will be discussed later.

The smallest class are rocky planets, also called terrestrial planets. Rocky planets typically have small radii of $R_\mathrm{p} < 2\,R_\mathrm{E}$. In our Solar System the inner planets Mercury, Venus, Earth and Mars belong to this class, as well as all dwarf planets, e.g. Pluto and Ceres. Planets in this class consist mostly of a solid planetary body and are silicate and metal rich. Their densities are therefore much larger than the densities of the bigger planet classes. Additionally, these planets can have gaseous envelopes in form of atmospheres or exospheres. The example of the Earth shows that planets can also have hydrospheres in form of oceans and a global water cycle. The icy moons of Jupiter and Saturn even have global oceans beneath their ice crust. Saturn's moon Titan is an example of an alternative type of hydrosphere consisting of nitrogen and methane (*Dermott and Sagan*, 1995; *Tokano et al.*, 2006).

Terrestrial planets have radii up to two Earth radii, which is considered to be the boundary towards Mini-Neptunes (*Fabrycky et al.*, 2014). A subclass of planets that may hypothetically exist at the boundary between Super-Earths and Mini-Neptunes are ocean planets (*Kuchner*, 2003; *Léger et al.*, 2004). Those worlds would have a thick surface layer of water in contrast to Mini-Neptunes that would have an extended hydrogen rich atmosphere (*de Mooij et al.*, 2012). Possible ocean planet candidates are GJ 1214 b (*Charbonneau et al.*, 2009; *Berta et al.*, 2012) and Kepler-62 e and f (*Kaltenegger et al.*, 2013).

The hypothetical rocky-planet-analogue to Hot Jupiters are the so-called lava planets. While Hot Jupiters heat up due to intense irradiation from the star, lava planets are believed to be primarily heated by extreme tidal forces from the star (*Henning et al.*, 2009). Recently *Kislyakova et al.* (2018) showed that magnetic induction in a planet embedded in a strong and variable magnetic field may cause internal heating that is comparable to Io's tidal heating and may cause volcanism on a planet. A potential candidate for such a planet subclass is COROT-7b (*Barnes et al.*, 2010).

2.1.2 Habitability

The search for extraterrestrial life is a major motivation for exoplanet research and strongly linked to the question of habitability. From the Solar System we know that by far not all planets support the evolution of life. In fact, life as we know it from Earth, requires very special conditions. Therefore this section is dedicated to the topic of planetary habitability.

The key concept behind the idea of planetary habitability is the *habitable zone*. In astrophysics this zone is defined as the distance range around a star where liquid water can exist on the surface of a terrestrial planet (*Seager*, 2013). Historically, the concept of a zone where the stellar irradiation affects the suitability of

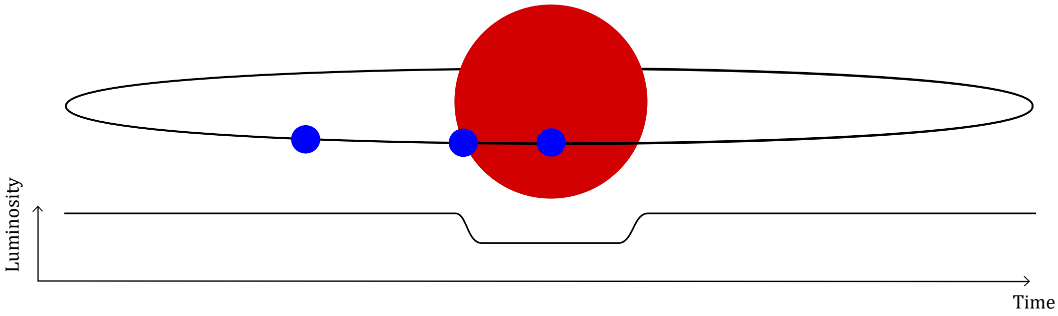

Figure 2.2: Sketch of the principle concept behind the transit method.

a planet for life, has first been published by *Huang* (1959). *Kasting et al.* (1993) modelled the habitable zone for main sequence stars and planets with Earth-like atmospheres, consisting of CO_2, H_2O and N_2. The planetary atmospheres ensure a stable temperature via a green house effect. The authors also describe a common extension of the habitable zone into a conservative and an optimistic habitable zone. In the conservative view, the inner edge of the habitable zone is determined by the photolysis of water and the escape of hydrogen. The outer edge is determined by the formation of CO_2 clouds. *Kasting et al.* (1993) estimate the conservative habitable zone to be in the range between 0.95 AU and 1.15 AU. The optimistic view extends the boundaries of the habitable zone. It is based on observations of Venus and Mars that indicate the presence of liquid water on both planets in the past. *Kasting et al.* (1993) estimate the solar radiation at the time of the presence of liquid water at both planets and conclude that early Mars received about 30% of today's Earth's radiation and recent Venus about 170%. The corresponding range extends from 0.75 AU to 1.77 AU. However, the estimation of the habitable zone varies due to several factors, especially the atmospheric composition and the assumed effects of the greenhouse effect. Therefore other authors come up with different estimates.

The concept of the habitable zone is of major interest in astronomy, since the orbital distance of a planet can be observed. Actual habitability however is also affected by various other effects. *Lammer et al.* (2009) review those factors including geophysical processes, like plate tectonics, a dynamo process and accordingly the existence of a planetary magnetic field. A magnetic field shields the atmosphere of a planet from the stellar wind and more dangerous effects like flares and coronal mass ejections (*Lammer et al.*, 2009). The authors also discuss the possibility of other types of habitats outside the habitable zone. The icy moons in our Solar System are known to harbour subsurface water oceans and therefore may be habitable. We know from Earth that early biotopes evolved around black smokers in the deep sea (*Lammer et al.*, 2009).

2.1.3 Detection Methods

Here we will introduce common methods to detect exoplanets. The focus lies on the two most important methods: the transit method and the radial velocity method. The next best notable methods are gravitational microlensing and direct imaging, but their contributions to the number of detections are small. There are other methods as well, which are sometimes specialisations of the mentioned methods, but until today, their detection numbers are negligible.

2.1.3.1 Transit Method

The principle behind the transit method is fairly simple: A star emits light and if a planet is in front of the star it blocks some of the emitted light. Figure 2.2 shows a sketch of the situation. One sees a star and measure its luminosity as a function of time. This observation technique is called photometry and yields a so-called stellar light curve, which is sketched below the star. The sketch further depicts a planet at three different positions on its orbit around the star and the effect on the stellar light curve. At first the planet is not in front of the stellar disk and has no effect on the light curve. Later it passes the stellar limb and initiates its transit across the stellar disk, visible as a ramp of decreasing luminosity in the light curve. As soon as the planet is completely in front of the star the dip in the light curve reaches its maximum. This is called the transit depth. Later the planet moves out of the stellar path and one sees the full stellar luminosity again.

In general the transit method can provide information about the planet's radius, the orbital period and, given the detector is sufficiently sensitive, also about the planetary atmosphere from absorption features. The Hot Jupiter HD 209458 b was the first planet, detected by the transit method (*Charbonneau et al.*, 2000). The method also allowed to probe the planetary atmosphere. For example *Charbonneau et al.* (2002) reported the first ever exoplanet atmosphere and *Barman* (2007) found evidence for water vapour in the planet's atmosphere.

The search for transits is more effective from space, because it avoids disturbing effects from Earth's atmosphere. The first space telescope designed to search for exoplanets with the transit method was the french COROT-mission from 2006 to 2013. The most successful 'planet hunter' to date is the Kepler space telescope. It started in March 2009 to follow the Earth on a solar orbit. The mission was designed to observe a fixed field of view for several years and detect Earth-like planets at about 1 AU around sun-like stars. After the failure of two reaction wheels, the original mission could not be prolonged but instead, the field of view was shifted into the ecliptic and changed every 83 days. The new mission was named K2 and should find more short-period planets from 2014 to 2018. *Borucki et al.* (2010) reported the first results on short period transiting exoplanets observed by the Kepler-mission. *Fressin et al.* (2012) found the first Earth-sized exoplanet and *Jenkins et al.* (2015) found the first Earth-sized exoplanet in the habitable zone of a sun-like star. The first planet found by the K2-mission was HIP 116454 b (*Vanderburg et al.*, 2015).

The NASA Exoplanet Archive lists 4141 exoplanets (23rd March 2020, as for the following numbers of this paragraph) where 2348 have been discovered by Kepler and 397 by K2. In addition both missions provided 3309 candidates that still have to be confirmed. Therefore Kepler is also the main reason that the transit method is the most successful method in detecting exoplanets so far. Kepler's successor, the TESS-telescope is currently in space (start 2018) and ends its primary mission mid 2020.

2.1.3.2 Radial Velocity Method

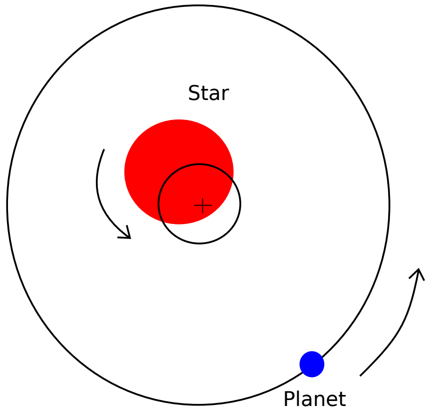

Figure 2.3: Physical principle behind the radial velocity method.

The radial velocity method bases on spectral variations of the stellar light. When a planet orbits a star, then both objects revolve around the mutual centre of mass. Figure 2.3 visualises the physics behind the idea. The black circles sketch the orbits of the stellar and the planetary orbits around centre of mass respectively, and the cross indicates the common centre of mass. Due to the many times larger mass of the star, the stellar motion is weaker than the planetary motion. The stellar motion however causes a Doppler shift of the stellar radiation. If the star moves towards the observer there is a blue shift and when it moves away from the observer there is a red shift. Blue shift means that the light has a shorter wavelength and red shift implies a slightly longer wavelength.

The radial velocity method is the oldest method, dating back to the discovery of the Hot Jupiter 51 Peg b (*Mayor and Queloz*, 1995). Today giant planets further away from their star are detectable or close in rocky planets around small stars. An example for Jupiter-analogues is HD 154345 b (*Wright et al.*, 2007; *Boisse et al.*, 2012). An example for small planets around a Red dwarf is Proxima Centauri b (*Anglada-Escudé et al.*, 2016)

2.1.3.3 Further Methods

There are a few more methods, which are not as successful as the methods described before. The most notable methods are gravitational microlensing and direct imaging.

Direct imaging is an approach to see an exoplanet directly. It typically requires a system close to our Solar System, where the planet is large and far away from its host star. In such a constellation one can distinguish the planet from the star. Due to typical planetary temperatures the maximum of the emissions lies in the infrared wavelength range. An early finding is the planet 2M1207b (*Chauvin et al.*, 2004), which orbits a faint brown dwarf at a distance of 55 AU. The planet is quite hot on its own due to gravitational contraction (*Mohanty et al.*, 2007)

Gavitational microlensing bases on relativistic effects. It requires two stars to be aligned in the line of sight. The closer star acts as a lens for the star behind it. The stellar mass bends the light around it. If a planet orbits the star this generates an observable signal. The first planet to be detected by this method was OGLE-2003-BLG-235Lb by *Bennett et al.* (2006).

2.2 A Short Note on Stars

We saw before that there are a lot of planets in our universe. Also, a lot of stars have at least one planet in an orbit around them. However, not all stars are like our sun. Most of them have completely different properties. Common for all stars

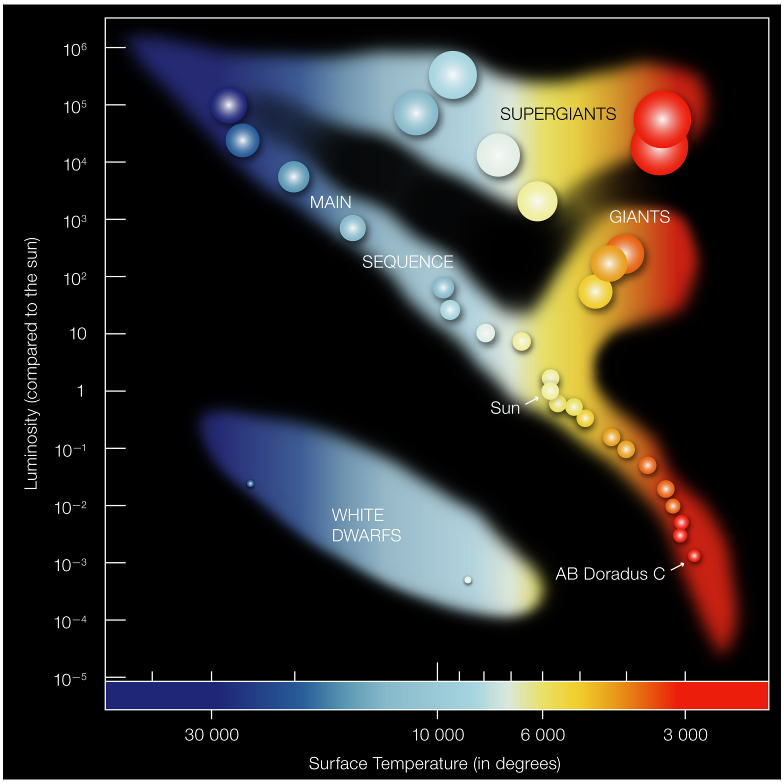

Figure 2.4: Hertzsprung-Russell diagram (Credit: ESO, `https://www.eso.org/public/images/eso0728c/`).

is their main source of energy: hydrogen fusion, the so-called hydrogen burning. This process fuses light hydrogen nuclei to the heavier helium nuclei and thereby releases energy (*Hansen et al.*, 2004).

This section will have a closer look at stars and brown dwarfs. It introduces, which types of stars exist and how stars are commonly categorised. Afterwards, the stellar structure and stellar magnetic fields are presented. A special focus lies on M-dwarf stars.

2.2.1 Types of Stars and Spectral Classes

All known stars and brown dwarfs can be described by their position in the Hertzsprung-Russell diagram (HR diagram, Figure 2.4). The HR diagram draws the luminosity of a stellar object against the effective temperature, which typically decreases in x-direction. The effective temperature is the temperature that a black body had to have to emit the same power as the star and is an indicator for the spectral class of a star. See *Hansen et al.* (2004) for further detail. Spectral classes represent a system to categorise stars according to their color and traditionally include the classes O, B, A, F, G, K, M (from hot to cool stars). This system goes back to *Morgan et al.* (1943) and bases strongly on stellar absorption features (*Hansen et al.*, 2004).

The HR diagram shows three big structures: The main sequence, the giant stars and the White dwarfs. The most prominent of these structures is the main sequence (Figure 2.4) going from high effective temperatures and luminosities (basically upper left corner) to low temperatures and luminosities (lower right corner of the diagram). The stars on the main sequence span the full range of spectral classes, which also represents the continuous decrease in stellar mass from O- to M-stars. Our sun is a star of spectral type G2. At the low-mass end of the stellar main sequence, there are the M-dwarfs. Those stars are also called Red dwarfs due to their reddish colour. Their mass lies below $0.3\,M_{\text{sun}}$ (*Hansen et al.*, 2004).

Not included in Figure 2.4 is the brown dwarf regime, which extends the main sequence on the low mass end. Brown dwarfs are commonly referred to as failed stars (*Burgasser*, 2008) because they never gained enough mass to ignite the fusion of hydrogen inside them. These objects are classified by the spectral classes M, L, T and Y, whereas the last three have been especially introduced for brown dwarfs (*Martín et al.*, 1999; *McLean et al.*, 2001; *Cushing et al.*, 2011).

Further notable populations according to the HR diagram are the White dwarfs and the giant stars. Giant stars are extremely luminous stars and lie above the main sequence. They evolve from sun-like main sequence stars that fused a certain amount of their hydrogen via the so-called proton-proton cycle (*Hansen et al.*, 2004). At that phase the temperature inside the star became so high that the CNO hydrogen burning becomes increasingly important and causes the star to expand enormously (*Hansen et al.*, 2004). The CNO cycle includes the heavy elements Carbon, Nitrogen, and Oxygen, to fuse hydrogen to helium. While giant stars represent a stage in the evolution of certain stars, white dwarfs are one of the three possible ways a star can end up after its "death" (*Hansen et al.*, 2004). White dwarfs are the cores of giant stars that got rid of their outer shells after the end of nuclear fusion. For heavier cores, the star might end up as a neutron star or even a black hole. White dwarfs have a low luminosity compared to the main sequence, although they may have extremely high effective temperatures (*Hansen et al.*, 2004).

2.2.2 Stellar Structure: Interior and Atmosphere

Just like planets, stars are stratified objects, with a certain internal structure that depends on the spectral class. The internal layers are mostly characterised by their role in energy production and transport. The Sun's interior, for example, is structured into a convective core, a radiative zone and a convection zone. The core extends to about $0.3\,R_{\text{sun}}$ and produces the majority of the stellar energy by fusion processes (*Hanslmeier*, 2007). In the radiation zone, heat transport happens by radiation. This zone extends up to about $0.6\,R_{\text{sun}}$ (*Hanslmeier*, 2007). As the energy is transported outward, the temperature decreases with radial distance from the core. Hence, the base of the convective zone is the hottest part of the layer. The resulting temperature gradient drives convection processes. Over the main sequence, the internal stratification varies. In low mass stars for example, the convective zone increases its relative size with decreasing stellar mass M_*. Low mass M-dwarfs with $M_* < 0.3\,M_{\text{sun}}$ have fully convective interiors (*Hansen et al.*, 2004).

Stars also have stratified atmospheres. The solar atmosphere is subdivided into photosphere, chromosphere, transition zone and corona (*Böhm-Vitense*, 1989). The photosphere is the lowest and densest part of the atmosphere (*Eddy and Ise*, 1979). Its temperature lies, in case of the sun, at about 5000 K and is comparable to the effective temperature. The chromosphere cools down on its basis to about

3800 K (*Avrett*, 2003) and rises up to the range of 10^4 K (*Eddy and Ise*, 1979; *Hanslmeier*, 2007). The transition zone is characterised by an extreme increase in temperature towards the coronal temperature of 10^6 K (*Eddy and Ise*, 1979; *Hanslmeier*, 2007).

The different atmospheric layers with their typical temperatures cause different types of emissions. Thermal emissions in form of visible light originate from the photosphere (*Böhm-Vitense*, 1989). The chromosphere exhibits emissions from the Hydrogen Balmer lines, metallic emission lines and ultraviolet emissions (*Böhm-Vitense*, 1989). Further upward, the extremely hot corona is the only source of stellar X-ray emissions (*Böhm-Vitense*, 1989).

2.2.3 Stellar Magnetic Fields and related Phenomena

Stars are highly magnetised objects. Most features of our Sun, as the best analysed star we know, are of magnetic origin. The large-scale magnetic field undergoes a cycle of 22 years, where it changes its direction, together with the sunspots, as an indicator of magnetic activity, that vary with an 11 years cycle (*Brun and Browning*, 2017). Sunspots are formed by strong, small-scale magnetic fields that emerge to the solar surface. The magnetic field inhibits convection flows, which transport heat to the surface (*Brun and Browning*, 2017). Therefore, the corresponding region is cooler than the surrounding and appears as a dark spot. Due to the strong magnetic fields, groups of sunspots are sources of eruptive events like flares and coronal mass ejections (*Brun and Browning*, 2017; *Toriumi and Wang*, 2019). Magnetic effects are also believed to be the main drivers of atmospheric heating at stars (*Brun and Browning*, 2017).

Fully convective M-dwarf stars ($M < 0.3M_{\text{sun}}$) appear to have a different field geometry than more massive stars. Right at the boundary towards the fully convective regime, i.e. at spectral class M3.5 (*Reiners and Basri*, 2009), the field appears to change from toroidal to mostly axisymmetric poloidal field structures (*Brun and Browning*, 2017). *Morin et al.* (2010) report two categories of magnetic fields on M-dwarfs. One type of star with strong axisymmetric dipole fields and on the other hand stars with weak magnetic fields and a non-axisymmetric component. (*Reiners and Basri*, 2009) report, that the majority of magnetic flux is stored in small-scale magnetic structures. In general, field strengths and geometries of late M-dwarfs are difficult to detect, because of the stars' faintness.

Flares are explosive phenomena, driven by small scale magnetic fields that can drastically enhance a star's luminosity. The first such event was the so called Carrington event (*Carrington*, 1859), named by the scientist who described it first. Until today, this flare is still among the most powerful flares that we know from our sun. The current standard model, the so called CSHKP-model, bases on the work of *Kopp and Pneuman* (1976) and has been extended since then. The name as well, since every important contributor's initial letter has been added. The model assumes, that open magnetic field lines reconnect, to form closed magnetic loops on the star. The outflowing stellar wind produces a shock inside the looped field, which heats the plasma. The wind eventually extends the magnetic loops and creates a reconnection zone. Oppositely directed magnetic field lines reconnect and release magnetic energy. A plasmoid is released together with radiative energy. For further details see the review from *Shibata and Magara* (2011). The details of the reconnection process are not yet fully understood, so quite possibly, the name of the model has to be further extended in the future. A flare can cause emissions in all atmospheric layers, whereas they are most commonly observed in coronal X-ray ranges (*Shibata and Magara*, 2011). For a large event, even the photosphere might react and emit white light (*Shibata and Magara*, 2011). Flares typically have a duration on the order of 10^3-10^5 s (*Shibata and Magara*, 2011) and erupt from active regions, like groups of starspots (*Toriumi and Wang*, 2019).

Coronal Mass Ejections (CME) are large scale phenomena that erupt large amounts of plasma from active regions on the sun. The mass, carried by CMEs, usually ranges between 10^{11} and 10^{13} kg and the material erupts with velocities of several hundred $\mathrm{km\,s^{-1}}$ (*Chen*, 2011). The review of *Chen* (2011) distinguishes between two types of CME, the so called narrow CME and the normal CME. The author describes narrow CMEs as elongated jet-like structures that move along open field lines. These CMEs are believed to be the result of reconnection between small-scale magnetic loops and open field lines. Thus, these CMEs are often accompanied by, what the author calls a compact flare. On the other hand, the so called normal CME, is the more common type of event. Normal CMEs have a leading structure loop-like structure, followed by a dark cavity and a bright core (*Chen*, 2011). As powerful eruptions of material into the interplanetary space, CMEs affect the Earth's space weather and can cause damage on technical devices and power grids (*Schwenn*, 2006; *Pulkkinen*, 2007).

2.3 TRAPPIST-1

The studies of this thesis base on the example of the TRAPPIST-1 system, due to the large number of close-in planets with accordingly short orbital periods. Therefore we will introduce the system in more detail and start with the stellar parameters and go on to the planets.

A short note on nomenclature: We usually apply the abbreviation T1x to indicate the planets. T1 stands for the star TRAPPIST-1 and the x is a placeholder for the letters b to h, depending on the planet.

2.3.1 The Star

TRAPPIST-1 is a star of spectral class M8. It is located at a distance of 39 light years in the constellation Aquarius. The star was first discovered during the 2MASS All Sky Survey, among other low mass stars (*Gizis et al.*, 2000). By that time, the star was only known under its 2MASS-identifier 2MASS J23062928-0502285. *Burgasser and Mamajek* (2017) determined the most probable age of TRAPPIST-1 to be 7.6 Gyr with an error range of 2 Gyr.

As an M8 low-mass star TRAPPIST-1 has a mass of 93 Jupiter masses M_J and a size of 84257 km or 1.18 Jupiter radii R_J (*Van Grootel et al.*, 2018). Earlier observations by *Gillon et al.* (2016) indicated an even lower mass of 84 M_J, which made it an object quite close to the border of the Brown Dwarf regime. *Gillon et al.* (2016) carried out optical spectroscopy and did not detect the 670.8 nm lithium line. This finding implies that TRAPPIST-1 belongs to the very low mass stars, instead of the Brown Dwarfs.

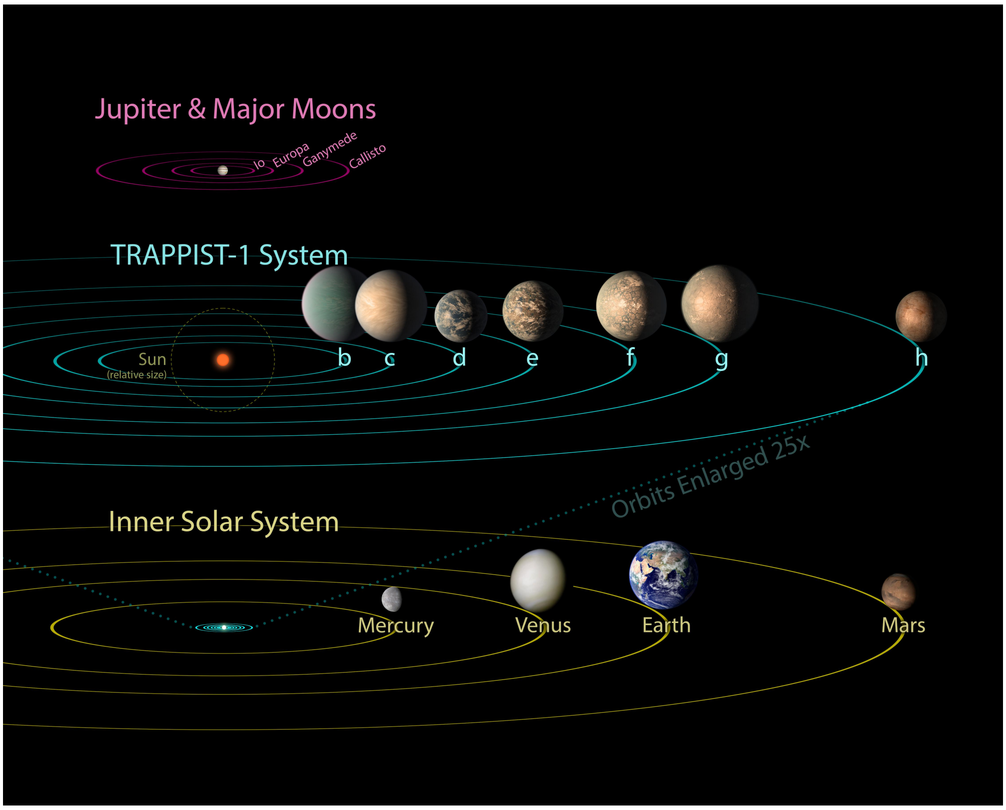

Figure 2.5: Comparison between Jupiter and its Galilean moons, the TRAPPIST-1 system and the inner Solar System (Credit: NASA/JPL-Caltech).

The atmosphere of the star has an effective temperature of about 2500 K in the photosphere (*Delrez et al.*, 2018). Observations in X-ray and UV ranges by *Bourrier et al.* (2017) and *Wheatley et al.* (2017) indicate the existence of a hot stellar corona and a moderately active Chromosphere.

The stellar rotation period T_* has been somewhat controversial in the past. Early measurements by *Reiners and Basri* (2010) and *Gillon et al.* (2016) reported a rotation period of around 1 d. *Luger et al.* (2017) and *Vida et al.* (2017) then proposed T_* to be 3.3 d based on photometric periodicities observed by K2. The latter is supported by *Reiners et al.* (2018) who conducted more precise radial velocity measurements and concluded a period of $T_* \sin\ i > 2.7$ d, whereas the inclination i is unknown. These new measurements are consistent with the rotation period obtained by *Luger et al.* (2017) and *Vida et al.* (2017). Recent observations by *Hirano et al.* (2020) showed that TRAPPIST-1's spin axis is not tilted against the orbital planes of the co-planar planets.

2.3.2 The Planetary System

Gillon et al. (2016) announced the finding of three planets around the star, followed one year later by *Gillon et al.* (2017) with the announcement of a total of seven confirmed exoplanets around TRAPPIST-1. All planets are approximately Earth-sized and in close orbits around their host star (*Gillon et al.*, 2017). Up to four of the planets may lie in the habitable zone of the star (*O'Malley-James and*

Table 2.1: Important parameters of the planets in the TRAPPIST-1 system, i.e. orbital distance and period, radius, mass and the average planetary density.

Planet	**Orbital distance** a $[R_*]$[1]	**Orbital period** T [d][2]	**Radius** R_p $[R_\mathrm{E}]$[1]	**Mass** M_p $[M_\mathrm{E}]$[1]	**Density** ρ_p $[\rho_\mathrm{E}]$[1]
b	20.5	1.51	1.121	1.017	0.726
c	28.08	2.42	1.095	1.156	0.883
d	39.55	4.05	0.784	0.297	0.616
e	51.99	6.10	0.910	0.772	1.024
f	68.4	9.21	1.046	0.934	0.816
g	83.2	12.35	1.148	1.148	0.759
h	109	18.77	0.773	0.331	0.719

[1] *Grimm et al.* (2018), [2] *Delrez et al.* (2018)

Kaltenegger, 2017). These are the reasons that this system gained much fame over the past three years. Figure 2.5 shows an artists view of the TRAPPIST-1 system (middle) in comparison to Jupiter with its Galilean moons (top) and the inner Solar System with the terrestrial planets (bottom). The size of the Solar System is reduced by a factor of 25 to compare it to the TRAPPIST-1 system (centre, just around the Sun). In size, the TRAPPIST-1 system is comparable to the Jupiter system. However, the appearance of the planets is subject to the artist's fantasy, as we do not know about it yet.

Table 2.1 lists the most important planetary parameters: semi-major axis a in stellar radii R_*, the orbital period T in days, the planetary radius R_p in Earth radii R_E, the planetary mass M_p in Earth masses M_E and the according planetary density ρ_p relative to Earth's density ρ_E. The planets orbit TRAPPIST-1 at distances between 20.5 and 109 stellar radii R_* (*Grimm et al.*, 2018) and have orbital periods between 1.5 days and 18.7 days (*Delrez et al.*, 2018). According to *Turbet et al.* (2018), all planets could be tidally locked, i.e. their rotational period equals their orbital period. *Luger et al.* (2017) report that all seven planets are in orbital resonance. Orbital resonance is the phenomenon that orbital periods of celestial objects like moons and planets are integral multiples of each other.

All planets belong to the class of terrestrial planets with radii between 0.773 and 1.148 R_E and masses between 0.297 and 1.156 M_E. Planets d and h are quite similar in size and mass. The two planets are the smallest of the system. The planets b, c, and g are all slightly larger than Earth (up to 15%) and slightly more massive (up to 15% as well). However, the planetary density is quite low compared to Earth. Only planet e with 1.024 ρ_E has a comparable density to Earth. All other planets range between 0.616 to 0.883 ρ_E. All parameters have been estimated by *Grimm et al.* (2018).

The interior of exoplanets to date is unknown and our knowledge bases on model estimates. A few studies have been conducted for TRAPPIST-1. *Barr et al.* (2018) modelled possible interiors of all planets in the TRAPPIST-1 system and estimated the tidal heat flux present in all planets. The authors conclude that all planets may have significant amounts of water. *Barr et al.* (2018) note that T1b and c may experience sufficient tidal heating to sustain magma oceans in their mantles. Planets d, e, and f are expected to have tidal heat fluxes that are twenty times higher than Earth's heat flux (*Barr et al.*, 2018). *Dorn et al.* (2018) conduct a similar study based on statistical modelling. The authors estimated that the planets have water mass fractions between 0% and 25%. The water mass would contribute to the thickness of the gas envelope that the authors estimated to be up to 5% of the respective planetary radius. However, all authors agree that interior estimates vary heavily with the accuracy of the input data, especially when only mass and radius are available.

After the discovery of the planets, their atmospheres are now primary targets for further observations. *Bourrier et al.* (2017) observed TRAPPIST-1 in the Lyman-α. During the observations, the authors were able to observe the transits of T1b and c and found that the observed dimming was too large to be caused by the solid planet alone. According to *Bourrier et al.* (2017), the observations suggest the existence of hydrogen exospheres on both inner planets. These exospheres extend up to seven planetary radii and in the case of T1c into a comet-like tail. *De Wit et al.* (2016) and *de Wit et al.* (2018) conclude from their observations that extended gas envelopes around all planets are unlikely. The authors do not expect that TRAPPIST-1's planets have hydrogen-dominated atmospheres.

2.4 State of Research about Electromagnetic Star-Planet Interaction

Star-planet interaction (SPI) accounts for two major types of interaction: gravitational and electromagnetic. Gravitational SPI typically involves gravitational effects that stars and planets exert on each other, e.g. tides and orbital motion. The radial velocity method (section 2.1.3.2) is an example of how gravitational SPI is employed to detect planets. Electromagnetic star-planet interaction (in the following only SPI) is a quite young field compared to gravitational SPI. The main driver is the interaction between a planet and the surrounding stellar wind and magnetic field, which couples star and planet to each other.

In our Solar System, we have no such SPI because the planets are all too far away from the sun. However, in other stellar systems, this process can occur. Therefore, we will introduce the current state of knowledge towards electromagnetic SPI. In the following, we will further address the coupling between moons and planetary magnetospheres as the closest analogue to SPI. Afterwards, we will look at observational evidence for SPI and will finally address theoretical models and numerical studies towards SPI.

2.4.1 The Situation in our Solar System

Moon-magnetosphere interaction (MMI) is the closest analogue to SPI that we have in the Solar System. Historically, it is much older than SPI. In SPI-research, the interaction between Io and Jupiter became a famous role model. However, many other large moons in the Solar System are known to generate MMI (*Kivelson et al.*, 2007).

The earliest evidence for MMI date back to *Bigg* (1964), who observed Jupiter in the radio wavelength range and found that Io controls the jovian decametric radio emission. *Goldreich and Lynden-Bell* (1969) developed a model to explain the observations that assumed the absence of plasma, called the unipolar inductor model. The Pioneer 10 spacecraft, however, observed the presence of plasma in the Jupiter system, and especially a torus-shaped cloud of plasma in Io's orbit (*Frank et al.*, 1976). Volcanic activity on Io is the main source of torus plasma (*Broadfoot et al.*, 1979). *Goertz* (1980) and *Neubauer* (1980) built upon these new findings and derived coupling models based on Alfvén waves. The model by *Neubauer* (1980) is the nowadays commonly applied Alfvén wing model. In-situ measurements during the flyby of the Voyager spacecraft (*Acuna et al.*, 1981) and subsequently with the Galileo spacecraft (*Kivelson et al.*, 1996a; *Frank et al.*, 1996) verified the model.

Connerney et al. (1993) observed Jupiter in infrared wavelengths and detected auroral emissions that result from MMI between Jupiter and Io. Later on, the ultraviolet wavelength range became the preferred wavelength range for observations of MMI, because the bulk of the emitted power lies in at UV wavelengths. Several authors performed observations of Io's footprints with the Hubble Space Telescope (HST), e.g. *Prangé et al.* (1996); *Clarke et al.* (1996); *Clarke et al.* (2002); *Bonfond et al.* (2008) or *Bonfond et al.* (2012). *Wannawichian et al.* (2010, 2013) and *Bonfond et al.* (2013) detected variations in the luminosity of the Io footprint. These variations come from the tilt in Jupiter's magnetic field and result in a variable Poynting flux (*Saur et al.*, 2013).

Io has also been subject in numerical modelling studies. *Linker et al.* (1988) analysed the occurring wave structures, i.e. Alfvén wings and Slow Mode waves. *Jacobsen et al.* (2007) and *Jacobsen et al.* (2010) simulated the reflections of Io's Alfvén wings at the boundary zones of the Io torus, which explain the occurrence of multiple auroral spots trailing behind the main footprint (*Clarke et al.*, 2002). *Blöcker et al.* (2018) studied the effect that a volcanic eruption on Io would have on the resulting MMI with an MHD model. The authors found that the volcanic plume locally enhances the strength of the interaction and result in a small Alfvén wing within the main wing, which they call Alfvén winglet.

The other three Galilean moons, Europa, Ganymede and Callisto, also host MMI (*Kivelson et al.*, 2007). Callisto was, for a long time, only assumed to host MMI, because the respective auroral footprint lies within the main auroral oval and could not be detected (*Clarke et al.*, 2002). Recently *Bhattacharyya et al.* (2018) published an analysis of HST data and claimed to have found Callisto's footprint within Jupiter's auroral oval.

The footprints of Europa (*Clarke et al.*, 2002; *Grodent et al.*, 2006) and Ganymede (*Clarke et al.*, 2002; *Grodent et al.*, 2009) were detected and identified much earlier, via HST observations. The identification of the spots was only possible because the telescope could spatially resolve Jupiter. Ganymede is a unique example because it is the only moon with an intrinsic magnetic field *Kivelson et al.* (1996b). Therefore, Ganymede is the only magnetised planetary object that generates sub-Alfvénic interaction. The interaction and the resulting Alfvén wings have been modelled successfully with MHD models by, e.g. *Jia et al.* (2008, 2009) and *Duling et al.* (2014).

Saturn's moon Enceladus also forms a torus, just like Io (*Dougherty et al.*, 2006). The torus consists of material that originates from plumes of water and ice on Enceladus. *Pryor et al.* (2011) observed the footprints of Enceladus' plasma interaction on Saturn. Prior to this finding *Tokar et al.* (2006) observed plasma interactions with Enceladus' atmosphere and *Saur et al.* (2007) modelled the occurring sub-Alfvénic interaction.

2.4.2 Observations of Star-Planet Interaction

Observations of SPI are challenging, mostly because of the intense intrinsic luminosity of the stellar hosts. Early suggestions for an observable relation between stars and planets date back to the year 2000. *Cuntz et al.* (2000) proposed a general increase in stellar activity, either by tidal interaction or by magnetic interaction. *Rubenstein and Schaefer* (2000) made hot Jupiters responsible for the eruption of superflares on sun-like stars.

Claims of observational evidence for SPI exist for HD 179949 (*Shkolnik et al.*, 2003; *Shkolnik et al.*, 2005; *Shkolnik et al.*, 2008) and υ And (*Shkolnik et al.*, 2005; *Shkolnik et al.*, 2008). The authors observed enhanced Ca II H & K emission in synchronisation with the orbital period of the close-in planets. At HD 179949 the synchronisation has been observed in four of six observational epochs. Similar effects have been reported for υ And as well. *Shkolnik et al.* (2008) accounted for this on-off behaviour of the interaction by invoking a changing stellar magnetic field structure. However, *Miller et al.* (2012) showed that a chromospheric hot spot might mimic the existence of SPI at HD 179949 and υ And. *Saar et al.* (2008) observed a possible link between stellar X-ray emission and HD 179949 b. X-ray observations of υ And conducted by *Poppenhaeger et al.* (2011) provided evidence of activity linked to the stellar rotation but no connection to the planet.

Later observations followed the idea that SPI excites chromospheric Ca II H & K emissions. *Walker et al.* (2008) observed the star τ Boo A photometrically and in the Ca II K line. The star rotates tidally locked to its planet and features a variable region in advance of the planet that *Walker et al.* (2008) attributed to magnetic SPI. *Staab et al.* (2017) observed the system WASP-43 and likewise saw enhanced Ca II H & K emissions, which they attributed to the existence of SPI. However, statistical analyses of several systems provide different results. *Canto Martins et al.* (2011) compares systems that have planets with semi-major axes $a < 0.2$ AU with stars that have no confirmed exoplanets. The authors saw no difference in the activity. *Krejčová and Budaj* (2012) see a difference between planet populations with semi-major axes $a < 0.15$ AU and $a > 0.15$ AU. The stars with close-in planets showed enhanced chromospheric activity and the others not.

Similarly to the chromospheric line emissions, analyses of X-ray emissions provide different results as well. *Miller et al.* (2012) observed the system WASP-18 in optical and X-ray wavelengths and saw no evidence for SPI. The authors claimed WASP-18 b to potentially generate the strongest interaction among the known planets at that time, based on planetary mass and semimajor axis. X-ray observations show that WASP-18 appears to be less active than expected from its estimated age, which indicates a much weaker stellar magnetic field than in HD

179949. This weaker magnetic field directly affects the strength of potential SPI. *Poppenhaeger and Wolk* (2014) found enhanced X-ray activity of a Hot-Jupiter hosting binary compared to binaries without Hot Jupiters. In a statistical analysis, *Scharf* (2010) saw correlations between stellar X-ray luminosities and orbiting planets. *Poppenhaeger et al.* (2010), however, did not find any correlation between X-ray and the existence of planets.

Shkolnik (2013); *France et al.* (2016) and *France et al.* (2018) used UV observations to find SPI-signals in stellar emissions. *Shkolnik* (2013) analysed GALEX data of systems with close-in planets ($a < 0.1$ AU) and compared these to systems with far-out planets ($a > 0.5$ AU). The author found an enhanced activity of Far Ultraviolet (FUV) emissions in the systems with close-in planets. *France et al.* (2016) and *France et al.* (2018) used Hubble Space Telescope observations to investigate the UV-properties of approximately 100 stars with spectral class K and M. The authors found no evidence for SPI in their data.

Another lane in the search for SPI comes from H-α and radio observations of brown dwarfs. *Hallinan et al.* (2015) observed the ultracool dwarf LSR J1835+3259 and reported the detection of auroral signals similar to those on Jupiter possibly caused by a planetary companion. *Kao et al.* (2016) report similar findings from different brown dwarfs. However, *Saur et al.* (2018) observed the object with the Hubble Space Telescope and show that the UV spectrum of LSR J1835+3259 rather resembles that of late M-dwarf but not auroral emissions similar to those from Jupiter.

There are intriguing observations of stellar systems that could hint at SPI. However, we saw that there are doubts and opposing results on those findings. Many stellar systems are expected to host electromagnetic SPI but lack convincing evidence (see review by *Lanza* (2015)). Convincing evidence will have to be backed by different observations, techniques and physical properties.

2.4.3 Theory and Modelling - an Overview

Observations and theoretical models have always infused each other with new perspectives and possibilities. However, the field of star-planet interaction bases strongly on analytic and numerical models, mainly because reliable observations are still pending. The research of moon-magnetosphere interaction has heavily influenced the research of SPI, but due to the stellar wind environment and the stellar host, modelling SPI also follows different routes.

Several analytic models aim to explain SPI. *Neubauer* (1980) derived the Alfvén wing model for the interaction between Jupiter and Io, but *Saur et al.* (2013) showed that it also applies in the context of SPI. In this model, the plasma interacts with the obstacle, e.g. through collisions with neutral atmospheric particles. This interaction causes a deceleration of the plasma, and due to the partly frozen-in magnetic field, this process builds up magnetic stresses. These perturbations propagate along the field lines as Alfvén waves. *Saur et al.* (2013) proposed the Alfvén wing model to model SPI, because, albeit the differing interaction geometry, the planets are obstacles that interact with magnetised plasma.

The models by *Lanza* (2009, 2012, 2013) are alternative approaches to SPI. The models assume magnetohydrostatic force-free magnetic fields that couple the planet and the star. In *Lanza* (2009) the interaction drives an electric current system that closes through reconnection near the planetary magnetopause. *Lanza* (2013) proposes another model based on the accumulation and release of stresses in magnetic flux tubes. The planet drives the interaction through its motion within the stellar magnetic field, since the plasma is static. This model bases on the strength of a planetary magnetic field, in contrast to the Alfvén wing model that applies for mechanical and magnetic obstacles and involves the local stellar magnetic field (*Saur et al.*, 2013). *Cauley et al.* (2019) apply the flux tube model by *Lanza* (2013) to estimate the magnetic field strengths of exoplanets. The reasoning for this choice is that the said SPI-model is the only one that explains the observed enormous powers at objects like HD 179949. The estimated magnetic field strengths are one to two orders of magnitude larger than what has been predicted by scaling laws. Another approach published by *Lanza* (2018) proposes three mechanisms that explain how planets may trigger flares on stars. *Zarka* (2007) derived scaling laws for radio emissions emanating from SPI. The author differentiates between the interaction of magnetised and non-magnetised planets with the surrounding stellar winds based on moon-magnetosphere interactions at Jupiter.

SPI has also been investigated in a variety of numerical studies. Early simulation studies were conducted by *Ip et al.* (2004), who investigated how the magnetospheres of Hot Jupiters interact with plasma under sub-Alfvénic conditions. *Preusse et al.* (2005) modelled the expected stellar wind environments around Hot Jupiters to determine those planets that experience sub-Alfvénic conditions. *Preusse et al.* (2006, 2007) simulated the interaction of Hot Jupiters and determined the Alfvén characteristics and the resulting current systems. *Kopp et al.* (2011) simulated the systems HD 179949, and υ And and confirmed the theoretical explanation for the phase shift between the planet and observed emissions. *Daley-Yates and Stevens* (2018) performed MHD simulations to determine the strength of planetary radio emissions emanating from the magnetosphere of Hot Jupiters. *Daley-Yates and Stevens* (2019) simulated the effect of escaping atmospheric material from the planet. The authors found that the material forms a disk around and accretes on the star.

Strugarek et al. (2012); *Strugarek et al.* (2014) simulated a magnetised and non-magnetised planetary body, the latter without atmosphere, that interacts with the stellar wind plasma. The authors further introduced stellar and planetary boundary conditions and estimated the amount of the angular momentum transfer between planet and star due to SPI. *Strugarek et al.* (2015) simulated SPI with a 3D MHD setup for different configurations of planetary and stellar magnetic fields. The study estimated the generated Poynting fluxes, as well as the resulting current systems in the planet's magnetosphere and Alfvén wing. *Strugarek* (2016) investigated the torques that result from SPI and derived scaling laws based on planetary and stellar properties, which might be applied to describe planet migration. *Strugarek et al.* (2019) investigated the system Kepler-78, where the authors applied observed stellar magnetic field maps and simulated the expected time-variable SPI with a combination of MHD simulations and analytic theory of SPI.

The first time-variable MHD simulation of a planet orbiting a star was published by *Cohen et al.* (2011). The authors used an internal boundary for the planet and let the Code update the position at each time-step. The planet had an intrinsic magnetic field, which interacted with the stellar wind. The simulation showed that SPI could generate hot spots in the stellar atmosphere. *Cohen et al.*

(2014) estimated the Alfvén surface of an M-dwarf star and simulated sub- and super-Alfvénic interactions between planets and stellar wind. *Cohen et al.* (2015) simulated the interaction between the atmosphere of a terrestrial planet and the stellar wind of an M-dwarf. The authors estimated atmospheric losses due to ion-neutral interactions.

3 Star-Planet Interaction - Theory and Concepts

In this chapter, we will outline the theoretical basis of star-planet interaction in the framework of Magnetohydrodynamics (MHD). Therefore we introduce the MHD equations and MHD wave theory. Afterwards, we describe the simplest stellar wind model, the Parker-Model. It defines the interaction geometry between stellar wind and planet and is essential for our studies. Afterwards, we will introduce sub-Alfvénic interaction and the Alfvén wing model. Alfvén wings connect planet and star and transfer energy. Therefore they are the most important part of SPI. In the final section, we present concepts for temporal variability in SPI. The section comprises analytic theory and thought experiments that have already been published by the author in *Fischer and Saur* (2019).

3.1 Magnetohydrodynamics and Wave Theory

Magnetohydrodynamics is a single-fluid approach to describe plasma. It is commonly applied to investigate SPI (see section 2.4.3). Therefore, we will introduce the MHD equations and linear MHD wave theory in this section.

3.1.1 MHD Equations

We will apply the so called ideal MHD, where the conductivity σ is infinite and we have no resistive terms in the equations. Therefore the equations we will in principle deal with are:

$$\frac{\partial \rho}{\partial t} + \nabla \cdot (\rho \boldsymbol{v}) = 0 \tag{3.1}$$

$$\rho \frac{\partial \boldsymbol{v}}{\partial t} + \rho (\boldsymbol{v} \cdot \nabla) \boldsymbol{v} = -\nabla p + \boldsymbol{j} \times \boldsymbol{B} \tag{3.2}$$

$$\frac{\partial p}{\partial t} + \boldsymbol{v} \cdot \nabla p + p \Gamma \nabla \cdot \boldsymbol{v} = 0 \tag{3.3}$$

$$\frac{\partial \boldsymbol{B}}{\partial t} = \nabla \times (\boldsymbol{v} \times \boldsymbol{B}) \, . \tag{3.4}$$

These four equations are the continuity equation, the equation of motion, the energy equation and the induction equation, respectively. They describe the evolution of the mass density ρ, the plasma velocity $\boldsymbol{v}$, the pressure p and the magnetic field $\boldsymbol{B}$. Further variables are the current density $\boldsymbol{j}$ and the polytropic index Γ.

The continuity equation 3.1 describes the conservation of mass. We will not include any type of mass source or sink term, e.g. ionisation or recombination, in the equation. Hence a change in density only happens via a mass flux $\rho \boldsymbol{v}$ into or out of a volume element.

Equation (3.2) is the equation of motion. In its primitive form here it is an evolution equation for the plasma velocity. The conservative form describes the conservation of momentum. For the theoretical considerations we discuss here the primitive form suffices. On the left hand side of the equation we have the inertial term $\partial_t \boldsymbol{v}$ and the advection term $(\boldsymbol{v} \cdot \nabla)\boldsymbol{v}$. Both together form the total derivative $d\boldsymbol{v}/dt$, which describes the change of velocity in time and space. On the right hand side we have the pressure gradient force $-\nabla p$ and the magnetohydrodynamic Lorentz force $\boldsymbol{j} \times \boldsymbol{B}$ with the current density $\boldsymbol{j}$. The Lorentz force connects the magnetic field to the plasma. To better discuss its physical effects we can rewrite it as

$$\boldsymbol{j} \times \boldsymbol{B} = -\nabla \frac{B^2}{2\mu_0} + \frac{1}{\mu_0} (\boldsymbol{B} \cdot \nabla) \boldsymbol{B} \tag{3.5}$$

by applying $\boldsymbol{j} = \nabla \times \boldsymbol{B} \mu_0^{-1}$. The first term of the Lorentz force is the magnetic pressure gradient force that points from regions of stronger magnetic fields to regions of weaker magnetic field strength. The second term describes magnetic tension. The easiest way to imagine the effect of magnetic tension is as the deformation of magnetic field lines.

The energy equation 3.3 describes the evolution of the thermal pressure p, i.e. the internal energy e via

$$e = \frac{p}{\Gamma - 1}. \tag{3.6}$$

with the polytropic index Γ. The energy may change along the flow of the plasma, and changes can occur through divergence and convergence of plasma.

Equation (3.4) is the so-called induction equation and describes the evolution of the magnetic field. Mathematically it closes the system of the MHD differential equations, as the magnetic field is an additional variable here. We can derive the induction equation from the Maxwell equations:

$$\nabla \cdot \boldsymbol{E} = \frac{\rho_\mathrm{c}}{m\epsilon_0} \tag{3.7}$$

$$\nabla \times \boldsymbol{B} = \mu_0 \boldsymbol{j} + \frac{1}{c^2} \frac{\partial \boldsymbol{E}}{\partial t} \tag{3.8}$$

$$\frac{\partial \boldsymbol{B}}{\partial t} = -\nabla \times \boldsymbol{E} \tag{3.9}$$

$$\nabla \cdot \boldsymbol{B} = 0 \tag{3.10}$$

with the electric field $\boldsymbol{E}$, the charge density ρ_c, the dielectric constant ϵ_0 and the magnetic permeability μ_0. Those are the basic equations to describe electric and magnetic fields. Together with Ohm's law

$$\boldsymbol{j} = \sigma (\boldsymbol{E} + \boldsymbol{v} \times \boldsymbol{B}) \tag{3.11}$$

where σ is the electric conductivity. We can derive the inductions equation by inserting Ohm's law into the induction law 3.9. Further we can replace $\boldsymbol{j}$ with equation (3.8), where we assume that the displacement current is negligible. By applying some vector algebra and using equation (3.10) we receive the full induction equation

$$\frac{\partial \boldsymbol{B}}{\partial t} = \nabla \times (\boldsymbol{v} \times \boldsymbol{B}) - \frac{1}{\mu_0 \sigma} \Delta \boldsymbol{B} \tag{3.12}$$

where the second term on the right-hand side describes magnetic diffusion. This process is responsible for magnetic reconnection and is important for, e.g. flares and some auroral generator mechanisms. Under the assumption of ideal MHD, i.e. $\sigma = \infty$, we receive the ideal induction equation from equation (3.4).

In the ideal MHD we can also derive the relation

$$\boldsymbol{E} = -\boldsymbol{v} \times \boldsymbol{B}, \tag{3.13}$$

from Ohm's law, which is the motional electric field or the frozen field theorem. Physically it implies that field lines are tied to plasma parcels and vice versa. Hence plasma flows can change the form of magnetic fields, and in other situations, the field can enforce plasma motions.

3.1.2 MHD Waves

The MHD allows three different wave modes: two compressible acoustic waves and Alfvén waves. Some authors, e.g. *Saur* (2019), also count a fourth wave mode, the so-called entropy mode. The Alfvén wave is the most important plasma wave mode. It is mainly responsible for the coupling between moons and planets and in our case stars and planets. For our studies, we are interested in the properties of those waves, to analyse the expected SPI wave structures. Therefore we outline the principles of linear MHD wave theory and derive the wave properties here.

The presented linear wave theory bases mostly on the theory from *Baumjohann and Treumann* (1996) and applies several simplifying assumptions. First of all, one switches the reference frame into the frame of the moving plasma, which implies that $\boldsymbol{v}_0 = 0$. Further one assumes that the plasma quantities are spatially and temporally constant but allows small perturbations that can vary in time and space, i.e.

$$\rho = \rho_0 + \delta\rho \tag{3.14}$$

$$p = p_0 + \delta p \tag{3.15}$$

$$\boldsymbol{B} = \boldsymbol{B}_0 + \delta \boldsymbol{B} \tag{3.16}$$

$$\boldsymbol{v} = \delta \boldsymbol{v}. \tag{3.17}$$

Now one inserts these relations into the set of MHD equations (equation (3.1) to 3.4). Since only the perturbations depend on time and space, we can drop the derivatives of the background values. Besides, one assumes that the perturbations are so small that any types of squared perturbations are too small to be further considered, i.e. $\delta\rho^2 = 0$ and analogous for the other variables. The result is a set of linearised MHD equations. By taking the derivative in time of the linearised equation of motion, one receives the MHD wave equation

$$\frac{\partial^2 \delta \boldsymbol{v}}{\partial t^2} = c_{\mathrm{ms}}^2 \nabla (\nabla \cdot \delta \boldsymbol{v}) + v_{\mathrm{A}}^2 \left[\nabla_{\parallel}^2 \delta \boldsymbol{v} - \nabla \left(\nabla_{\parallel} \cdot \delta \boldsymbol{v}\right) - \nabla_{\parallel} (\nabla \cdot \delta \boldsymbol{v})\right] \tag{3.18}$$

where the subscripts $\perp$ and $||$ indicate the respective derivatives perpendicular and parallel to the magnetic field. Magnetised plasmas behave highly anisotropic, due to the magnetic field that provides a preferntial direction. In this wave equation, we already interpreted the occurring pre-factors as the respective wave speeds:

$$v_{\mathrm{A}} = \frac{B_0}{\sqrt{\mu_0 \rho_0}} \tag{3.19}$$

$$c_{\mathrm{s}} = \sqrt{\frac{\Gamma p_0}{\rho_0}} \tag{3.20}$$

$$c_{\mathrm{ms}} = \sqrt{v_{\mathrm{A}}^2 + c_{\mathrm{s}}^2}. \tag{3.21}$$

From top to bottom: the Alfvén wave velocity, the sound speed and the magnetosonic wave speed. One further needs the wave dispersion relations, which are required to derive the directions of propagation and the disturbances relative to the magnetic field. To obtain the dispersion relations, one introduces the plane wave solution of the type

$$\delta A = \delta A_0 \exp\left[i\left(\boldsymbol{k} \cdot \boldsymbol{r} - \omega t\right)\right] \tag{3.22}$$

where A is a placeholder for the respective plasma variables. With this approach one can rewrite the linearised MHD equations as a set of algebraic equations that may be written in the form of a set of linear equations $\boldsymbol{M} \cdot \delta \boldsymbol{v} = 0$ where $\boldsymbol{M}$ is a 3×3 matrix originating from the linearised algebraic MHD equations. For $\det(\boldsymbol{M}) = 0$ one receives the non-trivial solutions of the system of equations

$$\omega = \pm k_{||} v_{\mathrm{A}} \tag{3.23}$$

$$\omega^2 = \frac{k^2}{2}\left[c_{\mathrm{ms}}^2 \pm \sqrt{\left(v_{\mathrm{A}}^2 - c_{\mathrm{s}}^2\right)^2 + 4 c_{\mathrm{s}}^2 v_{\mathrm{A}}^2 \frac{k_{\perp}^2}{k^2}}\right] \tag{3.24}$$

which are the wave dispersion relations. The linear dispersion relation in equation (3.23) describes the Alfvén wave. One can easily see that Alfvén waves only travel parallel or anti-parallel to the magnetic field but also that Alfvén waves are non-dispersive waves. The latter implies that the phase and group velocity of the Alfvén wave are the same. Equation (3.24) describes the two magnetosonic wave modes. The '-'-Solution represents the Slow Mode and the '+'-solution the Fast Mode.

We summarised the properties of all three waves in Table 3.1, i.e. the propagation direction, the wave speed and the expected wave disturbances $\delta \boldsymbol{v}$, $\delta \boldsymbol{B}$, $\delta \rho$ and δp. By inserting the dispersion relations 3.23 and 3.24 into $\boldsymbol{M}$ we receive the respective velocity disturbances $\delta \boldsymbol{v}$ for each wave. A case analysis provides the directions of propagation. And the linearised algebraic MHD equations give the remaining wave disturbances.

Both Alfvén and Slow Mode, propagate parallel to the background magnetic field. The Alfvén wave is a transversal, non-compressional wave. This implies that the disturbances in $\delta \boldsymbol{v}$ and $\delta \boldsymbol{B}$ are perpendicular to $\boldsymbol{k}$ and that there are no disturbances in density and pressure. The Slow Mode, in contrast, is a compressional,

Table 3.1: In this table we summarise the most important wave properties, predicted by linear MHD wave theory. We only consider the case that $v_{\mathrm{A}} > c_{\mathrm{s}}$, which is the relevant case for star-planet interaction.

	Alfvén wave	**Slow Mode**	**Fast Mode**[a]	**Entropy Mode**[b]
Propagation	$\boldsymbol{k} \parallel \boldsymbol{B}_0$	$\boldsymbol{k} \parallel \boldsymbol{B}_0$	$\boldsymbol{k} \perp \boldsymbol{B}_0$	-
Wave speed	v_{A}	c_{s}	c_{ms}	0
$\delta\boldsymbol{v}$	$\delta\boldsymbol{v}_\perp \neq 0$	$\delta\boldsymbol{v}_\parallel \neq 0$	$\delta\boldsymbol{v}_\perp \neq 0$	$= 0$
$\delta\boldsymbol{B}$	$\pm\frac{B_0}{v_{\mathrm{A}}}\delta\boldsymbol{v}$	0	$-\frac{B_0 \delta v_\perp}{c_{\mathrm{ms}}}\boldsymbol{e}_\parallel$	$= 0$
δp	0	$\frac{p_0\Gamma}{c_{\mathrm{s}}}\delta v_\parallel$	$\frac{p_0\Gamma}{c_{\mathrm{ms}}}\delta v_\perp$	$= 0$
$\delta\rho$	0	$\frac{\rho}{c_{\mathrm{s}}}\delta v_\parallel$	$\frac{\rho}{c_{\mathrm{ms}}}\delta v_\perp$	$\neq 0$

[a] We only present the direction perpendicular to $\boldsymbol{B}_0$ here, parallel to $\boldsymbol{B}_0$ the linear wave theory predicts the properties of an Alfvén wave.

[b] *Jeffrey and Taniuti* (1964)

longitudinal wave. Therefore there are disturbances in density and pressure that depend on a velocity disturbance parallel to $\boldsymbol{B}_0$. However, the Slow Mode generates no disturbances in the magnetic field. The Fast Mode propagates in all directions. However, only perpendicular to the magnetic field the Fast Mode has a phase velocity of c_{ms} and compressible properties. Whereas parallel to the magnetic field, the linear wave theory predicts the same wave properties as for the Alfvén wave. Perpendicular to the background field the wave has a $\delta\boldsymbol{v}$ perpendicular to $\boldsymbol{B}_0$, a parallel $\delta\boldsymbol{B}$ and disturbances in density and pressure. A special case among the MHD waves is the Entropy Mode, which does not propagate relative to the plasma, i.e. it has no wave speed on its own. Further, it only generates a disturbance in the density, but not in pressure, velocity or magnetic field (*Jeffrey and Taniuti*, 1964). Hence, it relates to a change in plasma temperature since the ideal gas law connects the thermodynamic variables.

3.2 Stellar Wind and Magnetic Field

In planetary magnetospheres, the rotating dipolar magnetic field forces the magnetospheric plasma to corotate. In the simplest case, the plasma only has an azimuthal velocity component of $\Omega_{\mathrm{p}} r$. Therefore the moon mostly experiences situations where the plasma flow is perpendicular to the magnetic field (*Saur et al.*, 2013). A planet around a star, however, experiences different interaction geometries. Therefore we describe an analytic stellar wind model that we will use later in our studies.

The first, and to date simplest, stellar wind model is the so-called Parker-model by *Parker* (1958). The Parker-model assumes a hot wind source region, the stellar corona. Plasma temperatures of several million Kelvin cause high pressure. The plasma density decreases with radius and so does the pressure. The resulting pressure gradient force accelerates the plasma. At the same time, the star‘s gravitation holds the plasma back. A force imbalance in favour of the accelerating pressure gradient then drives the stellar wind. The Parker-model was initially derived to describe the solar wind and describes a so-called thermally driven wind. Since very little is known about the winds of late M-dwarfs such as TRAPPIST-1, the literature commonly assumes that these winds are thermally driven (*Cohen et al.*, 2014; *Vidotto et al.*, 2011; *Garraffo et al.*, 2016; *Garraffo et al.*, 2017).

Parker (1958) derived the analytic model based on hydrodynamics, i.e. no magnetic field is involved in the wind dynamics. Further, it assumes radial symmetry, stationarity, an isothermal plasma and a non-rotating star.

Such a wind carries a total mass flux $\dot{M}$ in radial direction, given by

$$\dot{M} = 4\pi\, R_*^2\, v_0\, \rho_0 \tag{3.25}$$

at the stellar radius R_*. For instance the star is the only source for matter in the stellar wind, therefore the mass flux is a constant. Wind and mass flux allow to derive a radial density profile. Based on mass conservation, the radial density profile reads

$$\rho(r) = \rho_0 \left(\frac{R_*}{r}\right)^2 \frac{v_0}{v_{\mathrm{sw}}(r)}. \tag{3.26}$$

The equation of motion is given by

$$\rho(\boldsymbol{v}\cdot\nabla)\boldsymbol{v} = -\nabla p - \frac{GM_*}{r^2}. \tag{3.27}$$

By taking the radial component of the equation, applying equation (3.26) and introducing the sound speed $c_{\mathrm{s}} = \sqrt{\frac{dp}{d\rho}}$ and the critical radius(distance where the stellar wind velocity equals c_{s})

$$r_{\mathrm{c}} = \frac{GM}{2c_{\mathrm{s}}} \tag{3.28}$$

we finally obtain:

$$\left(\frac{v}{c_{\mathrm{s}}}\right)^2 - \ln\left(\frac{v}{c_{\mathrm{s}}}\right) = 4\ln\left(\frac{r}{r_{\mathrm{c}}}\right) + 4\frac{r_{\mathrm{c}}}{r} + \mathrm{const.} \tag{3.29}$$

The physically adequate solution to this equation reaches the speed of sound at the critical radius and then accelerates outward. From the condition that the solution has to include the critical point with $v(r_{\mathrm{c}} = c_{\mathrm{s}}$, one can estimate the constant to be -3 (*Parker*, 1958).

Other models, like the one from *Weber and Davis* (1967) assume that the star's rotation and magnetic field alter the wind dynamics. However, even in this model, the dominating wind velocity component is the radial component. Although *Parker* (1958) did not include these effects into his wind model, he describes the effect that the radial wind and a rotating star have on the magnetic field geometry. In the solar wind, field lines are quasi-open, which means they close at infinity. In such a field configuration the radial component is the dominant one. However, as the star rotates the magnetic field corotates with it. At the same time, the field lines are tied to the radially outflowing plasma due to the frozen field theorem (equation (3.13)). This results in a spiral structure, the so-called Parker spiral. The corresponding magnetic field components, according to *Parker* (1958), look like

$$B_r = B_0 \left(\frac{R_*}{r} \right)^2 \tag{3.30}$$

$$B_\varphi = -B_0 \frac{\Omega_* \, R_*^2}{v_{\mathrm{sw}} \, r}. \tag{3.31}$$

In our modelling studies of the TRAPPIST-1 system (chapter 4 and chapter 5) we assume a slightly adapted magnetic field. If we assume a large scale dipole field at the star, there is a region close to the star, where the field behaves like a dipole, i.e. declines with r^{-3}. We take this behaviour into account and assume that the magnetic field is a dipole up to a distance of r_2. We assume r_2 to be $5R_*$ in our studies. Further outside, at $r > r_2$, the field follows a Parker spiral (*Parker*, 1958), with

$$B_r = B_{r2} \left(\frac{r_2}{r} \right)^2 \tag{3.32}$$

where B_{r2} is the field strength at r_2.

3.3 Sub-Alfvénic Interaction

In this section, we will introduce the theoretical concepts of the Alfvén wing model according to *Neubauer* (1980). That includes the two essential types of interaction between plasma and planet and the Poynting flux carried by an Alfvén wing (*Saur et al.*, 2013).

3.3.1 Alfvén Wing Model

Exoplanets are embedded in the stellar wind plasma and the stellar magnetic field. Therefore, the planets excite Alfvén waves. How the interaction finally looks like is determined by the ratio of the plasma velocity to the Alfvén speed, i.e. the Alfvén Mach number

$$M_{\mathrm{A}} = \frac{v_{\mathrm{rel}}}{v_{\mathrm{A}}} \tag{3.33}$$

with the relative velocity$\boldsymbol{v}_{\mathrm{rel}} = v_{\mathrm{sw}} \, \boldsymbol{e}_r - \Omega_{\mathrm{orb}} r \, \boldsymbol{e}_\varphi$ between stellar wind and planet, where Ω_{orb} is the angular velocity of the planetary orbital motion. If $M_{\mathrm{A}} > 1$, i.e. $v_{\mathrm{rel}} > v_{\mathrm{A}}$, then this condition is called super-Alfvénic and if $M_{\mathrm{A}} < 1$, i.e. $v_{\mathrm{rel}} < v_{\mathrm{A}}$, the plasma condition is called sub-Alfvénic. The latter is important for SPI, because it allows the waves to travel upstream towards the star. Therefore only sub-Alfvénic conditions allow an electromagnetic coupling between planet and star.

Neubauer (1980) derived the non-linear Alfvén wing model to describe the interaction between Jupiter and its moon Io. The author used the constancy of the Elsässer variables, also known as Alfvén characteristics, in the rest frame of the orbiting object:

$$\boldsymbol{c}_{\mathrm{A}}^{\pm} = \boldsymbol{v}_{\mathrm{rel}} \pm \boldsymbol{v}_{\mathrm{A}}. \tag{3.34}$$

Only in the rest frame that moves with the planet the resulting wave structure is a standing wave structure (*Saur et al.*, 2013). Therefore, the characteristics are not parallel to the background magnetic field $\boldsymbol{B}_0$ anymore, but instead, they are inclined by an angle

$$\sin\Theta_{\mathrm{A}}^{\pm} = \frac{M_{\mathrm{A}}\cos\Theta}{\sqrt{1+M_{\mathrm{A}}^2 \pm 2M_{\mathrm{A}}\sin\Theta}}. \tag{3.35}$$

The angle Θ is the angle between $\boldsymbol{v}_{\mathrm{rel}}$ and the normal to $\boldsymbol{B}_0$. In the limit of very small Mach numbers one can approximate the angle as $\Theta_{\mathrm{A}} = \tan^{-1}(M_{\mathrm{A}})$.

The Alfvén characteristics fulfil the stationary equation of motion and the frozen field theorem (equation (3.13)) under the condition that density, pressure, magnetic field strength and Alfvén speed are constant (*Neubauer*, 1980). From there, one can derive that the current density parallel to the Alfvén characteristics reads

$$j_{\parallel} = \Sigma_{\mathrm{A}}\nabla\cdot\boldsymbol{E}. \tag{3.36}$$

The Alfvén wing acts like a conductor with conductance

$$\Sigma_{\mathrm{A}}^{\pm} = \frac{1}{\mu_0 v_{\mathrm{A}}\sqrt{1+M_{\mathrm{A}}^2 \pm 2M_{\mathrm{A}}\sin\Theta}}. \tag{3.37}$$

This conductance thereby determines the strength of the current systems carried by the wing.

The general non-linear solution for Alfvén waves according to *Neubauer* (1980) reads

$$\boldsymbol{B}_{\perp} = \mu_0\Sigma_{\mathrm{A}}\frac{\boldsymbol{c}_{\mathrm{A}}^{\pm}}{|\boldsymbol{c}_{\mathrm{A}}^{\pm}|}\times\boldsymbol{E} \tag{3.38}$$

$$B_{\parallel} = \pm\sqrt{B_0^2 - B_{\perp}^2}. \tag{3.39}$$

3.3.2 Types of Interaction

There are different ways of how planets and moons can interact with their surrounding plasma. The majority of moons in the solar system interacts via their atmosphere. A notable exception is Jupiter's moon Ganymede that has an intrinsic magnetic field and generates Alfvén wings (*Kivelson et al.*, 1996b). Also, bodies that absorb plasma and therefore disturb the plasma flow may generate Alfvén wings (*Simon et al.*, 2012). However, in this chapter, we will introduce mechanical interaction via atmospheres and electromagnetic interaction via planetary magnetic fields.

3.3.2.1 Intrinsic Planetary Magnetic Field

Many exoplanets likely possess intrinsic magnetic fields. However, clear and unquestionable detection of such magnetic fields is still pending.

In terms of SPI, an intrinsic planetary magnetic field increases the size of the planetary obstacle in the plasma flow, which increases the generated energy flux. According to *Saur et al.* (2013), the obstacle size can be approximated by

$$R_{\mathrm{obst}} = kR_{\mathrm{exo}} \sqrt[3]{\frac{B_{\mathrm{exo}}}{B_{\mathrm{loc}}}} \tag{3.40}$$

with the radius of the exoplanet R_{exo}, the field strength at the surface of the planet B_{exo} and the local stellar magnetic field strength B_{loc}. The factor k results from the orientation of the planetary dipole axis towards the stellar magnetic field and reads

$$k = \sqrt{3\cos(\frac{\Theta_{\mathrm{M}}}{2})} \tag{3.41}$$

with Θ_{M} being the angle between the planetary dipole moment $\boldsymbol{M}_{\mathrm{exo}}$ and $\boldsymbol{B}_{\mathrm{loc}}$.

The planetary magnetosphere decelerates the plasma flow and therefore alters the motional electric field (equation (3.13)). One can use this to define an interaction strength

$$\bar{\alpha} = 1 - \frac{E}{E_0} \tag{3.42}$$

with the perturbed electric field E and the unperturbed electric field E_0 (*Saur et al.*, 2013). If $\bar{\alpha} = 0$, no interaction takes place and for the other extreme of full interaction we receive $\bar{\alpha} = 1$.

The resulting Alfvén wing structure also alters the magnetic field lines. *Saur et al.* (2013) determines three classes of field lines: those that begin and end on the planet, those that connect the planet to the star and those that have no connection to the planet. *Strugarek et al.* (2015) simulated how different types of alignment of the planetary magnetic dipole field with the local stellar field affect the interaction. In the case of perfect alignment, the magnetosphere opens up, just like it happens at Ganymede (*Kivelson et al.*, 1996b). In case of anti-alignment the magnetosphere closes and the Alfvén wing forms behind the magnetosphere.

3.3.2.2 Mechanical Interaction

Although the literature on SPI often assumes intrinsic magnetic fields on exoplanets, we see in our solar system that mechanical interaction between neutral atmospheres and plasma drives the majority of sub-Alfvénic interactions (see section 2.4.1). Furthermore, the only terrestrial planetary bodies in our solar system that have intrinsic magnetic fields are Mercury, Earth, and Ganymede. Therefore it is fair to assume that most of the planets interact via their atmosphere.

Among the plasma particles, electromagnetic forces dominate mutual interactions. However, atmospheric neutral particles are not affected by electromagnetic forces. Therefore the plasma ions can collide with neutral particles. In that case, a planetary atmosphere acts as a sink for plasma momentum and kinetic energy, i.e. the plasma is slowed down.

Collisions can be parametrised by a collision frequency ν_{in}. Therefore an atmosphere acts as a conductive medium with the Pedersen conductivity

$$\sigma_{\mathrm{P}} = \frac{n\, e}{B} \frac{\nu_{\mathrm{in}}\omega_{\mathrm{ci}}}{\nu_{\mathrm{in}}^2 + \omega_{\mathrm{ci}}^2} \tag{3.43}$$

with the ion particle density n, the elementary charge e and the gyro frequency ω_{ci}. If one integrates the Pedersen conductivity along the magnetic field lines one receives the Pedersen conductance Σ_P. Together with the Alfvén conductance Σ_A one can define an approximate interaction strength for mechanical interaction (*Neubauer*, 1998; *Saur et al.*, 1999, 2013) given by

$$\bar{\alpha} = \frac{\Sigma_\mathrm{P}}{\Sigma_\mathrm{P} + \Sigma_\mathrm{A}}. \tag{3.44}$$

Atmospheric properties effectively determine the overall obstacle size and interaction strength. An exosphere with extremely low particle densities may not be able to provide a sufficient amount of collisions to generate a clear interaction.

3.3.3 Poynting Flux

Alfvén wings carry energy towards the star. The resulting wave disturbances carry the electromagnetic energy flux called Poynting flux. The Poynting theorem

$$\frac{\partial u}{\partial t} + \nabla \cdot \boldsymbol{s} = -\boldsymbol{j} \cdot \boldsymbol{E} \tag{3.45}$$

describes the electromagnetic energy balance of a system. The variables describe the electromagnetic energy density

$$u = \frac{B^2}{2\mu_0} + \frac{E^2 \epsilon_0}{2}, \tag{3.46}$$

the Poynting vector $\boldsymbol{s}$, the electric field $\boldsymbol{E}$, and the current density $\boldsymbol{j}$. The theorem has the form of a continuity equation, where $-\boldsymbol{j} \cdot \boldsymbol{E}$ describes the energy conversion in form of Joule heating. Apart from this sink term the energy density is only affected by the energy flux entering and leaving the volume element. The Poynting vector is given by

$$\boldsymbol{s} = \frac{\boldsymbol{E} \times \boldsymbol{B}}{\mu_0}. \tag{3.47}$$

Saur et al. (2013) derived an expression for the power in form of the Poynting flux that is generated by sub-Alfvénic interactions and deposited in the central body. This power has been derived for small Alfvén Mach numbers and in a reference frame where the background motional electric field is zero. The resulting ready-to-use formula is given by

$$S = 2\pi R_\mathrm{eff}^2 \frac{(\bar{\alpha}\, M_\mathrm{A}\, B_\mathrm{loc}\, \cos\theta)^2}{\mu_0} v_\mathrm{A}. \tag{3.48}$$

The choice of parameters allows investigating moon-magnetosphere interaction as well as star-planet interaction and mechanical interaction as well as intrinsic magnetic fields.

Sophisticated MHD-simulations of star-planet interaction by *Strugarek et al.* (2015) demonstrate that the analytic expression of equation 3.48 reproduces the numerically modelled values of the Poynting flux remarkably well.

3.4 Time-variability in Star-Planet Interaction

Stellar winds and magnetic fields are usually not perfectly rotationally symmetric. Instead there are asymmetries and inhomogeneities, caused by the magnetic fields. Since star-planet interaction heavily depends on the environmental conditions around the planets, these asymmetries can cause periodic variabilities in SPI. Here, we investigate four different mechanisms that could generate temporal variability in SPI and determine the expected periods.

Apart from slight editorial changes and adaptions to the context of this thesis, the texts and findings in this section have been published before in *Fischer and Saur* (2019).

3.4.1 Conceptual Basics for Time-Variability

Star-planet interaction is hard to observe because the generated power is expected to be much weaker than the bolometric stellar emission (*Saur et al.*, 2013). The equivalent to SPI from our solar system, the interaction between the giant planets and their moons, is comparably simple to observe. Emissions of the planetary aurora including the moons' auroral footprints can be spatially resolved in observations (*Clarke et al.*, 2002; *Pryor et al.*, 2011). In contrast, the emissions generated by SPI might be hard to distinguish from the stellar background but might be visible in the chromospheric Ca II H & K lines. Knowledge about the expected periodicities of time-variable SPI helps to identify planet-related emissions in observations. Stars usually have an intrinsic variability that is often connected to corotating features in their atmospheres and therefore allow to estimate the stellar rotation period. In addition to that, there is a certain randomness in the occurrence of flares, prominences and coronal mass ejections on stars. *Lanza* (2018) investigated how SPI can trigger flares. Therefore the periodic occurrences of flares might indicate the existence of electromagnetic star-planet interaction in a stellar system.

The most basic periods that occur in stellar systems are the rotation period of the star T_* and the orbital period of its planet T_P. Both are the respective sideric periods relative to a fixed star. In multi-planet systems, of course, there are also multiple orbital periods. Temporal variability of the SPI can come from both of these basic periods in a system. The reason is that the Alfvén wing's footpoint moves with the planet's orbital period across the stellar surface. The strength of the SPI is controlled by properties of the rotating star and properties of the orbiting planet. This combination results in a periodic time-variability with the synodic rotation period of the star as seen from the planet. The synodic periods generally are given by

$$T_{\mathrm{syn}} = \left| \frac{2\pi}{\Omega_{\mathrm{inner}} - \Omega_{\mathrm{outer}}} \right| \tag{3.49}$$

where Ω and $T = 2\,\pi/\Omega$ are the angular velocities and the sideric rotation periods, respectively. The subscript *inner* stands either for the stellar rotation or an inner

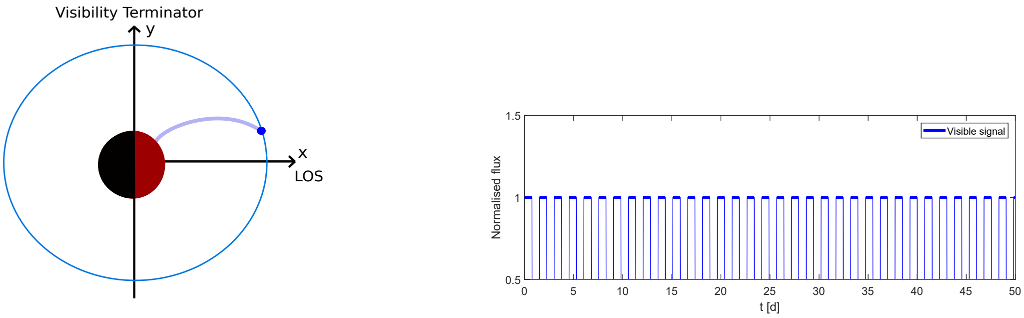

(a) Visibility Geometry (b) Visibility Lightcurve

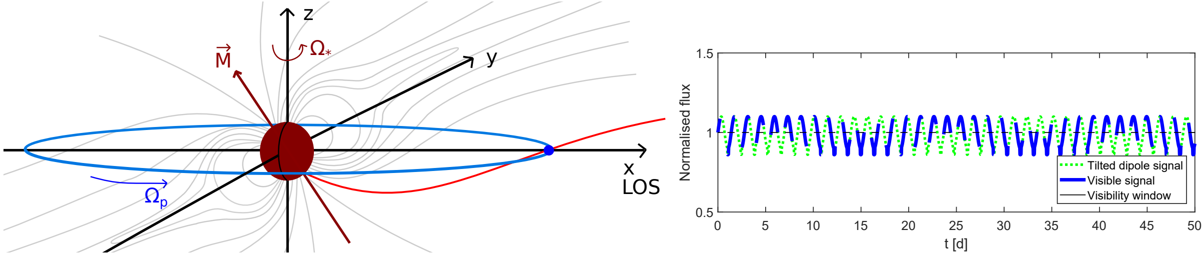

(c) Tilted dipole Geometry (d) Tilted dipole Lightcurve

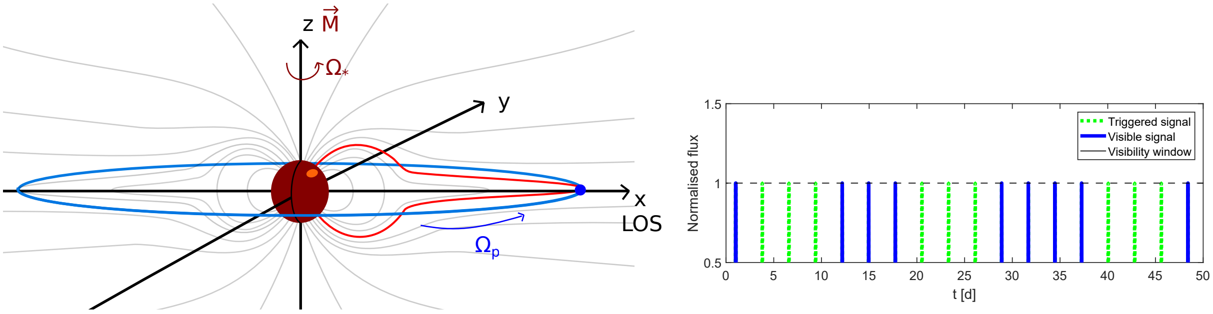

(e) Flare Trigger Geometry (f) Flare trigger Lightcurve

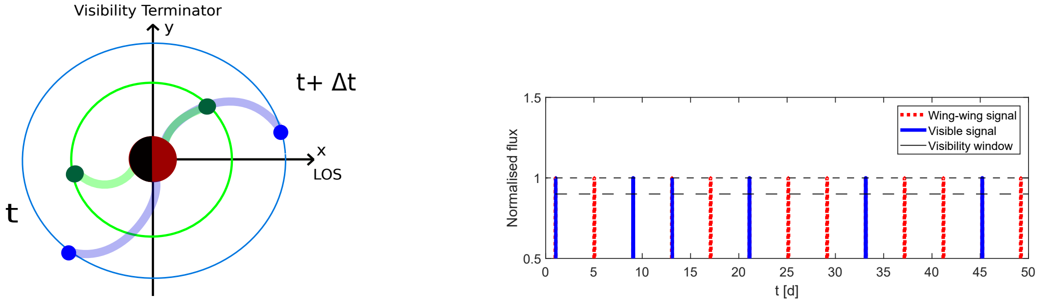

(g) Wing-wing Geometry (h) Wing-wing Lightcurve

Figure 3.1: Time-Variability mechanisms and light curves (*Fischer and Saur*, 2019).

planet in case of an interaction between two Alfvén wings. The subscript *outer* stands for the corresponding outer planet.

In our considerations about temporal variability, we make certain assumptions that allow an analytic treatment of these processes. We assume that the planet moves on a circular orbit, which likely holds well for close-in planets due to the tidal interaction with the star, just as it is the case in the TRAPPIST-1 system (*Gillon et al.*, 2017). Further, we assume a dominating dipolar magnetic field and a steady-state stellar wind.

Under these conditions, we identified four mechanisms that could cause a temporal variability in SPI. These mechanisms are the visibility of the Alfvén wing, effects related to a tilted dipole magnetic field, a magnetic anomaly on the star or the interaction of multiple Alfvén wings with each other. All of these causes for time-variability are presented in Figure 3.1. The corresponding panels show a sketch of the physical situation on the left and a corresponding light curve of the generated signal on the right. All related periods here are shown for the special case of TRAPPIST-1 and its planets T1b and T1c. These processes introduce three qualitatively different periods for the SPI: The orbital period of the planet T_p, the synodic period between stellar rotation and planetary orbit T_syn and the synodic period between two planets $T_\mathrm{syn}^\mathrm{planet}$. In the following sections, we will discuss these different mechanisms, which produce temporal variability with their respective properties. Also, we will outline in what way the star could respond to an interaction with Alfvén wings and how this in turn affects the observability of the SPI.

3.4.2 Visibility

The visibility of the Alfvén wing is the most basic process that causes a temporal variability. Due to the motion of the planet the Alfvén wing moves across the star and is either on the visible hemisphere or on the other side. The purest realisation of this process is if there are no latitudinal asymmetries altering the signal of the Alfvén wing.

Figure 3.1a shows a top view of the physical situation with the x-axis pointing into the line of sight (LOS) towards the observer and the z-axis of the coordinate system being aligned with the stellar spin axis. The shaded region on the star represents the non-visible hemisphere where the y-z-plane determines the visibility terminator. The planet orbits the star and creates the signal in Figure 3.1b. This shows the hypothetical normalised light curve over a time of 50 d and without any intrinsic luminosity coming from the star. We applied the periods of TRAPPIST-1 and its innermost planet as an example to demonstrate this process. The period of the signal is accordingly $T_\mathrm{SPI} = T_\mathrm{p}$ and has, in the simplest case of constant emission, the shape of a boxcar function. This boxcar function needs to be modified as a function of time depending on the optical depth of the emitted radiation through the stellar atmosphere.

3.4.3 Tilted Stellar Dipole Field

The energy flux generated at the planet depends on the magnetic field, the plasma density and the velocity of the stellar wind. In a tilted dipole magnetic field, all three parameters vary as a function of magnetic latitude. Thus the Poynting flux varies as a function of time.

Assuming that stellar winds form similar structures as the solar wind, there will be a fast wind originating from higher latitudes and a slow wind from lower latitudes. The slow wind zone also includes the stellar current sheet formed by a thin region of oppositely directed field lines. In the current sheet, the magnetic field lines are closed and thus the field strength decreases stronger with radial distance than in the ambient stellar wind. In order to maintain pressure balance, the plasma density in the current sheet is higher than in the surrounding stellar wind (*Smith*, 2001).

Figure 3.1c shows such a situation. The coordinate system is the same as in Figure 3.1a. The sketch shows a tilted stellar dipole field, represented by the magnetic dipole moment $\boldsymbol{M}$. We can see the region close to the star, where the lower-latitude field lines are closed dipole field lines. In polar regions, the field lines are quasi-open because the stellar wind stretches them much beyond the orbit of the planets. Current sheet field lines are stretched in the outward/inward direction and originate on latitudes around the magnetic equator.

For the planet, there are two hypothetical situations. The one presented in Figure 3.1c shows the planet located on quasi-open field lines. In the second situation, the planet is constantly located within closed field lines, which only occurs for close-in planets.

The expected period of the occurring signal is $T_{\mathrm{SPI}} = T_{\mathrm{syn}}/2$ for both situations, i.e., half the synodic rotation period of the star in the frame of the planet. The planet crosses the slow wind zone twice during each rotation of the star, which creates the quasi-periodic SPI signal with half the synodic period. In the slow wind zone and the current sheet the stellar wind properties (such as local density and magnetic field strength) change and affect the amplitude of the Poynting flux generated by the planets (see expression 3.48), which is the physical reason for temporal variability in SPI. Especially if the planet resides on quasi-open field lines, the differences to the current sheet might be strong. The resulting qualitative signal could have a shape like the green curve in Figure 3.1d. The figure shows the relative incoming energy flux of the star-planet interaction. If we further take visibility into account, we obtain the blue curve. We indicated the visibility windows with black bars, appearing with a period of T_{p} (in this case 1.51 d) and a duration of $T_{\mathrm{p}}/2$. Just as in section 3.4.2, these windows indicate the times when the Alfvén wing's footpoint resides on the visible hemisphere of the star. This effect breaks the periodicity of $T_{\mathrm{syn}}/2$ to some extent. Instead, we see a beat-like interference pattern with varying powers and a much larger period.

This mechanism is well known from the Jupiter system. Due to the tilt in Jupiter's magnetic field, the jovian moons experience time-variable magnetic field strengths and plasma densities, since the bulk of the plasma is concentrated in the centrifugal equator (*Hill and Michel*, 1976; *Bagenal et al.*, 1980). The Io footprint undergoes continuous brightness variations (*Wannawichian et al.*, 2010, 2013) caused by variable Poynting fluxes with a period of $T_{\mathrm{syn}}/2$ (*Saur et al.*, 2013).

3.4.4 Flare Triggering

The idea behind the trigger mechanism is, that the planet's Alfvén wing releases energy, for example stored in form of magnetic loops, on the star. It has been proposed by *Lanza* (2009, 2012, 2013) as a change in magnetic helicity, which releases free magnetic energy. This energy release causes a flare event with a significantly larger energy output compared to energy deposition of the Alfvén wing energy flux during a comparable time. *Lanza* (2018) describes three different mechanisms that result in the release of energy stored in magnetic loops and provides relations to estimate upper limits of the flare energies. For two of these mechanisms the planet may act as a trigger for the eruption of a flare. However flares can also erupt without the influence of a planet. According to *Lanza* (2018) both processes create flare energies of about 10^{26} J up to 10^{31} J, depending on the star. The third described mechanism only operates in the presence of a planet. The planet's interaction with an open coronal magnetic field generates the flare. The created energies are typically one to three orders of magnitude smaller than for the other two mechanisms.

Figure 3.1e depicts the simplest case of a large scale dipole field with an anomaly indicated by the orange dot on the star. The Alfvén wing, indicated in red, intersects this anomaly and triggers the release of energy. This situation causes a periodicity of $T_{\mathrm{SPI}} = T_{\mathrm{syn}}$ if the triggered signal is much stronger than the power of the plain Alfvén wing. The green curve in Figure 3.1f shows the expected signal of this mechanism. If we take visibility into account we receive the signals shown in blue. As for the tilted dipole the inclusion of visibility breaks the overall periodicity. We only see piecewise periodic signal peaks whereas there are large intervals with no signal.

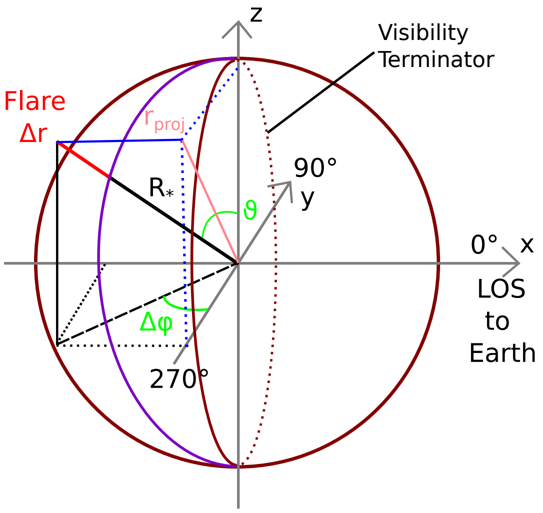

Figure 3.2: Extended visibility of triggered flares.

However the spatial extent of a flare will extend the visibility range to more than the visible half-sphere. Figure 3.2 shows a simplified geometry that allows the estimation of an extended visibility surface due to the elevation of flares. The coordinate system is the same as in Figure 3.1e, with the x-axis pointing towards the Earth and the z-axis being aligned with the spin axis of the star. The great circle in the y-z-plane is therefore the visibility terminator.

We assume that a flare ejects radially outward with a height Δr (Figure 3.2 bright red line) and is located on a colatitude ϑ and at an azimuthal position behind the visibility terminator $\Delta\varphi$ (both indicated in green). If such a flare is high enough that its top is visible above the visible disk, the flare's footpoint belongs to the range of extended visibility. We aim to find the longitudinal extent $\Delta\varphi$ into the non-visible side such that the top of the flare is still visible for a given flare height and flare latitude. In observations we see the top of the flare projected into the y-z-plane, which is given by $r_{\mathrm{proj}}^2 = y^2 + z^2$ (pink) with $y = (R_* + \Delta r)\sin\vartheta\cos\Delta\varphi$ and $z = (R_* + \Delta r)\cos\vartheta$. We use $r_{\mathrm{proj}}^2 > R_*^2$ and receive

$$\sin\Delta\varphi < \frac{\sqrt{1-\left(\frac{R_*}{R_*+\Delta r}\right)^2}}{\sin\vartheta} \tag{3.50}$$

which describes the maximum extension of the flare's visibility. The visible hemisphere covers 50% of the stellar surface and the extended visibility reaches up to

$$\text{Vis} = \frac{180^\circ + 2\Delta\varphi}{360^\circ} \cdot 100\%. \tag{3.51}$$

We note that this effect is more relevant for larger ratios of flare height to stellar radius. It is apparent from equation 3.50 that the visibility will be 100% for flares appearing at the poles, whereas the minimum of the visibility extension will be at the stellar equator.

Parker (1988) proposed the existence of nanoflares with an energy $< 10^{20}$ J on the sun. The main idea of this work was that the corona is heated by nanoflares that appear on large scales. *Aschwanden et al.* (2000) proposed a classification that divides solar flare events by their total energy with microflares being below 10^{23} J and nanoflares below 10^{20} J. The same study investigated the occurrence and typical emissions of different types of flares. High energy flares that emit hard X-rays are accordingly rare events. The flare frequency increases with decreasing flare energy. Nanoflares are about 10^5 to 10^{10} times more frequent than high energy flares. Microflares tend to emit soft X-rays while nanoflares emissions lie in the EUV range. An Alfvén wing might trigger a large number of these smaller events along its path across the star. Assuming quasi-constant flare triggering we expect those emissions to be pulsed with the period of the planet's orbit similar to the discussed effects in section 3.4.2. Also these events might account for the enhanced X-ray activity in some planet hosting stars. However strong flares in contrast might occur when regions with active magnetic loops are triggered by an Alfvén wing.

Lanza (2009, 2012, 2013) and *Saur et al.* (2013) discussed the relevance of a trigger mechanism in the case of HD 179949 (*Shkolnik et al.*, 2003; *Shkolnik et al.*, 2005). Both SPI models predict powers of about 10^{17} W that are generated by the planet, while the observations from *Shkolnik et al.* (2005) indicate excess powers of 10^{20} W, which lead to the introduction of the trigger mechanism. Another aspect is that *Shkolnik et al.* (2003); *Shkolnik et al.* (2005) observed emissions that are pulsed with the planetary orbital period. As discussed in this section we would expect the signal to appear with the respective synodic rotation period of the star as seen from the planet if flares are triggered at a fixed longitude on the star. In the case of HD 179949 the synodic period is approximately 4.5 d, considering the planetary orbital period of 3 d (*Shkolnik et al.*, 2003) and the stellar rotation period of 7 to 9 d (*Shkolnik et al.*, 2008). In case of triggering of flares across the surface of the star on time scales much smaller than the rotation period (*Lanza*, 2009), the resultant lightcurve will be dominated by the sideric rotation period of the planet.

3.4.5 Wing-Wing Interaction

Alfvén wings exist in Jupiter's magnetosphere, where the magnetic field can approximately be described as a dipole field. Therefore the Alfvén wings generated by each moon follow the field lines that are connected to the moon into the polar jovian ionosphere. This implies that Alfvén wings of different moons never interact with each other.

The situation could be different in stellar environments with SPI. Sufficiently far from the star, the magnetic field geometry differs from the dipole field lines around planets because the stellar magnetic field lines are carried out with the stellar wind. This effect leads to extremely stretched current sheet magnetic field lines, which are very close to the spin plane of the star. If the planets reside in the current sheet and two planets coincidently share the same quasi-open field line, the Alfvén wings of those planets might intersect and interact with each other. This interaction might mutually affect the two planets that are involved, e.g., by enhanced auroral activity. Therefore this interaction could alternatively be named planet-planet interaction. The idea is sketched in Figure 3.1g. The planets would have to lie within the current sheet while the field lines have to be sufficiently parallel to each other, in order to allow the Alfvén wings to merge. On the left there is a hypothetical situation at time t where both Alfvén wings are separated from each other and later at time $t + \Delta t$ both Alfvén wings merge into each other. Wing-wing interaction has not received attention in the literature to the authors' knowledge. The interaction of Alfvén wings generates non-linear effects, which might result in an intensification of a possible joint wing. The wing-wing interaction occurs at the difference of the orbital angular velocities of both planets, i.e., the synodic rotation period of one planet as seen in the rest frame of the other planet $T_{\mathrm{SPI}} = T_{\mathrm{syn}}^{\mathrm{planets}}$. The signal is indicated in red in Figure 3.1h on the example of T1b and T1c. To be visible the footprint of the wing-wing interaction has to lie on the visible hemisphere. As one can see in the blue curve this clearly breaks any periodicity of the signal.

4 Is SPI possible at TRAPPIST-1? - A Parameter Study

In this chapter, we will conduct a large parameter study about the question, if SPI is possible in the TRAPPIST-1 system and if so, how strong it could be. The parameter study will be carried out semi-analytically with the stellar wind model described in section 3.2 to estimate the Poynting flux (equation (3.48)) generated by the planets according to *Saur et al.* (2013).

We start by defining a suitable parameter range for the stellar wind parameters. Afterwards, we analyse the possibility for SPI by estimating the Alfvén Mach number to determine the sub-Alfvénic range. When we know, which planets can host SPI under which conditions, we calculate expected Poynting fluxes.

The findings and most of the texts of this chapter have previously been published in *Fischer and Saur* (2019). Editorial changes have been applied to fit the texts into the context of this thesis.

4.1 Parameter Space

To characterise possible SPI, we need to know the stellar wind and the magnetic field of TRAPPIST-1. However, only a few parameters which constrain its stellar wind have been observed for TRAPPIST-1, otherwise we take typical values that are known for other M-dwarfs. TRAPPIST-1 with its spectral class M8 belongs to the late-type M-dwarfs whereas most parameters are measured for early or mid M-dwarfs.

We chose the stellar wind model presented in section 3.2 in such a way that there are only three independent parameters: the coronal temperature T_c, the total mass flux $\dot{M}$ and the equatorial magnetic field B_0. *Reiners and Basri* (2010) estimated the mean magnetic field strength as 0.06 T, with an uncertainty range from 0.02 T to 0.08 T. The geometry of the field is unknown. *Garraffo et al.* (2017) applied a magnetic field map with a strongly tilted dipole based on observations of the mid M-dwarf GJ 3622.

TRAPPIST-1's coronal temperature T_c has not been measured yet. For M-dwarfs, temperatures of 2 to $3 \cdot 10^6$ K, similar to the solar coronal temperature, are applied in the literature (*Vidotto et al.*, 2014; *Garraffo et al.*, 2016). For TRAPPIST-1, *Garraffo et al.* (2017) chose a hot sun-like corona. *Wheatley et al.* (2017) report an X-ray luminosity of TRAPPIST-1 that is similar to the quiet sun and indicates the existence of a hot stellar corona. Therefore we can expect temperatures of about 10^6 K as in the solar corona. M-dwarfs generally also show evidence for very high coronal temperatures up to 10^7 K (*Schmitt et al.*, 1990; *Giampapa et al.*, 1996). Hence we choose our parameter space accordingly with T_c in the range 10^6-10^7 K.

The parameter $\dot{M}$ has been derived from observations for different M-dwarfs but not for TRAPPIST-1. *Vidotto et al.* (2014) infer a range between approximately

Table 4.1: Results and parameters of TRAPPIST-1 and its seven planets: Rotation or orbital Period T and the estimated synodic periods of the interaction. The remaining columns show the best-guess results for the Mach number M_A and the Poynting flux S

Object	T [d]	T_syn [d]	M_A [a]	S [10^{13}] [a]
T1	3.3			
T1b	1.51087	2.79	$0.38\ ^{20}_{0.02}$	$14.2\ ^{233}$
T1c	2.42182	9.10	$0.55\ ^{28}_{0.03}$	$2.5\ ^{4.3}$
T1d	4.0496	17.82	$0.80\ ^{40}_{0.05}$	$0.26\ ^{0.43}$
T1e	6.0996	7.19	$1.08\ ^{54}_{0.06}$	$0\ ^{2.5}$
T1f	9.2067	5.14	$1.45\ ^{72}_{0.09}$	$0\ ^{4.3}$
T1g	12.3529	4.50	$1.79\ ^{89}_{0.11}$	$0\ ^{1.6}$
T1h	18.767	4.00	$2.58\ ^{128}_{0.15}$	$0\ ^{0.49}$

[a] See ranges in figures 4.1and 4.3 for upper and lower boundaries. The lower boundaries for S are zero.

10^8 kg s^{-1} and 10^{12} kg s^{-1} based on observations from *Wood et al.* (2001) and *Mullan et al.* (1992). For Proxima Centauri the maximum $\dot{M}$ is estimated to be approximately 10^{10} kg s^{-1} (*Wargelin and Drake*, 2002). *Turnpenney et al.* (2018) and *Garraffo et al.* (2017) assume $2 \cdot 10^9$ kg s^{-1} for TRAPPIST-1, which corresponds to a sun-like mass outflow. The latter authors already assumed a similar value for their simulations of Proxima Centauri (*Garraffo et al.*, 2016). On this basis we chose a parameter range of $10^8 - 10^{12}$ kg s^{-1}.

Additionally to the parameter space study we apply a 'best guess' with corresponding values of $\dot{M} = 10^{10}$ kg s^{-1}, $T_c = 2 \cdot 10^6$ K and $B_0 = 0.06$ T. The magnetic field value is based on the observations by *Reiners and Basri* (2010) and the coronal temperature is a typically applied temperature in the literature. The mass flux of $\dot{M} = 10^{10}$ kg s^{-1} is taken from the estimated maximum mass flux of Proxima Centauri (*Wargelin and Drake*, 2002).

4.2 Where can we expect SPI?

We will give an approximate answer on which planets could host SPI in the TRAPPIST-1 system. Therefore we calculate the possible Alfvén Mach numbers for every planet. Further, we conduct a sensitivity study on how strongly the chosen parameter ranges affect the results.

4.2.1 Alfvén Mach Number

The Alfvén Mach number at each planet determines the planets ability to form an Alfvén wing and connect to the star. Our chosen parameter space leads to a range of M_A at the planets as displayed in Figure 4.1. The blue dots represent

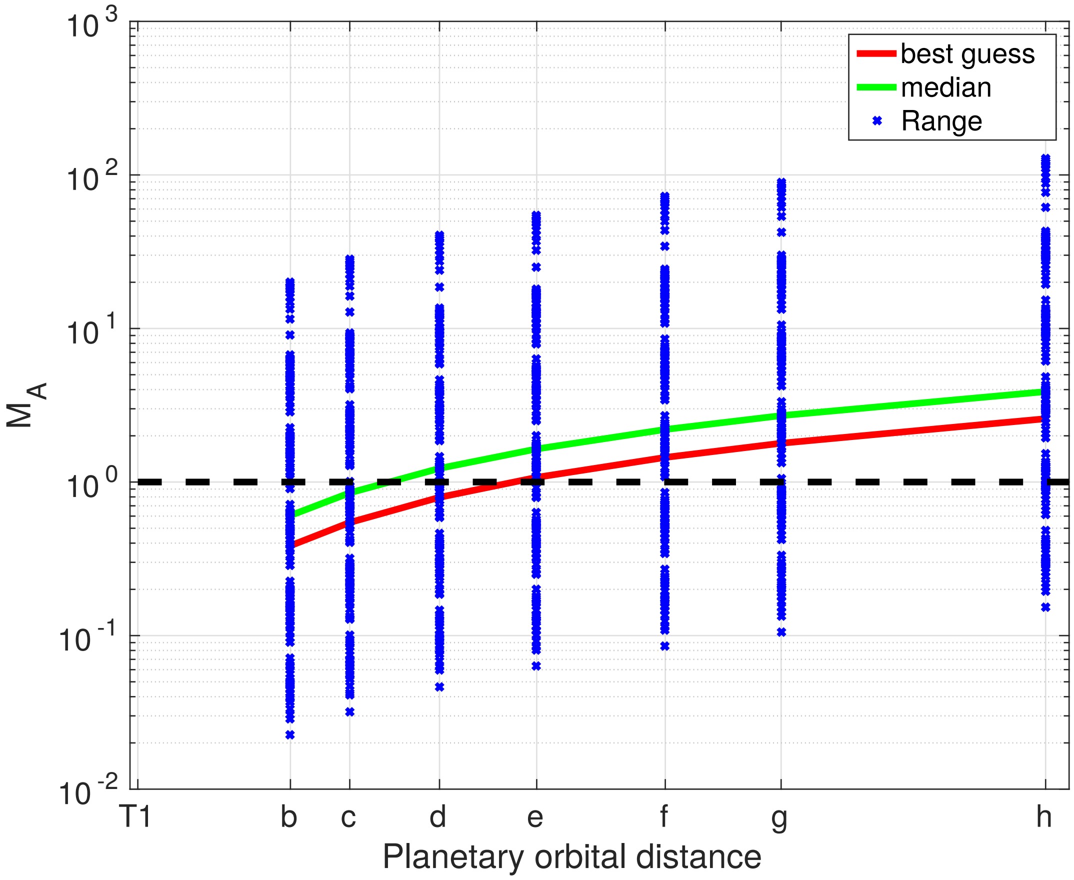

Figure 4.1: Alfvén Mach numbers for the chosen parameter space. Blue dots represent the different stellar wind conditions, the red line represnets the best guess and the green line is the median of the blue dots. Further indicated is $M_{\mathrm{A}} = 1$ by the thick dashed line. This figure has been published in *Fischer and Saur* (2019).

our estimated combinations of $\dot{M}$, B_0 and T_c, which we scanned logarithmically equally spaced within the limits given in section 4.1. Our 'best-guess' is shown in red (see section 4.1). In comparison, the green line shows the median of all M_{A}, which can be used as an indicator of the probability that a planet experiences $M_{\mathrm{A}} < 1$ within our assumed parameter space. Table 4.1 shows the basic quantities of the TRAPPIST-1 system that are required for our analysis. The last two columns present our best-guess results of the Mach numbers M_{A} with minimum and maximum values in sub- and superscripts and the same for the Poynting flux. It is visible that within our parameter space sub- and super-Alfvénic conditions are possible for all planets. For T1b and c the best-guess indicates M_{A} of 0.4 and 0.6 (table 4.1 and Figure 4.1) while the maximum lies at $M_{\mathrm{A}} = 20$ and 28 and the minimum at 0.02 and 0.03. The median lies around 0.6 and 0.9, respectively. This implies that T1b and c are more likely to be exposed to sub-Alfvénic flows than not and thus likely couple via Alfvén wings to the star. T1d has $M_{\mathrm{A}} = 0.8$ in the best-guess assumption (table 4.1) and the median lies at $M_{\mathrm{A}} = 1.1$, which makes it questionable if it constantly experiences sub-Alfvénic conditions. However due to variations in the stellar wind environment, it might occasionally be possible for T1d to form Alfvén wings. The other planets are unlikely to exhibit SPI because best-guess and median lie above $M_\mathrm{A} = 1$ (table 4.1 and Figure 4.1).

Garraffo et al. (2017) conclude from their simulations that all planets from T1b to T1g reside within the Alfvén shell for large parts of their orbits. Mainly this is due to a smaller mass flux in their model. If we apply $\dot{M} = 2 \cdot 10^9\,\mathrm{kg\,s^{-1}}$ in our best guess, we gain a similar result as *Garraffo et al.* (2017). In that case, all planets except T1h are within the Alfvén radius as well. A good indicator for the quality of our model compared to the MHD simulations is the dynamic pressure of the solar wind at each planet. *Garraffo et al.* (2017) investigate the space weather of the planets to find out how it might affect their habitability. The dynamic pressure is an important parameter in these estimations because it indicates the influence of the stellar wind on a planets atmosphere. We estimated the dynamic pressure for a similar set of parameters as *Garraffo et al.* (2017). The largest deviations appear at T1b with 40% and the smallest at T1e with 5%. On average, the relative deviation lies at 18%, which is small considering the uncertainties in the input parameters and the general differences in the applied models.

4.2.2 Sensitivity of the Alfvén Mach Number to Uncertainties of the Parameters

Our parameter ranges cover up to several orders of magnitude. Therefore we conduct an analysis of how sensitive the Mach number reacts towards uncertainties in the three model parameters. Figure 4.2 shows the dependence of the Mach number on the three model parameters. We vary only one parameter at a time within our defined parameter space. Figure 4.2a shows the Mach number in dependence of the coronal temperature T_c, similarly in Figure 4.2b) and 4.2c for B_0 and $\dot{M}$. For each sensitivity study, the other parameters are kept constant to their respective best-guess values.

We see in Figure 4.2a that the blue curve for 10^6 K represents the minimum curve, while for temperatures of 10^7 K (purple) the Mach numbers are larger due to the higher stellar wind velocities. The span between the resulting Mach numbers is about half an order of magnitude and thus smaller than the parameter spread of T_c itself. This variability is smaller than the variability of three orders of magnitude obtained in the Mach numbers in Figure 4.1. We obtain similar results from the magnetic field study in figure Figure 4.2b. B_0 is known within a small range of uncertainty compared to the other two parameters. The blue curve represents a stellar magnetic field of 0.02 T while the red and yellow curves represent 0.06 and 0.08 T. With less than half an order of magnitude the minimum-maximum spread of the obtained Mach numbers can not account for the spread of almost three orders of magnitude calculated with the whole parameter space. In the studies of T_c and B_0 the planets T1b and T1c always lie within the sub-Alfvénic range whereas T1e is the outermost candidate for SPI.

The mass flux (Figure 4.2c) is the least constrained quantity in our study and spans a range of four orders of magnitude between $10^8 - 10^{12}\,\mathrm{kg\,s^{-1}}$. We see that smaller mass fluxes cause smaller Mach numbers than large mass fluxes, which is due to its dependence on the plasma particle density. Therefore low mass fluxes result in lower Mach numbers. The resulting Mach numbers show a spread of two orders of magnitude. Therefore the uncertainty of the mass flux is responsible for the obtained large spread in the Mach numbers. As one can see in the red, yellow and

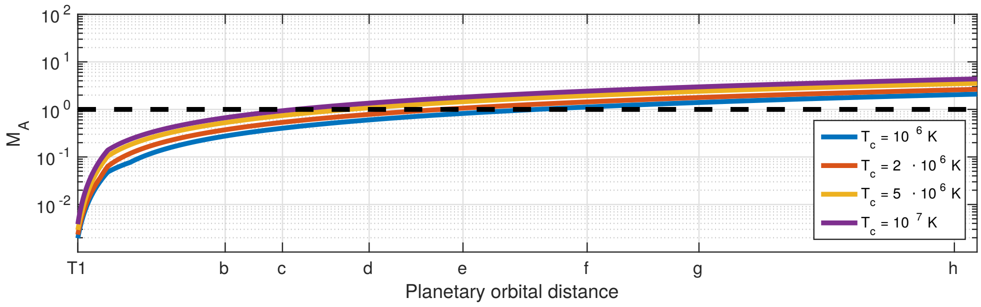

(a) Coronal temperature

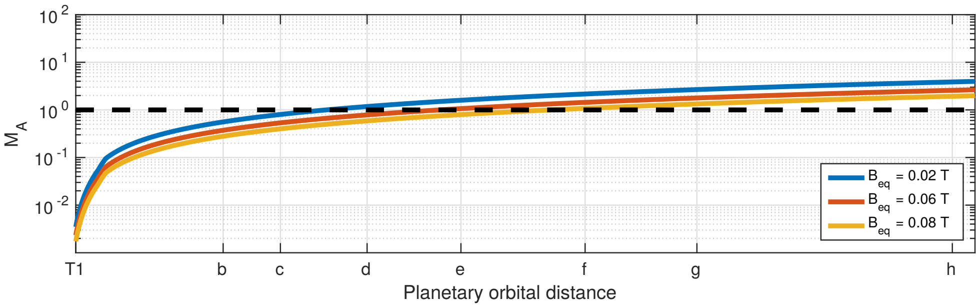

(b) Stellar magnetic field strength

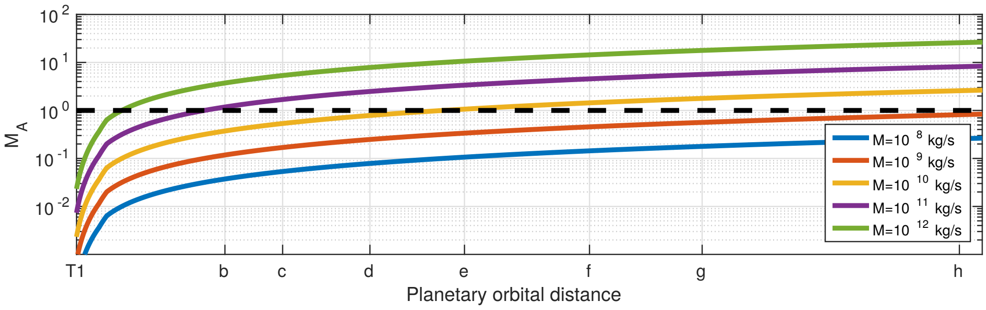

(c) Stellar wind mass flux

Figure 4.2: Sensitivity study of the Alfvén Mach number M_A for each of the three model parameters. This figure has been published in *Fischer and Saur* (2019).

purple curves, the difference of one order of magnitude in the mass flux compared to the best-guess (yellow) can lead to totally different results concerning SPI. For weaker mass fluxes all planets may cause SPI but with mass fluxes stronger than $10^{10}\,\mathrm{kg\,s^{-1}}$ there might be no SPI at all.

4.3 Expected Strength of the SPI

We now know under which conditions certain planets may experience sub-Alfvénic conditions. Therefore we can now estimate the expected strength of the Poynting flux for those planets. Again, we analyse the whole parameter range and look at how sensitive the total power reacts towards uncertainties in the stellar wind parameters. Finally, we look at how magnetic fields may affect the expected Poynting fluxes.

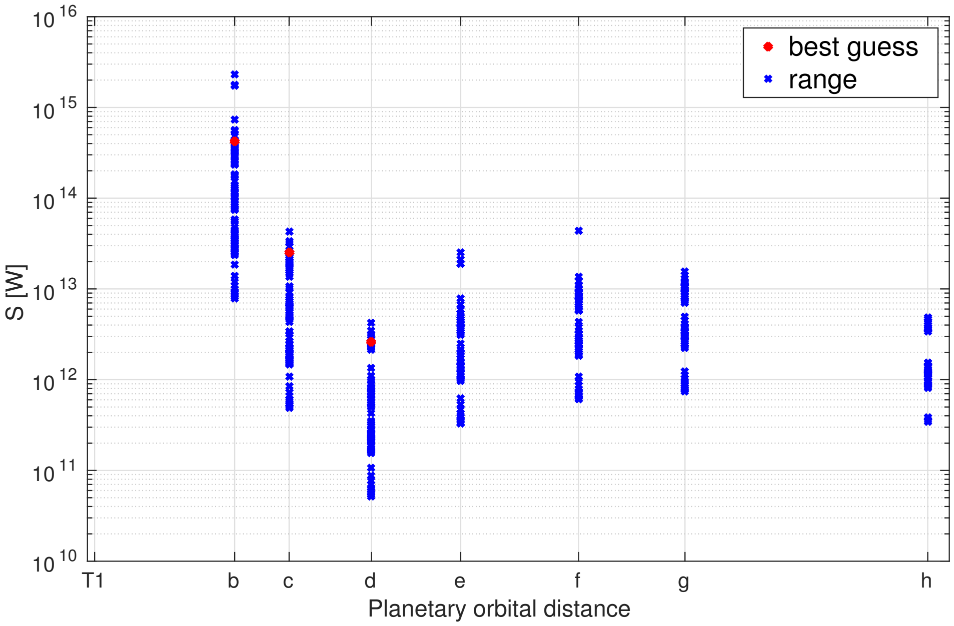

Figure 4.3: Poynting fluxes for those parameters that allow sub-Alfvénic conditions. Blue dots represent the different stellar wind conditions and the red dot represnet the best guess. This figure has been published in *Fischer and Saur* (2019).

4.3.1 Poynting Fluxes

The next step is to estimate the Poynting flux S for all planets, as shown in Figure 4.3. Table 4.1 summarises the Poynting fluxes calculated with the best-guess assumption. The superscripted numbers indicate the maximum Poynting flux that is possible with our parameter space. No lower values are given because our parameter space also allows non-existing Alfvén wings for each planet. We first assume that the planets do not possess intrinsic magnetic fields and no expanded atmospheres. For T1b and T1c the Poynting flux then lies between $5 \cdot 10^{11}$ W and 10^{15} W. The best-guess indicates powers of $4.2 \cdot 10^{14}$ W for T1b and $2.5 \cdot 10^{13}$ W for T1c (table 4.1). For some parameters, the planets T1d to T1h experience $M_\mathrm{A} < 1$ and generate Poynting fluxes between $5 \cdot 10^{10}$ and $3 \cdot 10^{14}$ W. Our best-guess gives $S = 0$ W because for these parameters the planets experience $M_\mathrm{A} > 1$. The Poynting flux generated by an exoplanet is strongly influenced by the angle Θ between the relative plasma velocity $\boldsymbol{v}_\mathrm{rel}$ and the normal of the stellar magnetic field $\boldsymbol{B}$ (*Saur et al.*, 2013). If this angle is 90° the magnetic field and the relative flow direction are parallel to each other. Therefore there is approximately no disturbance perpendicular to the magnetic field, which causes an Alfvén wave, and accordingly, there is no Poynting flux generated by the planet. TRAPPIST-1 rotates with a period of 3.3 d, so the point of field-parallel flow lies between T1c and T1d. Thus T1b generates the strongest Poynting flux, and T1d generates the weakest Poynting fluxes because it lies very close to this point of field-parallel flow. However, T1d is also the second-smallest planet in the system, which also causes a weaker Poynting flux than its neighbours.

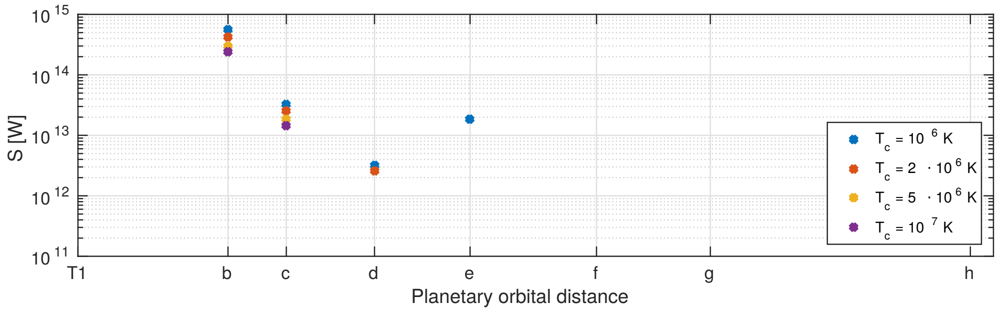

(a) Coronal temperature

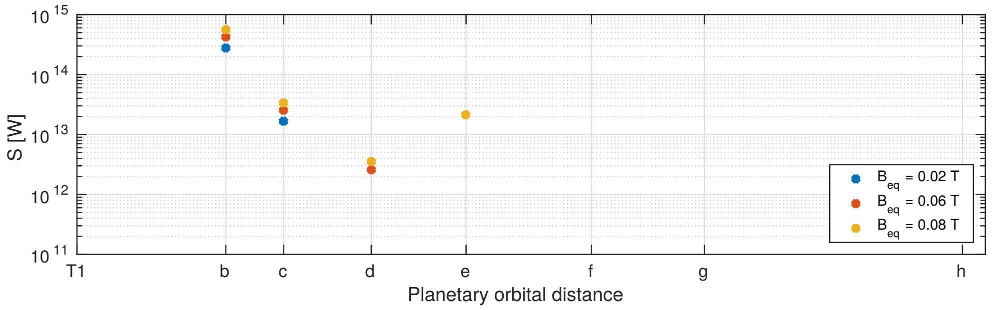

(b) tellar magnetic field strength

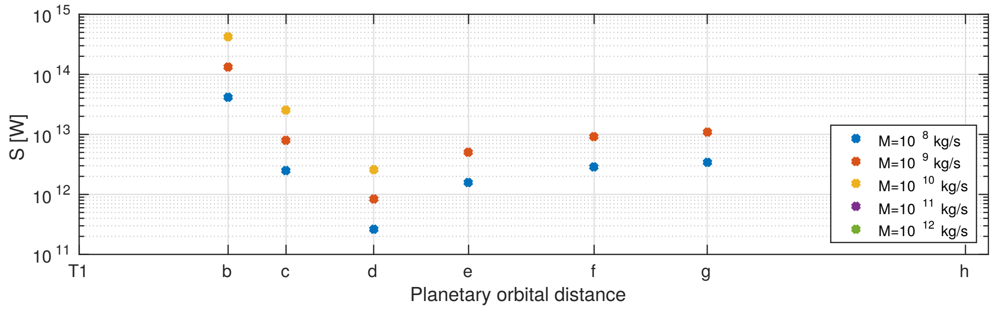

(c) Stellar wind mass flux

Figure 4.4: Sensitivity study of the Poynting flux S for each of the three model parameters. This figure has been published in *Fischer and Saur* (2019).

4.3.2 Sensitivity of the Poynting flux to Uncertainties of the Parameters

Figure 4.4 shows the Poynting flux in dependence of the three model parameters T_c, B_0 and $\dot{M}$ for all cases where $M_\mathrm{A} < 1$. This allows us to discuss the sensitivity of the Poynting flux on the different parameters similar to section 4.2.1.

In Figure 4.4a the red dots indicate the best-guess with $T_\mathrm{c} = 2 \cdot 10^6$ K, yellow and purple indicate higher temperatures and the blue dots represent 10^6 K. The temperature affects the Poynting flux via the stellar wind velocity. According to equation 3.48 one expects larger Poynting fluxes for higher coronal temperatures. However, in our study, lower temperatures lead to slightly larger Poynting fluxes. This is due to the additional effects of the geometry between the stellar wind and stellar magnetic field, represented by the angle Θ. TRAPPIST-1's planets are within a region close to the star where the flow is nearly aligned with the magnetic

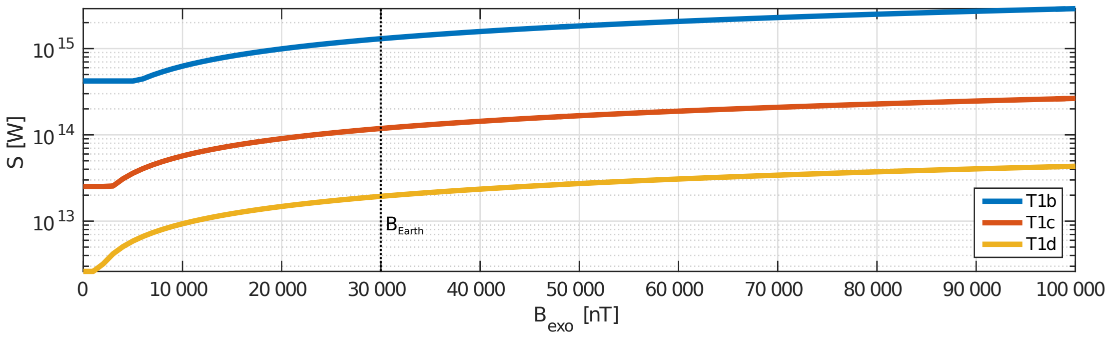

Figure 4.5: Changes in Poynting flux due to planetary magnetic field. This figure has been published in *Fischer and Saur* (2019).

field lines. For smaller stellar wind velocities (and T_c) the flow is less aligned with the magnetic field and causes stronger magnetic field perturbations resulting in stronger Poynting fluxes. At T1b one can see that the spread between minimum and maximum is about half an order of magnitude from $2 \cdot 10^{14}$ W to $6 \cdot 10^{14}$ W. The effect is similar at T1c with $1.5 \cdot 10^{13}$ W to $5 \cdot 10^{14}$ W. The spread therefore lies around half an order of magnitude and is similar to the spread of the Alfvén Mach number.

Figure 4.4b shows the dependence of the Poynting flux on the stellar magnetic field strength B_0. At T1b the Poynting flux spreads from $3 \cdot 10^{14}$ W to $6 \cdot 10^{14}$ W. At T1c the Poynting flux is lower and ranges from $1.8 \cdot 10^{13}$ W to $3.5 \cdot 10^{13}$ W. This small spread also is similar to the obtained Mach numbers and the narrow parameter range of B_0.

We have seen that the chosen parameter range of the mass flux has the strongest impact on the Mach numbers. However only the mass fluxes between $10^8 - 10^{10}\,\mathrm{kg\,s^{-1}}$ allow the existence of SPI. The best-guess value of $10^{10}\,\mathrm{kg\,s^{-1}}$ (yellow) allows three planets to generate SPI and the lower mass fluxes (red and blue) would enable all planets to generate SPI (Figure 4.4c). Due to the lower associated plasma densities, the Poynting flux depends proportionally on the mass flux. The minimum-maximum spread is about one order of magnitude at all three inner planets. This agrees well with the spread in the Mach numbers for the same parameter range which is also about one order of magnitude.

4.3.3 Changes in Case of Intrinsic Planetary Magnetic Fields

In case the planets possess intrinsic magnetic fields, the obstacle size responsible for SPI increases according to equation (3.40). Here we assume that the intrinsic dipole moment and the stellar magnetic field are parallel, which leads to the maximum effective size of the Alfvén wing of $R_\mathrm{eff} = \sqrt{3}\,R_\mathrm{obst}$.

Figure 4.5 shows how the Poynting flux depends on the intrinsic planetary magnetic field strength. We apply the best-guess to characterise the stellar wind and calculate the Poynting fluxes generated by the three innermost planets with their respective assumed magnetospheres. We chose equatorial magnetic field strengths between 0 nT, i.e., no magnetosphere at all, up to 100 000 nT. This range includes the strength of the terrestrial magnetic field of about $B_\mathrm{Earth} = 30\,000$ nT (black dashed line in Figure 4.5). Due to the strong stellar magnetic field and the resultant large stellar wind magnetic field near the orbital distances of the planets, the effective sizes may still not be larger than the planet itself. We took this into account and see that T1b starts to develop closed magnetospheric field lines with a surface field strength of 5000 nT, visible in the curve when the Poynting flux starts to deviate from the value of $4.2 \cdot 10^{14}$ W. For an earth-like magnetic field T1b produces $1.5 \cdot 10^{15}$ W. For stronger fields of up to 100 000 nT the expected Poynting fluxes increase by a factor of 2 towards $3 \cdot 10^{15}$ W. The same pattern applies for the other two planets, both show an increase of one order of magnitude for intrinsic magnetic fields up to 100 000 nT.

Turnpenney et al. (2018) carried out a study on the radio luminosity of SPI in several systems, including TRAPPIST-1. They included a parameter space of three hypothetical intrinsic magnetic field strengths based on the earth's magnetic field and found that the upper limits of the estimated radio luminosity may be observable for future radio telescopes. The authors apply stellar wind parameters with a solar mass flux of $2 \cdot 10^9\,\mathrm{kg\,s^{-1}}$ and therefore all planets generate SPI. For the terrestrial field strength, their model generates a magnetosphere with closed field lines only for the outer planets starting at T1d. Our model includes a range up to the distance $r_2 = 5\,R_*$ where the magnetic field behaves dipolar whereas *Turnpenney et al.* (2018) applied the Parker field configuration right from the star. Therefore our radial magnetic field strength is weaker and allows larger planetary magnetospheres. This shows that the stellar magnetic field geometry plays an important role in these types of studies. *Garraffo et al.* (2017) also investigated the case of a 50 000 nT field strength for all planets and estimated that T1b would have a magnetopause distance of approximately 1 to $1.5\,R_\mathrm{p}$ and T1c of approximately 1.2 to $1.5\,R_\mathrm{p}$. Our calculated obstacle sizes are similar with values of $R_\mathrm{obst} = 1.2\,R_\mathrm{p}$ for T1b and $1.5\,R_\mathrm{p}$ for T1c. This shows that our model results are similar to what can be estimated by numerical simulations, but our study allows the scan of a larger parameter space, which is not possible with computationally expensive MHD simulations.

5 SPI Wave Structures

We have seen in the chapter before that several planets around TRAPPIST-1 could couple to their star and generate a Poynting flux. However, we aim to understand star-planet interaction at a deeper level. Therefore we conduct time-dependent, three-dimensional MHD simulations of a planet interacting with a stellar wind. We will analyse the inward and outward directed wave structures and put special attention on the inward going Poynting flux.

5.1 MHD Simulation Setup

In this section, we will introduce the setup of our MHD model. We start with a general description of the PLUTO-Code by *Mignone et al.* (2007). The second part of this section comprises our setup for the stellar wind, including the details of the simulation domain, the boundary conditions and the initial conditions. In the last part, we will describe in detail how we extend the code to simulate the interaction between a planet and the stellar wind and how we make the planet orbit the star.

5.1.1 Model Equations and PLUTO Code

PLUTO is a modular multiphysics code that solves the single-fluid equations for astrophysical plasmas (*Mignone et al.*, 2007). The basic physics modules can solve hydrodynamic equations, magnetohydrodynamics and their relativistic extensions. However, we only use the magnetohydrodynamics module.

As a finite volume code, PLUTO solves conservative equations of the type

$$\frac{\partial \boldsymbol{U}}{\partial t} + \nabla \cdot \boldsymbol{T} = \boldsymbol{S} \tag{5.1}$$

where $\boldsymbol{U}$ is a vector of conservative quantities, $\boldsymbol{T}$ is a tensor that describes the fluxes of said conservative quantities and $\boldsymbol{S}$ describes physical and geometrical source terms, i.e. the classical right hand-side (*Mignone et al.*, 2007). The conservative MHD equations implemented in PLUTO, according to *Mignone et al.* (2007) and the PLUTO user guide, are

$$\frac{\partial \rho}{\partial t} + \nabla \cdot (\rho \boldsymbol{v}) = 0 \tag{5.2}$$

$$\frac{\partial \boldsymbol{m}}{\partial t} + \nabla \cdot \left(\boldsymbol{m}\boldsymbol{v} - \boldsymbol{B}\boldsymbol{B} + (p + \frac{B^2}{2})\mathbb{1} \right) = -\rho \nabla \Phi \tag{5.3}$$

$$\frac{\partial}{\partial t}(E + \rho\Phi) + \nabla \cdot \left((E + p + \frac{B^2}{2} + \rho\Phi)\boldsymbol{v} - \boldsymbol{B}(\boldsymbol{v} \cdot \boldsymbol{B}) \right) = 0 \tag{5.4}$$

$$\frac{\partial \boldsymbol{B}}{\partial t} + \nabla \cdot (\boldsymbol{v}\boldsymbol{B} - \boldsymbol{B}\boldsymbol{v}) = 0. \tag{5.5}$$

Hence the conservative quantities are the density, the momentum density

$$\boldsymbol{m} = \rho \boldsymbol{v}, \tag{5.6}$$

the total energy

$$E = \frac{p}{\Gamma - 1} + \frac{\boldsymbol{m}^2}{2\rho} + \frac{\boldsymbol{B}^2}{2} \tag{5.7}$$

and the magnetic field. An obvious addition compared to the MHD equations introduced in section 3.1.1 is the gravitational potential Φ, which represents the gravitation of the star. It is given by

$$\Phi = -\frac{M_* G}{r} \tag{5.8}$$

with the stellar mass M_* and the gravitational constant G.
PLUTO calculates the solution of the implemented physical problem by the reconstruct-solve-average approach (*Mignone et al.*, 2007). Therefore PLUTO converts the conservative quantities $\boldsymbol{U}$ into primitive quantities, represented by the vector $\boldsymbol{V}$. The primitive quantities are density, velocity, thermal pressure and magnetic field. The solver averages the quantities over the cell volume, which imposes a so-called Riemann-problem. Two neighbouring cells have different constant values in their quantities. That gives a discontinuity at the cell boundary, described by the left and right state of $\boldsymbol{V}$. A Riemann-solver provides the solution of this problem in the form of fluxes across the cell boundary. PLUTO then uses those fluxes to calculate the update in time, imposed on the conservative quantities $\boldsymbol{U}$. The latter usually happens by a common solver for differential equations, i.e. and Euler-scheme or better a Runge-Kutta-scheme. For a detailed description of the numerics, we refer to *Mignone et al.* (2007).

5.1.1.1 Equation of State

For the stellar wind we use an ideal equation of state. The one provided by PLUTO reads

$$\rho\epsilon = \frac{p}{\Gamma - 1} \tag{5.9}$$

with the specific internal energy ϵ. The polytropic index Γ can be set during compilation. For an adiabatic fluid Γ is 5/3. In the solar wind, the polytropic index varies, see, e.g. *Cohen et al.* (2007). For our stellar wind we assume $\Gamma = 1.2$.

5.1.1.2 Normalisation of Plasma Variables

PLUTO uses the CGS unit system and normalises all variables via three typical quantities: the reference length L_0 in cm, the reference velocity v_0 in cm/s and the reference density ρ_0 in g/cm^3. From these quantities, the code obtains typical values for all other quantities. Those are

$$t_0 = \frac{L_0}{v_0}$$
$$B_0 = v_0 \sqrt{4\pi\rho_0}$$
$$p_0 = \rho_0 v_0^2$$

the typical time scale, the typical magnetic field and the typical pressure, respectively.
We choose the following values

$$
\begin{aligned}
L_0 &= 84257 \cdot 10^5 \text{cm} = R_* \\
v_0 &= 130 \cdot 10^5 \text{cm/s} = c_\text{s}(r_\text{c}) \\
\rho_0 &= 2.1 \cdot 10^9 \text{cm}^{-3} u
\end{aligned}
$$

where L_0 is the stellar radius, v_0 is the sound speed at the Parker critical point r_c, i.e. the point where the sonic Mach number is exactly one, and ρ_0 is the coronal density estimated via equation (3.25) and equation (3.26) with $\dot{M} = 10^{10} \text{kg}\,\text{s}^{-1}$ multiplied with the atomic mass unit $u = 1.6605 \cdot 10^{-24}\text{g}$. Therefore we assume a hydrogen plasma.

5.1.1.3 Treatment of the Magnetic Field

Magnetic fields usually cause problems in numerical simulations. The most common issue in numerical MHD is the occurrence of non-physical magnetic divergences. Therefore, MHD Codes have to use additional methods to remove these occurring divergences.
We apply PLUTO's Hyperbolic Divergence Cleaning that has been developed by *Dedner et al.* (2002). This approach extends the conservative MHD equations by introducing a generalised Lagrange multiplier. According to *Dedner et al.* (2002), this technique transports divergence errors towards the domain boundaries, while they are damped on the way. This technique reduces divergence errors.
For strong magnetic fields like the one of TRAPPIST-1, PLUTO has a feature called Background magnetic field splitting, developed by *Powell* (1997). When activated, the magnetic field assumes the form

$$\boldsymbol{B} = \boldsymbol{B}_0(\boldsymbol{r}) + \delta \boldsymbol{B}(\boldsymbol{r}, t). \tag{5.10}$$

The background field $\boldsymbol{B}_0$ is constant in time, while only the deviation $\delta\boldsymbol{B}$ is evolved in time and space.
In our simulation, we assign the radial component of the magnetic field as the background field. We apply the same magnetic field model that we already used for our semi-analytic studies (see section 3.2). Therefore we calculate the magnetic field strength at a distance r_2 according to the dipole approximation. From there, we assume the radial Parker field according to equation (3.32). The ϑ- and φ-components are zero and left to the simulation since their magnitude is sufficiently small for the Code to evolve.

5.1.2 Stellar Wind Setup

In this section, we will describe our model setup to simulate a stellar wind. PLUTO provides the framework in which we solve our problem. That involves solvers for the MHD equations and the correct treatment of magnetic fields. In addition to that, we have to define a suitable grid for our problem and add certain user-defined boundary conditions. We will describe all this in the following section.

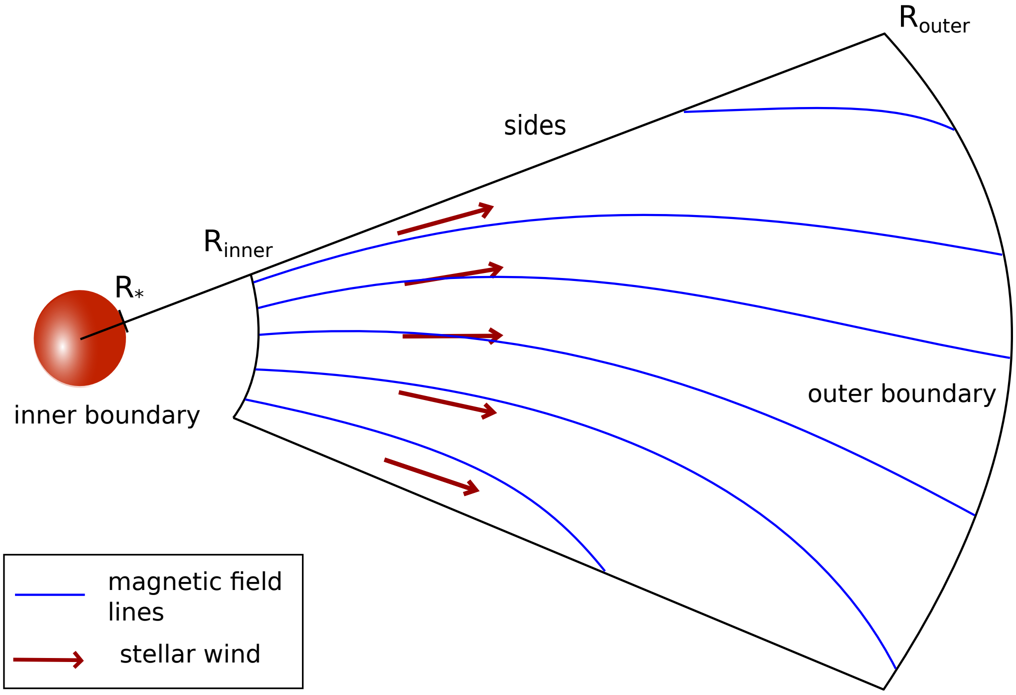

Figure 5.1: Sketch of the simulation domain. The red sphere in the centre is the star and the black spherical shell box resembles the boundaries of the simulations box in a top view. The inside of the box sketches magnetic field lines in blue and the stellar wind by the red arrows.

5.1.2.1 Simulation Domain and Boundary Conditions

The simulation domain is a three-dimensional spherical shell with the star in the centre (Figure 5.1). We solve the MHD equations in spherical coordinates with radius r, co-latitude ϑ and azimuth angle φ. Due to the 3D setup there are six boundaries, which all require certain conditions to work correctly. Furthermore, the azimuthal (i.e. rotational) plasma components need special treatment.

In Table 5.1 we summarised the domain extensions. The inner boundary of the box lies at a distance R_{inner} that is just outside the critical radius r_{c} (Figure 5.1). Therefore we simulate a fully developed thermally driven stellar wind that resembles a Parker wind (see section 3.2). Due to this choice, we avoid treating the stellar corona, i.e. the source region of the stellar wind, self-consistently. This approach greatly simplifies the whole setup but still enables us to address the research questions we intend to investigate. The wind driving variables, radial velocity, density and pressure, enter the simulation domain via Dirichlet type inflow boundary conditions of the form

$$v_r = c_{\text{s}} \tag{5.11}$$

$$\rho = \rho_0 \left(\frac{R_*}{R_{\text{inner}}}\right)^2 \frac{v_c}{v_r} \tag{5.12}$$

$$p = \frac{\rho}{m} k_{\text{B}} T. \tag{5.13}$$

As the boundary is close to the critical radius, we assume that the stellar wind has

Table 5.1: Locations of the domain boundaries in spherical coordinates. Given is the name of the boundary, the condition we apply and the actual value we give it in our simulations.

Coordinate	**Condition**	**Chosen value**
R_{inner}	$> r_{\text{c}} = \frac{GM_*}{2c_{\text{s}}^2}$	$5\,R_*$
R_{outer}	$> R_{\text{A}}$	$70\,R_*$
ϑ_{beg}	arbitrary	$0.43\,\pi$
ϑ_{end}	arbitrary	$0.56\,\pi$
φ_{beg}	arbitrary	$0\,\pi$
φ_{end}	arbitrary	$0.5\,\pi$

a velocity as fast as the speed of sound. The density follows the profile from equation (3.26) and the pressure follows from the ideal gas law via a given temperature and the density.

For the magnetic field and the remaining velocity components, we apply outflow conditions that ensure there is no derivative normal to the boundary surface:

$$\frac{\partial v_{\text{i}}}{\partial n} = 0 \tag{5.14}$$

$$\frac{\partial B_{\text{i}}}{\partial n} = 0 \tag{5.15}$$

where the index i represents the different components r, ϑ, φ. All other boundaries have outflow boundary conditions for all plasma variables. The boundaries defined by the ϑ and φ direction can take almost arbitrary extensions within the ranges given by the definition of spherical coordinates. However we chose ϑ in a narrow range around the stellar equator region and φ between 0 and 0.5π (see Table 5.1). For the outer boundary at R_{outer}, we have to be cautious because due to the outflow conditions Alfvén waves from the stellar wind may be reflected into the domain and cause non-physical behaviour. This problem has been addressed in the past by the introduction of outflow boundary conditions along the flow characteristics. For example, by *Nakagawa* (1981); *Wu et al.* (2006, 2010) and *Zanni and Ferreira* (2009) with their boundary conditions based on angular momentum transfer. All of them ensure proper handling even in sub-Alfvénic flow conditions. However, due to limited development time, the simple solution for us was, to extend R_{outer} into the super-Alfvénic regime, i.e. outside the Alfvén radius R_{A}. There, the Alfvén waves cannot travel upstream anymore.

PLUTO allows the user to control the domain, such that internal boundary conditions can be defined. We use this feature to impose conditions on the azimuthal components of velocity and magnetic field. *Zanni and Ferreira* (2009) published those boundary conditions that accurately calculate the rotation of the star and its effect on the plasma. The principal assumption for these conditions is that the plasma at the stellar surface is a perfect conductor with

$$\boldsymbol{E} = \boldsymbol{B} \times (\boldsymbol{v} - \boldsymbol{\Omega}_* \times \boldsymbol{r}) = 0. \tag{5.16}$$

According to *Zanni and Ferreira* (2009), the correct coupling between plasma and magnetic field is achieved by assigning the magnetic torque to the inner boundary zone. That will ensure a proper simulation of the stellar rotation. Therefore, one derives a Neumann boundary condition for the azimuthal magnetic field, which has the form

$$\frac{\partial B_\varphi}{\partial r} = f(\boldsymbol{r}, t) \tag{5.17}$$

with f representing the terms that result from deriving this expression from the angular momentum equation, which is given via $\boldsymbol{r}$ cross the equation of motion. The azimuthal velocity is a Dirichlet type boundary condition of the form

$$v_\varphi = r\Omega_* + \frac{v_\mathrm{p}}{B_\mathrm{p}} B_\varphi \tag{5.18}$$

with the poloidal velocity, given by $v_\mathrm{p} = \sqrt{v_r^2 + v_\vartheta^2}$, and analogous for the poloidal magnetic field. We apply these conditions in a region between R_inner and $R_\mathrm{inner} + 1R_*$.

5.1.2.2 Initial Conditions

Besides boundary conditions, one also requires initial conditions to solve partial differential equations like the MHD equations. For all those simulations that involve planets, we use a previously simulated steady-state stellar wind and apply it as initial conditions. The spatial structure of the respective steady-state stellar wind is described in section 5.2. To obtain the steady-state wind solution, we assume a given set of initial conditions given by

$$\begin{aligned}
v_r(r) &= c_s \\
v_\vartheta(r) &= 0 \\
v_\varphi(r) &= 0 \\
\delta B_r(r) &= 0 \\
B_\vartheta(r) &= 0 \\
B_\varphi(r) &= 0 \\
\rho(r) &= \rho_0 \left(\frac{R_*}{r}\right)^2 \frac{v_c}{v_r} \\
p(r) &= \frac{\rho}{m} k_\mathrm{B} T.
\end{aligned}$$

We give a constant radial velocity and the expected radial profiles for density and pressure. For the radial magnetic field, we use the Background magnetic field splitting feature provided by PLUTO described in section 5.1.1.3. Therefore we have to assume a zero-disturbance initial magnetic field. We initialise all remaining variables as zero.

5.1.3 SPI Setup

The setup of a stellar wind is the first step to simulate SPI. The crucial step, however, is the correct interaction. We will simulate a mechanical obstacle, i.e. a planet with an atmosphere and no intrinsic magnetic field. To do so, we have to extend the implemented model equations in order to incorporate ion-neutral collisions together with the motion of the planet. Moving planets are necessary to investigate multi-planet systems and the interaction with time-variable and non-axisymmetric stellar winds.

5.1.3.1 Ion-Neutral Collisions in the Model Equations

In hydrodynamic fluids, the particles interact via collisions with each other. In contrast, in a plasma, particles interact via electromagnetic forces with each other. The interaction between plasma ions and neutral particles, however, allows collisions. That is possible because the neutral particles are not affected by the electric forces exerted by ions. *Schunk* (1975) derived the corresponding fluid equations from the Boltzmann equation of the kinetic plasma theory.

To include this effect in our MHD simulations, we have to expand the equation of motion (equation (5.3)) and the energy equation (equation (5.4)). Physically, ion-neutral collisions are a sink for plasma momentum and energy. Source terms in the momentum and energy equation describe the transfer from the plasma to the neutral fluid. We use the terms given by *Chané et al.* (2013), which include ion-neutral collisions as well as a motion of the neutral gas. The equations then have the following form:

$$\frac{\partial \boldsymbol{m}}{\partial t} + \nabla \cdot \boldsymbol{F}_{\mathrm{m}} = \mathrm{rhs}_{\mathrm{m}} - \rho \nu_{\mathrm{in}} (\boldsymbol{v} - \boldsymbol{v}_{\mathrm{orb}}) \tag{5.19}$$

$$\frac{\partial E_{\mathrm{tot}}}{\partial t} + \nabla \cdot \boldsymbol{F}_{\mathrm{E}} = -\nu_{\mathrm{in}} \frac{p}{\Gamma - 1} + \frac{1}{2} \rho \nu_{\mathrm{in}} \left(\boldsymbol{v} - \boldsymbol{v}_{\mathrm{orb}}\right)^2 - \rho \nu_{\mathrm{in}} \left(\boldsymbol{v} - \boldsymbol{v}_{\mathrm{orb}}\right) \cdot \boldsymbol{v}. \tag{5.20}$$

For brevity, we simplified the left hand sides to the inertial terms for momentum density $\boldsymbol{m}$ and total energy E_{tot} and the divergences of their respective flux tensors $\boldsymbol{F}_{\mathrm{m}}$ and $\boldsymbol{F}_{\mathrm{E}}$. The equation of motion includes gravitation as a right hand side source term $\mathrm{rhs}_{\mathrm{m}}$, whereas the energy equation originally had no source terms.

The parameter that describes the collisions is the collision frequency ν_{in}. We calculate the collision frequency with the empirical formula

$$\nu_{\mathrm{in}} = 2.6 \cdot 10^{-9} \sqrt{\frac{\alpha_0}{\mu_{\mathrm{A}}}} n_{\mathrm{n}}(\boldsymbol{r}) \tag{5.21}$$

as given by *Banks and Kockarts* (1973). The parameter α_0 is the polarisability in $10^{-24}\mathrm{cm}^3$, μ_{A} is the reduced mass of the ion and the neutral gas species in atomic mass units, and n_{n} is the neutral gas density. The collision frequency ν_{in} has units of s^{-1}.

In our case we simplify the dynamics of the neutral gas by assuming that it only moves with the planet along its orbit with the orbital velocity $\boldsymbol{v}_{\mathrm{orb}} = \Omega_{\mathrm{p}} a_{\mathrm{p}} \boldsymbol{e}_{\varphi}$. Theoretically, the velocity due to the planet's rotation and the atmospheric dynamics themselves could be considered as well. However, the orbital velocity is much larger than those other velocities, which is why we neglect them.

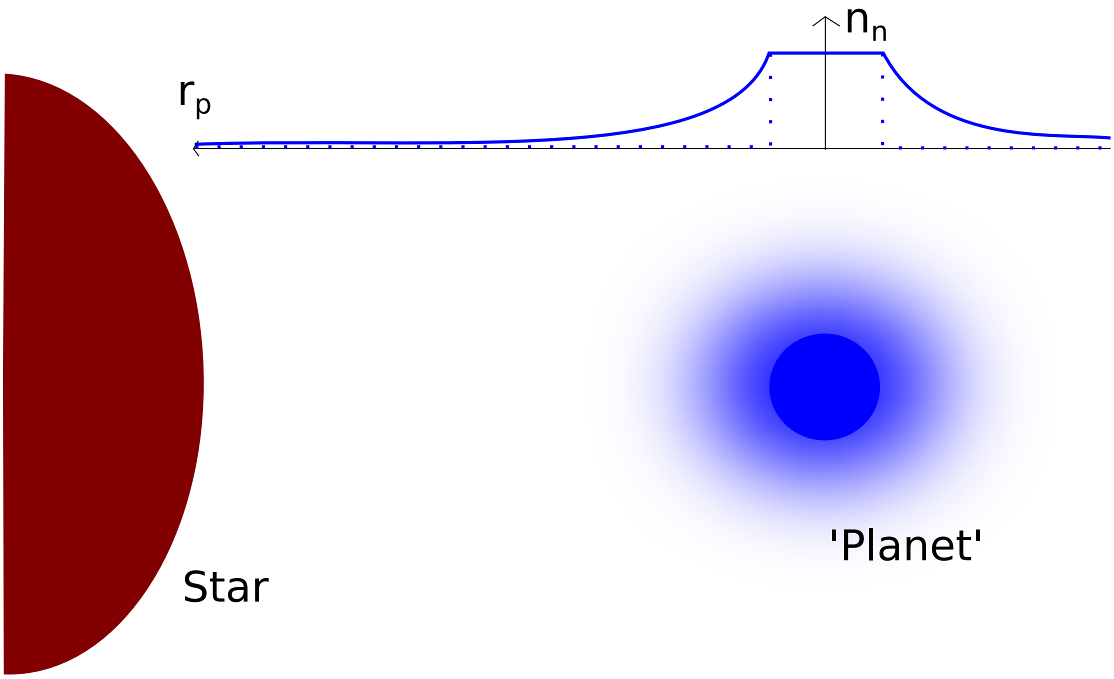

Figure 5.2: Planet parameterised by a cloud of neutral gas.

5.1.3.2 Parametrisation of the Planet

In order to simulate a planet accurately, one would require a non-conducting boundary within the simulation domain (*Duling et al.*, 2014) and an atmosphere on top. The boundary absorbs the plasma and insulation alters the magnetic field. Such a setup is well suited for so-called near-field studies of exoplanets and moons, e.g. by *Duling et al.* (2014); *Blöcker et al.* (2016, 2018).

In our study, we are interested in the far-field properties of SPI-effects. The atmosphere is the main driver of the interaction that generates the expected MHD waves. Therefore we can reduce the complexity of the planetary model in our simulation to a neutral gas cloud with specific planetary atmospheric properties (for the properties see section 5.1.4).

Figure 5.2 shows a sketch of the geometry and the neutral gas density profile. The red half-sphere is the star in the middle of the system and the planet orbits the star at an orbital distance a. The graph depicts the applied neutral gas density profile relative to the planet. The distance of the neutral gas in the planetographic system is given by

$$r_\mathrm{p} = |\boldsymbol{a} - \boldsymbol{r}_\mathrm{n}| \tag{5.22}$$

where $\boldsymbol{a}$ is the position vector of the planet in the simulation domain and $\boldsymbol{r}_\mathrm{n}$ the position vector of a neutral gas fluid element. For elements with $r_\mathrm{p} \leq R_\mathrm{p}$ we assume a constant neutral gas density n_0 (blue sphere). From R_p outward we apply an atmospheric scale height law of the form

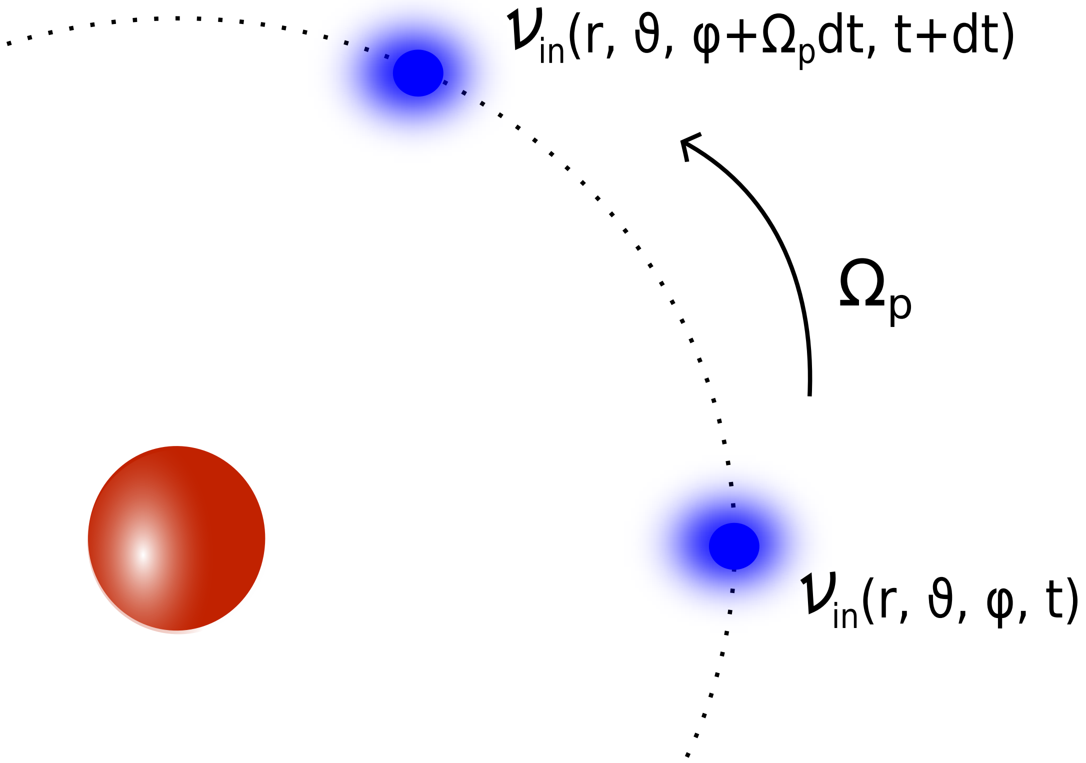

Figure 5.3: Schematic of the motion of the planet through the domain

$$n = n_0 \exp\left(\frac{R_\mathrm{p} - r_\mathrm{p}}{H}\right) \tag{5.23}$$

with the scale height H (blurred sphere).

5.1.3.3 Motion of the Planet

The collision terms in the MHD equations include the planetary motion. However, the position of the planet has to be updated at each time step accordingly. Figure 5.3 sketches the process physically. The collision frequency ν_in is a function of space and time in our model and it represents the planet. Therefore, we define the start position of the planet, by

$$\boldsymbol{a}_{init} = a \begin{pmatrix} \sin(\vartheta_\mathrm{init})\cos(\varphi_\mathrm{init}) \\ \sin(\vartheta_\mathrm{init})\sin(\varphi_\mathrm{init}) \\ \cos(\vartheta_\mathrm{init}) \end{pmatrix} \tag{5.24}$$

with an orbital distance a, the co-latitude ϑ_init, and the azimuth angle φ_init at initialisation. For each time step, we get the current time t of the simulation and rotate the position vector by $\Omega_p\, t$, where Ω_p is the angular velocity of the planet's orbital motion. Therefore we receive the current position vector, for which we can calculate the current distances relative to the planet by equation (5.22) and the neutral gas density according to equation (5.23).

For simplicity, we assume a circular planetary orbit. In principle, one could implement any type of orbital motion, but that complicates the setup of the static

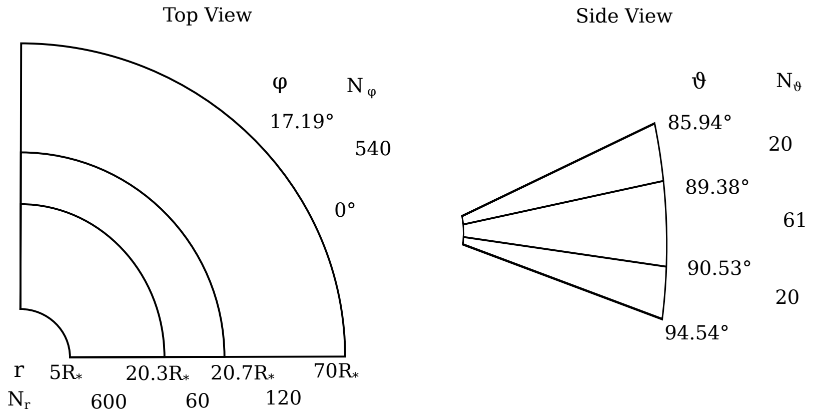

(a) ’inward wing’ scenario

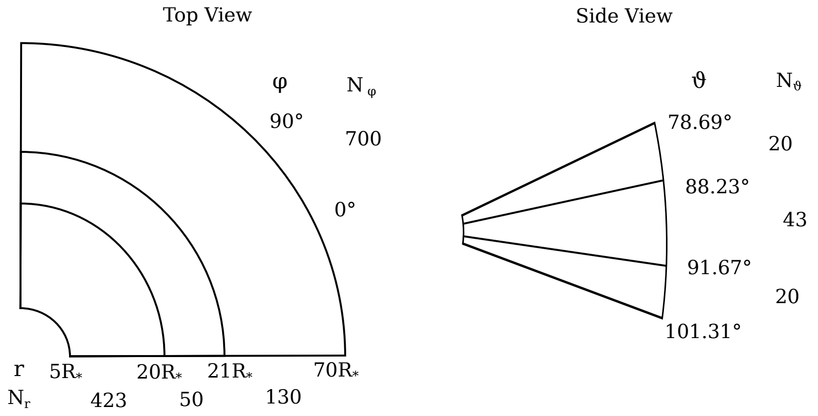

(b) ’single planet’ scenario

Figure 5.4: Grid dimensions and cell numbers for the scenarios with a single planet.

grid.

5.1.4 Grid Structures and Physical Parameters

In this section, we describe the simulations grid and the applied physical parameters.

5.1.4.1 Grids

For this chapter, we require two different scenarios: The ’single planet’ scenario and the ’inward wing’ scenario. The ’inward wing’ scenario simulates the inward going wave structure with high resolution. The ’single planet’ scenario applies a coarser resolution that allows simulating the outward going wave structures, that require more time to evolve.

We employ the static grid version of PLUTO, i.e. no adaptive mesh refinement. Therefore we have to plan the intended resolution. The planet and therefore its orbit require a much higher resolution than the stellar wind in general. So we have

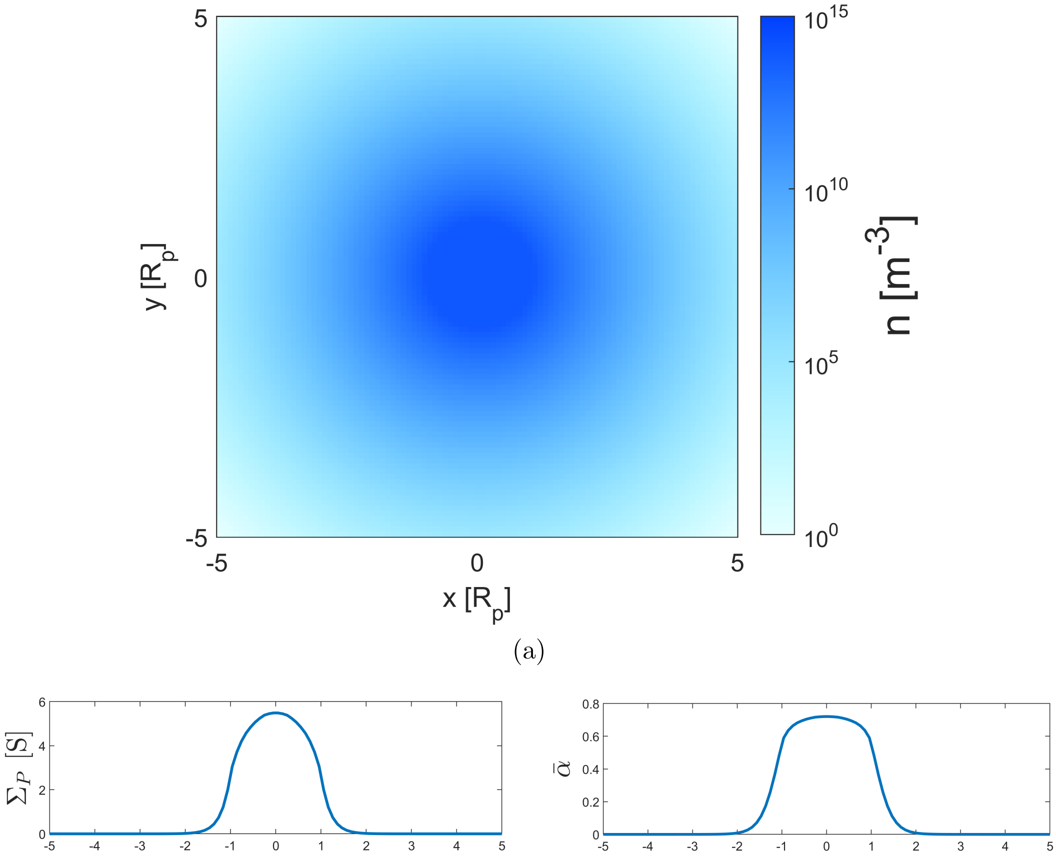

(a)

(b)

(c)

Figure 5.5: Atmospheric parameters, that determine the strength of the interaction.

to define a rather complex grid that changes for the respective scenario.

There is no general rule on how many grid cells should resolve the planet, but in our case, there has to be a compromise between resolution and numerical resources. Since we are interested in far-field interaction, the planet is a pure source of waves. In the 'single planet' scenario, we decided to resolve the planet with approximately six grid cells in r- and ϑ-direction. For the φ-direction we choose a resolution of 3.7 grid cells. For the highly resolved 'inward wing' scenario, the planet is resolved by 25 grid cells in r- and ϑ-direction, and 15 grid cells in φ-direction.

Figure 5.4 summarises the two different grid structures. The left side shows a top view of the grid, with the grid zones and cell numbers N_r in r-direction (below the sketch) and the grid dimensions and cell number N_φ in φ-direction on the side. The right side shows a side view with the structure in meridional direction and the cell numbers N_ϑ. PLUTO allows different types of grids. In uniform grid zones, the size of the cell in the respective dimension remains constant, whereas, in stretched grid zones, the cell size increases beginning with the neighbouring uniform cell size.

The grid of the 'inward wing' scenario (Figure 5.4a) is the special case among our simulations. It deviates from the standard domain extensions, given in Table 5.1 and has an extremely high resolution in the range of the inward going wave structures. For the r-direction the grid ranges from $5 - 20.3\,R_*$ with 600 uniform cells, from $20.3 - 20.7\,R_*$ with 60 uniform cells and from $20.7 - 70\,R_*$ with 120 stretched cells. For the ϑ-direction the grid ranges from $85.94° - 89.38°$ with 20 stretched grid cells, from $89.38° - 90.53°$ with 61 uniform grid cells and from $90.53° - 94.54°$ with 20 stretched grid cells. Finally, for the φ-direction we have 540 grid cells for the range between 0° and 17.19°.

The grid for the 'single planet' scenario (Figure 5.4b) assumes the standard measures given in Table 5.1. For the r-direction the grid ranges from $5 - 6\,R_*$ with 23 uniform cells, from $6 - 20\,R_*$ with 400 uniform cells, from $20 - 21\,R_*$ with 50 uniform cells and from $21 - 70\,R_*$ with 130 stretched cells. For the ϑ-direction the grid ranges from $0.43\pi - 1.54$ with 20 stretched grid cells, from $1.54 - 1.6$ with 43 uniform grid cells and from $1.6 - 0.56\pi$ with 20 stretched grid cells. Finally for the φ-direction we have 700 grid cells for the range between 0 and 0.5π.

5.1.4.2 Parameters

In chapter 4, we conducted an extensive parameter study, to investigate different possible stellar winds. However, such a study is not possible with MHD simulations of the formerly described type. Instead, one has to focus on case studies. Hence, we apply the best guess from section 4.1 for the plasma. Therefore, we assume a pure hydrogen plasma again, with the following parameters:

$$\begin{aligned} n_\mathrm{c} &= 2.1 \cdot 10^{15}\,\mathrm{m}^{-3} \\ T_\mathrm{c} &= 2\,000\,000\,\mathrm{K} \\ B_0 &= 0.06\,\mathrm{T} \\ c_\mathrm{s} &= 130\,\mathrm{kms}^{-1}. \end{aligned}$$

The variables are the coronal particle density n_c, the coronal temperature T_c, the magnetic field at the stellar equator B_0 and the sound speed c_s at R_inner.

In our simulations, we describe the atmosphere (respectively: the planet) directly, via a particle density. In contrast to chapter 4, where we parametrised the atmosphere through the interaction strength $\bar{\alpha}$. Nonetheless, we still need to know $\bar{\alpha}$, to estimate the correct parameter range for the atmosphere, because if $\bar{\alpha}$ becomes one, the simulation crashes. Hence, we require atmospheric parameters that guarantee $\bar{\alpha} < 1$.

We chose a base neutral gas density of $n_{\mathrm{n},0} = 10^{14}\,\mathrm{m}^{-3}$ and a scale height of $H = 1300$ km. Since *Bourrier et al.* (2017) observed an extended hydrogen exosphere at T1b, we assume a neutral hydrogen atmosphere. Therefore we find a polarisability of $\alpha_0 = 0.667 \cdot 10^{-24}\mathrm{cm}^3$ and a reduced mass of $\mu_\mathrm{A} = 0.5038$ amu (*Banks and Kockarts*, 1973).

Figure 5.5 shows the atmospheric parameters, including neutral gas density (Figure 5.5a), Pedersen Conductance (Figure 5.5b) and interaction strength (Figure 5.5c). We generated these plots to plan the actual simulations. Figure 5.5a shows the neutral gas density n_n. Inside one planetary radius, the density is constant at $10^{14}\,\mathrm{m}^{-3}$ and decreases exponentially to the outside, which increases the planetary obstacle to about $2\,R_\mathrm{p}$. *Bourrier et al.* (2017) state that the gas envelopes at T1b and T1c extend up to 7 planetary radii. However, the density of this extended exosphere remains unclear, which is why we conduct our simulations with quite conservative estimates of the atmospheric extent. The chosen

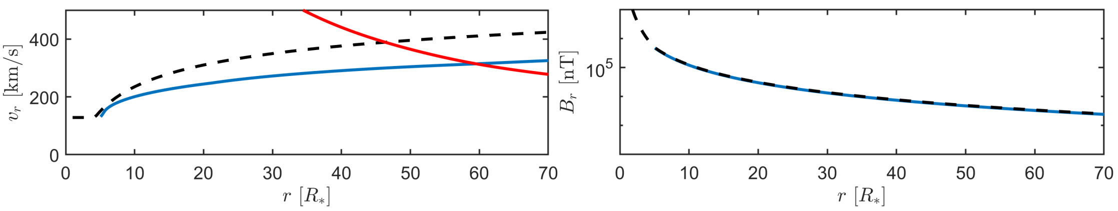

(a) Radial Profile v_r (b) Radial Profile B_r

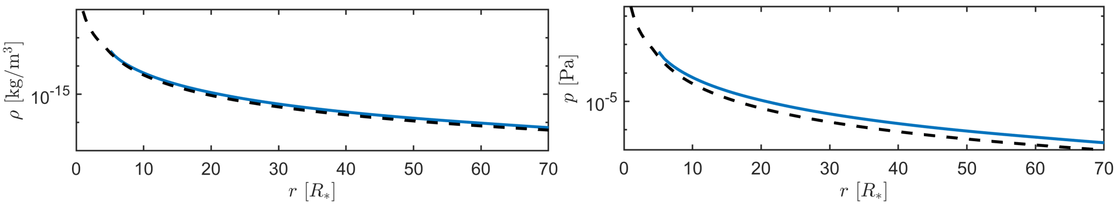

(c) Radial Profile ρ (d) Radial Profile p

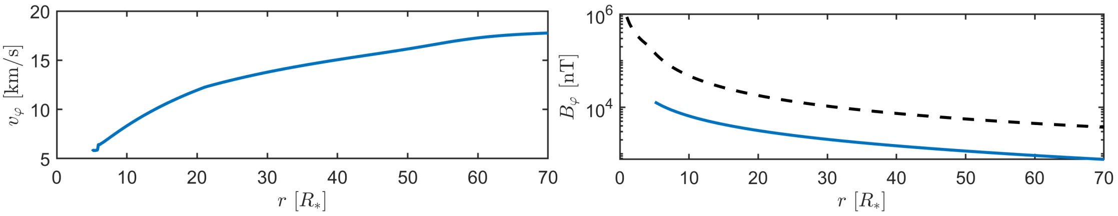

(e) Radial Profile v_φ (f) Radial Profile B_φ

(g) Plot Legend

Figure 5.6: Radial profiles of the most important stellar wind variables.

scale height corresponds approximately to scale heights estimated for Earth's thermosphere. The Pedersen Conductance Σ_P assume a maximum value of about 8 S, and the Alfvén conductance of $\Sigma_\mathrm{A} = 1.064$ S. Therefore we receive a maximum interaction strength of 0.7, according to equation (3.44). Such a value throughout the planet is acceptable for the code. Note that the Bell-like shape of the Pedersen conductance is not what one expects for a planet with an atmosphere. Instead, Σ_P should have spikes at $\pm R_\mathrm{p}$ (*Neubauer*, 1999), which comes from the planetary body that would naturally not contribute to the atmospheric conductivity. This deviation is a result of the chosen parametrisation for the planet as a neutral gas cloud.

5.2 Spatial Structure of the Steady-State Stellar Wind

The description of SPI in the far-field approach has to deal with the spatially variable stellar wind. Stellar winds are not homogeneous in the sense that all quantities are constant, as one could assume for near-field simulations in the close vicinity of a planet. Therefore we have to understand the stellar wind before we can go on towards the SPI.

Our stellar wind is radially symmetric and thermally driven. Figure 5.6 shows radial profiles of the radial stellar wind velocity v_r, the azimuthal velocity v_φ, the respective magnetic field components, the plasma density and the thermal pressure. We compare the simulated values (solid blue lines) with analytic model expectations (black dashed lines, see section 3.2). Additionally, we plot parts of the Alfvén speed radial profile (solid red line) to compare it with the stellar wind velocity.

Figure 5.6a shows v_r, which accelerates with increasing radius. The maximum speed in our simulation lies at about 310 $\mathrm{km\,s^{-1}}$, whereas the Parker model predicts maximum speeds of about 410 $\mathrm{km\,s^{-1}}$. We account this discrepancy to the applied polytropic index of 1.2 and the resulting pressure profile. The Parker model assumes an isothermal wind, but our model directly depends on the simulated polytropic pressure gradient force. Another aspect is the issue outlined in section 5.1.2, that Alfvén waves in the stellar wind reflect at the outflow boundary condition. We can see from the intersection of v_r and v_A that a box size up to $70R_*$ is sufficient to have super-Alfvénic conditions at the outer boundary. Our simulations would, therefore, allow sub-Alfvénic interaction up to T1e, although we will only consider T1b and T1c.

The radial magnetic field component B_r (Figure 5.6b) follows the expected profile. At first, this is not surprising, because PLUTO only writes deviations from the background magnetic field and the background field has to be added afterwards at the processing step. However, at this point, the absence of large deviations is good.

Closely tied to v_r, as the dominant velocity component, are the plasma density and the thermal pressure (Figure 5.6c and Figure 5.6d). The density nicely follows the expected profile determined from the continuity equation. A slight deviation due to the lower simulated velocity is visible but negligible. Same holds for the pressure, which follows a slightly flatter curve than expected from analytic theory. This smaller gradient may be part of the reason for the reduced stellar wind velocity.

Finally, we look at the azimuthal components, that represent the rotational components. Figure 5.6e shows v_φ and Figure 5.6f shows B_φ. For comparison, we plotted no analytic solution in the velocity and the corresponding Parker magnetic field, which assumes a non-rotating plasma. The azimuthal velocity reaches a maximum value of 20 $\mathrm{km\,s^{-1}}$ in the simulation, which is more than one order of magnitude smaller than the stellar wind velocity. Accordingly, the azimuthal magnetic field is about one order of magnitude weaker than the Parker magnetic field strength. The reason for these deviations is that the magnetic field cannot enforce full corotation. The field lines are largely parallel to the plasma flow, i.e. predominantly in the radial direction. Therefore the Lorenz force is too weak to maintain an efficient transport of angular momentum from the star to the plasma. The opposite happens in planetary magnetospheres like Jupiter's magnetosphere, where corotation due to the rotation of the magnetic field is the main driver for plasma motion (*Hill*, 1979; *Hill*, 2001; *Cowley and Bunce*, 2001).

We expect that the planet will generate all different types of MHD waves. Therefore we show radial profiles of the respective wave Mach numbers in Figure 5.7. The blue curve shows the Alfvén Mach number M_A, the red curve the sonic Mach number M_s and the yellow curve, the Fast Mach number M_f. Our stellar wind is,

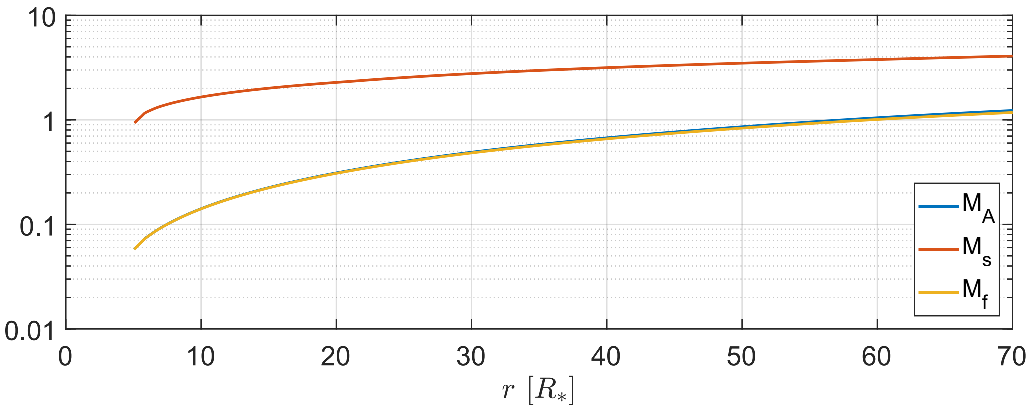

Figure 5.7: Radial Profiles of the Alfvén Mach number M_A, sound Mach number M_s and the fast Mach number M_f.

by construction super-sonic. Hence, the sonic Mach number is always greater than one. Accordingly, the Slow Mode will not travel upstream towards the star, and we can expect a purely Alfvénic interaction upstream of the planet. Alfvén and Fast Mach number appear to be almost equal since the magnetosonic wave speed c_ms is the euclidean norm of Alfvén speed, and sound speed (see equation (3.21)) and the Alfvén speed is much larger than the sound speed. In conclusion, we may expect an inward Alfvén wing, but radially outward there may be different types of waves.

5.3 Methods for the Wave Analysis

We expect different types of MHD waves, each with distinct properties, but several of them with a propagation direction parallel to the magnetic field. Therefore, we can try to distinguish those waves by determining their wave characteristics, i.e. their path from the planet within the stellar wind. Further, we can estimate a wave specific travel time, which gives further hints for the identification of the waves and later on for further simulations (see section 7.1.1).

The wave travel time from the planet to the boundary can be approximated by

$$\tau_\mathrm{A} = \sum_{i=n_p}^{n_\mathrm{inner}} \frac{\Delta r_i}{v_\mathrm{eff,i}} \tag{5.25}$$

for inward going waves, where Δr is the local grid cell size in r-direction that varies with r. The index n_p represents the position of the planet and n_inner the inner boundary. For outward going waves, the integration boundaries switch and n_inner becomes n_outer. The effective wave speed v_eff is the absolute value of the wave characteristics that typically have the form

$$\boldsymbol{c}^{\pm}_\mathrm{wave} = \boldsymbol{v} \pm \boldsymbol{v}_\mathrm{wave} \tag{5.26}$$

where $\boldsymbol{v}$ is the plasma velocity, $\boldsymbol{v}_\mathrm{wave}$ the wave speed and ± denoted the direction parallel or anti-parallel to the magnetic field.

To estimate the wave path, we treat the wave characteristics as a vector field. We can use the characteristics to solve a differential equation of the form

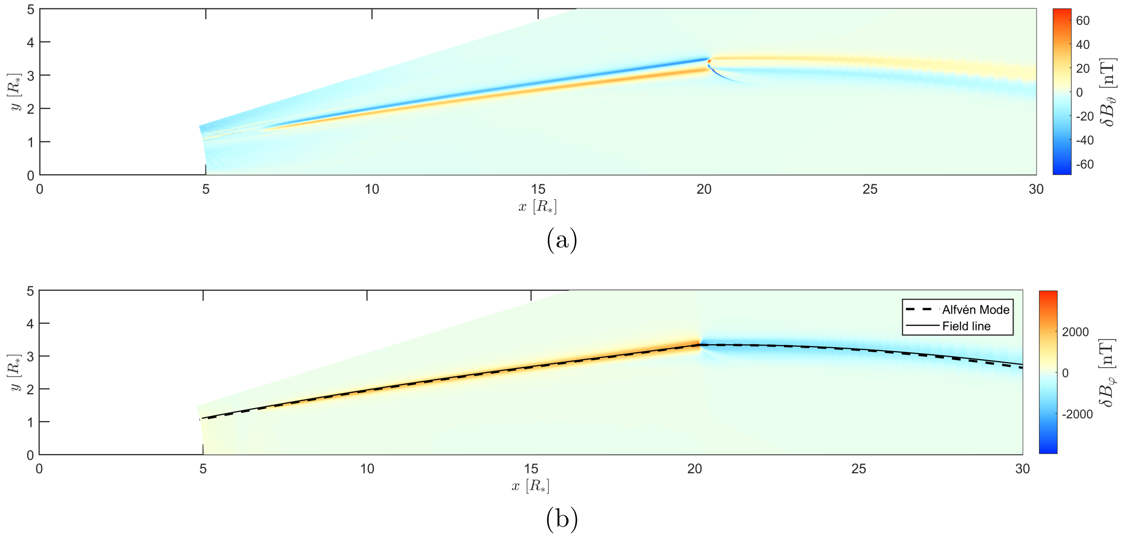

(a)

(b)

Figure 5.8: Close-ups of the equator plane, showing the disturbances in B_ϑ and B_φ at $t = 0.37$ hrs.

$$\frac{d\boldsymbol{r}}{dh} = \frac{\boldsymbol{c}_{\text{wave}}}{|\boldsymbol{c}_{\text{wave}}|}. \tag{5.27}$$

A Runge-Kutta scheme, therefore, gives the path of the respective wave. We always start at the location of the planet. The same technique can be applied to calculate magnetic field lines, where the unit vector in the direction of the magnetic field replaces the right-hand side.

5.4 The Inward Going Alfvén Wing

In our model, the inward going Alfvén wing corresponds to the c_{A}^- wing from *Neubauer* (1980) and *Saur et al.* (2013). It is the observationally relevant wing since it carries the Poynting flux towards the star where it may generate emissions.

The analysis of inward and outward going waves has to be separated from each other because the inner Alfvén wing reflects at the inner boundary region. Therefore here we chose a time when the inner Alfvén wing barely reached the inner boundary. The disadvantage is that the outer waves did not propagate sufficiently far from the planet to perform a proper analysis.

Here we will focus on the properties of the wing within the stellar wind. First, we look at the path of the wing and the wave disturbances. Finally, we investigate the Poynting flux carried by the wing.

5.4.1 Path in the Stellar Wind

We simulated TRAPPIST-1b, and at the chosen time of $t = 0.39$ hours, the planet is located at $x = 20.1R_*$ and $y = 3.3R_*$. Figure 5.8 presents a view of the equatorial plane with the magnetic disturbances that form the inward going Alfvén wing, with δB_ϑ in Figure 5.8a and δB_φ in Figure 5.8b. We calculated the disturbances by subtracting the background magnetic field. Therefore we can see the Alfvén wave only. Starting from the planet, we calculated the Alfvén characteristics given by equation (3.34) and plotted them on top of the simulation results. The solid black line is the magnetic field line that connects to the planet, and the dashed line shows the two Alfvén characteristics.

The Alfvén wave travels along the magnetic field line on which it was excited. In this particular case here, towards the star. In the reference frame of the planet, and in the absence of azimuthal inhomogeneities, the Alfvén wing appears as a stationary structure (*Saur et al.*, 2013). The effective wave speed for equation (5.25) is given by the upstream wave characteristics and assumes values of $v_{\text{eff}} = v_{\text{A}}(r) - v_r(r)$ in this case. The theoretical wave travel time, estimated from the velocity profiles presented in section 5.2, is $\tau_{\text{A}} = 0.40$ hours. The time of our chosen output time is 0.37 hours.

Due to the motion of the planet and the plasma, the Alfvén wing bends away from the magnetic field. Therefore the wing and the field line include an angle to each other. In Figure 5.8a we see that the Alfvén wing closely follows that magnetic field line. According to equation (3.35), we expect an angle of $\Theta_{\text{A}} = 2.35°$ at the location of the planet. By taking the components of $\boldsymbol{c}_{\text{A}}^{-}$ and $\boldsymbol{B}$ at the same position, we calculate a very similar angle of 2.42°.

5.4.2 Properties of the Wing

Alfvén waves have distinct wave properties, as we already saw in section 3.1.2. The generated disturbances are perpendicular to the background magnetic field. Since the background magnetic field goes predominantly into the radial direction and the planet moves into the azimuthal direction, we expect large disturbances in the azimuthal magnetic field. Accordingly, in the inward wing, we have an increase in B_φ with a disturbance of up to 4000 nT. The amplitude of the disturbance is largest close to the planet and then decreases towards the star. The same behaviour holds for B_ϑ, although the amplitude of δB_ϑ only goes up to about 70 nT in this representation.

To verify, that the inward wave structure is indeed an Alfvén wing, we compare simulation results with semi-analytic expectations. For Alfvén waves, we can apply the non-linear theory from *Neubauer* (1980) (see equations (3.38) and (3.39)) to compare simulated magnetic fields with expected magnetic fields. The solution of *Neubauer* (1980) requires the electric field $\boldsymbol{E}$, the Alfvén characteristic $\boldsymbol{c}_{\text{A}}^{-}$ and the Alfvén conductance Σ_{A}, which we can all calculate locally from simulation results. To compare simulation and expectation quantitatively, we take a profile along the φ-direction at a certain distance from the star.

Figure 5.9 shows such a quantitative comparison for all three magnetic field components at a distance of $15R_*$. We see the disturbances that belong to the Alfvén wing clearly because due to the rotational symmetry of our setup, the magnetic field is constant along the φ-direction. The r-component has a small disturbance (small compared to B_r) shown in Figure 5.9a. The amplitude in the inner Alfvén wing goes up to approximately 100 nT. The largest disturbances in B_r however, are caused by the outgoing wave structures that we will discuss in section 5.5. Since these data have been taken at the same co-latitude as in Figure 5.8, we see the oscillation of B_ϑ, between ± 40 nT (Figure 5.9b). The strongest disturbance appears, as expected from section 5.4.1, in B_φ. The field strength changes from -4300 nT to -2300 nT, i.e. a disturbance of 2000 nT. The interaction geometry of

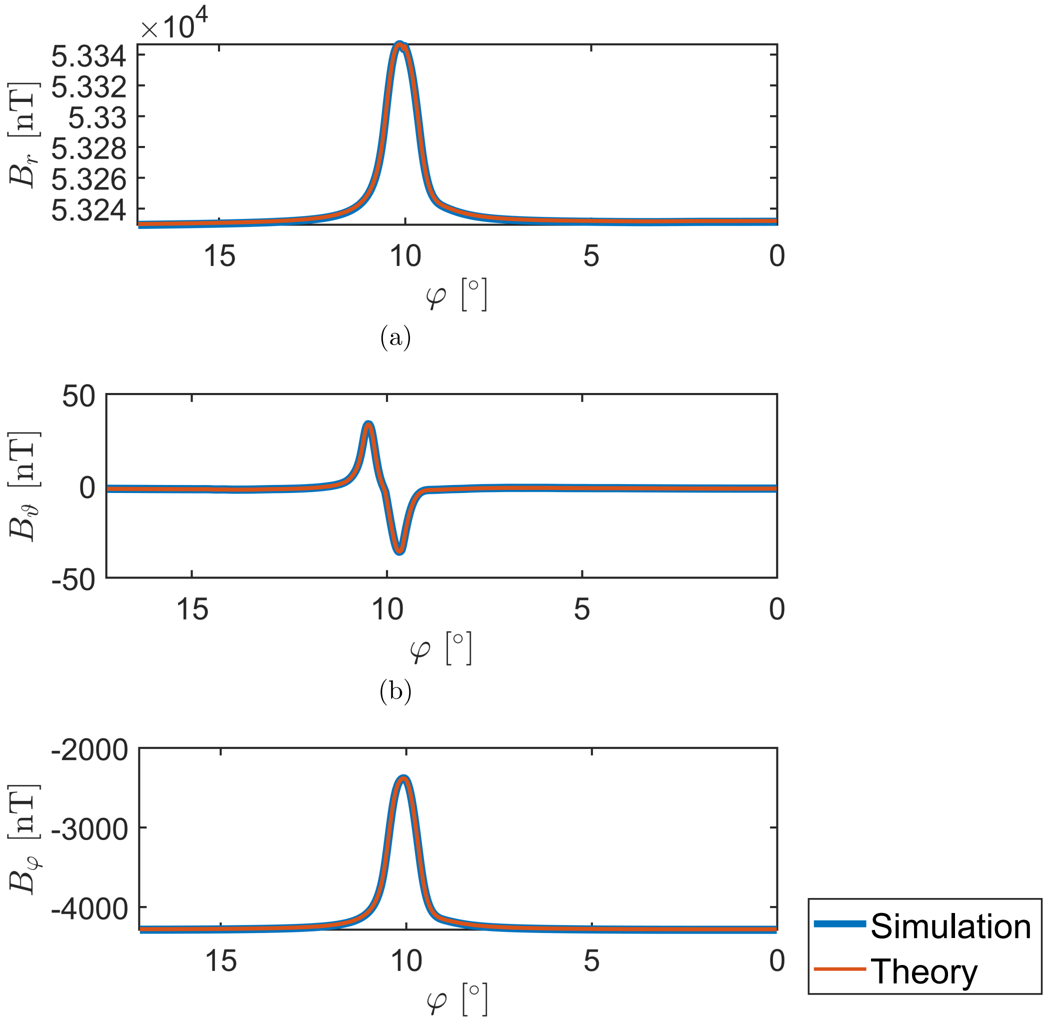

(a)

(b)

(c)

(d) Legend

Figure 5.9: Profile along φ-direction of all magnetic field components, compared to semi-analytic expectations, at a radius of $r = 15\,R_*$ at $t = 0.37$ hrs.

stellar wind flow and magnetic field, together with the motion of the planet, determine the strength of these components. The slight spiral geometry of the magnetic field lines and the resulting velocity vector between stellar wind and the moving planet $\boldsymbol{v}_{\mathrm{rel}} = v_r \boldsymbol{e}_r - (v_{\mathrm{orb}} - v_\varphi)\boldsymbol{e}_\varphi$, results in disturbances in all three components. In our case, the planet's orbital velocity of $v_{\mathrm{orb}} = 83\ \mathrm{km\,s^{-1}}$ is about eight times larger than the azimuthal stellar wind component. Due to the planetary motion, the φ-component becomes the strongest.

As one can see in Figure 5.9, semi-analytic expectations and simulation results show no apparent deviations. Therefore, one can consider the inward going wave structure as purely Alfvénic. We will see in section 5.5 that, in the case of strong non-Alfvénic contributions, both curves deviate from each other. Here in the case of the inward wing, this result implies that we have a pure Alfvénic interaction.

While the φ-component appears like a single structure (see Figure 5.8b), the ϑ-component divides into two parts in Figure 5.8a. To visualise the cross-sectional structure of the Alfvén wing Figure 5.10 presents two-dimensional cuts through the Alfvén wing at a radial distance of $15R_*$. Those plots show the $\varphi-\vartheta$-plane, centred

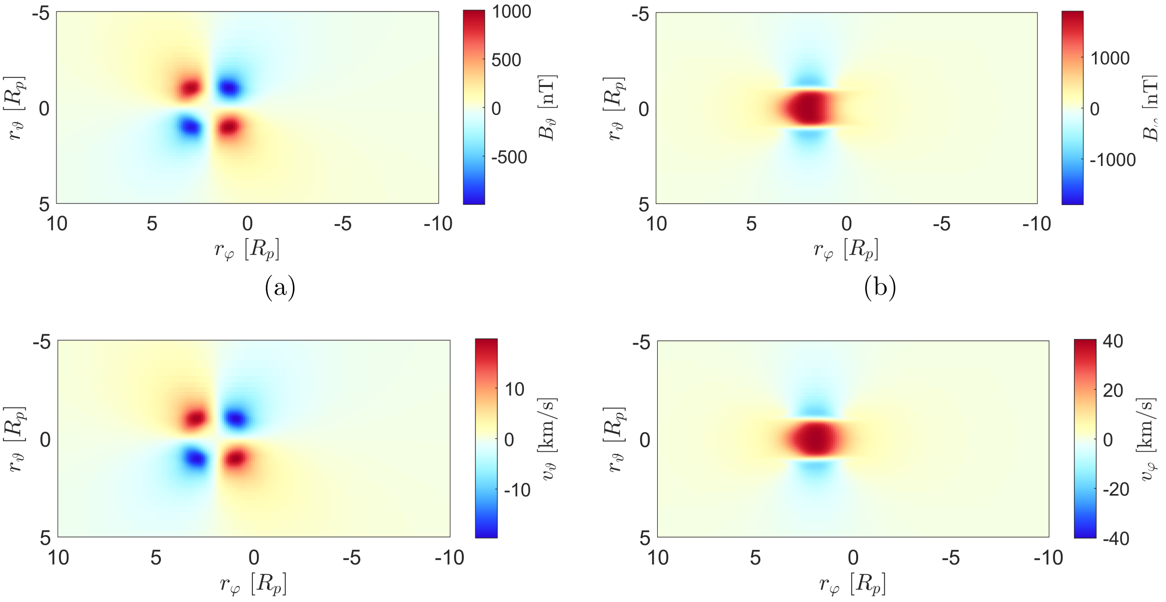

(a) (b)

(c) (d)

Figure 5.10: Cuts of the φ-ϑ plane at $r = 15R_*$ and $t = 0.37$ hrs.

around the position of the planet, i.e. the zero point lies at the axis spanning from the star to the planet. Therefore the Alfvén wing appears to be offset because it does not follow the radial direction.

We compare the ϑ- and φ-components of the magnetic field and velocity with each other. As expected from linear wave theory, the respectively matching components look qualitatively identical. The ϑ-components' cross-section is divided into quadrants with $\delta B_\vartheta = 0$ in the center cross (Figure 5.10a and 5.10c). The first quadrant (upper right) and the third quadrant (lower left) give a negative disturbance of $\delta B_\vartheta = -1000$ nT, respectively $\delta v_\vartheta = -20\,\mathrm{km\,s^{-1}}$. The second and fourth quadrants are positive counterparts. In general, the amplitudes of the ϑ-components are symmetric around zero. There is no difference between the quadrants apart from the sign. A feature of the ϑ-component is that the disturbances seem to lie mainly outside the central main Alfvén wing. The inferred range of the disturbances according to the colour scale, also goes up to a radius of $3R_\mathrm{p}$. In contrast to the ϑ-components, the φ-components indeed form a single structure with the maximum disturbance in the center (Figure 5.10b and 5.10d). The peak disturbance lies here at about $\delta B_\varphi = 2000$ nT, respectively $\delta v_\varphi = 40\,\mathrm{km\,s^{-1}}$.

5.4.3 Energetics of the Alfvén Wing

In this section, we will discuss the electromagnetic energy flux from the planet towards the star. We start with the methods to compute the Poynting vector field from simulation data and the power carried by the Alfvén wing. Afterwards, we discuss the results and will also look into some dissipative effects.

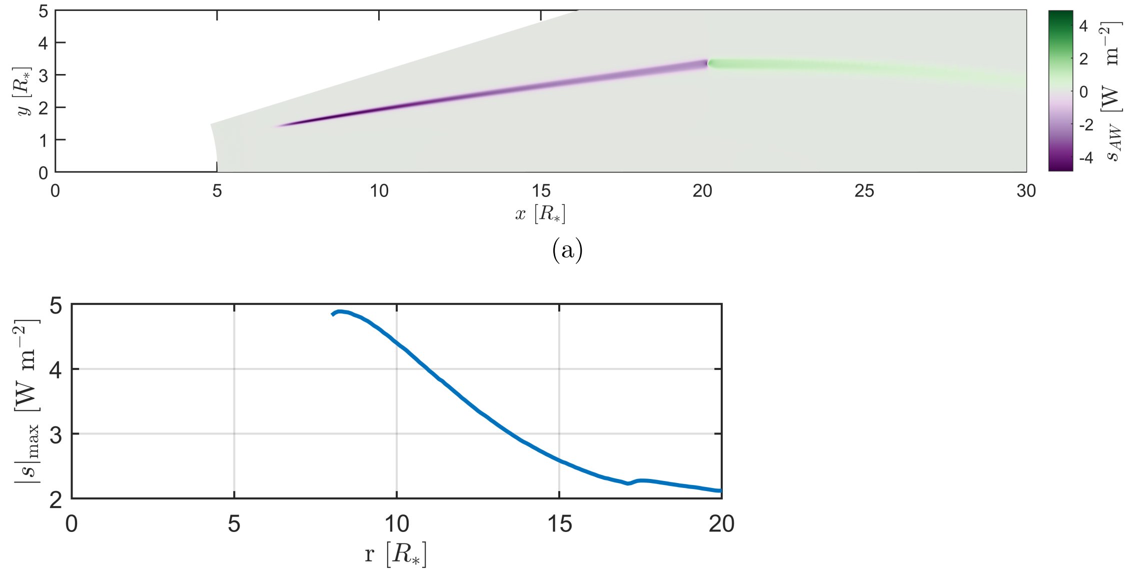

(a)

(b)

Figure 5.11: Close-up of the equator plane, showing the Poynting vector component pointing away from the planet at t = 0.37 hrs. Additionally, we show a line plot of the strongest flux towards the star, along the radial drection.

5.4.3.1 How to Calculate the Poynting Flux

The Poynting vector from equation (3.47) is the electromagnetic energy flux density that is carried by the Alfvén waves. Every plasma with a velocity field that is not parallel to the magnetic field carries such a Poynting vector. We refer to this flux as the background flux. However, *Saur et al.* (2013) provide the theory to obtain the energy flux that is solely carried by the Alfvén wing. Therefore, we have to apply a Galilei-transformation on the velocity field, to switch into the reference frame of the magnetic field. The transformation velocity $\boldsymbol{u}$ has to suffice the condition

$$\boldsymbol{E}_0 = (\boldsymbol{v}_0 - \boldsymbol{u}) \times \boldsymbol{B}_0 = 0 \tag{5.28}$$

where the subscript 0 denotes the background values of the respective plasma variables. The radial stellar wind however has to remain unchanged because we will not switch into the system of the plasma. Hence, $\boldsymbol{u}$ has to fulfil the following conditions:

$$\boldsymbol{v}_0 - \boldsymbol{u} \parallel \boldsymbol{B}_0 \tag{5.29}$$

$$u_r = 0. \tag{5.30}$$

To make the transformed velocity components in ϑ and φ parallel to $\boldsymbol{B}_0$, we apply

$$\frac{v_{\mathrm{i},0} - u_{\mathrm{i}}}{v_{r,0}} = \frac{B_{\mathrm{i},0}}{B_{r,0}} \tag{5.31}$$

with $i = \vartheta, \varphi$. The Poynting flux density carried by the Alfvén wing and in the inertial reference frame is then given by

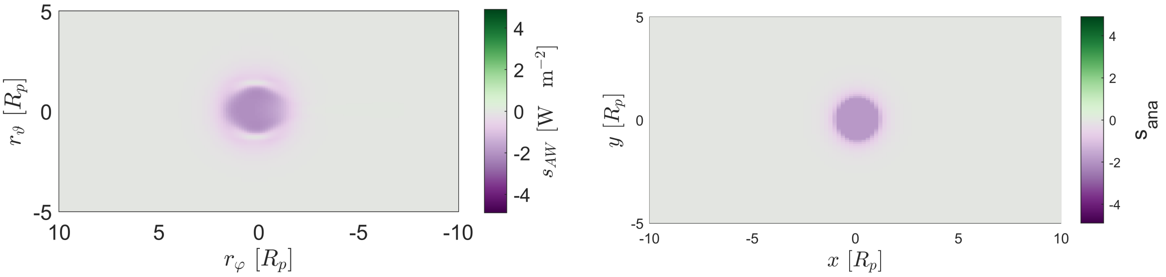

(a) 20 $R*$

(b) analytic

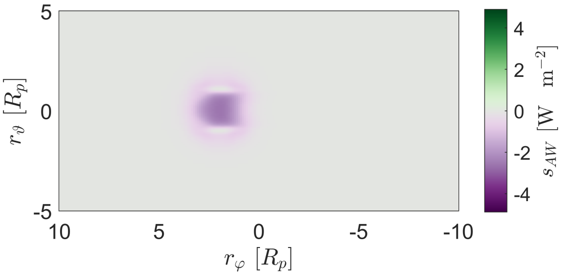

(c) 15 $R*$

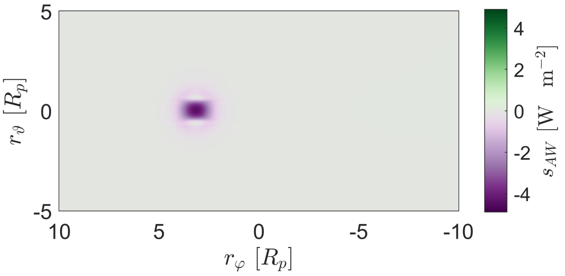

(d) 10 $R*$

Figure 5.12: Cuts of the Poynting flux density in the φ-ϑ plane at different distances from the star. The time is $t = 0.37$ hrs. All cuts are centered at the position of the planet. In comparison we show the analytically expected Poynting flux (*Saur et al.*, 2013).

$$s_{\mathrm{AW}} = \frac{[-(\boldsymbol{v} - \boldsymbol{u}) \times \boldsymbol{B}] \times \boldsymbol{B}}{\mu_0} \cdot \frac{\boldsymbol{B}_0}{|\boldsymbol{B}_0|}. \tag{5.32}$$

The Poynting vector is an energy flux density, with units of W/m^2. To receive the Poynting flux S transferred through the Alfven wing, i.e. the total power, we have to integrate s_{AW} over the cross-sectional area of the Alfven wing. We apply the Riemann integration formula over the ϑ-φ-plane at a certain distance r_{eval} where we evaluate the power. The simulation grid provides the area elements dA with

$$dA = r_{\mathrm{eval}}^2 \sin(\vartheta)\, d\vartheta\, d\varphi. \tag{5.33}$$

Accordingly, the simulated Poynting flux is given by

$$S = \sum_i \sum_j s_{\mathrm{AW,ij}} dA_{\mathrm{ij}}. \tag{5.34}$$

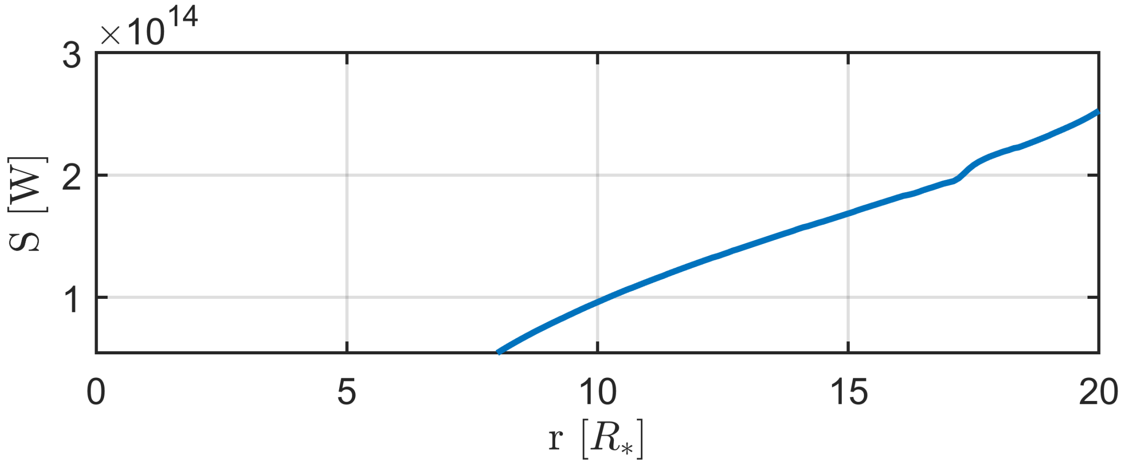

Figure 5.13: Radial dependence of the Poynting flux transported by the Alfvén wing.

5.4.3.2 Poynting Flux Towards the Star

The Poynting flux density depends on variations in the magnetic field and the velocity. Therefore the flux density varies along the Alfvén wing. Figure 5.11 displays the equatorial plane with the energy flux density s_{AW} carried by the Alfvén wing and the radial dependence of the strongest flux towards the star $|s|_{\max}$, according to equation (5.32). These results allow us to describe and analyse the Poynting flux along the Alfvén wing. Negative values (purple) describe a flux towards the star, and positive values (green) represent a flux away from the star. Both parts of the flux, however, flow away from the planet. The colour scale is limited to $|s|_{\max} = 4.9\,\mathrm{W\,m^{-2}}$, i.e. the strongest flux density towards the star.

Visible in Figure 5.11a is a confinement of the Alfvén wing flux tube towards the star. At the planet, the wing appears about twice as wide as at $10\,R_*$. This effect occurs due to the magnetic field geometry, where the distance between the field lines decreases towards the star. Due to the confinement of the flux tube, the flux density s_{AW} increases towards the star. In Figure 5.11a, we can identify this increase of the flux qualitatively by a gradual intensification in colour. Figure 5.11b shows the increase of s_{AW} quantitatively. At $20\,R_*$ the strongest flux density lies at $2.1\,\mathrm{W\,m^{-2}}$. Towards the star the flux density increases non-linearly towards about $4.9\,\mathrm{W\,m^{-2}}$.

Figure 5.12 provides a more quantitative view on the flux tube confinement and the resulting increase in the Poynting flux density s_{AW}. The Figures 5.12a, 5.12c and 5.12d show cross sections of the Alfvén wing in the φ-ϑ plane at radial distances of 20, 15, and $10\,R_*$ from the star. Figure 5.12b shows a cross-section of the analytically expected Poynting flux density according to *Saur et al.* (2013). All four subfigures have the same colour scale as in Figure 5.11a.

At $20\,R_*$, the Alfvén wing flux tube has an elliptical cross-section with $r_\vartheta = 1.2\,R_{\mathrm{b}}$ and $r_\varphi = 1.6\,R_{\mathrm{b}}$. The central Alfvén wing structure, formed by the disturbances in B_φ and v_φ, carries the strongest energy flux density with about $2\,\mathrm{W\,m^{-2}}$. According to *Saur et al.* (2013), the flux density in the central structure of the Alfvén wing is constant, whereas the flux density decreases outward the obstacle radius. Since we have no uniform interaction strength in our simulated obstacle, the flux density varies slightly within the central structure (Figure 5.12a). Outside the central structure within the mentioned axes r_ϑ and r_φ, the flux density decreases rapidly. Just above and below the central structure are banana-shaped regions with nearly zero flux density. These regions coincide with the regions of sign reversals in δB_φ and δv_φ (see Figures 5.10b and 5.10d), which explains the non-existent energy flux towards the star. These structures result from the incompressibility of the plasma flow. The deceleration in the centre of the Alfvén wing results in acceleration at the flanks.

According to the analytical model, one would expect a circular cross-section instead of an elliptic one. The elliptical shape of the simulated Alfvén wings develops further away from the planet. Close by the planet, the cross-section is spherical, although we have to deal with increasing influences from the Fast Mode. The Fast Mode appears in the form of pile-ups in magnetic field and density, which locally affect the Poynting flux density. Therefore, we decided to compare the analytic shape with the cross-section at $20\,R_*$. The elliptical shape, however, is a result of the azimuthal stellar wind velocity. *Saur et al.* (2013) assumed a purely radial stellar wind, where the shape follows from the inclination of the wing towards the magnetic field.

Figures 5.12c and 5.12d show the cross section of the Alfvén wing at $15\,R_*$ and $10\,R_*$, respectively. As expected from Figure 5.11a, the radius of the central wing structure decreases towards the star. For $15\,R_*$, there are $r_\vartheta = 0.9\,R_\mathrm{b}$ and $r_\varphi = 1.2\,R_\mathrm{b}$, while for $10\,R_*$ the structure is only $r_\vartheta = 0.46\,R_\mathrm{b}$ and $r_\varphi = 0.56\,R_\mathrm{b}$ wide. The slight elliptical shape remains, although the banana-shaped structures above and below the wing are, relative to the wing centre, larger than at $20\,R_*$.

The vital quantity for physical interpretations is the Poynting flux, i.e. the power carried by the Alfvén wing because it determines the energy budget for emissions from SPI. According to the formula by *Saur et al.* (2013), i.e. equation (3.48), we expect a Poynting flux of $S = 2.7 \cdot 10^{14}$ W if we insert the values of the plasma variables around the planet and the interaction strength of 0.7 (section 5.1.4). At $20\,R_*$, the simulated Poynting flux lies at about $2.5 \cdot 10^{14}$ W. Both, theoretical expectation and simulation are in excellent agreement with each other. Even the best-guess Poynting flux of $4.2 \cdot 10^{14}$ W, estimated in section 4.3.1, resembles the simulated Poynting flux well.

Figure 5.13 shows the radial dependence of the Poynting flux S, between $8\,R_*$ and $20\,R_*$. Further towards the star, the Poynting flux declines nearly linearly from $2.5 \cdot 10^{14}$ W and reaches values of $1 \cdot 10^{14}$ W at $10\,R_*$, respectively $0.55 \cdot 10^{14}$ W at $8\,R_*$. This decline corresponds to a linear slope of $0.16 \cdot 10^{14}\ \mathrm{W}\,R_*^{-1}$.

5.4.3.3 Dissipative Effects

Theoretically, the Poynting flux towards the star should remain constant in the absence of sources and sinks like Ohmic heating. In such a case, the Poynting theorem from equation (3.45) can be reduced to an expression for flux continuity, with $\nabla \cdot \boldsymbol{s} = 0$. Furthermore, we have $\nabla \cdot \boldsymbol{B} = 0$, which provides a direct relationship between magnetic field and energy flux density. If we assume, that the flux is parallel to the flux tube, we can estimate the expected strength of s_AW at an arbitrary distance, by

$$s_\mathrm{dist} = \frac{B_\mathrm{dist}}{B_{20}} s_{20} \tag{5.35}$$

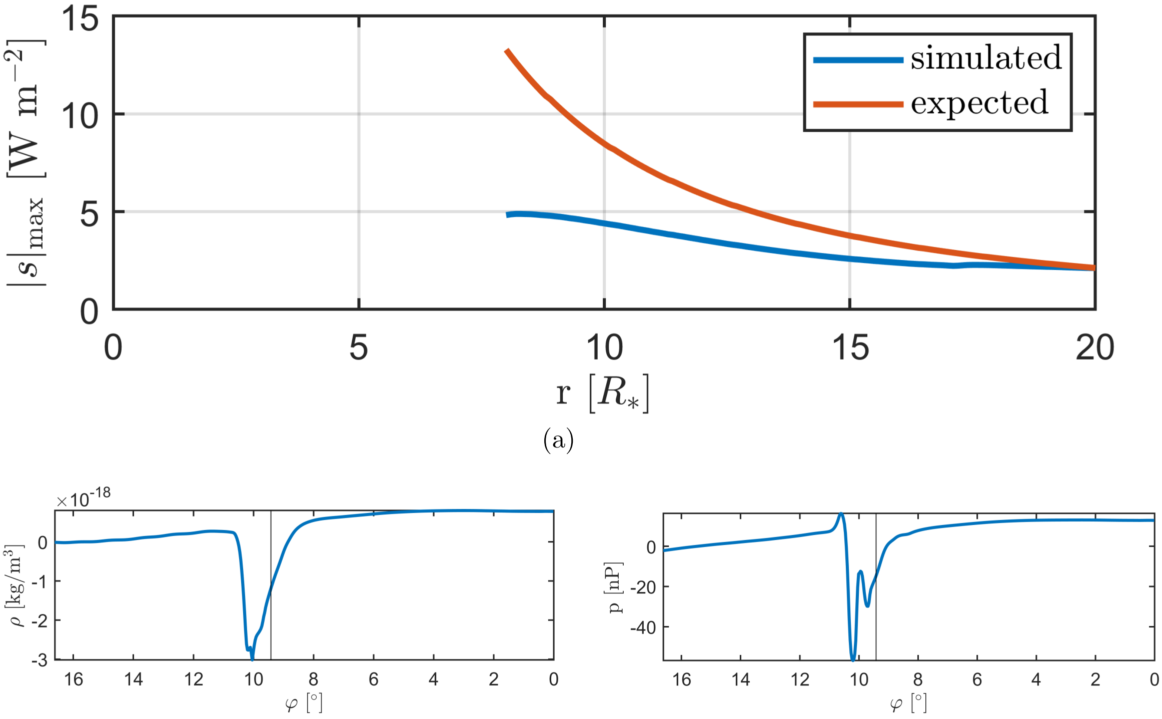

(a)

(b)

(c)

Figure 5.14: This figure shows the maximum Poynting flux density towards the star in the upper panel. In blue the simulated value and in red the expected value without dissipation. The bottom panel shows profiles along φ-direction of density and pressure perturbation at a radius of $r = 15\,R_*$.

where B_{20} and s_{20} are the magnetic field strength and the flux density at $20\,R_*$, which we choose as the base, to which we refer the other distances.

Figure 5.14a shows the simulated maximum Poynting flux density towards the star $|s|_{\max}$ as a function of radial distance in blue. This one is the same as in Figure 5.11b. Additionally, the figure compares $|s|_{\max}$ to the theoretically expected maximum Poynting flux density according to equation (5.35) in red.

The red curve provides overall larger values for the expected Poynting flux density than the simulation. For $10\,R_*$, we receive an expected flux density of $8.5\,\mathrm{W\,m^{-2}}$. This theoretical flux density is about 1.9 times larger than the simulated value of $4.4\,\mathrm{W\,m^{-2}}$. At $15\,R_*$, the expected value lies at $3.8\,\mathrm{W\,m^{-2}}$, which is about 1.5 times larger than the $2.6\,\mathrm{W\,m^{-2}}$ of the simulation.

The Poynting flux in our simulation obviously underlies some strong energy loss processes. A variety of physical processes and numerical dissipation may hold responsible for the loss. Numerical simulations typically produce numerical dissipation, even if the simulation does not directly include physical diffusion processes. The dissipation is a result of the segmentation of the physical space into grid cells. Although finite volume codes are conservative by design, a certain amount of dissipation occurs with coarse grids. Such a problem occurs when different length scales appear in the same simulation, like the stellar radius and the planetary radius here. Both differ by a factor of approximately 10. Due to the static grid and the time dependence, including planetary motion, we cannot resolve the whole path of the Alfvén wing equally well. Therefore numerical dissipation could pose a considerable problem that we can not quantify without extensive numerical studies.

Possible physical reasons for the energy loss are mode conversions from Alfvén waves to magnetosonic waves and reflections. *Wentzel* (1974) described the conversion of Alfvén waves into dissipative magnetosonic waves if the magnetic field bends into the direction parallel to the Alfvén wave disturbances. Such a situation occurs in our simulations, and one can indeed see weak disturbances in pressure and density. Figure 5.14b and Figure 5.14c show an excerpt of the density disturbance $\delta\rho$ and the pressure disturbance δp along the φ-direction at $15\,R_*$. The solid vertical line indicates the azimuthal position of the planet. Accordingly, the disturbances coincide with the position of the Alfvén wing and may belong to the magnetosonic wave modes. Future analyses will have to show the importance of this effect compared to numerical effects.

Reflections of Alfvén wings occur, for example, in the Jupiter-Io interaction. The reflections cause a fragmentation of the auroral footprint into several auroral spots (*Jacobsen et al.*, 2007). *Neubauer* (1980) identified the boundary zone of the Io torus and the ionosphere of Jupiter as possible reasons for reflections due to their strong gradients in the plasma density. In our case, the density decreases with distance from the star. Therefore, the inward going Alfvén wing experiences an increase in density along its path. One will have to determine if this gradient suffices to cause reflections and how much energy reflects on the way towards the star.

5.5 The Outward Going Wave Structures

The inward going Alfven wing may be crucial from an observational point of view. Nevertheless, the outward going waves affect the stellar wind and may also occasionally change the stellar wind conditions for other planets. Therefore we identify the occurring wave patterns and discuss the respective properties of those waves.

5.5.1 Wave pattern

For the outward going waves, we take a later time step of the 'single-planet' scenario. By the time of $t = 3.96$ hours the planet is located at $x = 12.35R_*$ and $y = 16.8R_*$. Figure 5.15 shows the disturbances in the radial magnetic field δB_r and the density $\delta\rho$. Those two variables allow us to identify the paths of the strongly anisotropic MHD wave modes. To increase the wave visibility over a large spatial range, we reduced the colour scale of δB_r to 1/10 of the maximum value and to 1/100 for $\delta\rho$.

According to the method outlined in section 5.3, we plot the wave characteristics. Here the Alfvén wing follows the +-path given by equation (3.34). Based on the propagation properties summarised in Table 3.1, we can construct characteristics for the other highly anisotropic waves:

$$\boldsymbol{c}_{\mathrm{SM}}^{\pm} = \boldsymbol{v} \pm \frac{\boldsymbol{B}}{|\boldsymbol{B}|} c_{\mathrm{s}} \tag{5.36}$$

$$\boldsymbol{c}_{\mathrm{w}} = \boldsymbol{v}. \tag{5.37}$$

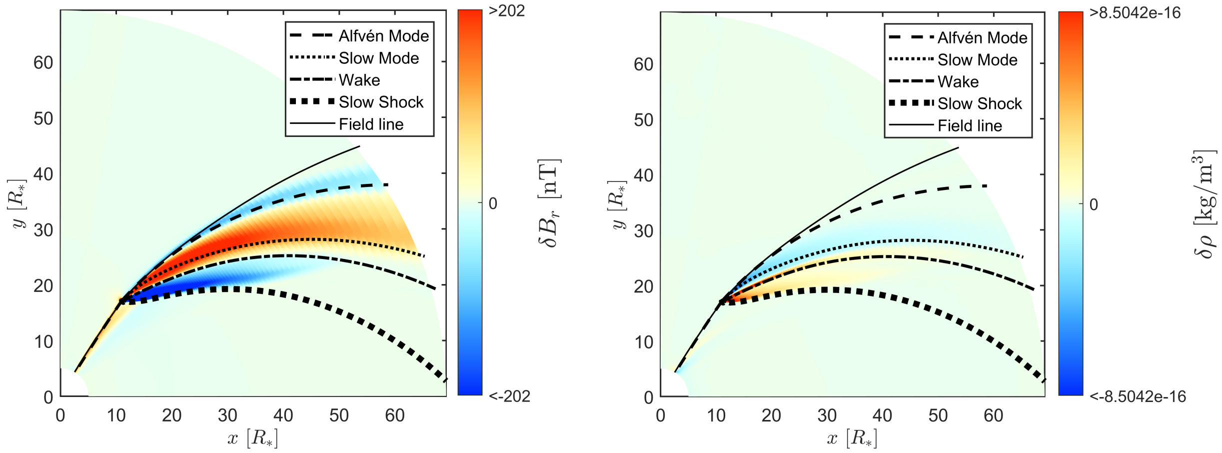

(a) δB_r (b) $\delta\rho$

Figure 5.15: Equator planes showing the wave disturbances of B_r and ρ together with the calculated characteristics at $t = 3.96$ hrs.

The expected position of the waves follows a sequence. The planet moves in the anti-clockwise direction, and the leading wave is the fastest, accordingly followed by the slower waves. However, the very first structure is the magnetic field line (solid line), which the waves follow behind.

The first wave mode is the Alfvén wave (dashed line). Here it is visible in a small negative δB_r (Figure 5.15a) and the fact that there is no disturbance in the density. The outward going Alfvén wave has an effective speed of $v_\mathrm{eff} = v_r + v_\mathrm{A}$ and requires about 1.6 hours to reach the outer boundary and leave the simulation domain at $70R_*$. The angle between Alfvén wing and field lines is theoretically 4.18° (see equation (3.35)) and according to the simulated values of $\boldsymbol{c}_\mathrm{A}^+$ and $\boldsymbol{B}$ it is 4.35°.

Following the waves in the clockwise direction, we see a region of increased B_r and decreased ρ (Figure 5.15). The corresponding wave characteristic belongs to the outward going Slow Mode (dotted line). This structure is very spacious and dominates the occurring wave structures. The effective wave speed of $v_\mathrm{eff} = v_r + c_\mathrm{s}$ is much smaller than the effective Alfvén velocity and therefore the suspected Slow Mode requires with 3 hours about twice as long for the way from the planet towards the outer boundary. This long travel time may also be the reason for it to have such a large spatial extent. In theory, the wave may propagate strictly along the magnetic field, but the wave's group velocity can also propagate non-parallel to the magnetic field (*Linker et al.*, 1988), except for the direction perpendicular to the magnetic field. Therefore, the wave also expands over time and space.

The next structure in the clockwise direction is the planetary wake (dot-dashed line). It strictly follows the flow of the plasma with an effective velocity of v. We cannot identify it in the magnetic field, but instead, there is a narrow density disturbance that exactly follows the plasma flow.

An interesting case is the last wave structure in the clockwise direction. Its position relative to the wake indicates a propagation speed that is slower than the plasma velocity. Furthermore, its disturbances cannot be explained by the MHD wave theory from section 3.1.2. We find that this structure propagates with an effective speed of $v_\mathrm{eff} = v_r - c_\mathrm{s}$ and therefore resembles the inward going Slow Mode.

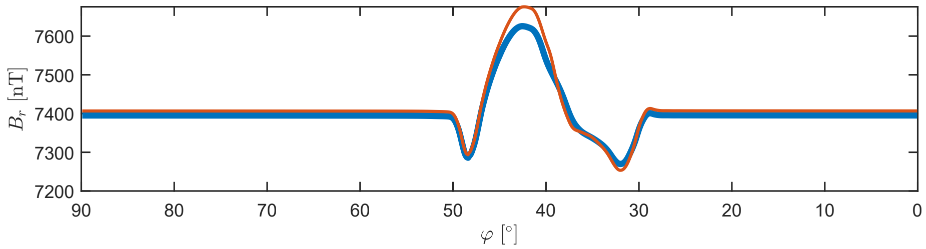

(a) B_r.

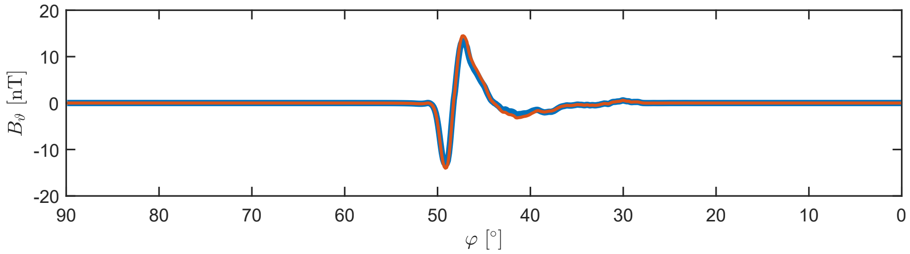

(b) B_ϑ.

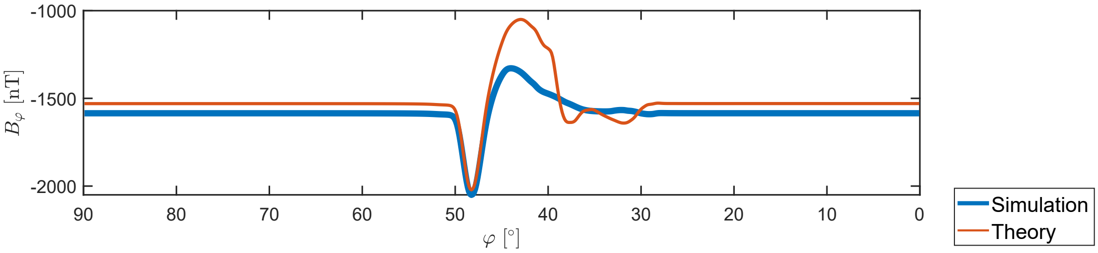

(c) B_φ. (d) Legend

Figure 5.16: Profile along φ-direction of all magnetic field components, compared to semi-analytic expectations, at a radius of $r = 40\,R_*$ at $t = 3.96$ hrs.

According to *Wu et al.* (1996), slow shocks propagate with a velocity of $v - c_\mathrm{s}$, which suits our finding. We will discuss the shock properties later in section 5.5.3, but we can say that this structure is the Slow Shock that results from the supersonic interaction at the planet. The expected travel time from the planet towards the outer boundary is 6 hours. However, after 3.96 hours, the structure reached a distance of approximately $50R_*$. This distance corresponds to the expected distance of $47R_*$as expected according to its travel time and effective speed.

5.5.2 Alfvén Wing

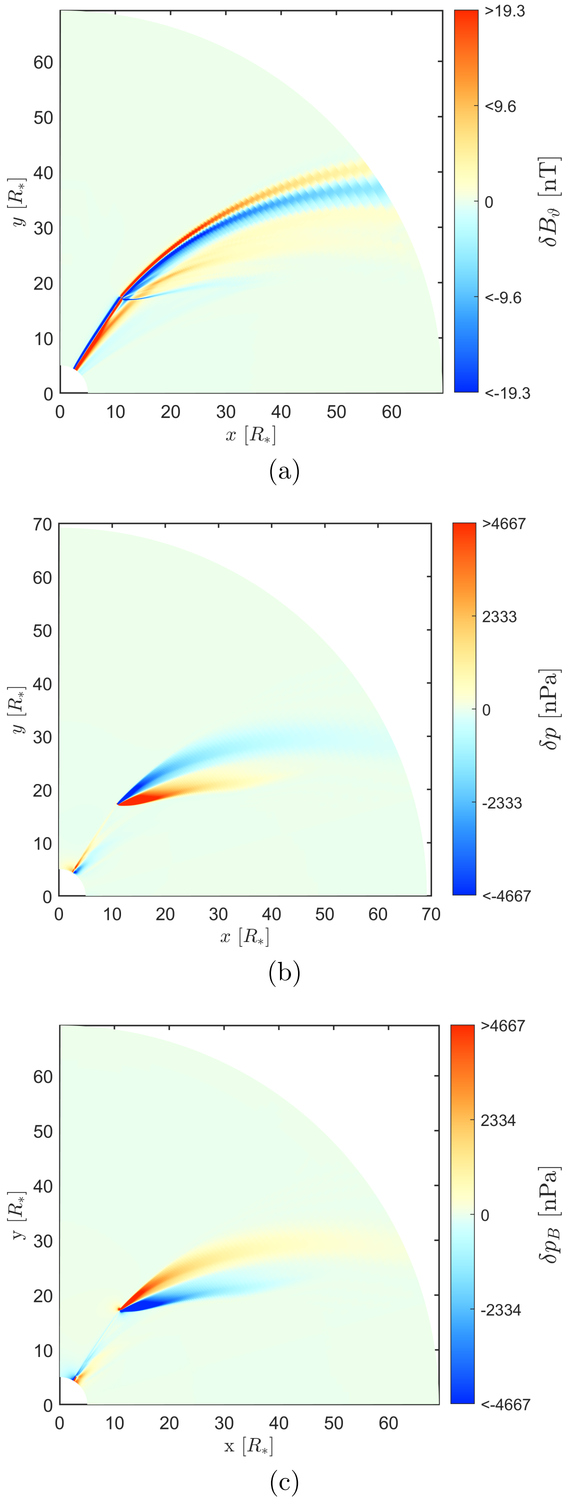

(a)

(b)

(c)

Figure 5.17: This figure shows equator planes with the wave disturbances of B_ϑ, B_r and ρ at $t = 3.96$ hrs.

The characteristics from Figure 5.15a are a first step to identify and describe the different waves. To show that the leftmost wave structure that is indicated by the characteristics is indeed an Alfvén wing, we compare semi-analytic expectations with actually simulated magnetic fields again (see section 5.4.2 for comparison). Figure 5.16 shows a line cut along the φ-direction that shows simulated magnetic field components in blue and expectations according to *Neubauer* (1980) in red. The line was evaluated at a distance of $40R_*$. At $\varphi = 48°$ the magnetic field has its leading perturbation in all three components (note that the φ-axis is reversed to resemble the equatorial plots). At this point, theory and simulation fit perfectly together, which implies that this structure is purely Alfvénic. The Alfvén wave extends from 51° to approximately 44°, visible from B_ϑ (Figure 5.16b). The magnetic ϑ-component is the only one where no deviations between simulation and theory occur, which implies that this component is only affected by the Alfvén Mode. The other components show deviations between theory and simulation, which indicates that other types of waves cause them.

Figure 5.17a shows δB_ϑ, which is the component where we expect the Alfvén Mode to be the dominating wave mode. The colour scale is limited to ±1/10 of the maximum disturbance to make the Alfvén wing better visible. We see that δB_ϑ resembles the split structure that we know from the inward going wing. However, the sign of the disturbances changed, which is due to the asymmetry of the magnetic Alfvén wave perturbations. The figures 5.15b and 5.17b show that the Alfvén wave as a

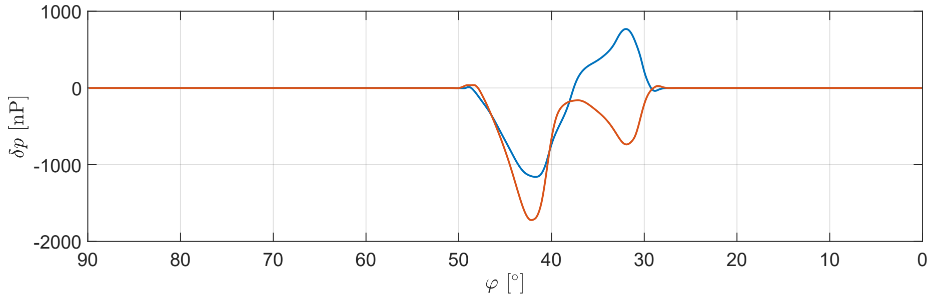

(a) δp

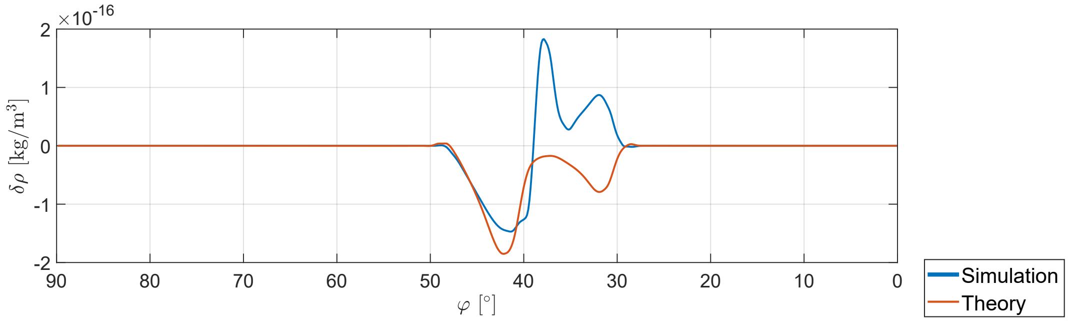

(b) $\delta\rho$

(c) Legend

Figure 5.18: Profile along φ-direction of density and pressure perturbation, compared to semi-analytic expectations, at a radius of $r = 40\,R_*$ at $t = 3.96$ hrs.

non-compressional wave produces no disturbances in density and pressure. Theoretically, the Alfvén wave will not change the magnetic field strength. In Figure 5.17c, we see that the magnetic pressure remains unchanged along the path of the Alfvén wing. Only the other wave modes cause perturbations of the magnetic field strength.

5.5.3 Slow Mode and Slow Shock

The Slow Mode is an unusual wave in our studies. Due to the super-sonic interaction, we expected a shock structure. However, according to the findings in section 5.5.1, we have an outward going Slow Mode and a shock that is probably related to the inward-directed Slow Mode. We will refer to those two structures as the Slow structures.

Shocks are connected to plasma waves and form highly non-linear structures. The most famous shocks in planetary sciences are the planetary bow shocks that form upstream of planets that experience super-fast plasma flows. In our case here, we have an intermediate situation of sub-Alfvénic and super-sonic conditions. The appearance of a so-called Slow Shock with distinct properties from other types of shocks (*Bazer and Ericson*, 1959) is, therefore, the best candidate for the assumed shock structure.

Shocks are special types of discontinuities and characterised by jumps, which means the plasma parameters have to change abruptly. The jump occurs in the flow direction, which is the radial direction in our case. According to *Baumjohann*

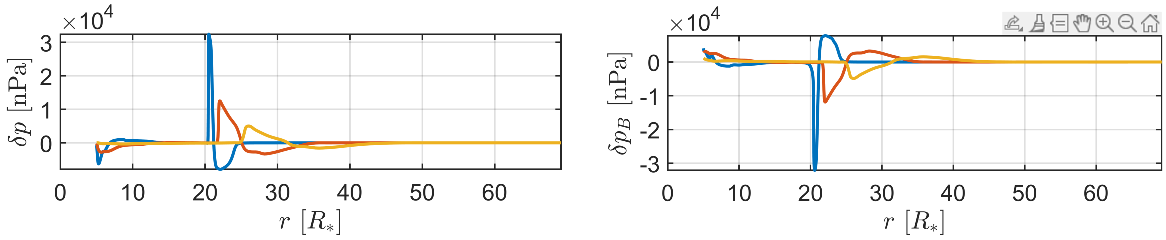

(a) δp (b) δp_{B}

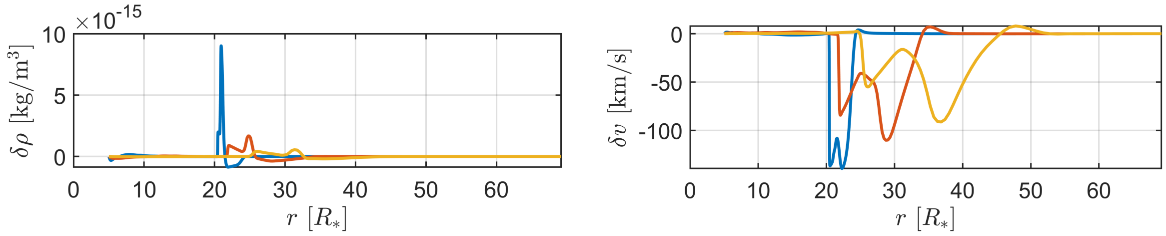

(c) $\delta \rho$ (d) δv

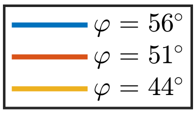

(e) Legend

Figure 5.19: Profiles along r-direction for different azimuth angles φ. Presented are the disturbances in pressure δp, magnetic pressure δp_{B}, density $\delta \rho$ and velocity δv at $t = 3.96$ hrs.

and Treumann (1996), a Slow Shock shows jumps in pressure, density, magnetic pressure and velocity. Pressure and density have to increase across the shock surface, while magnetic pressure and velocity have to decrease. A Fast Shock, in contrast, generates a reduced magnetic pressure.

5.5.3.1 Identifying the Wave Structures

To bring more light into the findings from section 5.5.1 and to identify the two structures related to the Slow Mode, we use the same method that we already applied for the Alfvén Mode. This time we only have the linear wave theory that we presented in section 3.1.2. We calculate the disturbances in pressure δp and density $\delta \rho$ that arise from the field-parallel velocity disturbance and compare them to the corresponding simulated disturbances. Figure 5.18 presents the results for a distance of $40 R_*$ along the φ-direction. Again, blue represents the simulation and red semi-analytic expectations.

We saw that the Alfvén wing lies at approximately 48°. The suspected Slow Mode is the next wave in the clockwise direction, i.e. decreasing φ. The strongest negative peak occurs at about $\varphi = 42°$ (section 5.5.1) in both disturbances. The location of this strongest interaction peak coincides in both simulation and expectations. However, there are deviations in strength. While the actual perturbation in the pressure goes to -1100 nPa, the semi-analytic expectation goes down to -1700 nPa. Similar in $\delta \rho$, where the simulation peaks at $-1.5\,\mathrm{kg\,m^{-3}}$ and the semi-analytic result lies at $-1.9\,\mathrm{kg\,m^{-3}}$. These deviations are not surprising because the linear theory assumes small disturbances. In the range of strong interaction that we have here, the disturbances are not small anymore. Effectively, the Slow Mode disturbances are about 63% and 64% of the local background pressure and density, respectively.

Further to the clockwise direction, we have a positive peak in δp and two peaks in $\delta\rho$. The Slow Mode wave properties can not in any way describe these structures as one can see from the comparison to the theoretical curve. However, the last structure at $\varphi = 33°$ shows some anti-parallel connection between both curves, which might arise from the origin of the Slow Shock in the Slow Mode. The narrow density peak at $\varphi = 37°$ will be discussed in section 5.5.4.

We finally conclude that we have identified the compressional structure behind the Alfvén wing (in the clockwise direction) as the outward going Slow Mode. This conclusion is, albeit the slight deviations, evident from the comparison between theory and simulation.

Now we will focus on the structure that we assume to be a Slow Shock. We extract line cuts along the radial direction for different azimuth angles φ, since jumps in the direction of the flow describe the shock. In this way, we can see the jumps and compare them. Figure 5.19 shows these profiles for the disturbances of the pressure δp (Figure 5.19a), the magnetic pressure δp_{B} (Figure 5.19b), the density $\delta\rho$ (Figure 5.19c) and the velocity δv (Figure 5.19d). We extracted the disturbances at azimuthal locations behind the planet with $\varphi = 56°$ (blue), 51° (red) and 44° (yellow).

Close to the inner boundary at small r, we see disturbances generated by the interaction between the inner Alfvén wing and the boundary. Those are, however, negligible and easy to distinguish from the disturbances generated by the planet.

When we follow the radial direction, we will first encounter the disturbance caused by the Slow Shock. In pressure and density, we see a sharp increase. Over less than one stellar radius the pressure increases by $3.3 \cdot 10^4$ nPa and the density increases by $2 \cdot 10^{-15}\,\mathrm{kg\,m^{-3}}$ in the blue curve. For the curves that are cut at an azimuth angle further behind the planet, the amplitudes decrease. The density is a special case because the disturbance that belongs to the wake is much stronger than the shock disturbance, which implies that we should not consider the highest density peak but the earliest one. The velocity and magnetic pressure decrease rapidly. The magnetic pressure appears to mirror the thermal pressure. Accordingly, the obtained properties fulfil the conditions for a Slow Shock, and we can consider this structure as identified.

5.5.3.2 Properties of the Slow Structures

According to the linear wave theory, the Slow Mode would not generate any magnetic field disturbance (see Table 3.1). However, we see disturbances in the magnetic field (Figure 5.15a) and in the magnetic pressure (Figure 5.17c) in regions where we just identified the Slow Mode. Figures 5.17b and 5.17c show that thermal pressure and magnetic pressure behave contrary to each other, i.e. the pressure decreases, but the magnetic pressure increases. This behaviour is quantitatively visible in Figure 5.19. All three curves of the pressure disturbance in Figure 5.19a are the exactly mirrored counterpart to the magnetic pressure disturbances in Figure 5.19b.

Linker et al. (1988) saw the same effect in their simulations. The authors explain this behaviour with pressure balance. When the thermal pressure experiences a disturbance by the Slow Mode, the magnetic field reacts to it, so that the total pressure remains constant. Hence, this phenomenon is not directly related to the wave itself but indirectly caused by the wave disturbance.

We know that a Slow Shock generates a disturbance in the magnetic field strength. The simulation results additionally show that thermal pressure and magnetic pressure show anti-parallel behaviour as well. Across the shock surface, there is no change in the total pressure, as δp an δp_B balance each other.

5.5.4 Wake

In Figure 5.15b we see a density structure, that appears in no other plasma variable. The structure follows the characteristic that we assume for the planetary wake (equation (5.37)). The entropy mode suits these obtained properties best since according to *Jeffrey and Taniuti* (1964), it only generates a disturbance in the density and does not propagate itself (see Table 3.1).

Figure 5.19c shows the radial profiles of the density disturbance $\delta\rho$ (as discussed in section 5.5.3). The largest peaks in $\delta\rho$ occur between the identified Slow Shock and the identified Slow Mode.

Schilling et al. (2008) simulated a similar setup as we do, but with Europa, where the moon and the plasma have the same direction of motion. They, however, found an increased density as well. The authors attribute the obtained increased density in their results to ionisation in the ionosphere of Europa, an effect that we have not included in our model.

In general, one expects a decreasing density and pressure in the wake, because typically, the planet would absorb plasma and somewhat shield the region downstream. However, our planet is only a gas cloud, but we have the limit of strong interaction. Therefore the planet decelerates the plasma to 30% of the initial speed. That results in a pile-up of plasma upstream of the planet. The planetary motion perpendicular to the main plasma flow directs the plasma in an asymmetric path around the planet. The density perturbation is then carried away by the stellar wind, which resembles the planetary wake.

6 Wing-Wing Interaction

The wing-wing interaction is one of the four possible mechanisms for time-variability in SPI (see section 3.4.5). This process has never been described before in planetary sciences because, in the solar system, two moons can never share the same magnetic field line. In a stellar wind with quasi-open field lines, however, two planets can share the same field line. To the author's knowledge, there are no other studies that have ever simulated electromagnetic SPI from multiple planets in one system. This feature is possible due to our time-dependent MHD setup.

In this chapter, we will investigate this hypothetical type of interaction between the planets T1b and T1c with the MHD model from chapter 5. First, we show the necessary adaptations to the model setup, to simulate two planets. In chapter 5 we have already analysed T1b in detail, so we will describe the interaction of T1c and compare it to T1b. Finally, we look into the temporal evolution of the interaction, when the planets come sufficiently close to affect each other.

6.1 MHD Setup with Two Planets

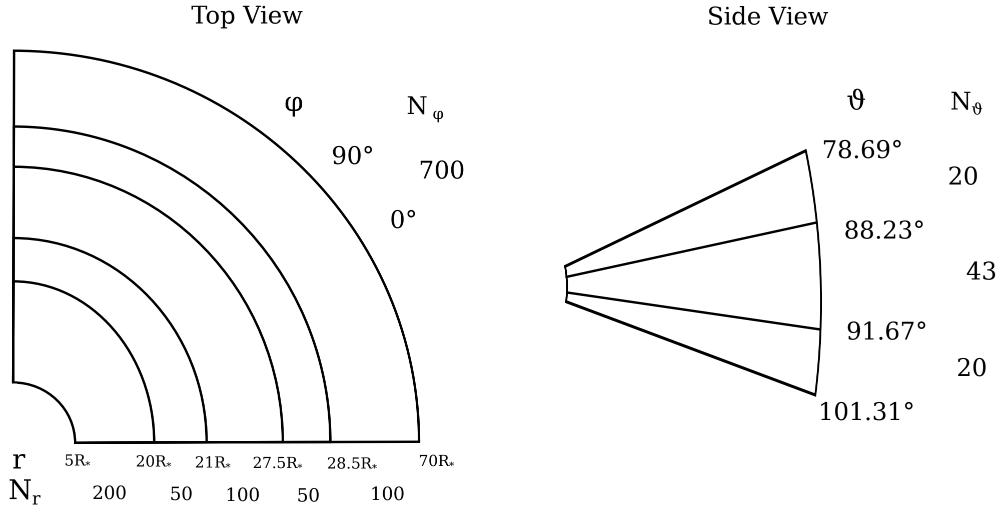

Figure 6.1: Grid structure for the 'wing-wing' scenario.

The simulation setup for two planets is principally the same as for one planet. We parametrise both planets as clouds of neutral gas, which is the main driver of the desired interaction. The simulation code has to be adapted (in fact, generalised) to treat each planet as a separate source term. The equations from section 5.1.3, i.e. equation (5.19) and 5.20, then take the form

$$\frac{\partial \boldsymbol{m}}{\partial t} + \nabla \cdot \boldsymbol{F}_{\mathrm{m}} = \mathrm{rhs}_{\mathrm{m}} - \sum_{k=1}^{n} \rho \nu_{\mathrm{in,k}} (\boldsymbol{v} - \boldsymbol{v}_{\mathrm{orb,k}}) \tag{6.1}$$

$$\frac{\partial E_{\mathrm{tot}}}{\partial t} + \nabla \cdot \boldsymbol{F}_{\mathrm{E}} = \sum_{k=1}^{n} \left(-\nu_{\mathrm{in,k}} \frac{p}{\Gamma - 1} + \frac{1}{2} \rho \nu_{\mathrm{in,k}} \left(\boldsymbol{v} - \boldsymbol{v}_{\mathrm{orb,k}}\right)^2 - \rho \nu_{\mathrm{in,k}} \left(\boldsymbol{v} - \boldsymbol{v}_{\mathrm{orb,k}}\right) \cdot \boldsymbol{v} \right) \tag{6.2}$$

with the maximum number of planets n. All other quantities with index k are the same as in section 5.1.3 but for the respective planet. In this case, the orbital velocity is the respective orbital velocity of T1b and T1c. The atmospheric parameters, i.e. a hydrogen atmosphere with base neutral gas density $n_{\mathrm{n0,k}}$ and scale height H, of both planets, are assumed to be the same, with values according to section 5.1.4. By setting the index k to 1, we can easily simulate a single-planet scenario again, in that way the extension for multiple planets is only a generalisation of the model.

The domain for the 'wing-wing' scenario (Figure 6.1) assumes the standard measures given in Table 5.1. Due to the second planet, we have to adapt the resolution of the r-direction. There, the grid ranges from $5 - 20\,R_*$ with 200 uniform cells, from $20 - 21\,R_*$ with 50 uniform cells, from $21 - 27.5\,R_*$ with 100 uniform cells, from $27.5 - 28.5\,R_*$ with 50 uniform cells and from $28.5 - 70\,R_*$ with 100 stretched cells. For the ϑ-direction the grid ranges from $0.43\pi - 1.54$ with 20 stretched grid cells, from $1.54 - 1.6$ with 43 uniform grid cells and from $1.6 - 0.56\pi$ with 20 stretched grid cells. Finally, for the φ-direction we have 700 grid cells for the range between 0 and 0.5π.

6.2 SPI From Two Planets

From chapter 4, we expect two of the seven planets to experience sub-Alfvénic conditions. The applied MHD model would allow up to four planets to experience those conditions. However, with increasing distance from the star, the expected powers, carried by the respective Alfvén wings, decrease rapidly the further the planets are away from the star. The power from T1c was estimated to be about one order of magnitude weaker than the one from T1b (Table 4.1). Similar relations hold for T1d, where the expected power is about two orders of magnitude smaller than from T1b (Table 4.1). Therefore, it becomes increasingly difficult to distinguish the weaker SPI-structures from the strong interaction of T1b. For the two innermost planets b and c, a comparison is still possible. The expected powers, according to Table 4.1, differ by a factor of seven.

Figure 6.2 shows the δv_ϑ, δv_φ, and δB_φ components, as well as the pressure disturbance at $t = 0.81$ hours. The colour scales are capped to ranges of $\delta v_\vartheta = \pm 3\,\mathrm{km\,s^{-1}}$, $\delta v_\varphi = \pm 50\,\mathrm{km\,s^{-1}}$ and $\delta B_\varphi = \pm 3000$ nT and $\delta p = 5.1 \cdot 10^{-6}$ Pa. This choice is determined by the differences in the obtained interactions from T1b and c.

The angle between the inward Alfvén characteristic and the magnetic field lines is 1°, measured as well as theoretically, according to equation (3.35). The travel time of the inward going Alfvén wave is $\tau = 0.84$ hours, which is the reason why we chose the particular time. The inward wave structures of both planets have developed, but are still sufficiently far away, to have not yet influenced each other.

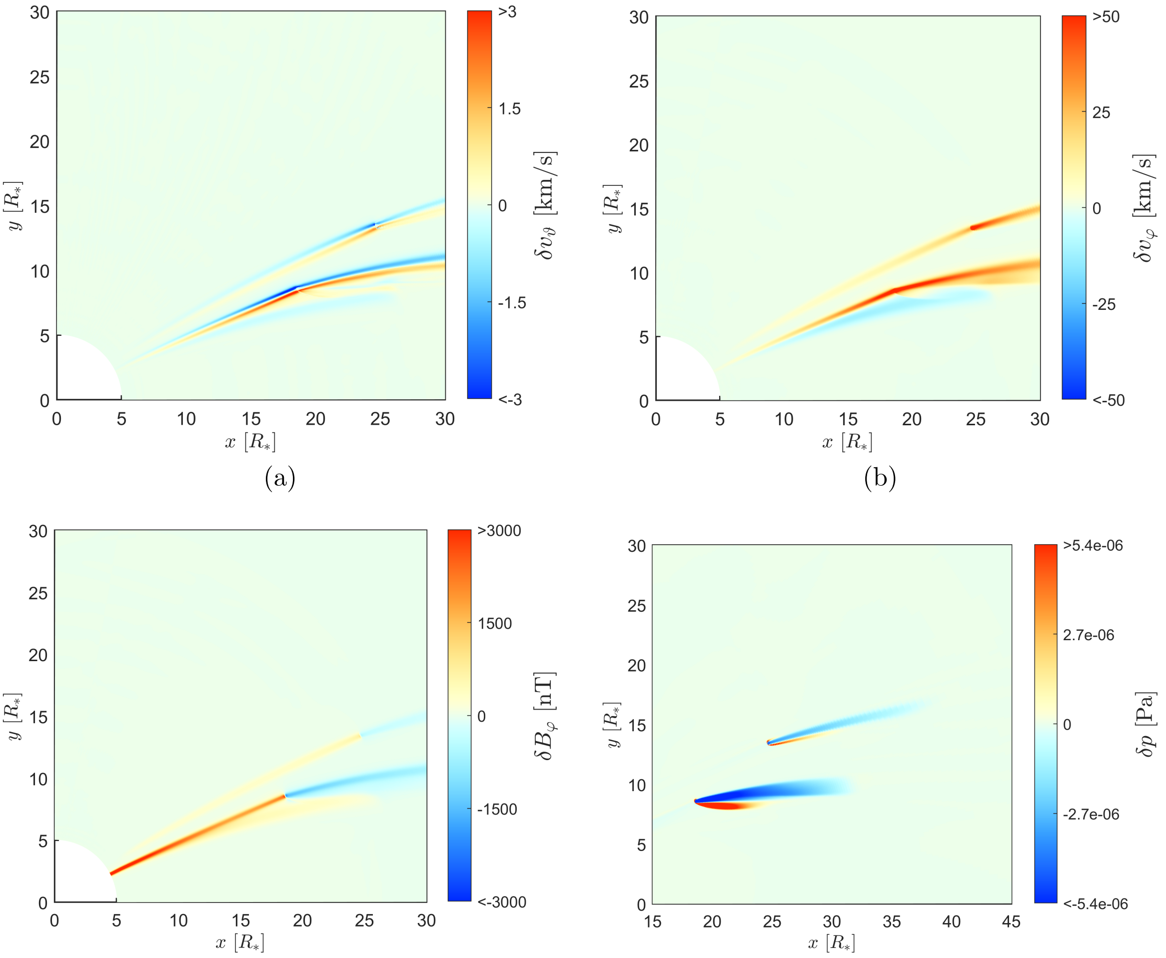

(a)

(b)

(c)

(d)

Figure 6.2: The interaction of T1b and T1c at $t = 0.81$ hours presented by δv_ϑ and δv_φ in the top row, and δB_φ and δp in the bottom row.

The non-capped amplitude in δv_ϑ lies in the range of $\pm 2\,\mathrm{km\,s^{-1}}$ close to T1c. From there, the local amplitude decreases towards the star. The same appears in δv_φ, with an amplitude of about $25\,\mathrm{km\,s^{-1}}$. For the magnetic field in the azimuthal direction, the amplitude goes up to 300 nT. In comparison, the respective amplitudes generated by T1b, go up to $\pm 4\,\mathrm{km\,s^{-1}}$ in δv_ϑ, $70\,\mathrm{km\,s^{-1}}$ in δv_φ and 2300 nT in δB_φ. The magnetic field disturbance increases towards the star, due to reflections at the inner boundary.

The outward going wave structures are principally the same as in the case of T1b. Although, most of these waves have not yet propagated very far from the respective planet at $t = 0.81$ hours. The travel time for the outward Alfvén wing is 1.4 hours, for the outward Slow Mode it is 2.5 hours, for the wake 3.2 hours and the Slow Shock requires 4.7 hours to reach the outer boundary. The first wave in the clockwise direction is the outward going Alfvén wing, visible in all velocity disturbances and δB_φ.

The compressional waves, i.e. the Slow structures, are best visible in the pressure disturbances in Figure 6.2d. This subfigure presents a shifted excerpt of the simulation domain. However, the axis scaling is the same as in the other subfigures of figure 6.2. In here, we can easily see the outward going wave structures, to describe them.

The outward going Slow Mode generates a negative pressure disturbance. The Slow Shock, associated with the inward going Slow Mode, generates a positive disturbance. According to our findings from section 5.5.3, the Slow Mode is the leading compressional wave, and the Slow Shock is the trailing wave with respect to the planet's motion. We can see that the Slow Structures of T1c are much more confined than the ones from T1b. Decreased wave speeds mainly cause the change in geometry. Additionally, the dominance of the radial stellar wind is larger at T1c than at T1b. The wind velocity increased by $20\,\mathrm{km\,s^{-1}}$ from T1b towards T1c, while the velocity of T1c is $12\,\mathrm{km\,s^{-1}}$ smaller than the one of T1b.

6.3 Temporal Evolution of the Star-Planet Interaction

In this section, we will describe the interaction between the wave structures of both planets as T1b overtakes T1c. Therefore, we first review what we have to expect from the interaction of Alfvén waves with each other. Afterwards, we analyse the evolution of the resulting star-planet interaction.

6.3.1 On Wave-Wave Interactions

The interaction between two Alfvén waves was investigated for the cases of coronal heating and laboratory plasmas. It appears that only Alfvén waves that propagate in opposite directions so-called counterpropagating waves interact with each other (*Chin and Wentzel*, 1972; *Howes and Nielson*, 2013). Waves that propagate into the same direction remain unaffected from each other. The authors considered the interaction of those counterpropagating waves as a source of energy dissipation for Alfvén waves, which are generally dissipation-free.

Coronal heating by Alfvén wave-wave interaction has been investigated by, e.g. *Chin and Wentzel* (1972) and *Wentzel* (1974). According to this theory, the interaction of counterpropagating waves generates another Alfvén wave and a Slow Mode wave. The latter then dissipates the received energy. This type of interaction results in a cascade of energy. *Howes and Nielson* (2013) describe similar processes. The authors derived an analytic solution for the resulting turbulent energy cascade from this type of wave-wave interaction based on incompressible MHD. *Drake et al.* (2013) conducted a laboratory experiment that verified the findings from *Howes and Nielson* (2013). *Howes et al.* (2018) applied the theory to astrophysical contexts and conclude for their simulations that wave-wave interaction locally accelerates plasma particles through Landau damping in resulting current sheets.

6.3.2 Alfvén Wings Over Time

According to the literature findings from section 6.3.1, we can expect, that wave-wave interaction occurs only between the outward going Alfvén wing of T1b and the inward going Alfvén wing of T1c. At $t = 0.8$ hours, we saw the interaction of both planets unaffected by each other. Figures 6.3 and 6.4 now present the wing-wing interaction and the aftermath, when T1c leaves the outer Alfvén wing

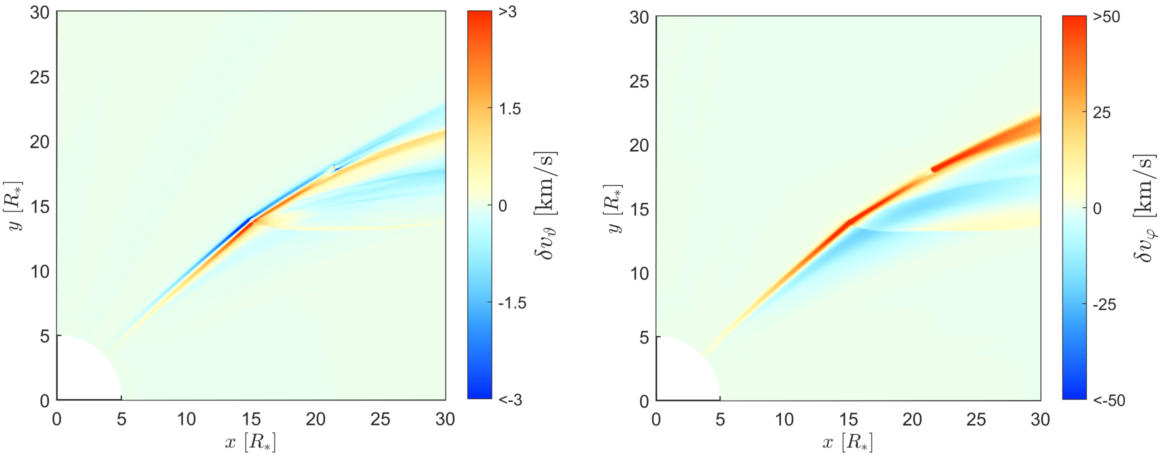

(a) $t = 2.6$ hours (b) $t = 2.6$ hours

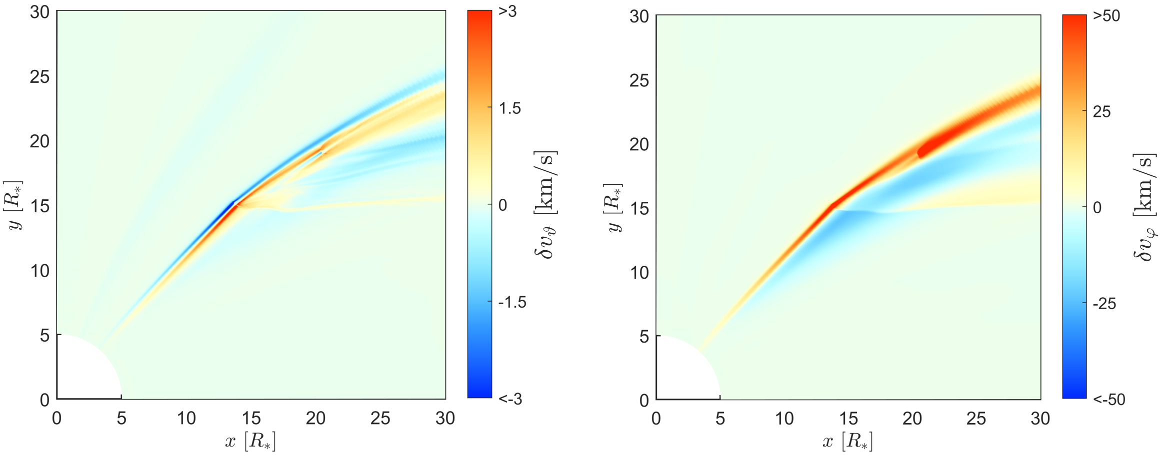

(c) $t = 3.1$ hours (d) $t = 3.1$ hours

Figure 6.3: Wing-wing interaction between T1b and T1c. The top row shows the interaction at $t = 2.6$ hours and the bottom row at $t = 3.1$ hours. Presented are top views on the equatorial planes for the disturbances in v_ϑ and v_φ.

of T1b. In Figures 6.3a and 6.3b, we see the disturbances in v_ϑ and v_φ at $t = 2.6$ hours, respectively. The colour scales are restricted to the same ranges as in Figures 6.2a and 6.2b. The δv_ϑ component is always on the left side and δv_φ is always on the right side. The other figures represent later time steps: Figures 6.3c and 6.3d display $t = 3.1$ hours, Figures 6.4a and 6.4b display $t = 3.6$ hours, and Figures 6.4c and 6.4d display $t = 4.0$ hours. We always show δv_ϑ and δv_φ, because both components together allow us to identify Alfvén wings, now that we know how Alfvén wings look like in stellar winds (section 5.4.1). In the subsequent analysis, the comparison to analytic solutions is not practical because the underlying Slow Mode related wave structures do not allow proper analysis. Furthermore, it is easier to distinguish the Alfvénic velocity disturbances from the reflections that occur at the inner boundary because the reflected velocity disturbance switched its sign.

As expected, the inward going Alfvén wing of T1b remains unaffected. The only interaction between the Alfvén wings happens within the range of T1b's outward

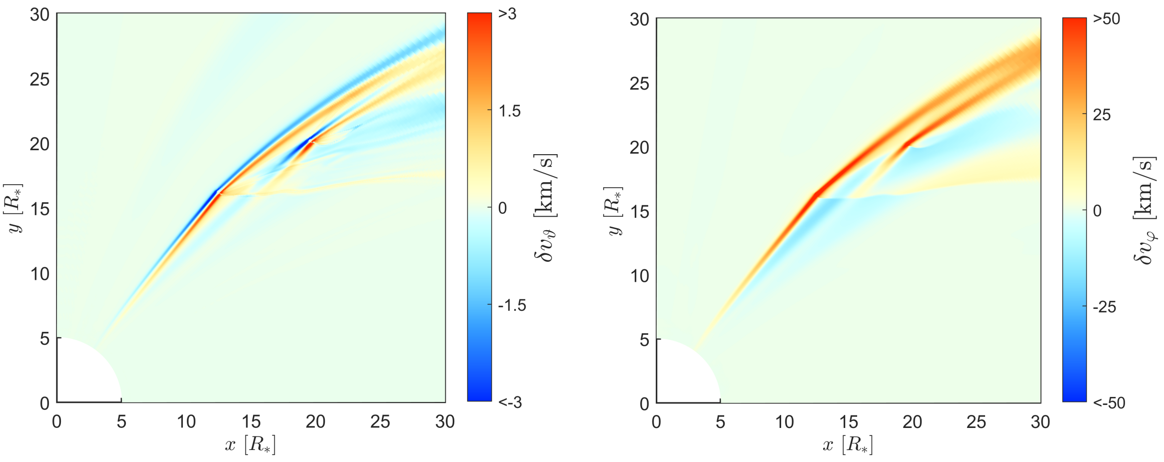

(a) $t = 3.6$ hours (b) $t = 3.6$ hours

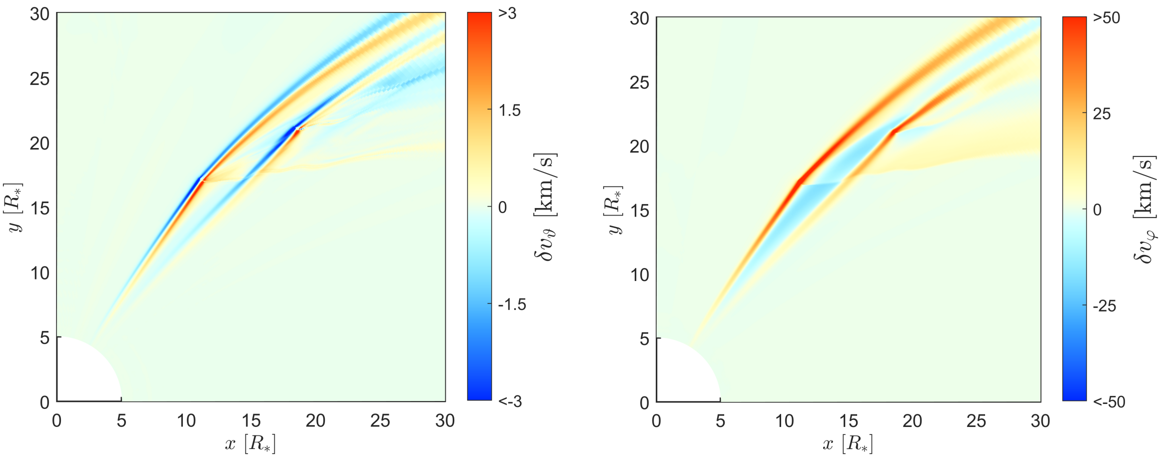

(c) $t = 4.0$ hours (d) $t = 4.0$ hours

Figure 6.4: Wing-wing interaction between T1b and T1c. The top row shows the interaction at $t = 3.6$ hours and the bottom row at $t = 4.0$ hours. Presented are top views on the equatorial planes for the disturbances in v_ϑ and v_φ.

going Alfvén wing and of course at T1c.

At $t = 2.6$ hours, the planet T1c lies entirely in the outward going Alfvén wing of T1b. In Figure 6.2b, we saw that the wave amplitudes emanating from T1b do not change significantly in the range towards T1c. However, at $t = 2.6$ hours, the velocity amplitude diminishes nearly completely towards T1c. The disturbance in v_ϑ widens towards T1c. At the same time, δv_φ increases in the range of the outward going Alfvén wing of T1c. By the time $t = 3.1$ hours, T1c reached the end of the Alfvén wing. The interaction evolved, and we see a broadening of the wave disturbance in the velocity components. This effect is probably due to the position of T1c relative to T1b's outward wing that generates the increased size.

At later times, i.e. $t = 3.6$ hours and 4.0 hours (Figure 6.4), we see that a new inward going wave structure forms at T1c. By the time of 3.6 hours, the newly forming wave propagated about three stellar radii away from T1c, while at 4.0 hours the wave reached the inner boundary. This time range, between 3.1 hours and 4.0 hours, resembles the estimated travel time of 0.83 hours from section 6.2.

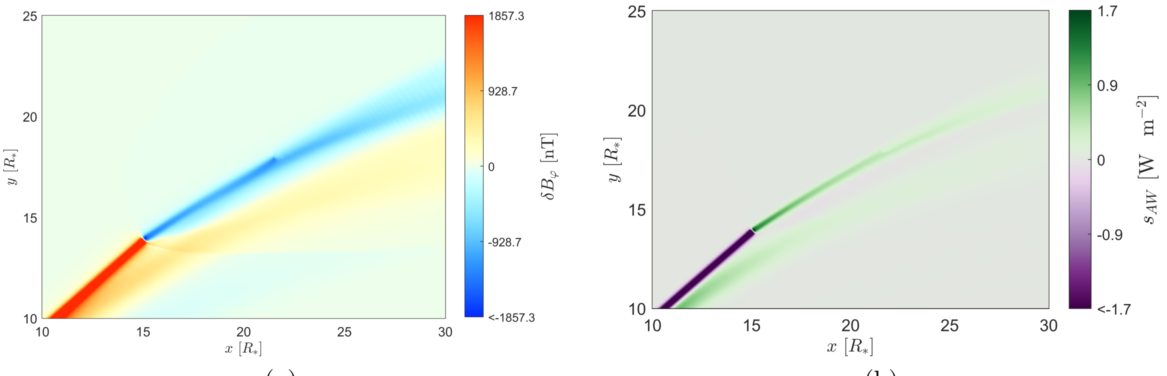

(a) (b)

Figure 6.5: Closer view on the interaction region between T1b and T1c at $t = 2.6$ hours. Presented are the Poynting flux density carried within the Alfvén wing and the magnetic field disturbance δB_φ.

Hence, the interactions within the outward going Alfvén wing of T1b connect to some sort of dissipation.

The new wave structure arises and evolves in the environment of T1b' Slow Structures. As we know from section 5.5.3, these wave structures alter the magnetic field strength and the density of the plasma. Both variables affect the Alfvén wave speed, which in turn affects the path of the Alfvén wing. The newly formed Alfvén wing assumes a larger angle to the unperturbed background magnetic field because it propagates through the altered environment of other wave structures.

We concluded from the fact that a new Alfvén wing forms after egress of T1c from T1b's outward Alfvén wing that both Alfvén wings experienced some kind of dissipation. According to *Wentzel* (1974), there should be an additional Slow Mode wave that dissipates the Alfvén wing energy. Figure 6.6 shows the pressure disturbances at the respective chosen time steps. In Figure 6.6a, we see the situation at $t = 2.6$ hours. However, the pressure disturbance around T1c is not visibly enhanced in the range of T1c's inward going Alfvén wing. If Slow Mode waves were present, we would see a somewhat altered pressure.

Howes and Nielson (2013) derived a cascade of mutually interacting Alfvén wave pairs that travel parallel to their parent waves. If we translate this situation to planetary Alfvén wings, the inward going waves will again interact with the strong Alfvén wing of T1b. The process will probably continue until the wave energy transferred to outward going Alfvén waves. Such a situation would explain the gradual decrease of the wave amplitudes towards T1c and the increase of the wave amplitudes downstream of T1c. However, we show the azimuthal magnetic field disturbance δB_φ in Figure 6.5a. There, we see a decrease in amplitude from both planets towards the middle and downstream of T1c. A similar effect appears in the Poynting flux, presented in Figure 6.5b. Between both planets, there is no apparent loss of energy flux, which may be due to the chosen colour scale. Directly at T1c, however, there is a decrease in the magnetic field disturbance and the Poynting flux. Either it is related to one of the interaction mechanisms mentioned above, or the Alfvén waves interact with the neutral gas, which then dissipates the wave energy.

One should perform more detailed analyses about the details of the wing-wing in-

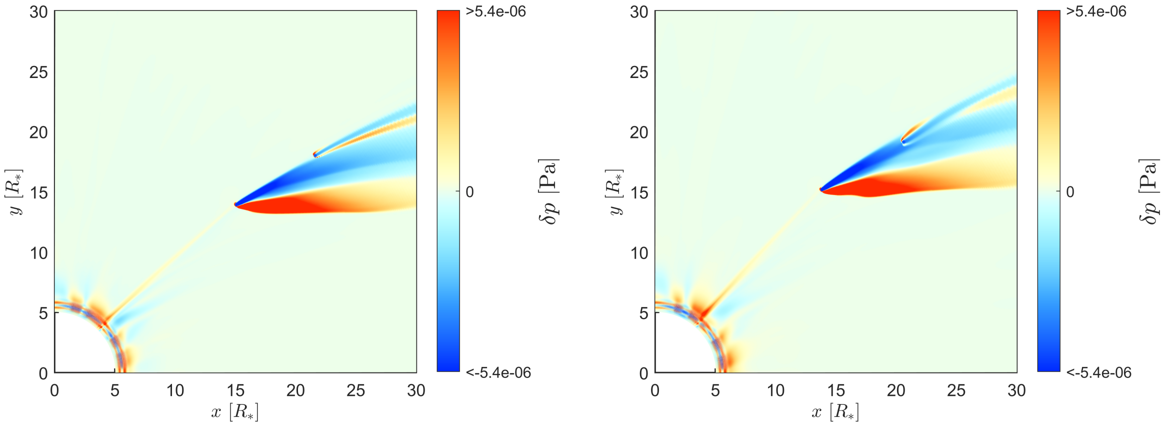

(a) $t = 2.6$ hours (b) $t = 3.1$ hours

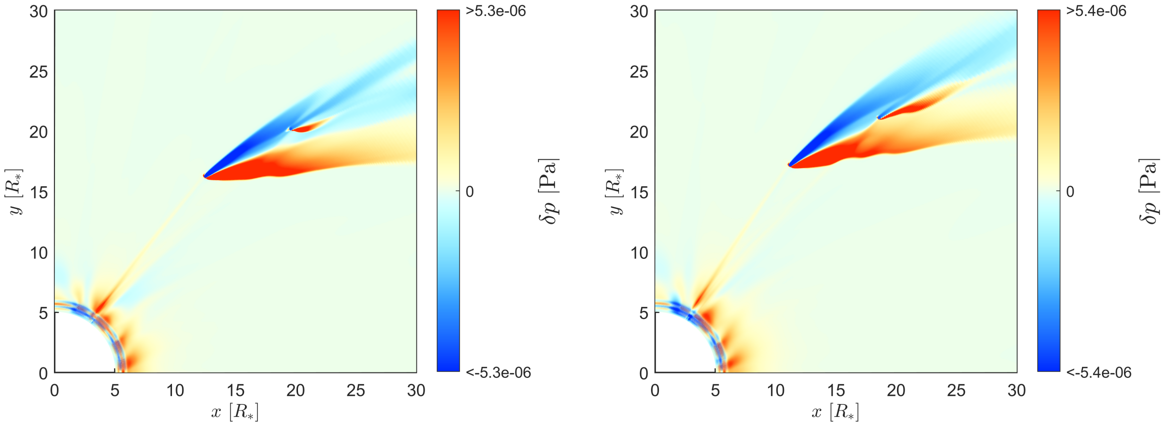

(c) $t = 3.6$ hours (d) $t = 4.0$ hours

Figure 6.6: This figure shows the evolution of the pressure disturbance as the planets T1b and T1c interact with each other. The presented time range lies between 2.6 hours and 4.0 hours

teraction. In the scope of this thesis, it was not possible to perform these analyses, which is why we have to rely on hypotheses here.

6.3.3 Compressional Waves Over Time

The section before was dedicated to the planetary Alfvén wings, due to their importance for observations of SPI. However, we give the more general picture again and involve the compressional MHD waves. We already saw in the discussion of Figure 6.4 that the Slow Structures coming from T1b affect the inward going Alfvén wing of T1c.

In Figure 6.6, we show the pressure disturbance δp for all four discussed time steps from $t = 2.6$ hours to 4.0 hours. In Figure 6.6a, we see the situation at 2.6 hours, when T1c resides in the outward going Alfvén wing of T1b. The Slow Structures of T1c have evolved, compared to the situation from $t = 0.8$ hours (Figure 6.2d). Now we see, that T1c produces wave structures that are not even similarly as bulky as the ones from T1b. The situation changes when T1c enters the vicinity of T1b's outward going Slow Mode. We see there, that T1c's Slow Structures reconfigure, due to the changes environment and possibly due to some sort of magnetosonic wave-wave interaction. In general, the Slow Structures develop much broader than in the unperturbed stellar wind.

One aspect that results from the interaction between T1b's Slow Shock and the inward going Alfvén wing of T1c is that the shock front bends and forms two wave-like curves (Figure 6.6d). We assume that those perturbations of the shock front come from the velocity disturbances of the Alfvén wing. The shock's front line then follows this new shape of the characteristics as the Alfvén waves perturb the stellar wind velocity.

6.4 Implications for Time-Variability in SPI

In section 3.4.5 (and therefore in *Fischer and Saur* (2019) as well), we presented wing-wing interaction as a hypothetical source of temporal variability. The expected period was assumed to be the synodic period between both planets. Our simulations generally support these hypotheses, but we did not find the expected peak in the generated power of the SPI (see Figure 3.1h).

Both planets together may produce a summed total power that is about 110% of the power generated by T1b (in our particular case here). Now, in the case of wing-wing interaction, the inward going Alfvén wing of T1c enters the outward going Alfvén wing of T1b, and the wave energy dissipates. Afterwards, the Alfvén wing of T1c has to evolve again, which would restore the total power that arrives at the star.

The temporal variability that arises from wing-wing interaction, therefore, appears as a drop in the total power. This drop will last at least the amount of the travel time that the Alfvén waves need to propagate from the outer planet to the star plus the time that the planet resides in the other planet's Alfvén wing.

7 The Effect of a Coronal Mass Ejection on SPI

Planets may cause a star to erupt flares. However, probably more common is the case that a flare erupts without the influence of a planet and a Coronal Mass Ejection (CME) might accompany the flare. In such a case, the ejected material could hit a planet in orbit around the star.

The interaction between CMEs and planets that experience super-Alfvénic conditions was studied before, the Earth is an example (*Gombosi et al.*, 2000). To our knowledge, there are no studies that investigated the impact of a CME on sub-Alfvénic SPI.

Such an interaction type causes its own types of variabilities in the star-planet interaction. In contrast to the mechanisms presented in section 3.4 and discussed in chapters 6 and 8, the variabilities caused by the influence of CMEs are typically non-periodic.

In this chapter, we will, therefore, model this exceptional type of interaction between CME and planet. The first step is a change to the MHD model to simulate coronal mass ejections. Afterwards, we will describe how the CME affects the stellar wind. Finally, we analyse the resulting wave pattern that results from the interaction between the planet and the CME.

7.1 Modelling CME and Planet

There are two possible ways to simulate a coronal mass ejection: self-consistently from magnetic anomalies on the star, or simplified, as a scripted event, that alters specific plasma parameters. We decided for the latter option because the self-consistent modelling of a CME requires substantial development time and is a project on its own.

We apply the same MHD model setup that we described and applied in chapter 5, with the exception that we now introduce a time-variable inner boundary at R_{inner} time-variable to emit a CME-like event. The event here represents the narrow CME, described in *Chen* (2011). Physically, the CME in our model is a localised event that erupts with

$$\rho_{\mathrm{CME}} = 10\,\rho_{\mathrm{inner}} \tag{7.1}$$

$$v_{\mathrm{r,CME}} = 2\,v_{\mathrm{r,inner}}, \tag{7.2}$$

which are heuristically chosen parameters. The variables with the subscript *inner* represent the state that is given by the boundary values. This smooth background state will be referred to as the ”quiet” state, in analogy to the nomenclature of stars that are called quiet, when they show no or small signs of activity, like CME

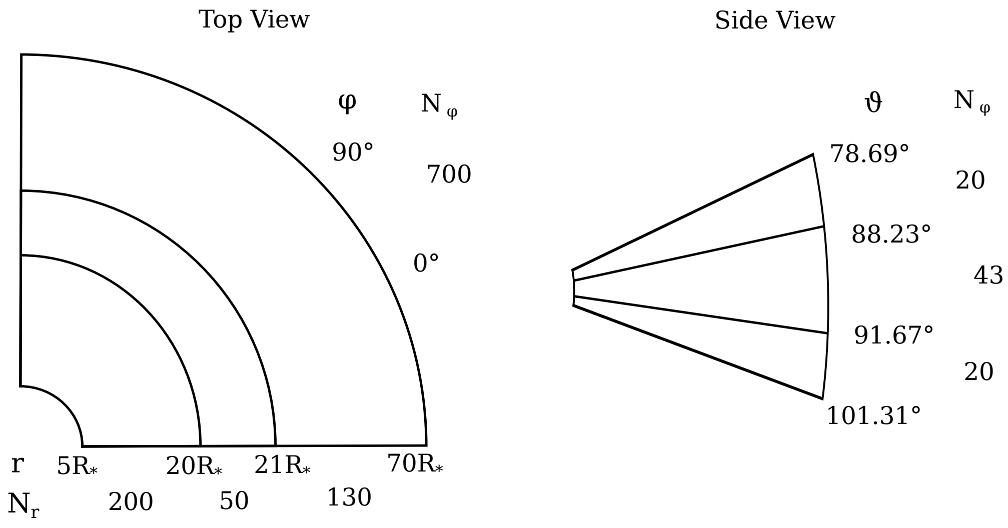

Figure 7.1: Grid of the 'CME' scenario.

events. The pressure p_{CME} results from the density, just like the quiet boundary values.

Our intended CME is located in the equator region of the star, in the range between $\varphi = 43°$ - 45.8°, and $\vartheta = 88.8°$ - 91.1°. A CME is further not a continuous structure but only has a certain duration. We chose a time-window that is slightly longer than one hour. In that time the additional material releases from the inner boundary.

7.1.0.1 Grid

The grid for the 'CME' scenario (figure 7.1) assumes the standard measures given in Table 5.1. For the r-direction the grid ranges from $5 - 20\,R_*$ with 200 uniform cells, from $20-21\,R_*$ with 50 uniform cells and from $21-70\,R_*$ with 130 stretched cells. For the ϑ-direction the grid ranges from $0.43\pi - 1.54$ with 20 stretched grid cells, from $1.54 - 1.6$ with 43 uniform grid cells and from $1.6 - 0.56\pi$ with 20 stretched grid cells. Finally for the φ-direction we have 700 grid cells for the range between 0 and 0.5π.

7.1.1 How to Align Planet and CME

As our CME appears to be a very localised event, we have to consider certain physical circumstances. The planet should interact with the CME but should also have developed wave structures. We assume here that a major part of the ejected plasma moves radially outward and therefore keeps the position around the assigned area on the boundary zone.

Based on the planet's velocity and the known wave travel time (sections 5.4 and 5.5), we can determine the planetary constraints on our simulation quite well. The constraint from the CME is that it reached the orbital distance of the planet by the time the planet is there.

Therefore, we let the planet start at $\varphi_{\mathrm{start}} = 11.5°$. This position gives the wave

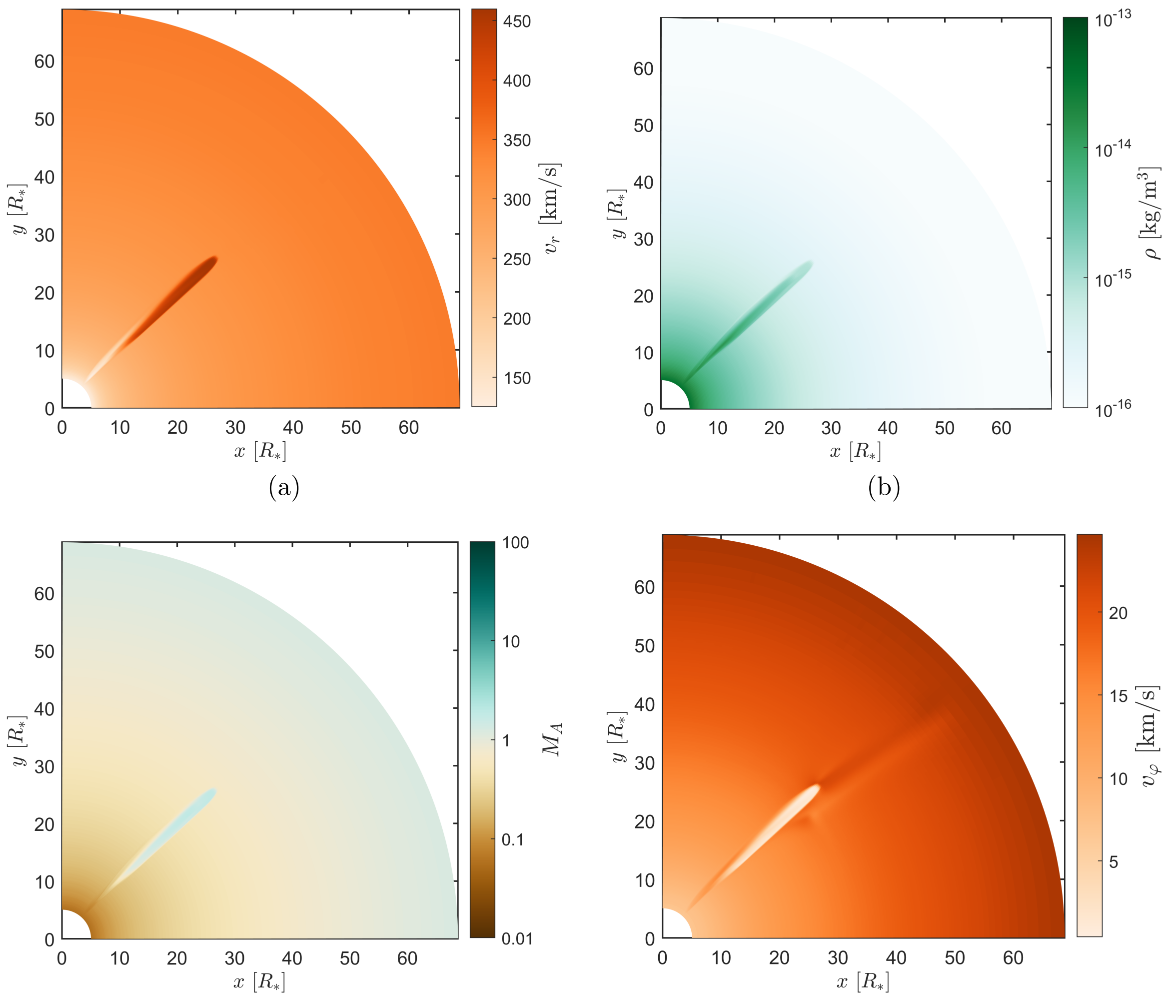

(a) (b)

(c) (d)

Figure 7.2: Structure of the stellar wind with the simulated CME after 1.8 hours. Displayed are radial velocity v_r, azimuthal velocity v_φ, density ρ, and Alfvén Mach number M_A.

structures about 3 hours to evolve, until the planet arrives at $\varphi_\mathrm{CME} = 44°$. To ensure that the planet moves into the CME main structure, we let the CME erupt between $t = 1.6$ hours and $t = 3.1$ hours.

7.2 The Stellar Wind with a CME

In this section, we will show, how the CME affects the quiet steady state stellar wind. The quiet stellar wind solution is the same as described in section 5.2. Figure 7.2 shows a top-view of the the equatorial plane. Presented are the radial stellar wind velocity v_r (Figure 7.2a), azimuthal velocity v_φ (figure 7.2d), density ρ (Figure 7.2b), and Alfvén Mach number M_A (Figure 7.2c).

The CME starts at $t = 0.36$ hours and ends at $t = 1.26$ hours. Hence, the CME lasts about 50 minutes. The current time of the results in Figure 7.2 is 1.8 hours, and the CME stopped to erupt about half an hour before. Now it propagates away from the star. After this time, the front of the CME main structure extends to

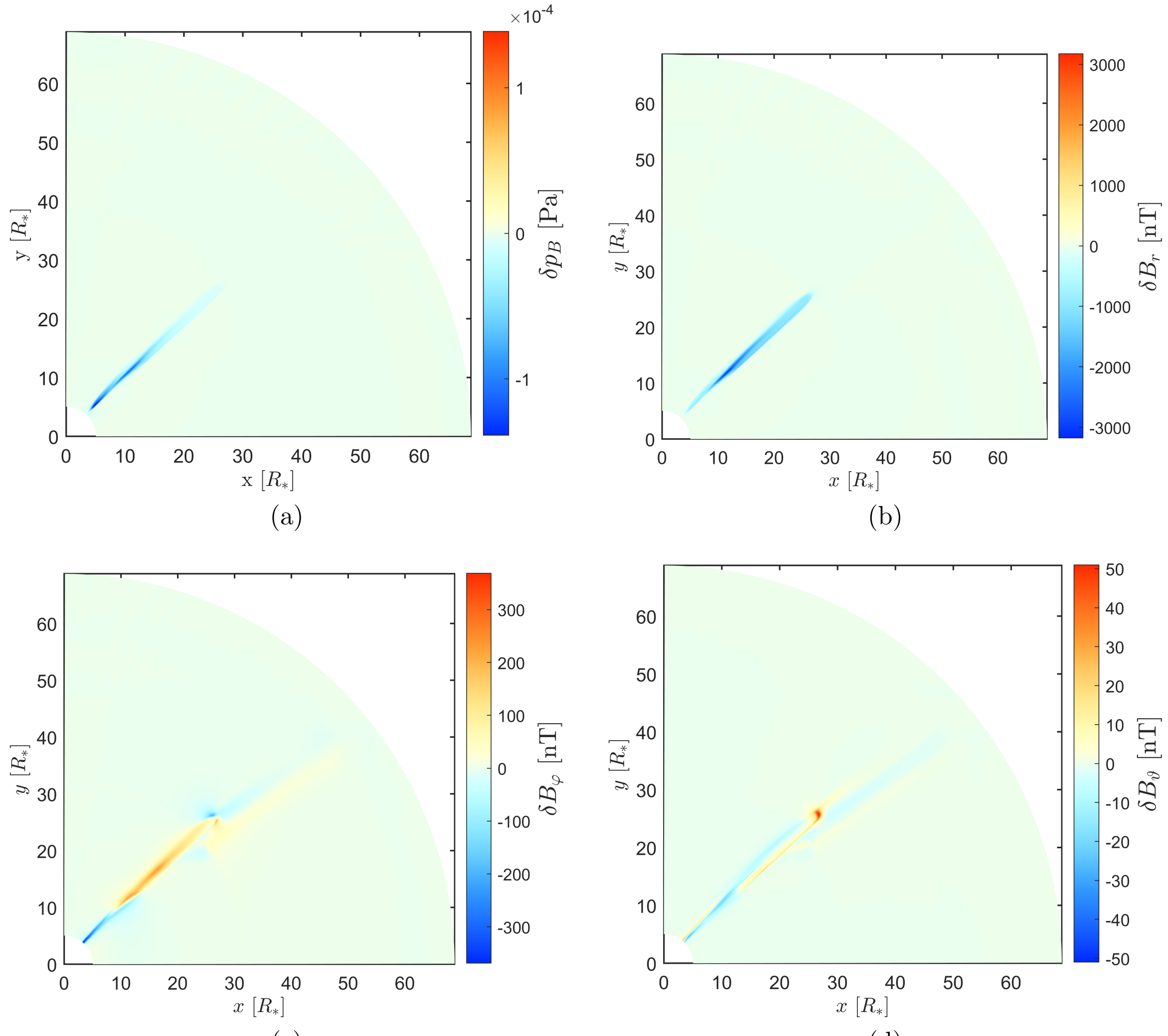

(a) (b)

(c) (d)

Figure 7.3: Disturbances in the magnetic field components and magnetic pressure caused by the CME.

about $35\,R_*$. The CME has the elongated structure that *Chen* (2011) compares to a jet.

The peak in the radial velocity of the ejected plasma lies at $450\,\mathrm{km\,s^{-1}}$ (Figure 7.2a), which is about 1.5 times faster than the fastest steady-state wind velocity in our simulations. The CME started with a velocity of $260\,\mathrm{km\,s^{-1}}$ at the inner boundary. From there, the plasma accelerates rapidly and flows strictly radially outward. The high-velocity plasma carries the material with a density that is enhanced by a factor of ten (Figure 7.2b) compared to the quiet wind. The density remains high, compared to the environment but towards the front, the density decreases. In the wake of the CME, the velocity reduces to about $130\,\mathrm{km\,s^{-1}}$. Therefore the density can remain on a higher level, compared to the environment, because the mass flux is smaller than in the CME.

The Alfvén Mach number M_A is an essential factor for SPI. We saw in section 5.2 that the Alfvén radius, i.e. the extent of the region that allows SPI, lies at $60\,R_*$. The same holds for our quiet background wind. Due to the large density, the local Alfvén wave speed decreases in the CME and together with the increased radial velocity, the Mach number increases. The CME, therefore, has a Mach number clearly above one. Hence, it generates a localised super-Alfvénic zone. Due to the decreased radial velocity in the CME-wake, the Alfvén Mach number is smaller than one again.

In the azimuthal velocity, the CME main structure is visible as a region with zero velocity. That explains the strictly radial motion of the CME. Additionally, we see disturbances far ahead of the CME. These disturbances are excited by the CME that disturbs the curved magnetic field and excites Alfvén waves. Those waves then travel with an effective wave speed of $v_r + v_\mathrm{A}$ in the inertial frame and are therefore much faster than the CME.

The magnetic field plays a crucial role in star-planet interaction. Therefore, we will describe the related effects of the CME on the magnetic field with Figure 7.3. The figures show the disturbances in the magnetic pressure p_B (Figure 7.3a), and the three magnetic field components from Figures 7.3b and 7.3d.

The magnetic field reacts in three ways onto the presence of the CME. Figure 7.3a shows that the magnetic pressure decreases down to $1.3 \cdot 10^{-4}$ Pa. This decrease corresponds to the increase in the thermal pressure. The same behaviour of the magnetic field occurs in the presence of Slow Mode waves, where the magnetic pressure balances disturbances of the thermal pressure (see section 5.5.3). Mainly responsible for the decrease of p_B is the B_r component. The largest disturbance in B_r goes down to -3000 nT and lies at the back end of the CME. Towards the front, there is a gradient in p_B and B_r. The gradient resembles the spatial structure of the density and therefore, the pressure (Figure 7.2b). The decrease of p_B in the wake of the CME probably links to the combined effect of B_r and B_φ.

The second effect that the CME exerts on the magnetic field is visible in the B_φ component (Figure 7.3c). In the range of the main CME structure, B_φ is enhanced by about 100 nT. We explain this anomaly such, that, due to the strictly radial outflow of the CME, the magnetic field locally straightens into the radial direction. Hence, the positive disturbance of B_φ.

The third effect comprises the aforementioned Alfvén waves that are generated by the CME. The related magnetic disturbances are well visible at the front of the CME. The B_ϑ component is enhanced by 50 nT and the B_φ component shows the split structure, that we know from the B_ϑ component of planetary Alfvén wings (see section 5.4 for details). We have encountered Alfvén waves in the form of Alfvén wings that were generated by a planet that moves almost perpendicular to the magnetic field. In this case here, the assumed generator is the CME that moves parallel to the stellar wind and only assumes a small angle to the magnetic field. While the CME propagates outward, it generates new waves. Therefore there might appear a pile-up of outgoing waves and waves that were just generated.

7.3 Time-Variable Wave Pattern

In section 5.4 and 5.5, we analysed the structure of the SPI-related waves in a steady-state wind environment. In this section, we will analyse the evolution of the inward Alfvén wing between the planet's ingress into the CME and its egress.

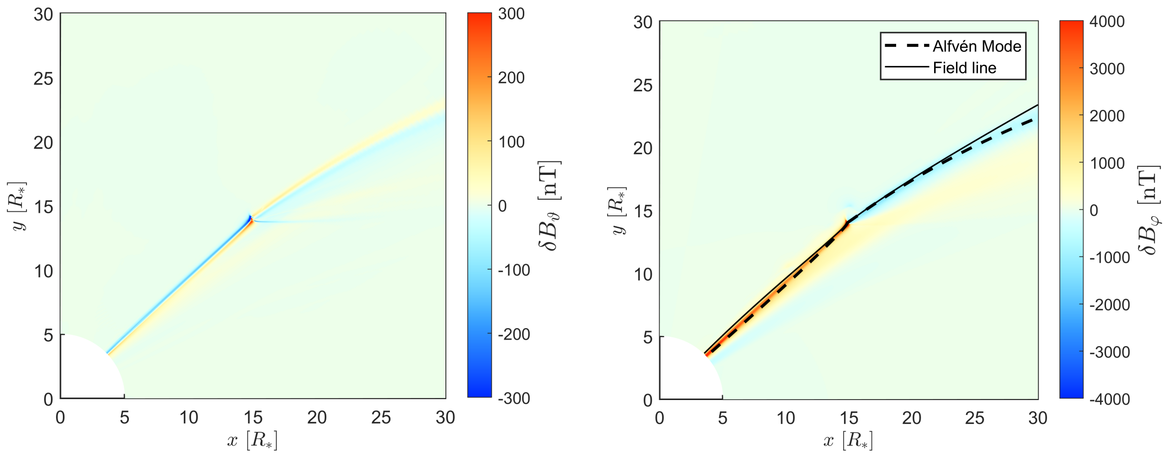

(a) $t = 2.5$ hours (b) $t = 2.5$ hours

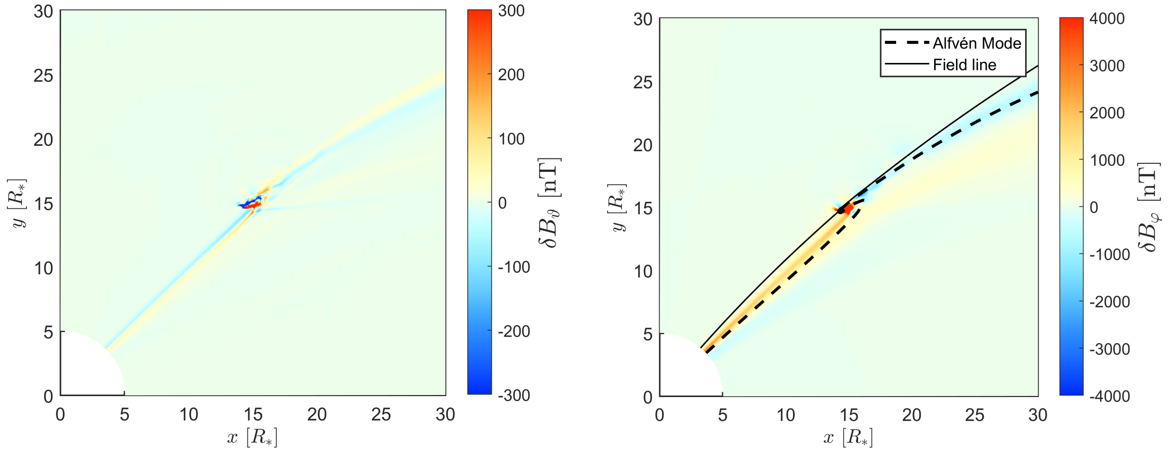

(c) $t = 2.8$ hours (d) $t = 2.8$ hours

Figure 7.4: The interaction of the Alfvén wings with the CME, while entering the CME. Presented by the B_ϑ and B_φ components, for times of $t = 2.5$ hours, and 2.8 hours. The plots of B_φ show the field line that connects to the planet and the Alfvén characteristics.

7.3.1 The Alfvén Wing at Ingress

Figure 7.4 shows the disturbances in B_ϑ and B_φ at the time $t = 2.5$ hours (Figures 7.4a and 7.4b) and $t = 2.8$ hours (Figures 7.4c and 7.4d). On top of δB_φ, we plot the magnetic field line that connects to the planet (solid line) and the Alfvén characteristics (dashed lines). The characteristics directly show the effect of the CME on the inward Alfvén wing.

At 2.5 hours, the planet starts to enter the CME. It is visible in a small asymmetry of δB_ϑ close to the planet and an increased angle between Alfvén wing and field line Θ_A. In this case, the super-Alfvénic conditions cause the Alfvén wing to bend back. At the same time, the interaction strength increases due to the increased velocity that hits the planet.

At 2.8 hours, the planet has fully entered the CME and is subject to super-Alfvénic conditions. The amplitudes of δB_ϑ and δB_φ increase by factors of about 10 compared to the results of 2.5 hours (we capped the colour scale to ± 300 nT for δB_ϑ and ± 4000 nT for δB_φ). The resulting amplitudes are larger than the

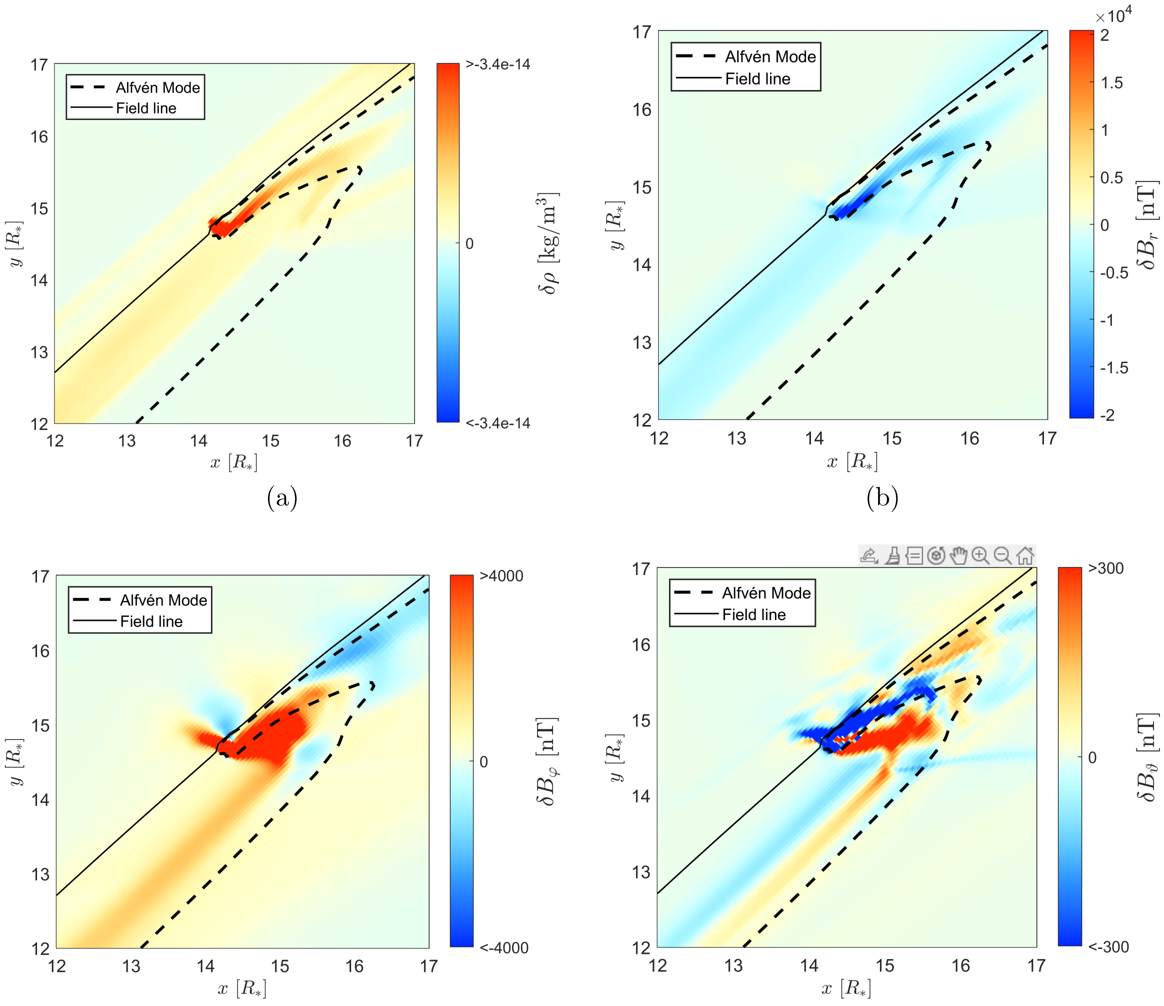

(a)

(b)

(c)

(d)

Figure 7.5: Close-ups of the planet during the interaction with the CME at $t = 2.8$ hours.

amplitudes of the CME itself (see section 7.2). So possible interferences are not visible.

Theoretically, we expect the formation of a Bow Shock around the planet, because the Alfvén Mach number is larger than one. However, before the shock reaches its steady state, the waves reach the flanks of the CME and enter sub-Alfvénic conditions again. From there, the Alfvén waves form an Alfvén wing and move towards the star.

Figure 7.5 shows the situation in a close area around the planet at $t = 2.8$ hours. The figure presents the density disturbance $\delta\rho$ and the disturbances of the magnetic field components.

The planet resides just in the middle of the CME, as one can see in the increased density in Figure 7.5a. The increased density and velocity of the CME cause a strong super-Alfvénic interaction. Hence, the resulting density-disturbing waves drape around the planet and move radially outward. The motion of the planet causes waves and plasma to move around the planet's backside. These waves eventually reach the boundary of the CME and connect to their sub-Alfvénic counterparts that were generated when the planet resided in the quiet stellar wind. Those earlier generated waves did not propagate as far as the CME-waves, due to the slower effective velocity. The same structures are visible in δB_r (Figure 7.5b), which are related to the disturbances of the Slow Shock.

The path of the inward going Alfvén wing deviates from the calculated path, as visible in all presented variables. This deviation might come from the choice of the starting point from where we calculated the characteristics. However, simulation and calculated characteristics show the same general behaviour, as the Alfvén waves abruptly change their direction and propagate towards the star as soon as they leave the CME. The turning point of the calculated characteristics lies at $x = 16\,R_*$ and $x = 15.5\,R_*$, about $2\,R_*$ away from the planet. The simulated waves reach the turning point about $1\,R_*$ away from the planet, at $x = 15\,R_*$ and $x = 14.5\,R_*$.

As visible in Figures 7.5c and 7.5d, the Alfvén wave accumulates in a triangular structure with amplitudes far above 4000 nT for δB_φ and ±300 nT for δB_ϑ. The δB_ϑ component looks like a turbulent structure. The pattern might be a result of mutually interfering waves, due to sudden changes in the plasma conditions.

7.3.2 The Alfvén Wing at Egress

In this section, we will describe how the interaction changes when the planet leaves the direct influence of the CME. Figure 7.6 shows the situation of the inward going Alfvén wing at $t = 3.1$ hours and $t = 3.3$ hours, i.e. after egress of the planet from the CME. From $t = 3.1$ hours on, the Alfvén wing proceeds to go into its normal undisturbed state.

In Figures 7.6a and 7.6b, we see strong magnetic disturbances coming from the planet. The magnetic field line that connects to the planet bends in the φ-direction. In the same range, there are strong magnetic disturbances. Parts of those wave disturbances move outward again after they initially travelled towards the star. Those outward moving waves are either reflections at the higher density of the CME or parts of the Afvén wing become subject to super-Alfvénic conditions and therefore turn around.

At time $t = 3.3$ hours (Figures 7.6c and 7.6d), the planet moved further away from the CME. The bent in the magnetic field line elongates to about $r = 10\,R_*$. The strongest magnetic disturbance followed the bent in the field line and propagated towards the star. The region, where the field line bends, i.e. where the disturbances are the largest, is still a source of disturbances that travel radially outward within the CME.

Figure 7.7 shows the between 10 and $17\,R_*$ at $t = 3.1$ hours. We will use the presented variables, to identify the process that generates the outward going waves we saw in Figure 7.6. In Figures 7.7a and 7.7b, we see δB_φ and δB_ϑ respectively. The source region of the wave structure that moves outward within the CME is exactly the head of the Alfvén wave that moves towards the star, i.e. where the bend of the field line lies. Hypothetically, we may have reflections, because the CME poses a strong density gradient, and the wave is about to move into this gradient. Otherwise, it may be the same effect that we saw at the ingress of the planet into the CME, where waves experience super-Alfvénic conditions and move outward.

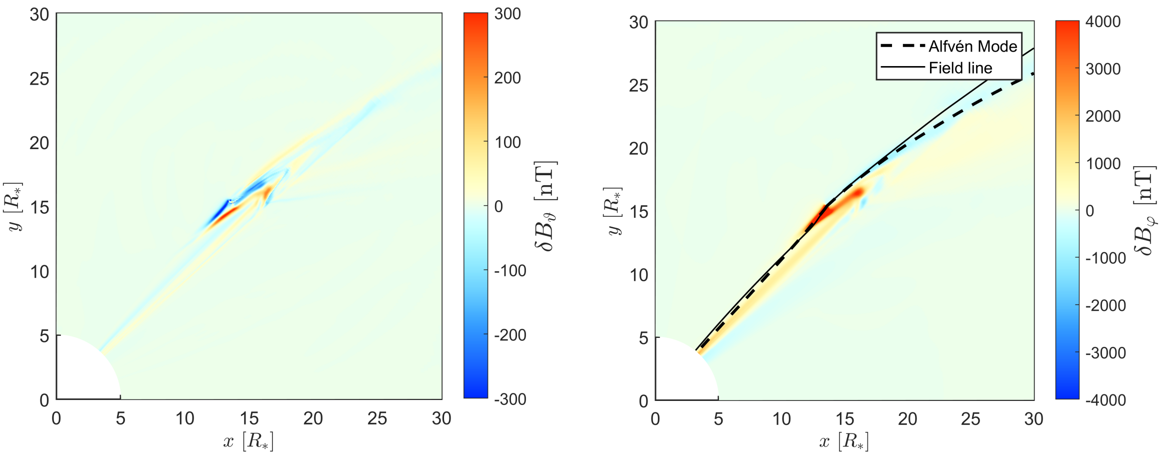

(a) $t = 3.1$ hours

(b) $t = 3.1$ hours

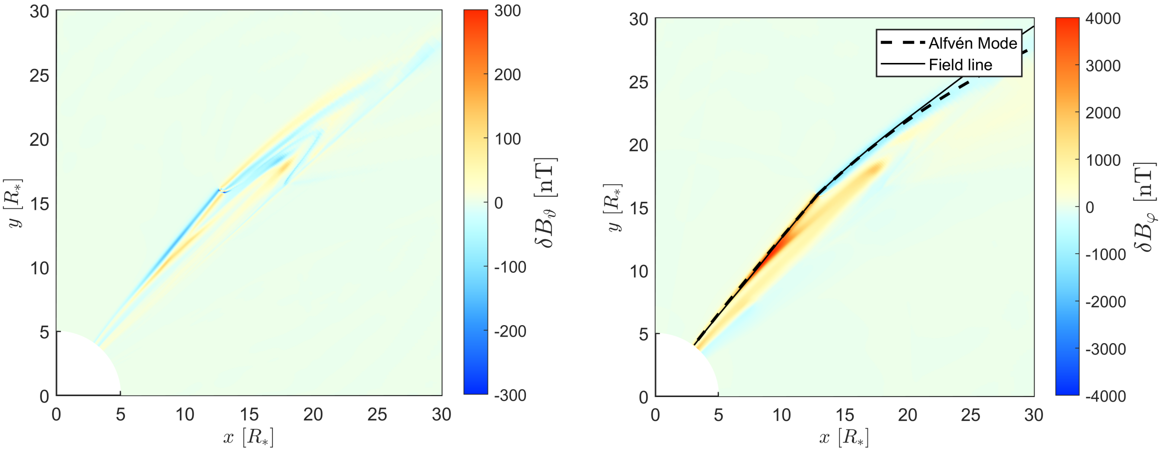

(c) $t = 3.3$ hours

(d) $t = 3.3$ hours

Figure 7.6: The interaction of the Alfvén wings with the CME, while leaving the CME. Presented by the B_ϑ and B_φ components, for times of 3.1 hours, and 3.3 hours. The plots of B_φ show the field line that connects to the planet and the Alfvén characteristics.

Reflections occur at regions with a density gradient (*Wright*, 1987; *Jacobsen et al.*, 2007), respectively a gradient in the Alfvén speed. We saw in section 7.2 that the CME carries an enhanced density and, due to the increased pressure a reduced magnetic field strength. Therefore, we have a change in density and Alfvén speed in the azimuthal direction. According to *Wright* (1987) and *Jacobsen et al.* (2007), the Alfvénic magnetic field disturbance changes its sign at negative changes of the plasma density and remains unchanged in case of positive gradients. The velocity disturbance shows the opposite behaviour. If we compare δB_φ (Figure 7.7a) with δv_φ (Figure 7.7c), we see that neither of the two disturbances changes its sign. We conclude that reflections are probably not the cause for the outgoing waves.

The Alfvén Mach number increases to values above one within the CME (Figure 7.7d). The planet generates an Alfvén wing with a radius greater than the planetary radius, due to the extended atmosphere. Therefore, the trailing side of the Alfvén wing may be subject to super-Alfvénic conditions, when the Alfvén wing follows the locally curved field line towards the CME. As one can see in Figures 7.7a and 7.7c, the wave amplitude that is forced to go outward, is about a

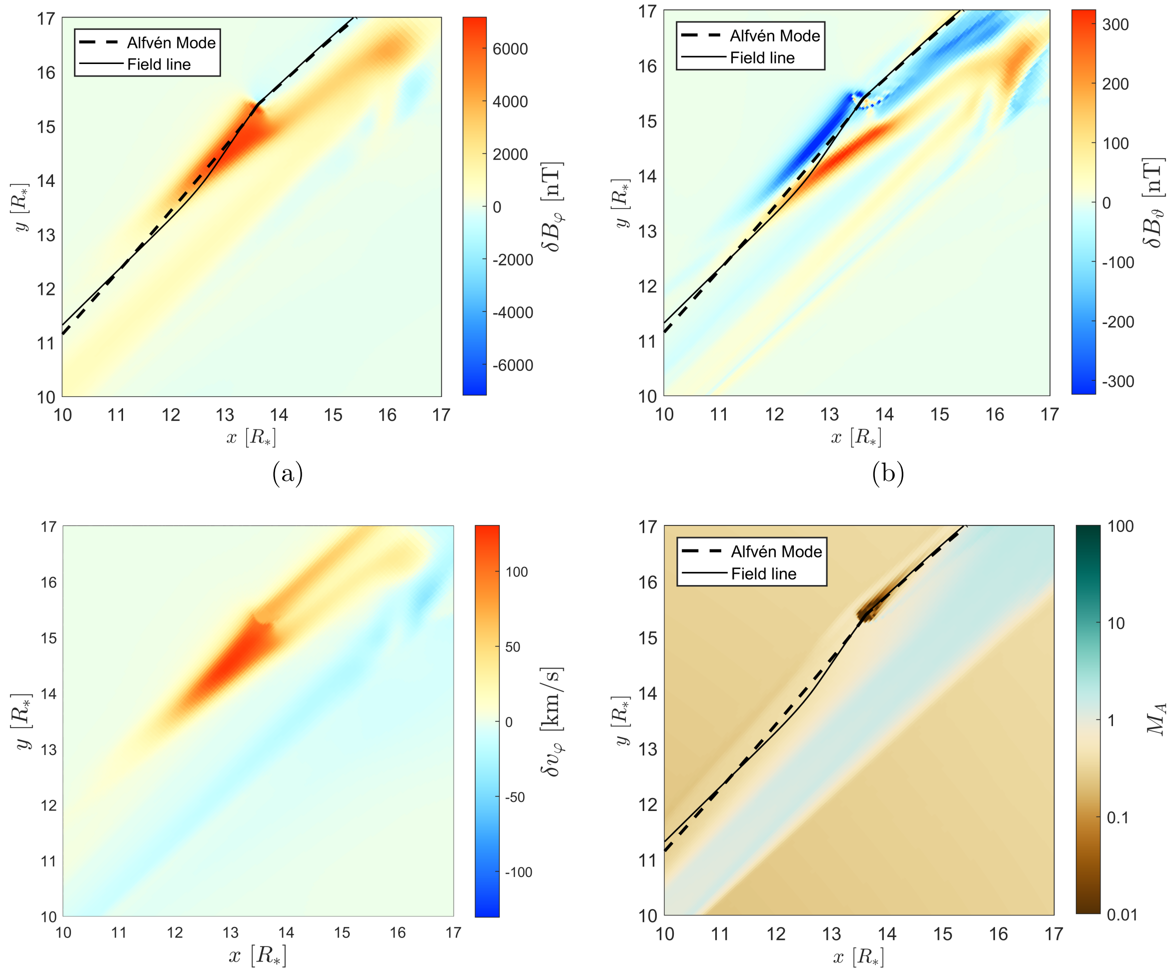

(a)

(b)

(c)

(d)

Figure 7.7: Close-ups of the planet during the interaction with the CME at $t = 3.1$ hours.

factor of two smaller than the one that propagates towards the star, which indicates that it may originate from the flanks of the Alfvén wing.

8 Flare Triggering at TRAPPIST-1

In section 3.4, we discussed the possible occurrence of flares that are periodically triggered by SPI. Chapter 4 and 5 showed that SPI is possible in the TRAPPIST-1-system. Therefore flare triggering may be possible. Here, we conduct statistical analyses of flares observed at TRAPPIST-1 and look for signals which may originate from planetary influence.

In this chapter, we present and test these results. Before we analyse TRAPPIST-1's flares, we discuss the possibility that SPI may generate observable aurora-like features on the star. Then we introduce the flare light curve from TRAPPIST-1 and describe the applied statistical methods. Afterwards, we discuss the results of the analysis and their statistical significance. Finally, we look at the possibly extended visibility of flares.

Parts of this chapter have been published before in *Fischer and Saur* (2019). This includes mainly sections 8.1, 8.2, 8.3.1, 8.3.2, 8.4.1 and 8.5. Editorial changes have been applied to fit the texts into the context of this thesis. The remaining texts present methods and results that are new and have not been published yet.

8.1 Observability of SPI

TRAPPIST-1 has a bolometric luminosity of approximately $2 \cdot 10^{25}$ W (*Van Grootel et al.*, 2018), which corresponds to an energy flux density of $2.4 \cdot 10^{8}$ $\mathrm{W\,m^{-2}}$ on its surface. Assuming that T1b possesses an intrinsic magnetic field with 30 000 nT, its Alfvén wing carries an energy flux of $1.3 \cdot 10^{15}$ W in the best-guess assumption (section 4.1). Using $\nabla \cdot \boldsymbol{B} = 0$, we can estimate the approximate size of the Alfvén wing's footprint and find an energy flux density of 10^{4} $\mathrm{W\,m^{-2}}$ at the surface of the star. This flux density is about 10^{-4} of the stellar background. Temporal variability due to the plain visibility of the Alfvén wing's footpoint or through a tilted stellar dipole field is thus expected to be hardly observable in broadband photometric lightcurves.

In this study, we take the Poynting flux as the upper limit for the incoming power at the star and also the expected emissions. Alfvén waves in smooth magnetic fields are, even in the non-linear case, neither dispersive nor dissipative (*Neubauer*, 1980). Details of the propagation properties, however, depend on the mostly unknown properties of the stellar winds.

Observations at X-ray wavelengths conducted by *Wheatley et al.* (2017) revealed an X-ray luminosity of $L_{\mathrm{X}}/L_{\mathrm{bol}} = (2 - 4) \cdot 10^{-4}$. Observations with the Hubble Space Telescope by *Bourrier et al.* (2017) showed that TRAPPIST-1's Lyman-α emissions are about three times weaker than its X-ray luminosity. TRAPPIST-1's chromosphere is only moderately active compared to its corona and transition region, according to *Bourrier et al.* (2017). The corresponding flux density in X-ray and Lyα is therefore of the same order of magnitude as our estimate for T1b's energy flux density. This example shows that the detectability of SPI enhances strongly if the associated emissions are concentrated in certain wavelength bands only. However, both of these observations are, at 7.8 hours in the X-ray (*Wheatley et al.*, 2017) and four HST orbits (*Bourrier et al.*, 2017), too short to identify temporally variable planetary signals.

8.2 Flares at TRAPPIST-1

Luger et al. (2017) published TRAPPIST-1's K2-lightcurve, that is corrected for systematic errors and has low-frequency trends removed. The respective Figure 2(b) from *Luger et al.* (2017) is reprinted in figure 8.1a. The stellar variability is well visible, and flares appear as sudden increases in luminosity and sometimes as single spikes (*Luger et al.*, 2017). For our analysis, we read out the times and relative fluxes of flare events by eye (shown as red spikes in Figure 8.1b). Our sample of 41 flares coincides mostly with the sample from *Vida et al.* (2017), who identified 42 flares by eye as well. *Vida et al.* (2017) estimated typical integrated flare energies of $10^{23} - 10^{26}$ J. However only one flare reached a total energy of 10^{26} J in this light curve. The bulk of the flares has much lower energies of 10^{23} to 10^{24} J. Thus the observed flares fit well into the theoretical flare energy expectations from *Lanza* (2018). According to this theory, we calculate a range of maximum flare energies of $3 \cdot 10^{24}$ J to $2 \cdot 10^{27}$ J for TRAPPIST-1.

8.3 Analysis of the Flare Time-Series

We analyse the flares of TRAPPIST-1 in light of our findings towards temporal variability from section 3.4.4. In this section, we will describe the respective methods. First, we describe how we treat the flares in the numerical and analytic analysis. We follow with an outline of the applied Fourier transformation and autocorrelation. Additionally, we describe the statistical tests, that we apply, to determine the significance of the obtained results and if the results can be explained by flare triggering from SPI.

8.3.1 Giving Flares a Duration

To find possibly existing periods among the flare events, we perform a statistical analysis of the flare light curve. We describe the flares in two different ways. One suits an analytic treatment and assumes the flares to be Dirac-delta peaks. The other gives the flares a temporal extent and suits a numerical analysis.

For the analytic treatment, we approximate the flares as Delta-peaks via

$$f(t) = \sum_{\mathrm{n}=1}^{N} A_{\mathrm{n}}\, \delta(t - t_{\mathrm{n}}) \tag{8.1}$$

with N the total number of flares, t_{n} the time when each flare occurs and A_{n} its amplitude. In this representation, the flare has a vanishingly small duration.

The alternative representation flares via a finite duration is given through the empirical flare template by *Davenport et al.* (2014), i.e. by their equations (1) and (4). *Vida et al.* (2017) and *Vida and Roettenbacher* (2018), for example, apply this shape for their analysis of TRAPPIST-1's flares. This flare template describes the shape of a flare with a sharp rise phase and a decay phase after the main event in terms of the full time width at half maximum $t_{1/2}$. For our analysis of the flares we apply two different $t_{1/2}$ (Figure 8.1b), one narrow representation with $t_{1/2} = 0.1$ d (blue) and one broad representation with $t_{1/2} = 0.3$ d (cyan).

8.3.2 Fourier Analysis and Autocorrelation

In this section, we present the Fourier series representation of a delta-flare light curve. We assume the N flares to be delta-peaks with amplitude A_n represented by the function

$$f(t) = \sum_{\mathrm{n}=1}^{N} A_\mathrm{n}\, \delta(t - t_\mathrm{n}). \tag{8.2}$$

The function $f(t)$ can be represented by a Fourier series $f(t) = \sum_{\mathrm{k}=-\infty}^{\infty} \alpha_\mathrm{k} \exp\left(i\omega_\mathrm{k} t\right)$ with the Fourier coefficients α_k and $\omega_\mathrm{k} = 2\pi k/T$ with the period T, which is assumed to be the length of the time-series t_max here. The Fourier coefficients are given by

$$\alpha_\mathrm{k} = \frac{1}{t_\mathrm{max}} \sum_{\mathrm{n}=1}^{N} A_\mathrm{n} \exp\left(-i\omega_\mathrm{k} t_\mathrm{n}\right). \tag{8.3}$$

Therefore the light curve can be represented by

$$f(t) = \frac{1}{t_\mathrm{max}} \sum_{\mathrm{k}=-\infty}^{\infty} \sum_{\mathrm{n}=1}^{N} A_\mathrm{n} \exp\left(-i\omega_\mathrm{k}(t - t_\mathrm{n})\right). \tag{8.4}$$

To complete our analytic analysis of the delta-flare light curve, we also calculate the autocorrelation of an arbitrary flare light curve. We again apply equation 8.2 to represent our flare lightcurve via delta-peaks. The autocorrelation function is defined by

$$R(\tau) = \int_{-\infty}^{\infty} f(u+\tau)\, f(u)\, du \tag{8.5}$$

and in our case specifies to

$$R(\tau) = \int_{-\infty}^{\infty} \left[\sum_{\mathrm{i}=1}^{N} A_\mathrm{i}\, \delta(u + \tau - t_\mathrm{i})\right] \left[\sum_{\mathrm{j}=1}^{N} A_\mathrm{j}\, \delta(u - t_\mathrm{j})\right] du. \tag{8.6}$$

After applying the calculation rules of the delta-distribution, we receive

$$R(\tau) = \sum_{\mathrm{i}=1}^{N} \sum_{\mathrm{j}=1}^{N} A_\mathrm{i}\, A_\mathrm{j}\, \delta(\tau - t_\mathrm{i} + t_\mathrm{j}). \tag{8.7}$$

8.3.3 Significance Tests

Fourier transform and autocorrelation provide information about the existence of periodicities. To test, whether the flare triggering model can explain the obtained signals, we conduct statistical significance tests.

Our statistical tests generally consist of a sample of 1000 artificial flare time series with a fixed number of 41 flares each. For every time series, we conduct the same numerical analysis that we apply to the observed time series of TRAPPIST-1. Hence, the flares have an assigned time point and receive a temporal extent according to *Davenport et al.* (2014) (see section 8.3.1) of $t_{1/2} = 0.1$ days and $t_{1/2} = 0.3$ days. For the calculated autocorrelations and Fourier transforms, we determine the average and the standard deviation. So far, we will not include flare amplitudes in this analysis.

To determine an estimate of the significance of signals in the TRAPPIST-1 time series, we define a null hypothesis. As a Null hypothesis, we assume principally random flare occurrences on stars. We define the respective flare occurrence times by

$$t_{\mathrm{i}} = p t_{\mathrm{max}} \tag{8.8}$$

with the maximum time of the time series of $t_{\mathrm{max}} = 78$ days and a uniformly distributed random number p between 0 and 1, generated by the random number generator of Matlab.

In addition to the significance test, we perform statistical tests that simulate certain physical models or assumptions and their effects on the flare time series. In these tests, we assume that flares occur with a specific period between a random starting time and t_{max}. The resulting number of flares is smaller than 41, and the difference will be filled with random flares, as described above.

There are two types of possible periodic signals that we can apply. The most important signal are flares that are triggered by a planet, either T1b or T1c. This model assumes that a magnetic anomaly interacts with the planetary Alfvén wing and generates a periodic signal with the respective synodic period $T^{\mathrm{b}}_{\mathrm{syn}}$ or $T^{\mathrm{c}}_{\mathrm{syn}}$. The second model signal includes flares that appear with the stellar rotation period T_{rot}. This model assumes that a flaring anomaly rotates into the visible hemisphere and erupts flares.

Each of the periodic signals receives a certain occurrence probability w_{occ} between 0 and 1. Therefore each flare has a chance of w_{occ} to erupt. A probability of 0 implies that no flares occur with the respective period, while a probability of 1 entails that every possible flare occurs and we have a perfectly periodic signal. Every occurrence probability $w_{\mathrm{occ}} < 1$ will likely result in a quasi-periodic signal because there is a chance that some flares do not occur.

So far, we do not know the exact physical processes that are involved in the triggering of flares. We include three different effects into our analysis, which we call the 'non-idealised effects'.

Likely, the resulting flares will not occur strictly periodic. We included this effect to some extent, by giving the flares an occurrence probability. Additionally, an erupting flare may occur slightly earlier or later, because the assumed anomaly may be larger or because the required state to allow a triggering builds up while the Alfvén wing already interacts with the anomaly. Such hypothetical deviations

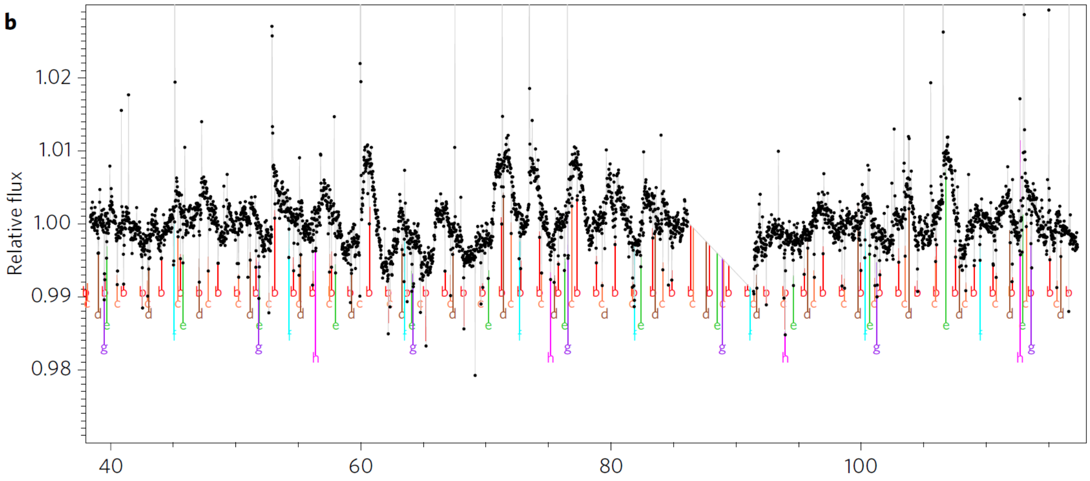

(a) K2-lightcurve of TRAPPIST-1 as originally published by *Luger et al.* (2017).

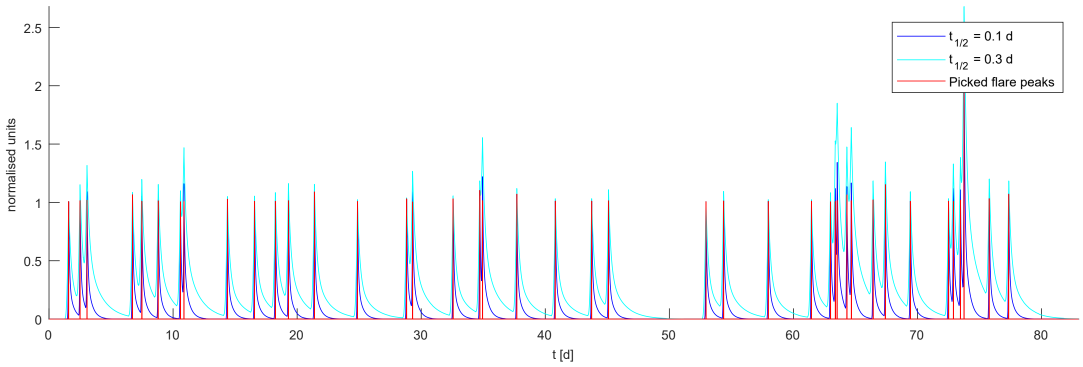

(b) Flare time series with fitted Flares

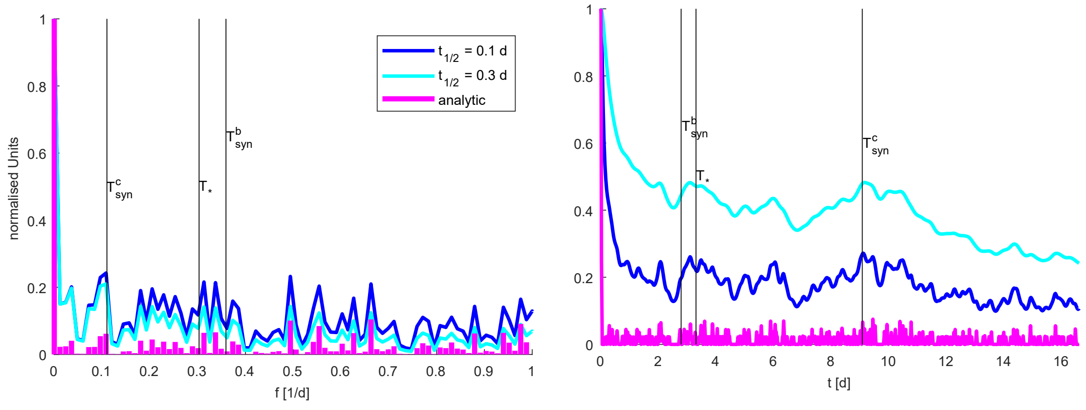

(c) Fourier series

(d) Autocorrelation

Figure 8.1: Original lightcurve reprinted from Figure 2(b) of *Luger et al.* (2017) compared to the fitted Flare time series and analysis re-used from *Fischer and Saur* (2019).

from the period can be included statistically by adding a deviation time of δt. To determine δt, we define a maximum deviation time $\delta t_{\max}$ and let another random number generator that bases on a normal distribution generate numbers with $-\delta t_{\max} < \delta t < \delta t_{\max}$.

A second possible effect assumes that there is a second anomaly that interacts with a planetary Alfvén wing. In that case, there are two separate planetary signals with the respective synodic period. In our model, we can include this effect from two anomalies as well. The signals will then have a defined offset time t_{os} to each other.

The third possibility for non-idealised occurrences of flares is that the assumed magnetic anomaly exists a limited amount of time $< t_{\max}$. The resulting subinterval with $t_{\mathrm{start}} > 0$ and $t_{\mathrm{stop}} < t_{\max}$ has a different length in each artificially generated time-series and therefore exhibits an according number of quasi-periodic flares.

The code allows incorporating a synodic planetary flare signal (especially from T1c) together with the three effects that we call the non-idealised effects. With the described modules, we can test how flare time series with quasi-periodic signals in them may appear statistically. The best-fitting model parameters will approximate the findings from the TRAPPIST-1 light curve.

8.4 Triggered Flares at TRAPPIST-1?

In this section, we will present the results of the analysis, according to sections 8.3.1 and 8.3.2. This part resembles the already published results from *Fischer and Saur* (2019). Additionally, we present the results of the statistical tests.

8.4.1 Fourier Spectra and Autocorrelation

Figure 8.1c shows the respective power spectra of the delta-peak time series in magenta and the empirical representation of the flares in blue and cyan. All power spectra are arbitrarily normalised because we are only interested in identifying specific frequencies. We show the spectral area of interest between $f = 0$ and 1 day^{-1} and highlight the rotation period of TRAPPIST-1 T_* and the expected synodic periods of T1b and T1c. We see a local maximum at the synodic period of T1c. However, this maximum is not significantly larger than other local maxima in this range. There is also a slightly offset maximum at the stellar rotation period but no indication for a signal that connects to T1b.

In Figure 8.1d we see the autocorrelation of the template-fitted flares in blue and cyan, together with the analytic autocorrelation of the delta-peak flare light curve (magenta). To resolve the synodic period of T1c, we computed the autocorrelation for lags of up to $0.2\,t_{\max}$. The analytic autocorrelation shows a clustering of correlation peaks around the synodic period of T1c and the stellar rotation period T_*. For the blue template-fitted flares the correlation is generally about 0.1 with local maxima of above 0.2 at the highlighted periods. A broadening of the flares makes the autocorrelation more tolerable to small variations in a quasi-periodic occurrence of flares and shows a stronger correlation among the flares. Therefore the autocorrelation of the broad fitting curves (cyan) shows hints for a periodicity of around 9 d, which would correspond to a signal that appears with T1c's synodic period. The corresponding correlation lies around 0.5. The interval around the stellar rotation period of 3.3 d and T1b's synodic period of 2.78 d also shows a local maximum of about 0.5 in the cyan curve. However, it is uncertain if this peak indicates a signal, related to T1b or the stellar rotation, although similar to the power spectrum, it shows a tendency towards T_*.

Generally, we would expect a signal from T1b, because its Poynting flux is one order of magnitude larger than the one from T1c and additionally, its synodic period of 2.78 d is much shorter compared to the period of 9.1 d of T1c. However, in case that T1b's Alfvén wing acts as a flare trigger, it requires that a magnetic anomaly lies on its path across the star. Therefore an anomaly on the same latitude as the footpoint of the Alfvén wing from T1c and no anomaly near T1b's footpoint could explain our findings. Star spots could be such magnetic anomalies that erupt flares. *Rackham et al.* (2018) analysed the spot and faculae covering fractions of TRAPPIST-1 based on its rotational variability. The group estimated a spot covering fraction of 8% with small spots and a faculae covering fraction of 54%. On the sun the sunspots only occur at lower latitudes around the equator, which would probably not allow the Alfvén wings to interact with these magnetic anomalies. However, there is evidence that starspots and active regions on M-dwarfs occur on all latitudes (*Barnes and Collier Cameron*, 2001). That makes M-dwarfs like TRAPPIST-1 attractive targets to further look for this trigger mechanism because starspots might occur at higher latitudes as well, where SPI of planets more than several stellar radii away will couple to the star and can trigger flares that should be visible to an observer on Earth.

8.4.2 Null Hypothesis

The null hypothesis is our assumed standard case to test the specific result of TRAPPIST-1. Figure 8.2 principally shows the same results as the ones presented in figures 8.1c and 8.1d. Here, we only left out the analytic analysis, which is difficult to test, and we separated the Fourier transformations of the two different $t_{1/2}$. The colour codes are the same. What we added is the red line, that represents the respective mean or average of the statistical ensemble time-series. Additionally, we plot the standard deviation, i.e. the $1\,\sigma$ level, which allows an estimate of the significance.

For 1000 time-series, the resulting curves are sufficiently smooth and show that the resulting autocorrelation resembles a Poisson-distribution (Figure 8.2a). The flares were assumed to appear randomly and independent from each other, which are necessary conditions for Poisson-distributed events. The results of autocorrelation and Fourier analysis stay mostly within the $1\,\sigma$ level. This result indicates that the majority of TRAPPIST-1's flares occurred randomly and independent from each other.

An outstanding exception is a feature at 9 days that we attribute to the influence of SPI by T1c. For the broad flare duration of $t_{1/2} = 0.3$ days (cyan), the resulting autocorrelation at this point lies at $2.1\,\sigma$. Similarly for the narrow duration of $t_{1/2} = 0.1$ days (blue), which lies slightly higher at $2.6\,\sigma$.

The resulting local maximum around T_{rot} sticks out by 1.1σ in the cyan curve and 1.6σ in the blue one. Another notable local maximum lies at about $t = 6$ days, which approximates twice the stellar rotation period and is probably an effect from the autocorrelation, that shows multiples of existing periods along with those existing periods.

The Fourier transformation is less clear than the autocorrelation (Figure 8.2b). The majority of the energy lies at high frequencies, because of the very narrow peaks that we analyse here, despite the assigned duration. Hence, the peaks that

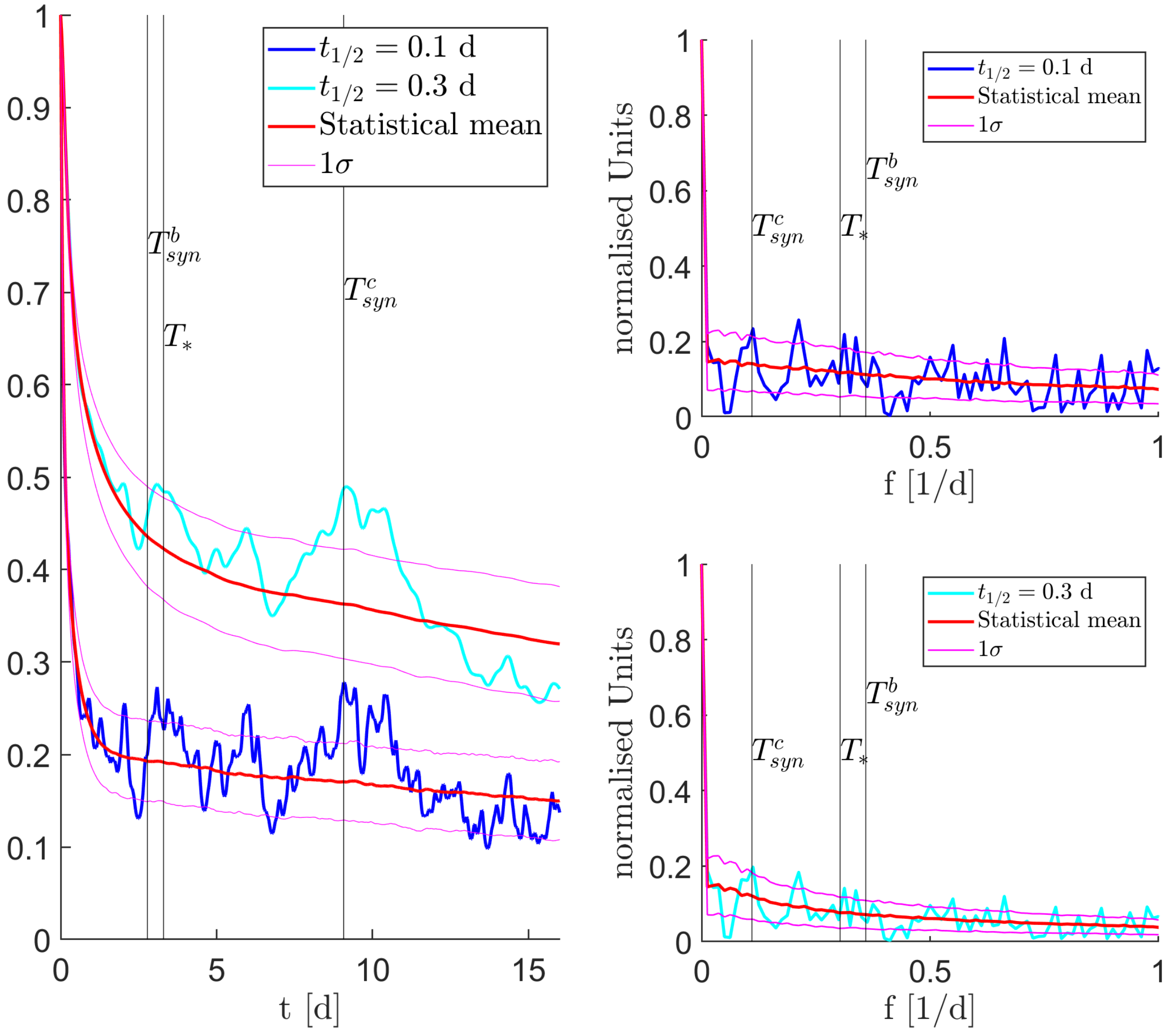

(a) (b)

Figure 8.2: Autocorrelation and Fourier spectrum of TRAPPIST-1 with the statistical results of the null hypothesis.

belong to the expected periods all lie between 1.2σ and 1.5σ.

8.4.3 Artificial Triggering Signals

As we saw in section 8.4.1, the synodic period of T1c is the most probable explanation for the increased autocorrelation at nine days. However, we would like to investigate and understand the system better. We will start the statistical tests with an analysis of the three expected periods. The following analysis includes the described non-idealised effects from section 8.3.3. In the end, we will present what we consider to be the best-fit explanation with the flare triggering model.

8.4.3.1 Pure Quasi-Periodic Signals

The results of the null hypothesis tests showed that there might indeed be a signal that appears with the synodic period of T1c. In this section, we investigate how well our assumed flare triggering model explains the obtained results of

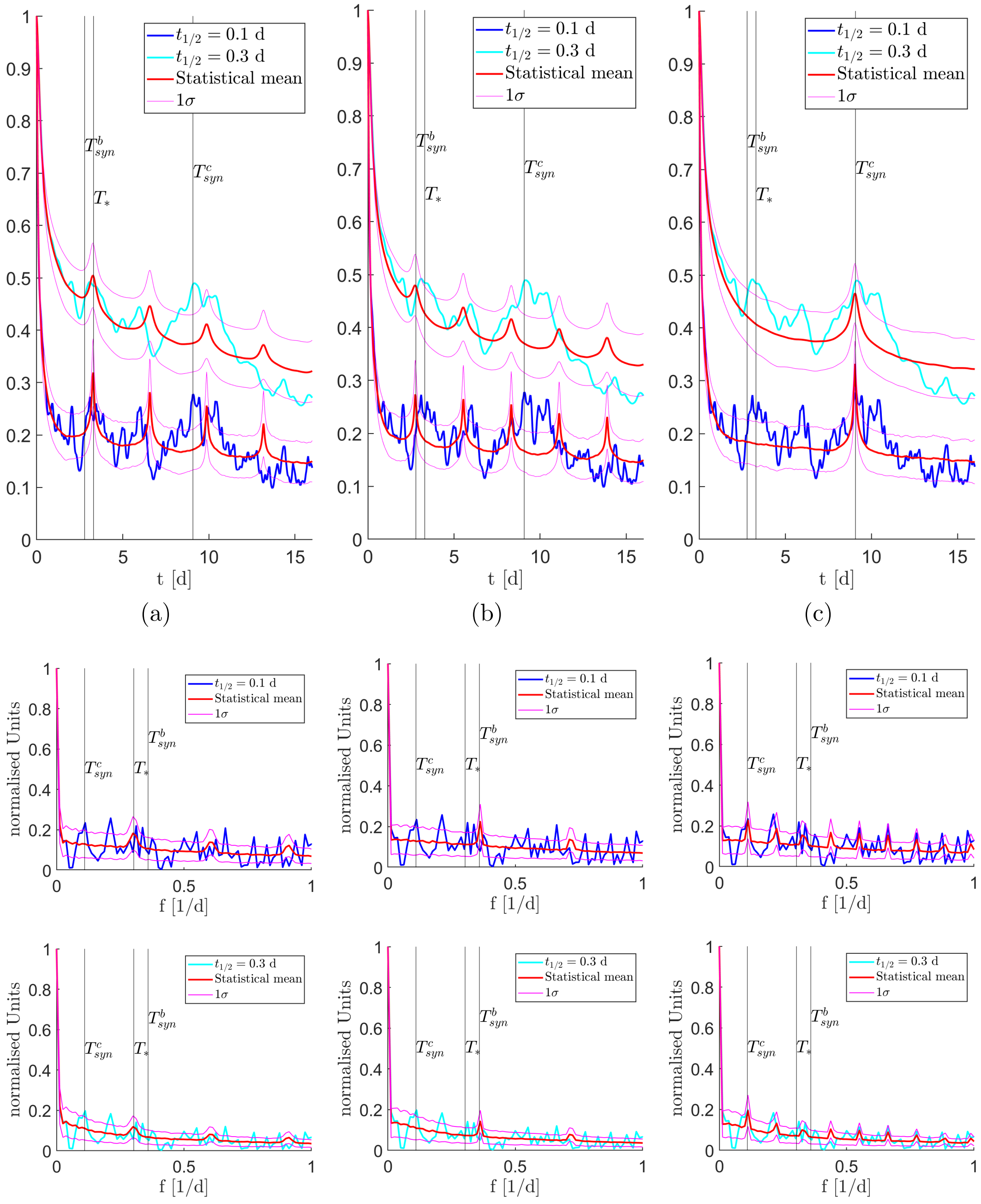

(a) (b) (c)

(d) (e) (f)

Figure 8.3: Hypothetical signals that appear with the rotation period T_{rot} and a probability of 0.3, the synodic period of T1b $T^{\mathrm{b}}_{\mathrm{syn}}$ and a probability of 0.4, and the synodic period of T1c $T^{\mathrm{c}}_{\mathrm{syn}}$ and a probability of 1.0. The upper row shows the aurocorrelation, the lower one the Fourier transforms.

TRAPPIST-1. We start with an analysis of (quasi-)periodic signals coming from the stellar rotation period and the synodic period of the two innermost planets.

Figure 8.3 shows the results of these tests. The way of presentation and the color code are the same as in the null hypothesis. Each column represents tests of one periodic signal, i.e. Figures 8.3a and 8.3d show a signal that appears with the stellar rotation period T_{rot}, Figures 8.3b and 8.3e show the results with the synodic period of T1b $T^{\mathrm{b}}_{\mathrm{syn}}$, and Figures 8.3c and 8.3f show the results with the synodic period of T1c $T^{\mathrm{c}}_{\mathrm{syn}}$.

For the rotation period, we chose an occurrence probability of $w_{\mathrm{occ}} = 0.3$, i.e. each flare has a 30% chance to erupt. In the cyan curve in Figure 8.3a, i.e. the autocorrelation of the long-duration flare light curve, the statistical mean approximates the local peak amplitude. However, the period is offset. In contrast, the chosen model can not fit the autocorrelation amplitude of the short flare duration (blue). In the Fourier transformation, the amplitudes of the statistical mean are lower for both flare duration times (Figure 8.3d).

Additionally, we see peaks at periods that are multiples of T_{rot}. These multiples are similar to the effect of aliasing, where an apparent longer period occurs due to coarse sampling frequencies that result in periods of $\tau = nT_{\mathrm{rot}}$, where n is a positive integer number. However, the obtained correlations are weaker because there are fewer signal peaks. The occurring multiples in the statistical test do mostly not correlate with other maxima in the autocorrelations and Fourier spectra, obtained from the observations.

The same conclusions hold for the statistical test with the synodic period of T1b. Here, we chose an occurrence probability of $w_{\mathrm{occ}} = 0.4$, to approximate the obtained amplitudes in autocorrelations and Fourier spectra. Neither the signal peak of $T^{\mathrm{b}}_{\mathrm{syn}}$, nor the one of T_{rot} can explain features of the real flare light curve. The tests with T_{rot} and $T^{\mathrm{b}}_{\mathrm{syn}}$, however, show that their respective multiples may not find their equivalent in the observational results, but most of the weak peaks in the blue and cyan curves relate to the period of three days. This relation is apparent from the fact that the multiples of T1b and the rotation, surround existing peaks in the observational curves. The signal peak at three days may, therefore, hint at the existence of a signal that we can currently not explain with the Flare triggering model.

Figures 8.3c and 8.3f show the results for a strictly periodic triggered flare signal from T1c surrounded by otherwise random flares. In this case, we assumed an occurrence probability of 1, i.e. every possible flare occurs. This idealised assumption shows a discrepancy between the two flare durations again. While the statistical mean underestimates the long-flare duration autocorrelation (cyan), it is vice-versa in the short-flare autocorrelation.

Additionally, the respective peaks of the statistical means in the autocorrelation are too narrow, compared to the obtained results from TRAPPIST-1. This discrepancy comes from the strict periodicity of the assumed signal, an issue that we will address in the next part.

Within the Fourier spectrum (Figure 8.3f), there are multiples of the associated frequency of $T^{\mathrm{c}}_{\mathrm{syn}}$. Those peaks mostly coincide with existing peaks in the obtained Fourier spectra of TRAPPIST-1's flares.

8.4.3.2 Non-Idealised Effects

Here, we present the influence of effects like possible deviations from the strict periodicity, the presence of a possible second anomaly that interacts with the planet and signals on a subinterval. We will focus on the signals from T1c because this planet is the strongest candidate for quasi-periodic flare triggering so far.

Figure 8.4 shows the case results for the mentioned non-idealised effects. The way of presentation and the color code are the same as in the null hypothesis

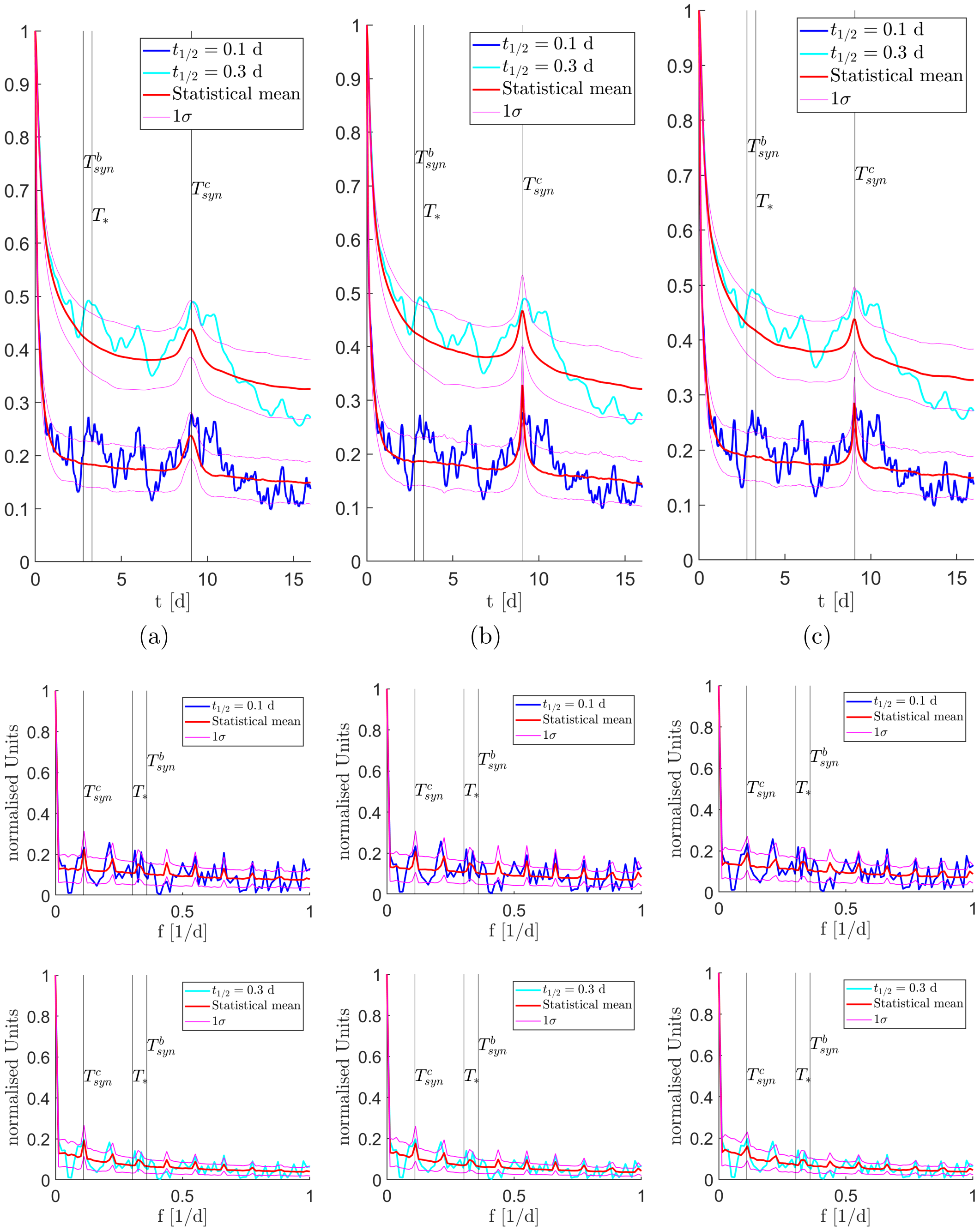

(a) (b) (c)

(d) (e) (f)

Figure 8.4: Quasi-periodic signals of T1c, with deviations in the period, two anomalies and flares that only occur on a limited interval time. The upper row shows the aurocorrelation, the lower one the Fourier transforms.

(Figure 8.2). Each column represents tests for one considered effect, i.e. Figures 8.4a and 8.4d show the result with a maximum δt of 0.3 days, Figures 8.4b and 8.4e show the results of an interaction between T1c with two magnetic anomalies, and Figures 8.4c and 8.4f show results with the synodic period of T1c $T^{\mathrm{c}}_{\mathrm{syn}}$ and the rotation period T_{rot}.

An alteration of the signal period through random deviations δt takes into account that the interaction between Alfvén wing and magnetic anomaly is probably non-linear and underlies yet unknown constraints. In the presented scenario in Figures 8.4a and 8.4d, we assume a flare time-series that is triggered by T1c and has a flare occurrence probability of $w_{\mathrm{occ}} = 1$. The scenario is effectively identical to the one presented in Figures 8.3c and 8.3f. Except, we allow the flares to deviate from the assigned period of $T^{\mathrm{b}}_{\mathrm{syn}}$ with $\delta t_{\mathrm{max}} = 0.3$ days.

In the statistical test, we see that in this case, both statistical means underestimate the autocorrelations of the real light curve. Only the $+\sigma$-level touches the obtained peaks at nine days. In the autocorrelation, the short flare duration of $t_{1/2} = 0.1$ days (blue) is more sensitive to deviations from a strict periodicity, as it occurs here. The obtained peak is much lower than in Figure 8.3c, while the effect on the flares with $t_{1/2} = 0.3$ days is weaker.

The Fourier transform appears to be quite robust to changes in the period. The obtained results in Figure 8.4d barely differ from the results in Figure 8.3f. In general, the deviations δt cause the obtained mean autocorrelation peaks to become wider. At the same time, the amplitude reduces. Due to the variation of the flare occurrence period, the autocorrelation varies accordingly. Temporal deviations from the strict periodicity likely occur in the time series of TRAPPIST-1.

The second effect assumes a second anomaly and creates a second quasi-periodic flare signal for the test. We saw in the discussion of Figures 8.3c and 8.3f, as well as Figures 8.4a and 8.4d, that the obtained mean autocorrelations cannot explain the results obtained from TRAPPIST-1, even not by an occurrence probability of $w_{\mathrm{occ}} = 1$. We saw in the light curve of TRAPPIST-1 that flares might appear in clusters. Clusters may, just as single flares, be associated to the influence of SPI. A clustering test would, however, require extensive knowledge of the flaring processes and the resulting statistical properties. What we require right now are more flares with a certain period. A second anomaly can provide this and mimic the effects of clusters.

Figures 8.4b and 8.4e show the respective results for a case where the triggered flares have a 70% chance to occur with both anomalies. The results resemble the ones, obtained with a single signal time series but 100% occurrence probability. Both signals are offset by $t_{\mathrm{OS}} = 0.3$ days. The obtained mean autocorrelations reach values of about 0.45 (long flare duration) and 0.35 (short flare duration). Those correlations are similar to the single periodic signal from T1c with $w_{\mathrm{occ}} = 1$ (see Figure 8.3c). However, with the assumption of two magnetic anomalies, there is a chance to generate the necessary amount of flares to explain the obtained autocorrelations.

The third and last non-idealised effect is the possibility that the magnetic anomaly only has a limited lifespan and flares occur on a limited time-interval. Figures 8.4c and 8.4f show the signals of T1c with $w_{\mathrm{occ}} = 1$. We allow a minimal interval of two periodic flares and a maximum of eight flares in a row. Start and stop time are chosen accordingly. As expected, due to the smaller number of flares, the obtained mean autocorrelations are smaller than in the case of 100% occurrence rate over the whole time (see Figure 8.3c).

In general, the Fourier spectra obtained under the influence of the presented effects appear to be quite robust to these uncertainties. The calculated power spectra look almost the same. That might be because the presented frequency range only carries remnants of the power, which is mostly stored in higher frequencies.

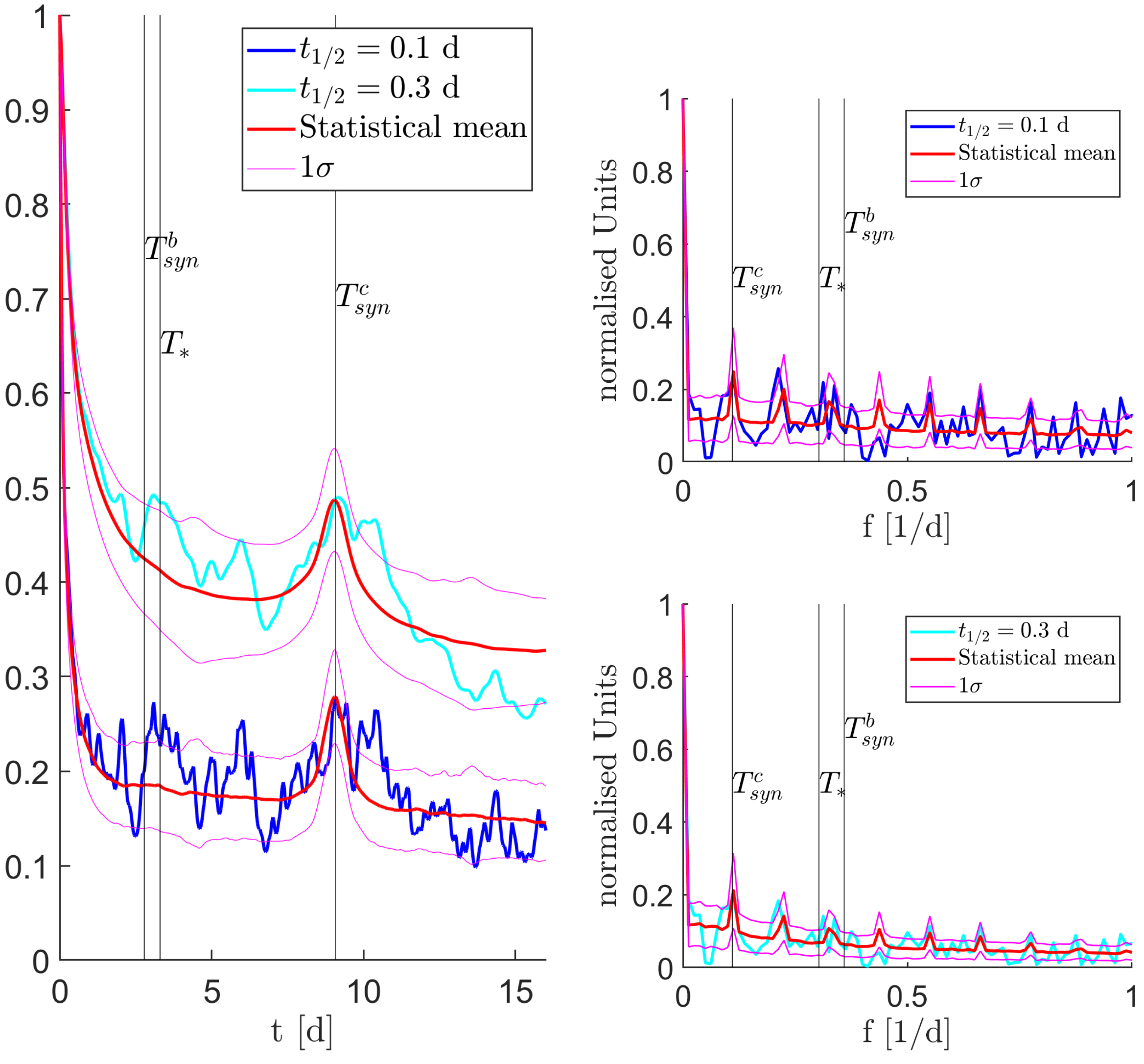

(a) (b)

Figure 8.5: Autocorrelation and Fourier spectrum of TRAPPIST-1 with the statistical results of the null hypothesis.

8.4.3.3 Best-Fit Result

After the discussion of the different triggered periods and possible additional effects that result in a quasi-periodicity of the assumed signals, we present, what we call the best fit result. We determine this result via the trial-and-error method and not via quantifiable inversion techniques. Figure 8.5 presents the resulting autocorrelations and Power spectra.

We decided, to assume the existence of two magnetic anomalies because this approach yields the required amount of flares to explain the peaks of the autocorrelations with both flare durations. We, however assume an occurrence probability of $w_{\text{occ}} = 0.9$. Additionally, we assume maximum deviations from strict periods by $\delta t_{\max} = 0.3$ days. Here, we assume no subintervals or influences from other periodic signals.

In the result, we obtain statistical means that fit the peaks of 0.5 for long-duration flares and 0.28 for short-duration flares. The width of the mean curves also approximates the obtained autocorrelations from TRAPPIST-1.

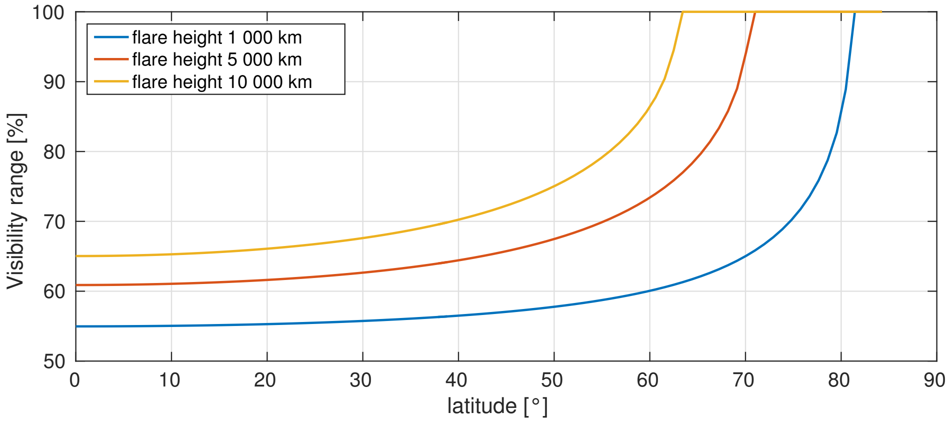

Figure 8.6: Visibility extension for different flare heights re-used from *Fischer and Saur* (2019).

We saw before that the power spectra are quite robust to slight stochastic changes in the periodicity of flares. Hence, the obtained mean spectra fit the computed observational spectra well, with the exception of a multiple at 0.4day^{-1} that has no similarly strong observational peak.

8.5 Visibility of Triggered Flares at TRAPPIST-1

Observations of flares are also subject to the visibility concern introduced in section 3.4.4. If flares have negligible height, they are only visible 50% of the time. Reliable flare height estimations are only available for solar flares. Early studies from *Warwick* (1955) and *Warwick and Wood* (1959) about flare height distributions showed that most solar flares have low altitudes of a few thousand kilometres. A few huge flares appeared to have heights of 20 000 to 50 000 km (*Warwick and Wood*, 1959). Observations of a solar limb flare by *Battaglia and Kontar* (2011) showed that white light originated from heights of 1500 to 3000 km, hard X-rays from 800 to 1700 km and EUV emissions from around 3000 km. *Pillitteri et al.* (2010) observed a flare on the K-type star HD 189733 and estimated the furthest extent of the flaring loop to be on the order of the stellar radius (0.76 solar radii). These studies show that flares appear with a large variety of sizes, but the heights of flares on M-dwarfs like TRAPPIST-1 are currently unknown. In our study, we assume typical sun-like flare heights in a range between 1000 km and 10 000 km. Those heights are non-negligible compared to the small radius of TRAPPIST-1 and can considerably extend the visible area.

Figure 3.2 and equation (3.50) show that the visibility increases for various flare heights depending on their latitudinal location. In Figure 8.6, we show how much the flare visibility extends at TRAPPIST-1. The visibility range is presented as a function of latitude and in different colours for different flare heights Δr. TRAPPIST-1 has a radius of $R_* = 81342$ km (*Gillon et al.*, 2017). The blue curve shows $\Delta r = 1\,000$ km, the orange one $\Delta r = 5\,000$ km and the yellow curve $\Delta r = 10\,000$ km. They represent typical sizes of solar flare white light emissions. In this study, we assume these flare heights for TRAPPIST-1. We see that the visibility of a flare at the equator extends to 55% for $\Delta r = 1\,000$ km and to 65%

for 10 000 km. All three curves increase towards a 100% visibility with increasing latitude. Large flares with a height of 10 000 km reach a 100% visibility at a latitude of 65°. The investigated smaller flares reach this threshold at 70° and 80°.

For the analysis of flare observations, we have to know where the footpoints of the planetary Alfvén wings lie on the stellar surface. As a simple estimate, we apply a magnetic dipole model and use the field line equation to map the field lines connecting the planets with the star given by $\cos^2(\lambda) = R_*/a$ with the latitude λ and the planetary orbital distance a. We receive footpoint latitudes of $\lambda_\mathrm{b} = 77°$ and $\lambda_\mathrm{c} = 79°$ for T1b and T1c, respectively. Therefore the visibility is likely significantly enhanced for a planetary triggered flare at high or mid-latitudes and lies around 70% to 100% for the assumed flare heights. The planets likely reside on quasi-open field lines, and thus the Alfvén wings' footpoints probably lie even closer to the poles.

9 Conclusions

In the course of this thesis, we investigated Star-Planet Interaction in the TRAPPIST-1 system. The main focus lied on the properties of SPI and possible temporal variabilities. We investigated those effects via semi-analytic modelling, numerical MHD modelling and statistical time-series analyses.

Time-variability in SPI relies on environmental variations at the interacting planet, due to its orbital motion and the rotation of the host star. On that basis, we presented four mechanisms that can cause time-variable SPI with different periods. The easiest one of these mechanisms assumes that the variability appears with the planetary orbital period. The planetary Alfvén wing would generate some kind of emission that is visible if it appears on the hemisphere that is in the line of sight and otherwise not. The second mechanism is similar but assumes that the stellar magnetic field is tilted. That causes a periodically changing plasma environment at the planet. Due to the stellar rotation, the planetary orbital motion, and the tilt in the magnetic field, the period of the signal appears with half the synodic rotation period of the star, as seen from the planet. The third mechanism assumes a non-linear, periodic interaction between the planetary Alfvén wing and a magnetic anomaly on the star. The result is a periodic series of flares that appear with the synodic rotation period. Finally, we proposed the possibility of mutual interactions between two planetary Alfvén wings, called wing-wing interaction. This type of interaction can only occur if two planets share the same set of quasi-open magnetic field lines.

We spent the following two chapters to understand and characterise SPI in the TRAPPIST-1 system. In chapter 4, we conducted a semi-analytic parameter study to estimate if SPI is possible, which planets are likely to host SPI and how strong the expected SPI will be. Chapter 5 introduces the MHD model setup based on the PLUTO Code to simulate time-dependent SPI. We simulate the interaction between a thermally driven stellar wind and the innermost planet T1b and analyse the resulting wave structures in detail. The inward going wave structure, i.e. the one pointing towards the star, is purely Alfvénic and carries energy towards the star. The outward going waves are much more diverse, apart from the Fast Mode, we see all possible MHD waves. One can distinguish all waves by their relative position to each other based on the respective characteristic wave speed. We further identified each wave and the occurring Slow Shock from their distinct properties.

After the general properties of SPI, we investigated time-variable effects. The first study analyses wing-wing interaction between T1b and T1c (chapter 6). From the MHD simulations, we found that visible variability results from the dissipation of T1c's inward going Alfvén wing. For a certain amount of time, the total power, transferred from both planets towards the star, lacks the contribution of the outer planet. The inferred time range involves the time, the outer planet requires to pass through the Alfvén wing, and the travel time of the inward going Alfvén wave from the outer planet. The next modelling study investigated the effect of a coronal mass ejection on SPI (chapter 7). Such events are non-periodic because the CME has to erupt before the planet can trigger it. The simulated CME is spatially localised and moves solely radially outward. Within the CME-structure, the planet experiences super-Alfvénic conditions. Accordingly, a shock structure forms around the planet and propagates outward. At the flank of the CME, the Alfvén waves can turn towards the star again and form a dislocated Alfvén wing. In chapter 8, we analysed a flare light curve of TRAPPIST-1, observed with the K2 mission. In the autocorrelation, one can see a peak at the synodic period of T1c. We performed statistical tests and found that the result has a significance of about 2σ against a null hypothesis with random flares. Statistical tests have shown that the obtained result can be explained by flare triggering from T1c.

The research of time-variable SPI relies heavily on numerical simulations. Analytic model studies, like the one in chapter 4, allow large parameter studies to gain an overall insight into the properties of a system like TRAPPIST-1. However, analytic models often require major simplifying or idealising assumptions, in order to treat complex phenomena like stellar winds (*Parker*, 1958) or SPI (*Saur et al.*, 2013). In that way, this type of models is often limited to provide steady-state results and in our case, parameters that we can apply to numerical simulations. Numerical MHD models allow much more detailed investigations of SPI because we can calculate the interaction self-consistently. This degree of physical complexity comes at the cost of the large parameter space because one has to focus on certain case studies.

A problem of numerical simulations is dissipation due to the simulation grid. Our applied simulation grids were fine to investigate SPI on a global scale. They allowed to compute wave characteristics (sections 5.4.1 and 5.5.1) and to identify the occurring wave structures. However, even with an enhanced grid resolution, we were not able to distinguish physical from numerical dissipation in the energetic analysis of the inward going Alfvén wing (see section 5.4.3). A finer resolution would increase the convergence of the solution and reduce dissipation effects, but from a technical point of view, we would not be able to handle such large output data sets. A solution to this problem would be the application of Adaptive Mesh Refinement. However, due to limitations in time, we were not yet able to apply this feature of PLUTO to our model setup.

Despite numerical issues that have to be solved or at least reduced in future iterations of the described model setup, this thesis represents a fundamental basis for future research in the field of time-dependent SPI. We proposed four highly idealised mechanisms that can be responsible for variations within the interaction. In the frame of this work, we managed to simulate one of these mechanisms numerically. Wing-wing interaction is only possible in regions of quasi-open field lines. Such regions exist close to magnetic poles, where the stellar wind extends the field lines so far that they close at infinity. Considering that both required planets orbit in the stellar equatorial plane of the star, the magnetic field either has to be strongly tilted or both planets have to be sufficiently far away from the star to reside in open-field line regions. Further studies with tilted dipole fields or observed surface magnetic field maps have to be applied to find out how wing-wing interaction appears to work under less idealised conditions.

Further studies that lie within the possibilities of the current model state may focus on the impact that wing-wing interaction has on the involved planets. Alfvén wings carry power and complex current systems. According to our very first results, the Poynting flux of the stronger Alfvén wing, i.e. the one from the inner planet, seems to dissipate only in the atmosphere of the outer planet. Further analyses have to show if the dissipated power heats up the plasma or the atmosphere. The current systems are an additional line of research that we did not include at all in this thesis. It is possible that current systems of the inner planet's Alfvén wing enhance the auroral activity on the outer planet. Towards the star, the current density of an Alfvén wing increases, because the cross-section of the Alfvén wing decreases, as a result of current continuity. In the outward going Alfvén wing, the opposite happens, and the current density decreases. One might estimate if the current density suffices to accelerate particles to high energies so that they can produce aurora.

The extension of the MHD model to simulate SPI in a tilted stellar dipole field will also allow investigating the second variability mechanism. So far, we were not able to include a tilted stellar dipole magnetic field and based our studies on the simplified Parker-model for stellar wind and magnetic field (*Parker*, 1958). In the literature, there has, to our knowledge, never been a numerical study, where this type of interaction has been simulated fully self-consistent. Alternative approaches were either global simulations that provided boundary conditions for near field simulations (*Garraffo et al.*, 2016; *Garraffo et al.*, 2017) or that SPI was analysed semi-numerically, i.e. a numerical simulation provided the parameters for analytic models (*Strugarek et al.*, 2019). A fully time-dependent simulation will eventually show how the waves behave under changing stellar wind conditions. Alfvén wings will probably reflect at meridional density gradients, just like Io's Alfvén wings do in the Jupiter system (*Jacobsen et al.*, 2007, 2010). An interesting region is the stellar current sheet. In section 3.4.3 we suspected, that it only generates an exceptional dip within the time-variable Poynting flux. If it provides super-Alfvénic conditions instead, the Alfvén wing might behave in a similar way as it did in our simulations with the coronal mass ejection. The Alfvén wave might be dislocated until the planet leaves the current sheet into the sub-Alfvénic wind environment. In a further extension, the model may include observed magnetic field maps and simulate real stellar winds, with corresponding inhomogeneities.

In addition to the partly fundamental numerical studies towards time-variable SPI, we also performed an analysis of observed flares at TRAPPIST-1 and received surprisingly good results. In the course of the performed tests, we saw that flare triggering by SPI is indeed a realistic explanation for the obtained spectral and statistical results.

The analysis of TRAPPIST-1's flares is a first case study of a promising planetary system. Future studies should provide a larger sample of several more systems. Therefore, we will see if the results from TRAPPIST-1 are outliers, or if flare triggering is a frequent process. An important step in the verification of the flare triggering process would be a control group of stars that has no planets. Accordingly, the flares of these stars will provide an empirical null hypothesis for tests, instead of the yet unverified assumption of random flares. Therefore, one could include flares more efficiently into the search for SPI.

In addition to the proposed observational studies, a further extension of the MHD model could investigate the physical processes of the flare triggering process. So far, there is an analytic prediction for the process by *Lanza* (2018). However, a self-consistent model of a magnetic anomaly on the stellar surface, together with star-planet interaction, will provide further insight into the process itself. Our simulations of an interaction between a scripted CME event and the planet are the first step. While our assumed CME was not calculated self-consistently, the example shows that complex interactions like these are indeed possible. Open questions are if flare triggering is possible within the framework of the MHD equations and how and when the flare triggering happens exactly. If it is possible, there is the open question, how much the strength of the SPI, i.e. the Poynting flux, affects occurrence or non-occurrence of flares. These studies will finally allow us to refine our statistical test scenarios.

In conclusion, we can say, that we have made an important step into a deeper understanding of star-planet interaction with this thesis. We presented four idealised mechanisms for time-variability in SPI and outlined, which periods we expect to appear. Furthermore, we simulated the proposed variability mechanism called wing-wing interaction and found first evidence for the flare triggering mechanism in the flares of TRAPPIST-1. In addition, we performed an extensive analysis of wave modes, associated with SPI.

Bibliography

Acuna, M. H., F. M. Neubauer, and N. F. Ness (1981), Standing Alfvén Wave Current System at Io: Voyager 1 Observations, *Journal of Geophysical Research*, *86*(A10), 8513–8521, doi:10.1029/JA086iA10p08513.

Anglada-Escudé, G., P. J. Amado, J. Barnes, Z. M. Berdiñas, R. P. Butler, G. A. L. Coleman, I. de La Cueva, S. Dreizler, M. Endl, B. Giesers, S. V. Jeffers, J. S. Jenkins, H. R. A. Jones, M. Kiraga, M. Kürster, M. J. López-González, C. J. Marvin, N. Morales, J. Morin, R. P. Nelson, J. L. Ortiz, A. Ofir, S.-J. Paardekooper, A. Reiners, E. Rodríguez, C. Rodríguez-López, L. F. Sarmiento, J. P. Strachan, Y. Tsapras, M. Tuomi, and M. Zechmeister (2016), A terrestrial planet candidate in a temperate orbit around Proxima Centauri, *Nature*, *536*(7617), 437–440, doi:10.1038/nature19106.

Aschwanden, M. J., T. D. Tarbell, R. W. Nightingale, C. J. Schrijver, A. Title, C. C. Kankelborg, P. Martens, and H. P. Warren (2000), Time Variability of the "Quiet" Sun Observed with TRACE . II. Physical Parameters, Temperature Evolution, and Energetics of Extreme-Ultraviolet Nanoflares , *The Astrophysical Journal*, *535*(2), 1047–1065, doi:10.1086/308867.

Avrett, E. H. (2003), The Solar Temperature Minimum and Chromosphere, in *Current Theoretical Models and Future High Resolution Solar Observations: Preparing for ATST*, *Astronomical Society of the Pacific Conference Series*, vol. 286, edited by A. A. Pevtsov and H. Uitenbroek, p. 419.

Bagenal, F., J. D. Sullivan, and G. L. Siscoe (1980), Spatial distribution of plasma in the Io torus, *Geophysical Research Letters*, *7*(1), 41–44.

Banks, P. M., and G. Kockarts (1973), *Aeronomy.*

Barman, T. (2007), Identification of Absorption Features in an Extrasolar Planet Atmosphere, *The Astrophysical Journal Letters*, *661*(2), L191–L194, doi:10.1086/518736.

Barnes, J. R., and A. Collier Cameron (2001), Starspot patterns on the M dwarfs HK Aqr and RE 1816 +541, *Monthly Notices of the Royal Astronomical Society*, *326*(3), 950–958, doi:10.1046/j.1365-8711.2001.04649.x.

Barnes, R., S. N. Raymond, R. Greenberg, B. Jackson, and N. A. Kaib (2010), CoRoT-7b: Super-Earth or Super-Io?, *The Astrophysical Journal Letters*, *709*(2), L95–L98, doi:10.1088/2041-8205/709/2/L95.

Barr, A. C., V. Dobos, and L. L. Kiss (2018), Interior structures and tidal heating in the TRAPPIST-1 planets, *Astronomy and Astrophysics*, *613*, A37, doi:10.1051/0004-6361/201731992.

Battaglia, M., and E. P. Kontar (2011), Height structure of X-ray , EUV , and white-light emission, *Astronomy & Astrophysics*, *533*(L2), L2, doi:10.1051/0004-6361/201117605.

Baumjohann, W., and R. A. Treumann (1996), *Basic space plasma physics*, doi:10.1142/p015.

Bazer, J., and W. B. Ericson (1959), Hydromagnetic Shocks., *The Astrophysical Journal*, *129*, 758, doi:10.1086/146673.

Bennett, D. P., J. Anderson, I. A. Bond, A. Udalski, and A. Gould (2006), Identification of the OGLE-2003-BLG-235/MOA-2003-BLG-53 Planetary Host Star, *The Astrophysical Journal Letters*, *647*(2), L171–L174, doi:10.1086/507585.

Berta, Z. K., D. Charbonneau, J.-M. Désert, E. Miller-Ricci Kempton, P. R. McCullough, C. J. Burke, J. J. Fortney, J. Irwin, P. Nutzman, and D. Homeier (2012), The Flat Transmission Spectrum of the Super-Earth GJ1214b from Wide Field Camera 3 on the Hubble Space Telescope, *The Astrophysical Journal*, *747*(1), 35, doi:10.1088/0004-637X/747/1/35.

Bhattacharyya, D., J. T. Clarke, J. Montgomery, B. Bonfond, J.-C. Gérard, and D. Grodent (2018), Evidence for Auroral Emissions From Callisto's Footprint in HST UV Images, *Journal of Geophysical Research (Space Physics)*, *123*(1), 364–373, doi:10.1002/2017JA024791.

Bigg, E. K. (1964), Influence of the Satellite Io on Jupiter's Decametric Emission, *Nature*, *203*(4949), 1008–1010, doi:10.1038/2031008a0.

Blöcker, A., J. Saur, and L. Roth (2016), Europa's plasma interaction with an inhomogeneous atmosphere: Development of Alfvén winglets within the Alfvén wings, *Journal of Geophysical Research: Space Physics*, *121*(10), 9794–9828, doi:10.1002/2016JA022479.

Blöcker, A., J. Saur, L. Roth, and D. F. Strobel (2018), MHD Modeling of the Plasma Interaction With Io's Asymmetric Atmosphere, *Journal of Geophysical Research: Space Physics*, *123*(11), 9286–9311, doi:10.1029/2018JA025747.

Böhm-Vitense, E. (1989), *Introduction to stellar astrophysics. Vol. 2. Stellar atmospheres.*, vol. 2, Cambridge University Press.

Boisse, I., F. Pepe, C. Perrier, D. Queloz, X. Bonfils, F. Bouchy, N. C. Santos, L. Arnold, J. L. Beuzit, R. F. Díaz, X. Delfosse, A. Eggenberger, D. Ehrenreich, T. Forveille, G. Hébrard, A. M. Lagrange, C. Lovis, M. Mayor, C. Moutou, D. Naef, A. Santerne, D. Ségransan, J. P. Sivan, and S. Udry (2012), The SOPHIE search for northern extrasolar planets. V. Follow-up of ELODIE candidates: Jupiter-analogs around Sun-like stars, *Astronomy and Astrophysics*, *545*, A55, doi:10.1051/0004-6361/201118419.

Bonfond, B., D. Grodent, J. C. Gérard, A. Radioti, J. Saur, and S. Jacobsen (2008), UV Io footprint leading spot: A key feature for understanding the UV Io footprint multiplicity?, *Geophysical Research Letters*, *35*(5), L05107, doi:10.1029/2007GL032418.

Bonfond, B., D. Grodent, J. C. Gérard, T. Stallard, J. T. Clarke, M. Yoneda, A. Radioti, and J. Gustin (2012), Auroral evidence of Io's control over the magnetosphere of Jupiter, *Geophysical Research Letters*, *39*(1), L01105, doi:10.1029/2011GL050253.

Bonfond, B., S. Hess, J. C. Gérard, D. Grodent, A. Radioti, V. Chantry, J. Saur, S. Jacobsen, and J. T. Clarke (2013), Evolution of the Io footprint brightness I: Far-UV observations, *Planetary and Space Science*, *88*, 64–75, doi:10.1016/j.pss.2013.05.023.

Borucki, W. J., D. Koch, G. Basri, N. Batalha, T. Brown, D. Caldwell, J. Caldwell, J. Christensen-Dalsgaard, W. D. Cochran, E. DeVore, E. W. Dunham, A. K. Dupree, T. N. Gautier, J. C. Geary, R. Gilliland, A. Gould, S. B. Howell, J. M. Jenkins, Y. Kondo, D. W. Latham, G. W. Marcy, S. Meibom, H. Kjeldsen, J. J. Lissauer, D. G. Monet, D. Morrison, D. Sasselov, J. Tarter, A. Boss, D. Brownlee, T. Owen, D. Buzasi, D. Charbonneau, L. Doyle, J. Fortney, E. B. Ford, M. J. Holman, S. Seager, J. H. Steffen, W. F. Welsh, J. Rowe, H. Anderson, L. Buchhave, D. Ciardi, L. Walkowicz, W. Sherry, E. Horch, H. Isaacson, M. E. Everett, D. Fischer, G. Torres, J. A. Johnson, M. Endl, P. MacQueen, S. T. Bryson, J. Dotson, M. Haas, J. Kolodziejczak, J. Van Cleve, H. Chandrasekaran, J. D. Twicken, E. V. Quintana, B. D. Clarke, C. Allen, J. Li, H. Wu, P. Tenenbaum, E. Verner, F. Bruhweiler, J. Barnes, and A. Prsa (2010), Kepler planet-detection mission: Introduction and first results, *Science*, *327*(5968), 977–980.

Bourrier, V., D. Ehrenreich, P. J. Wheatley, E. Bolmont, M. Gillon, J. De Wit, A. J. Burgasser, E. Jehin, D. Queloz, and A. H. Triaud (2017), Reconnaissance of the TRAPPIST-1 exoplanet system in the Lyman- α line, *Astronomy and Astrophysics*, *599*(L3), L3, doi:10.1051/0004-6361/201630238.

Broadfoot, A. L., M. J. S. Belton, P. Z. Takacs, B. R. Sand el, D. E. Shemansky, J. B. Holberg, J. M. Ajello, S. K. Atreya, T. M. Donahue, H. W. Moos, J. L. Bertaux, J. E. Blamont, D. F. Strobel, J. C. McConnell, A. Dalgarno, R. Goody, and M. B. McElroy (1979), Extreme Ultraviolet Observations from Voyager 1 Encounter with Jupiter, *Science*, *204*(4396), 979–982, doi:10.1126/science.204.4396.979.

Brun, A. S., and M. K. Browning (2017), Magnetism, dynamo action and the solar-stellar connection, *Living Reviews in Solar Physics*, *14*(1), 4, doi:10.1007/s41116-017-0007-8.

Burgasser, A. J. (2008), Brown dwarfs: Failed stars, super Jupiters, *Physics Today*, *61*(6), 70–71, doi:10.1063/1.2947658.

Burgasser, A. J., and E. E. Mamajek (2017), On the Age of the TRAPPIST-1 System, *The Astrophysical Journal*, *845*(2), 110, doi:10.3847/1538-4357/aa7fea.

Canto Martins, B. L., M. L. Das Chagas, S. Alves, I. C. Leão, L. P. de Souza Neto, and J. R. de Medeiros (2011), Chromospheric activity of stars with planets, *Astronomy and Astrophysics*, *530*, A73, doi:10.1051/0004-6361/201015314.

Carrington, R. C. (1859), Description of a Singular Appearance seen in the Sun on September 1, 1859, *Monthly Notices of the Royal Astronomical Society*, *20*, 13–15, doi:10.1093/mnras/20.1.13.

Cauley, P. W., E. L. Shkolnik, J. Llama, and A. F. Lanza (2019), Magnetic field strengths of hot Jupiters from signals of star–planet interactions, *Nature Astronomy*, *3*(12), 1128–1134, doi:10.1038/s41550-019-0840-x.

Chané, E., J. Saur, and S. Poedts (2013), Modeling Jupiter's magnetosphere: Influence of the internal sources, *Journal of Geophysical Research: Space Physics*, *118*(5), 2157–2172, doi:10.1002/jgra.50258.

Charbonneau, D., T. M. Brown, D. W. Latham, and M. Mayor (2000), Detection of Planetary Transits Across a Sun-like Star, *The Astrophysical Journal Letters*, *529*(1), L45–L48, doi:10.1086/312457.

Charbonneau, D., T. M. Brown, R. W. Noyes, and R. L. Gilliland (2002), Detection of an extrasolar planet atmosphere, *The Astrophysical Journal*, *568*(1), 377–384, doi:10.1086/338770.

Charbonneau, D., Z. K. Berta, J. Irwin, C. J. Burke, P. Nutzman, L. A. Buchhave, C. Lovis, X. Bonfils, D. W. Latham, S. Udry, R. A. Murray-Clay, M. J. Holman, E. E. Falco, J. N. Winn, D. Queloz, F. Pepe, M. Mayor, X. Delfosse, and T. Forveille (2009), A super-Earth transiting a nearby low-mass star, *Nature*, *462*(7275), 891–894, doi:10.1038/nature08679.

Chauvin, G., A. M. Lagrange, C. Dumas, B. Zuckerman, D. Mouillet, I. Song, J. L. Beuzit, and P. Lowrance (2004), A giant planet candidate near a young brown dwarf. Direct VLT/NACO observations using IR wavefront sensing, *Astronomy and Astrophysics*, *425*, L29–L32, doi:10.1051/0004-6361:200400056.

Chen, P. F. (2011), Coronal Mass Ejections: Models and Their Observational Basis, *Living Reviews in Solar Physics*, *8*(1), 1, doi:10.12942/lrsp-2011-1.

Chin, Y.-C., and D. G. Wentzel (1972), Nonlinear Dissipation of Alfvén Waves, *Astrophysics and Space Science*, *16*(3), 465–477, doi:10.1007/BF00642346.

Clarke, J. T., G. E. Ballester, J. Trauger, R. Evans, J. E. P. Connerney, K. Stapelfeldt, D. Crisp, P. D. Feldman, C. J. Burrows, S. Casertano, I. Gallagher, John S., R. E. Griffiths, J. J. Hester, J. G. Hoessel, J. A. Holtzman, J. E. Krist, V. Meadows, J. R. Mould, P. A. Scowen, A. M. Watson, and J. A. Westphal (1996), Far-Ultraviolet Imaging of Jupiter's Aurora and the lo "Footprint", *Science*, *274*(5286), 404–409, doi:10.1126/science.274.5286.404.

Clarke, J. T., J. Ajello, G. Ballester, L. B. Jaffel, J. Connerney, J. C. Gérard, G. R. Gladstone, W. Pryor, J. Trauger, and J. H. Waite (2002), Ultraviolet emissions from the magnetic footprints of Io, Ganymede and Europa on Jupiter, *Nature*, *415*(6875), 997–1000, doi:10.1038/415997a.

Cohen, O., I. V. Sokolov, I. I. Roussev, C. N. Arge, W. B. Manchester, T. I. Gombosi, R. A. Frazin, H. Park, M. D. Butala, F. Kamalabadi, and M. Velli (2007), A Semiempirical Magnetohydrodynamical Model of the Solar Wind, *The Astrophysical Journal*, *654*(2), L163—-L166, doi:10.1086/511154.

Cohen, O., V. L. Kashyap, J. J. Drake, I. V. Sokolov, C. Garraffo, and T. I. Gombosi (2011), The dynamics of stellar coronae harboring hot Jupiters. I. A time-dependent magnetohydrodynamic simulation of the interplanetary environment in the HD 189733 planetary system, *Astrophysical Journal*, *733*(1), 67, doi:10.1088/0004-637X/733/1/67.

Cohen, O., J. J. Drake, A. Glocer, C. Garraffo, K. Poppenhaeger, J. M. Bell, A. J. Ridley, and T. I. Gombosi (2014), Magnetospheric structure and atmospheric Joule heating of habitable planets orbiting M-dwarf stars, *Astrophysical Journal*, *790*(1), doi:10.1088/0004-637X/790/1/57.

Cohen, O., Y. Ma, J. J. Drake, A. Glocer, C. Garraffo, J. M. Bell, and T. I. Gombosi (2015), THE INTERACTION of VENUS-LIKE, M-DWARF PLANETS with the STELLAR WIND of THEIR HOST STAR, *Astrophysical Journal*, *806*(1), doi:10.1088/0004-637X/806/1/41.

Connerney, J. E. P., R. Baron, T. Satoh, and T. Owen (1993), Images of Excited H_3$\hat{+}$ at the Foot of the Io Flux Tube in Jupiter's Atmosphere, *Science*, *262*(5136), 1035–1038, doi:10.1126/science.262.5136.1035.

Connerney, J. E. P., S. Kotsiaros, R. J. Oliversen, J. R. Espley, J. L. Joergensen, P. S. Joergensen, J. M. G. Merayo, M. Herceg, J. Bloxham, K. M. Moore, S. J. Bolton, and S. M. Levin (2018), A New Model of Jupiter's Magnetic Field From Juno's First Nine Orbits, *Geophysical Research Letters*, *45*(6), 2590–2596, doi: 10.1002/2018GL077312.

Cowley, S. W. H., and E. J. Bunce (2001), Origin of the main auroral oval in Jupiter's coupled magnetosphere-ionosphere system, *Planetary and Space Science*, *49*(10-11), 1067–1088, doi:10.1016/S0032-0633(00)00167-7.

Cuntz, M., S. H. Saar, and Z. E. Musielak (2000), On Stellar Activity Enhancement Due to Interactions with Extrasolar Giant Planets, *The Astrophysical Journal*, *533*(2), L151–L154, doi:10.1086/312609.

Cushing, M. C., J. D. Kirkpatrick, C. R. Gelino, R. L. Griffith, M. F. Skrutskie, A. Mainzer, K. A. Marsh, C. A. Beichman, A. J. Burgasser, L. A. Prato, R. A. Simcoe, M. S. Marley, D. Saumon, R. S. Freedman, P. R. Eisenhardt, and E. L. Wright (2011), The discovery of y dwarfs using data from the wide-field infrared survey explorer (WISE), *Astrophysical Journal*, *743*(1), doi:10.1088/0004-637X/743/1/50.

Daley-Yates, S., and I. R. Stevens (2018), Inhibition of the electron cyclotron maser instability in the dense magnetosphere of a hot jupiter, *Monthly Notices of the Royal Astronomical Society*, *479*(1), 1194–1209, doi:10.1093/mnras/sty1652.

Daley-Yates, S., and I. R. Stevens (2019), Hot Jupiter accretion: 3D MHD simulations of star-planet-wind interaction, *Monthly Notices of the Royal Astronomical Society*, *483*(2), 2600–2614, doi:10.1093/mnras/sty3310.

Davenport, J. R. A., S. L. Hawley, L. Hebb, J. P. Wisniewski, A. F. Kowalski, E. C. Johnson, M. Malatesta, J. Peraza, M. Keil, S. M. Silverberg, T. C. Jansen, M. S. Scheffler, J. R. Berdis, D. M. Larsen, and E. J. Hilton (2014), Kepler flares.

II. The temporal morphology of white-light flares on GJ 1243, *Astrophysical Journal*, *797*(2), 122, doi:10.1088/0004-637X/797/2/122.

de Mooij, E. J. W., M. Brogi, R. J. de Kok, J. Koppenhoefer, S. V. Nefs, I. A. G. Snellen, J. Greiner, J. Hanse, R. C. Heinsbroek, C. H. Lee, and P. P. van der Werf (2012), Optical to near-infrared transit observations of super-Earth GJ 1214b: water-world or mini-Neptune?, *Astronomy and Astrophysics*, *538*, A46, doi:10.1051/0004-6361/201117205.

De Wit, J., H. R. Wakeford, M. Gillon, N. K. Lewis, J. A. Valenti, B. O. Demory, A. J. Burgasser, A. Burdanov, L. Delrez, E. Jehin, S. M. Lederer, D. Queloz, A. H. M. J. Triaud, and V. Van Grootel (2016), A combined transmission spectrum of the Earth-sized exoplanets TRAPPIST-1 b and c, *Nature*, *537*(7618), 69–72, doi:10.1038/nature18641.

de Wit, J., H. R. Wakeford, N. K. Lewis, L. Delrez, M. Gillon, F. Selsis, J. Leconte, B.-O. Demory, E. Bolmont, V. Bourrier, A. J. Burgasser, S. Grimm, E. Jehin, S. M. Lederer, J. E. Owen, V. Stamenković, and A. H. M. J. Triaud (2018), Atmospheric reconnaissance of the habitable-zone Earth-sized planets orbiting TRAPPIST-1, *Nature Astronomy*, *2*, 214–219, doi:10.1038/s41550-017-0374-z.

Dedner, A., F. Kemm, D. Kröner, C. D. Munz, T. Schnitzer, and M. Wesenberg (2002), Hyperbolic Divergence Cleaning for the MHD Equations, *Journal of Computational Physics*, *175*(2), 645–673, doi:10.1006/jcph.2001.6961.

Delrez, L., M. Gillon, A. H. Triaud, B. O. Demory, J. de Wit, J. G. Ingalls, E. Agol, E. Bolmont, A. Burdanov, A. J. Burgasser, S. J. Carey, E. Jehin, J. Leconte, S. Lederer, D. Queloz, F. Selsis, and V. Van Grootel (2018), Early 2017 observations of TRAPPIST-1 with Spitzer, *Monthly Notices of the Royal Astronomical Society*, *475*(3), 3577–3597, doi:10.1093/mnras/sty051.

Dermott, S. F., and C. Sagan (1995), Tidal effects of disconnected hydrocarbon seas on Titan, *Nature*, *374*(6519), 238–240, doi:10.1038/374238a0.

Dorn, C., K. Mosegaard, S. L. Grimm, and Y. Alibert (2018), Interior Characterization in Multiplanetary Systems: TRAPPIST-1, *The Astrophysical Journal*, *865*(1), 20, doi:10.3847/1538-4357/aad95d.

Dougherty, M. K., K. K. Khurana, F. M. Neubauer, C. T. Russell, J. Saur, J. S. Leisner, and M. E. Burton (2006), Identification of a Dynamic Atmosphere at Enceladus with the Cassini Magnetometer, *Science*, *311*(5766), 1406–1409, doi:10.1126/science.1120985.

Drake, D. J., J. W. R. Schroeder, G. G. Howes, C. A. Kletzing, F. Skiff, T. A. Carter, and D. W. Auerbach (2013), Alfvén wave collisions, the fundamental building block of plasma turbulence. IV. Laboratory experiment, *Physics of Plasmas*, *20*(7), 072901, doi:10.1063/1.4813242.

Duling, S., J. Saur, and J. Wicht (2014), Consistent boundary conditions at nonconducting surfaces of planetary bodies: Applications in a new Ganymede MHD model, *Journal of Geophysical Research: Space Physics*, *119*(6), 4412–4440, doi:10.1002/2013JA019554.

Eddy, J. A., and R. Ise (1979), *A new sun : the solar results from SKYLAB*.

Fabrycky, D. C., J. J. Lissauer, D. Ragozzine, J. F. Rowe, J. H. Steffen, E. Agol, T. Barclay, N. Batalha, W. Borucki, D. R. Ciardi, E. B. Ford, T. N. Gautier, J. C. Geary, M. J. Holman, J. M. Jenkins, J. Li, R. C. Morehead, R. L. Morris, A. Shporer, J. C. Smith, M. Still, and J. Van Cleve (2014), Architecture of Kepler's Multi-transiting Systems. II. New Investigations with Twice as Many Candidates, *The Astrophysical Journal*, *790*(2), 146, doi:10.1088/0004-637X/790/2/146.

Fischer, C., and J. Saur (2019), Time-variable Electromagnetic Star–Planet Interaction: The TRAPPIST-1 System as an Exemplary Case, *The Astrophysical Journal*, *872*(1), 113, doi:10.3847/1538-4357/aafaf2.

France, K., R. O. P. Loyd, A. Youngblood, A. Brown, P. C. Schneider, S. L. Hawley, C. S. Froning, J. L. Linsky, A. Roberge, A. P. Buccino, J. R. A. Davenport, J. M. Fontenla, L. Kaltenegger, A. F. Kowalski, P. J. D. Mauas, Y. Miguel, S. Redfield, S. Rugheimer, F. Tian, M. C. Vieytes, L. M. Walkowicz, and K. L. Weisenburger (2016), The MUSCLES Treasury Survey. I. Motivation and Overview, *The Astrophysical Journal*, *820*(2), 89, doi:10.3847/0004-637X/820/2/89.

France, K., N. Arulanantham, L. Fossati, A. F. Lanza, R. O. P. Loyd, S. Redfield, and P. C. Schneider (2018), Far-ultraviolet Activity Levels of F, G, K, and M Dwarf Exoplanet Host Stars, *The Astrophysical Journal Supplement Series*, *239*(1), 16, doi:10.3847/1538-4365/aae1a3.

Frank, L. A., K. L. Ackerson, J. H. Wolfe, and J. D. Mihalov (1976), Observations of plasmas in the Jovian magnetosphere, *Journal of Geophysical Research*, *81*(4), 457, doi:10.1029/JA081i004p00457.

Frank, L. A., W. R. Paterson, K. L. Ackerson, V. M. Vasyliunas, F. V. Coroniti, and S. J. Bolton (1996), Plasma Observations at lo with the Galileo Spacecraft, *Science*, *274*(5286), 394–395, doi:10.1126/science.274.5286.394.

Fressin, F., G. Torres, J. F. Rowe, D. Charbonneau, L. A. Rogers, S. Ballard, N. M. Batalha, W. J. Borucki, S. T. Bryson, L. A. Buchhave, D. R. Ciardi, J.-M. Désert, C. D. Dressing, D. C. Fabrycky, E. B. Ford, I. Gautier, Thomas N., C. E. Henze, M. J. Holman, A. Howard, S. B. Howell, J. M. Jenkins, D. G. Koch, D. W. Latham, J. J. Lissauer, G. W. Marcy, S. N. Quinn, D. Ragozzine, D. D. Sasselov, S. Seager, T. Barclay, F. Mullally, S. E. Seader, M. Still, J. D. Twicken, S. E. Thompson, and K. Uddin (2012), Two Earth-sized planets orbiting Kepler-20, *Nature*, *482*(7384), 195–198, doi:10.1038/nature10780.

Garraffo, C., J. J. Drake, and O. Cohen (2016), The Space Weather of Proxima Centauri b, *The Astrophysical Journal Letters*, *833*(1), L4, doi:10.3847/2041-8205/833/1/L4.

Garraffo, C., J. J. Drake, O. Cohen, J. D. Alvarado-Gómez, and S. P. Moschou (2017), The Threatening Magnetic and Plasma Environment of the TRAPPIST-1 Planets, *The Astrophysical Journal*, *843*(2), L33, doi:10.3847/2041-8213/aa79ed.

Giampapa, M. S., R. Rosner, V. Kashyap, T. A. Fleming, J. H. Schmitt, and J. A. Bookbinder (1996), The Coronae of low-mass dwarf stars, *The Astrophysical Journal*, *463*, 707–725.

Gillon, M., E. Jehin, S. M. Lederer, L. Delrez, J. De Wit, A. Burdanov, V. Van Grootel, A. J. Burgasser, A. H. M. J. Triaud, C. Opitom, B. O. Demory, D. K. Sahu, D. Bardalez Gagliuffi, P. Magain, and D. Queloz (2016), Temperate Earth-sized planets transiting a nearby ultracool dwarf star, *Nature*, *533*(7602), 221–224, doi:10.1038/nature17448.

Gillon, M., A. H. M. J. Triaud, B. O. Demory, E. Jehin, E. Agol, K. M. Deck, S. M. Lederer, J. De Wit, A. Burdanov, J. G. Ingalls, E. Bolmont, J. Leconte, S. N. Raymond, F. Selsis, M. Turbet, K. Barkaoui, A. Burgasser, M. R. Burleigh, S. J. Carey, A. Chaushev, C. M. Copperwheat, L. Delrez, C. S. Fernandes, D. L. Holdsworth, E. J. Kotze, V. Van Grootel, Y. Almleaky, Z. Benkhaldoun, P. Magain, and D. Queloz (2017), Seven temperate terrestrial planets around the nearby ultracool dwarf star TRAPPIST-1, *Nature*, *542*(7642), 456–460, doi:10.1038/nature21360.

Gizis, J. E., D. G. Monet, I. N. Reid, J. D. Kirkpatrick, J. Liebert, and R. J. Williams (2000), New Neighbors from 2MASS: Activity and Kinematics at the Bottom of the Main Sequence, *Astronomical Journal*, *120*(2), 1085–1099, doi:10.1086/301456.

Goertz, C. K. (1980), Io's interaction with the plasma torus, *Journal of Geophysical Research*, *85*(A6), 2949–2956, doi:10.1029/JA085iA06p02949.

Goldreich, P., and D. Lynden-Bell (1969), Io, a jovian unipolar inductor, *The Astrophysical Journal*, *156*, 59–78, doi:10.1086/149947.

Gombosi, T. I., D. L. DeZeeuw, C. P. T. Groth, K. G. Powell, and Q. F. Stout (2000), Multiscale MHD simulation of a coronal mass ejection and its interaction with the magnetosphere-ionosphere system, *Journal of Atmospheric and Solar-Terrestrial Physics*, *62*(16), 1515–1525, doi:10.1016/S1364-6826(00)00091-2.

Grimm, S. L., B.-O. Demory, M. Gillon, C. Dorn, E. Agol, A. Burdanov, L. Delrez, M. Sestovic, A. H. M. J. Triaud, M. Turbet, É. Bolmont, A. Caldas, J. de Wit, E. Jehin, J. Leconte, S. N. Raymond, V. Van Grootel, A. J. Burgasser, S. Carey, D. Fabrycky, K. Heng, D. M. Hernandez, J. G. Ingalls, S. Lederer, F. Selsis, and D. Queloz (2018), The nature of the TRAPPIST-1 exoplanets, *Astronomy and Astrophysics*, *613*, A68, doi:10.1051/0004-6361/201732233.

Grodent, D., J. C. Gérard, J. Gustin, B. H. Mauk, J. E. P. Connerney, and J. T. Clarke (2006), Europa's FUV auroral tail on Jupiter, *Geophysical Research Letters*, *33*(6), L06201, doi:10.1029/2005GL025487.

Grodent, D., B. Bonfond, A. Radioti, J.-C. Gérard, X. Jia, J. D. Nichols, and J. T. Clarke (2009), Auroral footprint of Ganymede, *Journal of Geophysical Research (Space Physics)*, *114*(A7), A07212, doi:10.1029/2009JA014289.

Hallinan, G., S. P. Littlefair, G. Cotter, S. Bourke, L. K. Harding, J. S. Pineda, R. P. Butler, A. Golden, G. Basri, J. G. Doyle, M. M. Kao, S. V. Berdyugina, A. Kuznetsov, M. P. Rupen, and A. Antonova (2015), Magnetospherically driven optical and radio aurorae at the end of the stellar main sequence, *Nature*, *523*(7562), 568–571, doi:10.1038/nature14619.

Hansen, C. J., S. D. Kawaler, and V. Trimble (2004), *Stellar interiors : physical principles, structure, and evolution*, Springer Science+ Business Media, LLC.

Hanslmeier, A. (2007), *The Solar Atmosphere and Active Regions*, pp. 47–95, Springer Netherlands, Dordrecht, doi:10.1007/978-1-4020-5604-8_3.

Helled, R., N. Nettelmann, and T. Guillot (2020), Uranus and Neptune: Origin, Evolution and Internal Structure, *Space Science Reviews*, *216*(3), 38, doi:10.1007/s11214-020-00660-3.

Henning, W. G., R. J. O'Connell, and D. D. Sasselov (2009), Tidally Heated Terrestrial Exoplanets: Viscoelastic Response Models, *The Astrophysical Journal*, *707*(2), 1000–1015, doi:10.1088/0004-637X/707/2/1000.

Hill, T. W. (1979), Inertial Limit on Corotation., *Journal of Geophysical Research*, *84*(A11), 6554–6558, doi:10.1029/JA084iA11p06554.

Hill, T. W. (2001), The Jovian auroral oval, *Journal of Geophysical Research*, *106*(A5), 8101–8108, doi:10.1029/2000JA000302.

Hill, T. W., and F. C. Michel (1976), Heavy Ions From the Galilean Satellites and the Centrifugal Distortion of the Jovian Magnetosphere., *J Geophys Res*, *81*(25), 4561–4565, doi:10.1029/JA081i025p04561.

Hirano, T., E. Gaidos, J. N. Winn, F. Dai, A. Fukui, M. Kuzuhara, T. Kotani, M. Tamura, M. Hjorth, S. Albrecht, D. Huber, E. Bolmont, H. Harakawa, K. Hodapp, M. Ishizuka, S. Jacobson, M. Konishi, T. Kudo, T. Kurokawa, J. Nishikawa, M. Omiya, T. Serizawa, A. Ueda, and L. M. Weiss (2020), Evidence for Spin-Orbit Alignment in the TRAPPIST-1 System, *The Astrophysical Journal Letters*, *890*(2), L27, doi:10.3847/2041-8213/ab74dc.

Howes, G. G., and K. D. Nielson (2013), Alfvén wave collisions, the fundamental building block of plasma turbulence. I. Asymptotic solution, *Physics of Plasmas*, *20*(7), 072302, doi:10.1063/1.4812805.

Howes, G. G., A. J. McCubbin, and K. G. Klein (2018), Spatially localized particle energization by Landau damping in current sheets produced by strong Alfvén wave collisions, *Journal of Plasma Physics*, *84*(1), 905840105, doi:10.1017/S0022377818000053.

Huang, S.-S. (1959), Occurrence of Life in the Universe, *American Scientist*, *47*(3), 397–402.

Hubbard, W. B., W. J. Nellis, A. C. Mitchell, N. C. Holmes, S. S. Limaye, and P. C. McCandless (1991), Interior Structure of Neptune: Comparison with Uranus, *Science*, *253*(5020), 648–651, doi:10.1126/science.253.5020.648.

Ip, W.-H., A. Kopp, and J.-H. Hu (2004), On the Star-Magnetosphere Interaction of Close-in Exoplanets, *The Astrophysical Journal*, *602*(1), L53—-L56, doi:10.1086/382274.

Jacobsen, S., F. M. Neubauer, J. Saur, and N. Schilling (2007), Io's nonlinear MHD-wave field in the heterogeneous Jovian magnetosphere, *Geophysical Research Letters*, *34*(10), 1–5, doi:10.1029/2006GL029187.

Jacobsen, S., J. Saur, F. M. Neubauer, B. Bonfond, J.-C. Gérard, and D. Grodent (2010), Location and spatial shape of electron beams in Io's wake, *Journal of Geophysical Research: Space Physics*, *115*(A4), A04,205, doi:10.1029/2009ja014753.

Jeffrey, A., and T. Taniuti (1964), *Non-linear wave propagation.*

Jenkins, J. M., J. D. Twicken, N. M. Batalha, D. A. Caldwell, W. D. Cochran, M. Endl, D. W. Latham, G. A. Esquerdo, S. Seader, A. Bieryla, E. Petigura, D. R. Ciardi, G. W. Marcy, H. Isaacson, D. Huber, J. F. Rowe, G. Torres, S. T. Bryson, L. Buchhave, I. Ramirez, A. Wolfgang, J. Li, J. R. Campbell, P. Tenenbaum, D. Sand erfer, C. E. Henze, J. H. Catanzarite, R. L. Gilliland, and W. J. Borucki (2015), Discovery and Validation of Kepler-452b: A 1.6 R $\oplus$ Super Earth Exoplanet in the Habitable Zone of a G2 Star, *Astronomical Journal*, *150*(2), 56, doi:10.1088/0004-6256/150/2/56.

Jia, X., R. J. Walker, M. G. Kivelson, K. K. Khurana, and J. A. Linker (2008), Three-dimensional MHD simulations of Ganymede's magnetosphere, *Journal of Geophysical Research (Space Physics)*, *113*(A6), A06212, doi:10.1029/2007JA012748.

Jia, X., R. J. Walker, M. G. Kivelson, K. K. Khurana, and J. A. Linker (2009), Properties of Ganymede's magnetosphere inferred from improved three-dimensional MHD simulations, *Journal of Geophysical Research (Space Physics)*, *114*(A9), A09209, doi:10.1029/2009JA014375.

Kaltenegger, L., D. Sasselov, and S. Rugheimer (2013), Water-planets in the Habitable Zone: Atmospheric Chemistry, Observable Features, and the Case of Kepler-62e and -62f, *The Astrophysical Journal Letters*, *775*(2), L47, doi:10.1088/2041-8205/775/2/L47.

Kao, M. M., G. Hallinan, J. S. Pineda, I. Escala, A. Burgasser, S. Bourke, and D. Stevenson (2016), Auroral Radio Emission From Late L and T Dwarfs: a New Constraint on Dynamo Theory in the Substellar Regime, *The Astrophysical Journal*, *818*(1), 24, doi:10.3847/0004-637x/818/1/24.

Kasting, J. F., D. P. Whitmire, and R. T. Reynolds (1993), Habitable Zones around Main Sequence Stars, *Icarus*, *101*(1), 108–128, doi:10.1006/icar.1993.1010.

Kislyakova, K. G., L. Fossati, C. P. Johnstone, L. Noack, T. Lüftinger, V. V. Zaitsev, and H. Lammer (2018), Effective Induction Heating around Strongly Magnetized Stars, *The Astrophysical Journal*, *858*(2), 105, doi:10.3847/1538-4357/aabae4.

Kivelson, M. G., K. K. Khurana, R. J. Walker, J. Warnecke, C. T. Russell, J. A. Linker, D. J. Southwood, and C. Polanskey (1996a), Lo's Interaction with the Plasma Torus: Galileo Magnetometer Report, *Science*, *274*(5286), 396–398, doi: 10.1126/science.274.5286.396.

Kivelson, M. G., K. K. Khurana, C. T. Russell, R. J. Walker, J. Warnecke, F. V. Coroniti, C. Polanskey, D. J. Southwood, and G. Schubert (1996b), Discovery of Ganymede's magnetic field by the Galileo spacecraft, *Nature*, *384*(6609), 537–541, doi:10.1038/384537a0.

Kivelson, M. G., F. Bagenal, W. S. Kurth, F. M. Neubauer, C. Paranicas, and J. Saur (2007), *Magnetospheric Interactions with Satellites*, p. 513.

Kopp, A., S. Schilp, and S. Preusse (2011), Magnetohydrodynamic simulations of the magnetic interaction of hot jupiters with their host stars: A numerical experiment, *Astrophysical Journal*, *729*(2), 116, doi:10.1088/0004-637X/729/2/116.

Kopp, R. A., and G. W. Pneuman (1976), Magnetic reconnection in the corona and the loop prominence phenomenon., *Solar Physics*, *50*(1), 85–98, doi:10.1007/BF00206193.

Krejčová, T., and J. Budaj (2012), Evidence for enhanced chromospheric Ca II H and K emission in stars with close-in extrasolar planets, *Astronomy and Astrophysics*, *540*, A82, doi:10.1051/0004-6361/201118247.

Kuchner, M. J. (2003), Volatile-rich Earth-Mass Planets in the Habitable Zone, *The Astrophysical Journal Letters*, *596*(1), L105–L108, doi:10.1086/378397.

Lammer, H., J. H. Bredehöft, A. Coustenis, M. L. Khodachenko, L. Kaltenegger, O. Grasset, D. Prieur, F. Raulin, P. Ehrenfreund, M. Yamauchi, J. E. Wahlund, J. M. Grießmeier, G. Stangl, C. S. Cockell, Y. N. Kulikov, J. L. Grenfell, and H. Rauer (2009), What makes a planet habitable?, *The Astronomy and Astrophysics Review*, *17*(2), 181–249, doi:10.1007/s00159-009-0019-z.

Lanza, A. F. (2009), Stellar coronal magnetic fields and star-planet interaction, *Astronomy and Astrophysics*, *505*(1), 339–350, doi:10.1051/0004-6361/200912367.

Lanza, A. F. (2012), Star-planet magnetic interaction and activity in late-type stars with close-in planets, *Astronomy and Astrophysics*, *544*(A23), A23, doi: 10.1051/0004-6361/201219002.

Lanza, A. F. (2013), Star-planet magnetic interaction and evaporation of planetary atmospheres, *Astronomy and Astrophysics*, *557*(A31), A31, doi:10.1051/0004-6361/201321790.

Lanza, A. F. (2015), Star-Planet Interactions, *18*, 811–830.

Lanza, A. F. (2018), Close-by planets and flares in their host stars, *Astronomy and Astrophysics*, *610*, A81, doi:10.1051/0004-6361/201731414.

Léger, A., F. Selsis, C. Sotin, T. Guillot, D. Despois, D. Mawet, M. Ollivier, A. Labèque, C. Valette, F. Brachet, B. Chazelas, and H. Lammer (2004), A new family of planets? "Ocean-Planets", *Icarus*, *169*(2), 499–504, doi:10.1016/j.icarus.2004.01.001.

Linker, J. A., M. G. Kivelson, and R. J. Walker (1988), An MHD simulation of plasma flow past Io: Alfvén and slow mode perturbations, *Geophysical Research Letters*, *15*(11), 1311–1314, doi:10.1029/GL015i011p01311.

Luger, R., M. Sestovic, E. Kruse, S. L. Grimm, B. O. Demory, E. Agol, E. Bolmont, D. Fabrycky, C. S. Fernandes, V. Van Grootel, A. Burgasser, M. Gillon, J. G. Ingalls, E. Jehin, S. N. Raymond, F. Selsis, A. H. M. J. Triaud, T. Barclay, G. Barentsen, S. B. Howell, L. Delrez, J. De Wit, D. Foreman-Mackey, D. L. Holdsworth, J. Leconte, S. Lederer, M. Turbet, Y. Almleaky, Z. Benkhaldoun, P. Magain, B. M. Morris, K. Heng, and D. Queloz (2017), A seven-planet resonant chain in TRAPPIST-1, *Nature Astronomy*, *1*(May), 1–36, doi:10.1038/s41550-017-0129.

Martín, E. L., X. Delfosse, G. Basri, B. Goldman, T. Forveille, and M. R. Zapatero Osorio (1999), Spectroscopic Classification of Late-M and L Field Dwarfs, *Astronomical Journal*, *118*(5), 2466–2482, doi:10.1086/301107.

Mayor, M., and D. Queloz (1995), A Jupiter-mass companion to a solar-type star, *Nature*, *378*(6555), 355–359, doi:10.1038/378355a0.

McLean, I. S., L. Prato, S. S. Kim, M. K. Wilcox, J. D. Kirkpatrick, and A. Burgasser (2001), Near-Infrared Spectroscopy of Brown Dwarfs: Methane and the Transition between the L and T Spectral Types, *The Astrophysical Journal Letters*, *561*(1), L115–L118, doi:10.1086/324380.

Mignone, A., G. Bodo, S. Massaglia, T. Matsakos, O. Tesileanu, C. Zanni, and A. Ferrari (2007), PLUTO: A Numerical Code for Computational Astrophysics, *The Astrophysical Journal Supplement Series*, *170*(1), 228–242, doi:10.1086/513316.

Militzer, B., F. Soubiran, S. M. Wahl, and W. Hubbard (2016), Understanding Jupiter's interior, *Journal of Geophysical Research (Planets)*, *121*(9), 1552–1572, doi:10.1002/2016JE005080.

Miller, B. P., E. Gallo, J. T. Wright, and A. K. Dupree (2012), On the detectability of star-planet interaction, *Astrophysical Journal*, *754*(2), 137, doi:10.1088/0004-637X/754/2/137.

Mohanty, S., R. Jayawardhana, N. Huélamo, and E. Mamajek (2007), The Planetary Mass Companion 2MASS 1207-3932B: Temperature, Mass, and Evidence for an Edge-on Disk, *The Astrophysical Journal*, *657*(2), 1064–1091, doi:10.1086/510877.

Morgan, W. W., P. C. Keenan, and E. Kellman (1943), *An atlas of stellar spectra, with an outline of spectral classification.*

Morin, J., J. F. Donati, P. Petit, X. Delfosse, T. Forveille, and M. M. Jardine (2010), Large-scale magnetic topologies of late M dwarfs, *Monthly Notices of the Royal Astronomical Society*, *407*(4), 2269–2286, doi:10.1111/j.1365-2966.2010.17101.x.

Mullan, D. J., J. G. Doyle, R. O. Redman, and M. Mathioudakis (1992), Limits on detectability of mass loss from cool dwarfs, *The Astrophysical Journal*, *397*, 225–231.

Nakagawa, Y. (1981), Evolution of magnetic field and atmospheric response. I - Three-dimensional formulation by the method of projected characteristics. II - Formulation of proper boundary equations, *The Astrophysical Journal*, *247*, 707–733, doi:10.1086/159082.

Neubauer, F. M. (1980), Nonlinear standing Alfvén wave current system at Io: Theory, *Journal of Geophysical Research: Space Physics*, *85*(A3), 1171–1178, doi:10.1029/ja085ia03p01171.

Neubauer, F. M. (1998), The sub-Alfvénic interaction of the Galilean satellites with the Jovian magnetosphere, *Journal of Geophysical Research*, *103*(E9), 19,843–19,866, doi:10.1029/97JE03370.

Neubauer, F. M. (1999), Alfvén wings and electromagnetic induction in the interiors: Europa and Callisto, *Journal of Geophysical Research: Space Physics*, *104*(A12), 28,671–28,684, doi:10.1029/1999ja900217.

O'Malley-James, J. T., and L. Kaltenegger (2017), UV surface habitability of the TRAPPIST-1 system, *Monthly Notices of the Royal Astronomical Society: Letters*, *469*(1), L26—-L30, doi:10.1093/mnrasl/slx047.

Parker, E. N. (1958), Dynamics of the Interplanetary Gas and Magnetic Fields., *The Astrophysical Journal*, *128*, 664, doi:10.1086/146579.

Parker, E. N. (1988), Nanoflares and the Solar X-Ray Corona, *The Astrophysical Journal*, *330*, 474–479.

Pillitteri, I., S. J. Wolk, O. Cohen, V. Kashyap, H. Knutson, C. M. Lisse, and G. W. Henry (2010), XMM-Newton observations of HD 189733 during planetary transits, *Astrophysical Journal*, *722*(2), 1216–1225, doi:10.1088/0004-637X/722/2/1216.

Poppenhaeger, K., and S. J. Wolk (2014), Indications for an influence of hot Jupiters on the rotation and activity of their host stars, *Astronomy and Astrophysics*, *565*(L1), L1, doi:10.1051/0004-6361/201423454.

Poppenhaeger, K., J. Robrade, and J. H. M. M. Schmitt (2010), Coronal properties of planet-bearing stars, *Astronomy and Astrophysics*, *515*(A98), A98, doi:10.1051/0004-6361/201014245.

Poppenhaeger, K., L. F. Lenz, A. Reiners, J. H. M. M. Schmitt, and E. Shkolnik (2011), A search for star-planet interactions in the υ Andromedae system at X-ray and optical wavelengths, *Astronomy and Astrophysics*, *528*, A58, doi:10.1051/0004-6361/201016008.

Powell, K. G. (1997), *An Approximate Riemann Solver for Magnetohydrodynamics*, pp. 570–583, Springer Berlin Heidelberg, Berlin, Heidelberg, doi: 10.1007/978-3-642-60543-7_23.

Prangé, R., D. Rego, D. Southwood, P. Zarka, S. Miller, and W. Ip (1996), Rapid energy dissipation and variability of the lo-Jupiter electrodynamic circuit, *Nature*, *379*(6563), 323–325, doi:10.1038/379323a0.

Preusse, S., A. Kopp, J. Büchner, and U. Motschmann (2005), Stellar wind regimes of close-in extrasolar planets, *Astronomy and Astrophysics*, *434*(3), 1191–1200, doi:10.1051/0004-6361:20041680.

Preusse, S., A. Kopp, J. Büchner, and U. Motschmann (2006), A magnetic communication scenario for hot Jupiters, *Astronomy and Astrophysics*, *460*(1), 317–322, doi:10.1051/0004-6361:20065353.

Preusse, S., A. Kopp, J. Büchner, and U. Motschmann (2007), MHD simulation scenarios of the stellar wind interaction with Hot Jupiter magnetospheres, *Planetary and Space Science*, *55*(5), 589–597, doi:10.1016/j.pss.2006.04.037.

Pryor, W. R., A. M. Rymer, D. G. Mitchell, T. W. Hill, D. T. Young, J. Saur, G. H. Jones, S. Jacobsen, S. W. H. Cowley, B. H. Mauk, A. J. Coates, J. Gustin, D. Grodent, J. C. Gérard, L. Lamy, J. D. Nichols, S. M. Krimigis, L. W. Esposito, M. K. Dougherty, A. J. Jouchoux, A. I. F. Stewart, W. E. McClintock, G. M. Holsclaw, J. M. Ajello, J. E. Colwell, A. R. Hendrix, F. J. Crary, J. T. Clarke, and X. Zhou (2011), The auroral footprint of Enceladus on Saturn, *Nature*, *472*(7343), 331–333, doi:10.1038/nature09928.

Pulkkinen, T. (2007), Space Weather: Terrestrial Perspective, *Living Reviews in Solar Physics*, *4*(1), 1, doi:10.12942/lrsp-2007-1.

Rackham, B. V., D. Apai, and M. S. Giampapa (2018), The Transit Light Source Effect: False Spectral Features and Incorrect Densities for M-dwarf Transiting Planets, *The Astrophysical Journal*, *853*(2), 122, doi:10.3847/1538-4357/aaa08c.

Reiners, A., and G. Basri (2009), On the magnetic topology of partially and fully convective stars, *Astronomy and Astrophysics*, *496*(3), 787–790, doi:10.1051/0004-6361:200811450.

Reiners, A., and G. Basri (2010), A volume-limited sample of 63 M7-M9.5 dwarfs. II. Activity, magnetism, and the fade of the rotation-dominated dynamo, *Astrophysical Journal*, *710*(2), 924–935, doi:10.1088/0004-637X/710/2/924.

Reiners, A., M. Zechmeister, J. A. Caballero, I. Ribas, J. C. Morales, S. V. Jeffers, P. Schöfer, L. Tal-Or, A. Quirrenbach, P. J. Amado, A. Kaminski, W. Seifert, M. Abril, J. Aceituno, F. J. Alonso-Floriano, M. Ammler-Von Eiff, R. Antona, G. Anglada-Escudé, H. Anwand-Heerwart, B. Arroyo-Torres, M. Azzaro, D. Baroch, D. Barrado, F. F. Bauer, S. Becerril, V. J. S. Béjar, D. Benítez, Z. M. Berdinas, G. Bergond, M. Blümcke, M. Brinkmöller, C. Del Burgo, J. Cano, M. C. Cárdenas Vázquez, E. Casal, C. Cifuentes, A. Claret, J. Colomé, M. Cortés-Contreras, S. Czesla, E. Díez-Alonso, S. Dreizler, C. Feiz,

M. Fernández, I. M. Ferro, B. Fuhrmeister, D. Galadí-Enríquez, A. Garcia-Piquer, M. L. García Vargas, L. Gesa, V. G. Galera, J. I. González Hernández, R. González-Peinado, U. Grözinger, S. Grohnert, J. Guàrdia, E. W. Guenther, A. Guijarro, E. D. Guindos, J. Gutiérrez-Soto, H. J. Hagen, A. P. Hatzes, P. H. Hauschildt, R. P. Hedrosa, J. Helmling, T. Henning, I. Hermelo, R. Hernández Arabí, L. Hernández Castaño, F. Hernández Hernando, E. Herrero, A. Huber, P. Huke, E. N. Johnson, E. D. Juan, M. Kim, R. Klein, J. Klüter, A. Klutsch, M. Kürster, M. Lafarga, A. Lamert, M. Lampón, L. M. Lara, W. Laun, U. Lemke, R. Lenzen, R. Launhardt, M. López Del Fresno, J. López-González, M. López-Puertas, J. F. López Salas, J. López-Santiago, R. Luque, H. Magán Madinabeitia, U. Mall, L. Mancini, H. Mandel, E. Marfil, J. A. Marín Molina, D. Maroto Fernández, E. L. Martín, S. Martín-Ruiz, C. J. Marvin, R. J. Mathar, E. Mirabet, D. Montes, M. E. Moreno-Raya, A. Moya, R. Mundt, E. Nagel, V. Naranjo, L. Nortmann, G. Nowak, A. Ofir, R. Oreiro, E. Pallé, J. Panduro, J. Pascual, V. M. Passegger, A. Pavlov, S. Pedraz, A. Pérez-Calpena, D. P. Medialdea, M. Perger, M. A. C. Perryman, M. Pluto, O. Rabaza, A. Ramón, R. Rebolo, P. Redondo, S. Reffert, S. Reinhart, P. Rhode, H. W. Rix, F. Rodler, E. Rodríguez, C. Rodríguez-López, A. Rodríguez Trinidad, R. R. Rohloff, A. Rosich, S. Sadegi, E. Sánchez-Blanco, M. A. Sánchez Carrasco, A. Sánchez-López, J. Sanz-Forcada, P. Sarkis, L. F. Sarmiento, S. Schäfer, J. H. M. M. Schmitt, J. Schiller, A. Schweitzer, E. Solano, O. Stahl, J. B. P. Strachan, J. Stürmer, J. C. Suárez, H. M. Tabernero, M. Tala, T. Trifonov, S. M. Tulloch, R. G. Ulbrich, G. Veredas, J. I. Vico Linares, F. Vilardell, K. Wagner, J. Winkler, V. Wolthoff, W. Xu, F. Yan, and M. R. Zapatero Osorio (2018), The CARMENES search for exoplanets around M dwarfs: High-resolution optical and near-infrared spectroscopy of 324 survey stars, *Astronomy and Astrophysics*, *612*, A49, doi:10.1051/0004-6361/201732054.

Rubenstein, E. P., and B. E. Schaefer (2000), Are Superflares on Solar Analogues Caused by Extrasolar Planets?, *The Astrophysical Journal*, *529*(2), 1031–1033, doi:10.1086/308326.

Saar, S. H., M. Cuntz, V. L. Kashyap, and J. C. Hall (2008), First observation of planet-induced X-ray emission: The system HD 179949, in *Exoplanets: Detection, Formation and Dynamics*, *IAU Symposium*, vol. 249, edited by Y.-S. Sun, S. Ferraz-Mello, and J.-L. Zhou, pp. 79–81, doi:10.1017/S1743921308016414.

Saur, J. (2019), Mini-magnetospheres and Moon-magnetosphere interactions: Overview Moon-magnetosphere Interactions, *arXiv e-prints*, arXiv:1908.06446.

Saur, J., F. M. Neubauer, D. F. Strobel, and M. E. Summers (1999), Three-dimensional plasma simulation of Io's interaction with the Io plasma torus: Asymmetric plasma flow, *Journal of Geophysical Research: Space Physics*, *104*(A11), 25,105–25,126, doi:10.1029/1999ja900304.

Saur, J., F. M. Neubauer, and N. Schilling (2007), Hemisphere coupling in Enceladus' asymmetric plasma interaction, *Journal of Geophysical Research (Space Physics)*, *112*(A11), A11209, doi:10.1029/2007JA012479.

Saur, J., T. Grambusch, S. Duling, F. M. Neubauer, and S. Simon (2013), Magnetic energy fluxes in sub-Alfvénic planet star and moon planet interactions, *Astronomy and Astrophysics*, *552*(A119), A119, doi:10.1051/0004-6361/201118179.

Saur, J., C. Fischer, A. Wennmacher, P. D. Feldman, L. Roth, D. F. Strobel, and A. Reiners (2018), The UV Spectrum of the Ultracool Dwarf LSR J1835+3259 Observed with the Hubble Space Telescope , *The Astrophysical Journal*, *859*(1), 74, doi:10.3847/1538-4357/aabb55.

Scharf, C. A. (2010), Possible constraints on exoplanet magnetic field strengths from planet-star interaction, *Astrophysical Journal*, *722*(2), 1547–1555, doi:10.1088/0004-637X/722/2/1547.

Schilling, N., F. M. Neubauer, and J. Saur (2008), Influence of the internally induced magnetic field on the plasma interaction of Europa, *Journal of Geophysical Research (Space Physics)*, *113*(A3), A03203, doi:10.1029/2007JA012842.

Schmitt, J. H., A. Collura, S. Sciortino, G. S. Vaiana, F. R. Harnden, and R. Rosner (1990), Einstein observatory coronal temperatures of late-type stars, *The Astronomical Journal*, *365*, 704–728.

Schunk, R. W. (1975), Transport equations for aeronomy, *Planetary and Space Science*, *23*(3), 437–485, doi:10.1016/0032-0633(75)90118-X.

Schwenn, R. (2006), Space Weather: The Solar Perspective, *Living Reviews in Solar Physics*, *3*(1), 2, doi:10.12942/lrsp-2006-2.

Seager, S. (2013), Exoplanet Habitability, *Science*, *340*(6132), 577–581, doi:10.1126/science.1232226.

Shibata, K., and T. Magara (2011), Solar Flares: Magnetohydrodynamic Processes, *Living Reviews in Solar Physics*, *8*(1), 6, doi:10.12942/lrsp-2011-6.

Shkolnik, E., G. A. H. Walker, and D. A. Bohlender (2003), Evidence for Planet-induced Chromospheric Activity on HD 179949, *The Astrophysical Journal*, *597*(2), 1092–1096, doi:10.1086/378583.

Shkolnik, E., G. A. H. Walker, D. A. Bohlender, P. Gu, and M. Kurster (2005), Hot Jupiters and Hot Spots: The Short- and Long-Term Chromospheric Activity on Stars with Giant Planets, *The Astrophysical Journal*, *622*(2), 1075–1090, doi:10.1086/428037.

Shkolnik, E., D. A. Bohlender, G. A. H. Walker, and A. Collier Cameron (2008), The On/Off Nature of Star-Planet Interactions, *The Astrophysical Journal*, *676*(1), 628–638, doi:10.1086/527351.

Shkolnik, E. L. (2013), An Ultraviolet Investigation of Activity on Exoplanet Host Stars, *The Astrophysical Journal*, *766*(1), 9, doi:10.1088/0004-637X/766/1/9.

Simon, S., H. Kriegel, J. Saur, A. Wennmacher, F. M. Neubauer, E. Roussos, U. Motschmann, and M. K. Dougherty (2012), Analysis of Cassini magnetic field observations over the poles of Rhea, *Journal of Geophysical Research (Space Physics)*, *117*(A7), A07211, doi:10.1029/2012JA017747.

Smith, E. J. (2001), The heliospheric current sheet, *Journal of Geophysical Research: Space Physics*, *106*(A8), 15,819–15,831, doi:10.1029/2000ja000120.

Staab, D., C. A. Haswell, G. D. Smith, L. Fossati, J. R. Barnes, R. Busuttil, and J. S. Jenkins (2017), SALT observations of the chromospheric activity of transiting planet hosts: Mass-loss and star-planet interactions, *Monthly Notices of the Royal Astronomical Society*, *466*(1), 738–748, doi:10.1093/mnras/stw3172.

Strugarek, A. (2016), Assessing Magnetic Torques and Energy Fluxes in Close-in Star–Planet Systems, *The Astrophysical Journal*, *833*(2), 140, doi:10.3847/1538-4357/833/2/140.

Strugarek, A., A. S. Brun, and S. Matt (2012), On close-in magnetized star-planet interactions, in *SF2A-2012: Proceedings of the Annual meeting of the French Society of Astronomy and Astrophysics*, edited by S. Boissier, P. de Laverny, N. Nardetto, R. Samadi, D. Valls-Gabaud, and H. Wozniak, pp. 419–423.

Strugarek, A., A. S. Brun, S. P. Matt, and V. Réville (2014), On the diversity of magnetic interactions in close-in star-planet systems, *Astrophysical Journal*, *795*(1), 86, doi:10.1088/0004-637X/795/1/86.

Strugarek, A., A. S. Brun, S. P. Matt, and V. Réville (2015), MAGNETIC GAMES between A PLANET and ITS HOST STAR: The KEY ROLE of TOPOLOGY, *Astrophysical Journal*, *815*(2), 111, doi:10.1088/0004-637X/815/2/111.

Strugarek, A., A. S. Brun, J.-F. Donati, C. Moutou, and V. Réville (2019), Chasing Star–Planet Magnetic Interactions: The Case of Kepler-78, *The Astrophysical Journal*, *881*(2), 136, doi:10.3847/1538-4357/ab2ed5.

Tokano, T., C. P. McKay, F. M. Neubauer, S. K. Atreya, F. Ferri, M. Fulchignoni, and H. B. Niemann (2006), Methane drizzle on Titan, *Nature*, *442*(7101), 432–435, doi:10.1038/nature04948.

Tokar, R. L., R. E. Johnson, T. W. Hill, D. H. Pontius, W. S. Kurth, F. J. Crary, D. T. Young, M. F. Thomsen, D. B. Reisenfeld, A. J. Coates, G. R. Lewis, E. C. Sittler, and D. A. Gurnett (2006), The Interaction of the Atmosphere of Enceladus with Saturn's Plasma, *Science*, *311*(5766), 1409–1412, doi:10.1126/science.1121061.

Toriumi, S., and H. Wang (2019), Flare-productive active regions, *Living Reviews in Solar Physics*, *16*(1), 3, doi:10.1007/s41116-019-0019-7.

Turbet, M., E. Bolmont, J. Leconte, F. Forget, F. Selsis, G. Tobie, A. Caldas, J. Naar, and M. Gillon (2018), Modeling climate diversity, tidal dynamics and the fate of volatiles on TRAPPIST-1 planets, *Astronomy and Astrophysics*, *612*, A86, doi:10.1051/0004-6361/201731620.

Turnpenney, S., J. D. Nichols, G. A. Wynn, and M. R. Burleigh (2018), Exoplanet-induced Radio Emission from M Dwarfs, *The Astrophysical Journal*, *854*(1), 72, doi:10.3847/1538-4357/aaa59c.

Van Grootel, V., C. S. Fernandes, M. Gillon, E. Jehin, J. Manfroid, R. Scuflaire, A. J. Burgasser, K. Barkaoui, Z. Benkhaldoun, A. Burdanov, L. Delrez, B.-O. Demory, J. de Wit, D. Queloz, and A. H. M. J. Triaud (2018), Stellar Parameters for Trappist-1, *The Astrophysical Journal*, *853*(1), 30, doi:10.3847/1538-4357/aaa023.

Vanderburg, A., B. T. Montet, J. A. Johnson, L. A. Buchhave, L. Zeng, F. Pepe, A. Collier Cameron, D. W. Latham, E. Molinari, S. Udry, C. Lovis, J. M. Matthews, C. Cameron, N. Law, B. P. Bowler, R. Angus, C. Baranec, A. Bieryla, W. Boschin, D. Charbonneau, R. Cosentino, X. Dumusque, P. Figueira, D. B. Guenther, A. Harutyunyan, C. Hellier, R. Kuschnig, M. Lopez-Morales, M. Mayor, G. Micela, A. F. J. Moffat, M. Pedani, D. F. Phillips, G. Piotto, D. Pollacco, D. Queloz, K. Rice, R. Riddle, J. F. Rowe, S. M. Rucinski, D. Sasselov, D. Ségransan, A. Sozzetti, A. Szentgyorgyi, C. Watson, and W. W. Weiss (2015), Characterizing K2 Planet Discoveries: A Super-Earth Transiting the Bright K Dwarf HIP 116454, *The Astrophysical Journal*, *800*(1), 59, doi:10.1088/0004-637X/800/1/59.

Vida, K., and R. M. Roettenbacher (2018), Finding flares in Kepler data using machine-learning tools, *Astronomy and Astrophysics*, *616*(A163), A163, doi:10.1051/0004-6361/201833194.

Vida, K., Z. Kővári, A. Pál, K. Oláh, and L. Kriskovics (2017), Frequent Flaring in the TRAPPIST-1 System—Unsuited for Life?, *The Astrophysical Journal*, *841*(2), 124, doi:10.3847/1538-4357/aa6f05.

Vidotto, A. A., M. Jardine, M. Opher, J. F. Donati, and T. I. Gombosi (2011), Powerful winds from low-mass stars: V374 Peg, *Monthly Notices of the Royal Astronomical Society*, *412*(1), 351–362, doi:10.1111/j.1365-2966.2010.17908.x.

Vidotto, A. A., M. Jardine, J. Morin, J. F. Donati, M. Opher, and T. I. Gombosi (2014), M-dwarf stellar winds: The effects of realistic magnetic geometry on rotational evolution and planets, *Monthly Notices of the Royal Astronomical Society*, *438*(2), 1162–1175, doi:10.1093/mnras/stt2265.

Walker, G. A. H., B. Croll, J. M. Matthews, R. Kuschnig, D. Huber, W. W. Weiss, E. Shkolnik, S. M. Rucinski, D. B. Guenther, A. F. J. Moffat, and D. Sasselov (2008), MOST detects variability on τ Bootis A possibly induced by its planetary companion, *Astronomy and Astrophysics*, *482*(2), 691–697, doi:10.1051/0004-6361:20078952.

Wannawichian, S., J. T. Clarke, and J. D. Nichols (2010), Ten years of Hubble Space Telescope observations of the variation of the jovian satellites' auroral footprint brightness, *Journal of Geophysical Research: Space Physics*, *115*(2), A02,206, doi:10.1029/2009JA014456.

Wannawichian, S., J. T. Clarke, F. Bagenal, C. A. Peterson, and J. D. Nichols (2013), Longitudinal modulation of the brightness of Io's auroral footprint emission: Comparison with models, *Journal of Geophysical Research: Space Physics*, *118*(6), 3336–3345, doi:10.1002/jgra.50346.

Wargelin, B. J., and J. J. Drake (2002), Stringent X-Ray Constraints on Mass Loss from Proxima Centauri, *The Astrophysical Journal*, *578*(1), 503–514, doi: 10.1086/342270.

Warwick, C., and M. Wood (1959), A Study of Limb Flares and Associated Events., *The Astrophysical Journal*, *129*, 801, doi:10.1086/146676.

Warwick, C. S. (1955), Flare Height and Association with SID's., *The Astrophysical Journal*, *121*, 385, doi:10.1086/145997.

Weber, E. J., and J. Davis, Leverett (1967), The Angular Momentum of the Solar Wind, *The Astrophysical Journal*, *148*, 217–227, doi:10.1086/149138.

Wentzel, D. G. (1974), Coronal Heating by Alfvén Waves, *Solar Physics*, *39*(1), 129–140, doi:10.1007/BF00154975.

Wheatley, P. J., T. Louden, V. Bourrier, D. Ehrenreich, and M. Gillon (2017), Strong XUV irradiation of the Earth-sized exoplanets orbiting the ultracool dwarf TRAPPIST-1, *Monthly Notices of the Royal Astronomical Society: Letters*, *465*(1), L74—-L78, doi:10.1093/mnrasl/slw192.

Wood, B. E., J. L. Linsky, H.-R. Müller, and G. P. Zank (2001), Observational Estimates for the Mass-Loss Rates of α Centauri and Proxima Centauri Using Hubble Space Telescope Lyα Spectra, *The Astrophysical Journal Letters*, *547*(1), L49–L52, doi:10.1086/318888.

Wright, A. N. (1987), The interaction of Io's Alfvén waves with the Jovian magnetosphere, *Journal of Geophysical Research*, *92*(A9), 9963–9970, doi: 10.1029/JA092iA09p09963.

Wright, J. T., G. W. Marcy, D. A. Fischer, R. P. Butler, S. S. Vogt, C. G. Tinney, H. R. A. Jones, B. D. Carter, J. A. Johnson, C. McCarthy, and K. Apps (2007), Four New Exoplanets and Hints of Additional Substellar Companions to Exoplanet Host Stars, *The Astrophysical Journal*, *657*(1), 533–545, doi: 10.1086/510553.

Wu, C.-C., J. K. Chao, S. T. Wu, and M. Dryer (1996), Numerical Simulation of Slow Shocks in the Solar Wind, *Solar Physics*, *165*(2), 377–393, doi:10.1007/BF00149720.

Wu, S. T., A. H. Wang, Y. Liu, and J. T. Hoeksema (2006), Data-driven Magnetohydrodynamic Model for Active Region Evolution, *The Astrophysical Journal*, *652*(1), 800–811, doi:10.1086/507864.

Wu, S. T., A. H. Wang, and J. Cassibry (2010), Characteristic Boundary Conditions for Numerical Magnetohydrodynamic (MHD) Simulation of Solar and Laboratory Plasma Flows, in *Numerical Modeling of Space Plasma Flows, Astronum-2009*, *Astronomical Society of the Pacific Conference Series*, vol. 429, edited by N. V. Pogorelov, E. Audit, and G. P. Zank, p. 294.

Zanni, C., and J. Ferreira (2009), Mhd simulations of accretion onto a dipolar magnetosphere: I. accretion curtains and the disk-locking paradigm, *Astronomy and Astrophysics*, *508*(3), 1117–1133, doi:10.1051/0004-6361/200912879.

Zarka, P. (2007), Plasma interactions of exoplanets with their parent star and associated radio emissions, *Planetary and Space Science*, *55*(5), 598–617, doi: 10.1016/j.pss.2006.05.045.

Research Data Management

The data, Codes and scripts that were produced and written for this thesis are archived on the server
`neptun@geo.uni-koeln.de`
via the path
`/raid0/archivierung/absolventen_archivierung/2020_PhD_CFischer_SPI_Exoplanets`.
All data can be accessed via the Institute for Geophysics and Meteorology at the University of Cologne.

Necessary information about the structure of the archive are summarised in a *README*. The overall structure consists of three folders. The folder `Codes_and_Scripts` archives the necessary codes and scripts that we used to simulate physical processes, analyse data and generate images. The folder `MHD_data` stores the results of the MHD simulations and `Flare_data` stores the flare data of TRAPPIST-1 that we read out from *Luger et al.* (2017).

The use of the data and codes underlies a license that is further specified in the file *LICENSE*.

Acknowledgements

Saying thank you after a long project is always a pleasure because you can look back and see that you were not alone on your way.

First and foremost, I want to thank my supervisor J. Saur for his guidance, the time that he spent for me and my project, and of course, all the discussions and explanations.

A big thank you, goes to S. Janser, S. Schlegel and the other friends and colleagues at the Institute for the fun and the discussions we had on whatever topic.

Further, I want to acknowledge the funding by Verbundforschung für Astronomie und Astrophysik through grant No. 50 OR 170, the Regional Computing Centre of the University of Cologne for providing access to the HPC Cluster Cheops and A. Strugarek for pointing out the importance of certain Boundary Conditions.

A dissertation is long and full of errors. Therefore, thanks to S. Janser, S. Schlegel, C. Willmes and A. Oberdevermann for proofreading!

Some personal acknowledgements go to all the people, who were not directly involved in the science part but who supported me and kept me sane during my studies. Special thanks go to my family, my girlfriend, and my close friends, who supported me all the time!

Last but not least: Thanks to my beloved dog Buck for enjoyable interruptions during online meetings and for keeping me in shape in the time of writing.

Eidesstattliche Erklärung

Hiermit versichere ich an Eides statt, dass ich die vorliegende Dissertation selbstständig und ohne die Benutzung anderer als der angegebenen Hilfsmittel und Literatur angefertigt habe. Alle Stellen, die wörtlich oder sinngemäß aus veröffentlichten und nicht veröffentlichten Werken dem Wortlaut oder dem Sinn nach entnommen wurden, sind als solche kenntlich gemacht. Ich versichere an Eides statt, dass diese Dissertation noch keiner anderen Fakultät oder Universität zur Prüfung vorgelegen hat; dass sie - abgesehen von unten angegebenen Teilpublikationen und eingebundenen Artikeln und Manuskripten - noch nicht veröffentlicht worden ist sowie, dass ich eine Veröffentlichung der Dissertation vor Abschluss der Promotion nicht ohne Genehmigung des Promotionsausschusses vornehmen werde. Die Bestimmungen dieser Ordnung sind mir bekannt. Darüber hinaus erkläre ich hiermit, dass ich die Ordnung zur Sicherung guter wissenschaftlicher Praxis und zum Umgang mit wissenschaftlichem Fehlverhalten der Universität zu Köln gelesen und sie bei der Durchführung der Dissertation zugrundeliegenden Arbeiten und der schriftlich verfassten Dissertation beachtet habe und verpflichte mich hiermit, die dort genannten Vorgaben bei allen wissenschaftlichen Tätigkeiten zu beachten und umzusetzen. Ich versichere, dass die eingereichte elektronische Fassung der eingereichten Druckfassung vollständig entspricht.

Teilpublikationen:
Fischer, C., & Saur, J. 2019, Time-variable Electromagnetic Star–Planet Interaction: The TRAPPIST-1 System as an Exemplary Case, The Astrophysical Journal, 872, 113. http://dx. doi.org/10.3847/1538-4357/aafaf2

Köln, 13. Juli 2020

Christian Fischer